



PREPARATION AND OPERATIONS OF THE MISSION PERFORMANCE
CENTRE (MPC) FOR THE COPERNICUS SENTINEL-3 MISSION

S3MPC OPT Annual Performance Report - Year 2020



*Mission
Performance
Centre*



Ref.: S3MPC.ACR.APR.007
Issue: 1.1
Date: 28/04/2021
Contract: 4000111836/14/I-LG

Customer: ESA	Document Ref.: S3MPC.ACR.APR.007
Contract No.: 4000111836/14/I-LG	Date: 28/04/2021
	Issue: 1.1

Project:	PREPARATION AND OPERATIONS OF THE MISSION PERFORMANCE CENTRE (MPC) FOR THE COPERNICUS SENTINEL-3 MISSION		
Title:	S3MPC OPT Annual Performance Report - Year 2020		
Author(s):	L. Bourg and D. Smith with inputs from all OPT ESLs, F. Rouffi, C. Hénocq, J. Bruniquel, C. Cox, M. Etxaluze, E. Polehampton		
Approved by:	O. Lesne, QA Manager	Authorized by	J. Bruniquel, Service Manager
Distribution:	Pierre Féménias and Steffen Dransfeld, ESA + S3MPC		
Accepted by ESA	S. Dransfeld, Deputy TO		P. Féménias, TO
Filename	S3MPC.ACR.APR.007 - i1r1 - OPT Annual Performance Report - Year 2020.docx		

Copyright ©2021 – ACRI-ST

All rights reserved.

No part of this work may be disclosed to any third party translated, reproduced, copied or disseminated in any form or by any means except as defined in the contract or with the written permission of ACRI-ST

ACRI-ST

260 route du Pin Montard

06904 Sophia-Antipolis, France

Tel: +33 (0)4 92 96 75 00 Fax: +33 (0)4 92 96 71 17

www.acri-st.fr

Disclaimer

The work performed in the frame of this contract is carried out with funding by the European Union. The views expressed herein can in no way be taken to reflect the official opinion of either the European Union or the European Space Agency.





Sentinel-3 MPC
S3MPC OPT Annual Performance
Report - Year 2020

Ref.: S3MPC.ACR.APR.007
Issue: 1.1
Date: 28/04/2021
Page: iii

Changes Log

Version	Date	Changes
1.0	26/02/2021	First version
1.1	28/04/2021	FRP results included

List of Changes

Version	Section	Answers to RID	Changes
1.1	2.2.1		Section on SLSTR FRP NTC added in the executive summary
	6.3.2		New section on FRP products

Table of content

1	INTRODUCTION	19
1.1	SCOPE OF THE DOCUMENT	19
1.2	APPLICABLE DOCUMENTS	19
1.3	REFERENCE DOCUMENTS.....	19
1.4	ACRONYMS AND ABBREVIATIONS	19
2	EXECUTIVE SUMMARY	20
2.1	OLCI	20
2.2	SLSTR.....	22
2.2.1	SLSTR-A.....	22
2.2.2	SLSTR-B.....	24
2.3	SYN.....	25
3	PROCESSING BASELINE DESCRIPTION	27
3.1	OLCI	27
3.2	SLSTR.....	28
3.3	SYN.....	29
4	CALIBRATION AND CHARACTERISATION CHANGES	30
4.1	OLCI	30
4.1.1	<i>Instrument settings</i>	30
4.1.2	<i>Evolutions in Radiometric Calibration of EO data</i>	30
4.2	SLSTR.....	30
4.2.1	<i>Instrument settings</i>	30
4.2.2	<i>Evolutions in Radiometric Calibration of EO data</i>	31
5	SUMMARY OF PERFORMANCES – OLCI	32
5.1	INSTRUMENT PERFORMANCES	32
5.1.1	<i>Temperature stability</i>	32
5.1.2	<i>Signal to noise ratio</i>	33
5.1.3	<i>Spectral Calibration</i>	38
5.1.4	<i>Radiometric stability</i>	43
5.1.5	<i>Ageing of radiometric diffuser</i>	47
5.2	L1 PRODUCTS PERFORMANCES	51
5.2.1	<i>Geometric Performance</i>	51
5.2.2	<i>Radiometric Gain Model Performance</i>	58
5.2.3	<i>Radiometric Validation</i>	62
5.3	L2 PRODUCT PERFORMANCES.....	75
5.3.1	<i>Level 2 cloud screening</i>	75
5.3.2	<i>Integrated Water Vapour (IWV)</i>	86
5.3.3	<i>OLCI Global Vegetation Index (OGVI), a.k.a. FAPAR, and OLCI Terrestrial Chlorophyll Index (OTCI)</i>	92
5.3.4	<i>Water leaving Reflectance</i>	104
5.3.5	<i>Case 1 Chlorophyll product (OC4Me)</i>	120
5.3.6	<i>Alternative Atmospheric Correction and products for complex waters</i>	121
5.3.7	<i>Aerosol Optical Thickness and Angström Exponent</i>	124



6	SUMMARY OF PERFORMANCES – SLSTR	131
6.1	INSTRUMENT PERFORMANCES	131
6.1.1	<i>Instrument temperatures</i>	<i>131</i>
6.1.2	<i>Detector Temperatures</i>	<i>133</i>
6.1.3	<i>Scanner performance</i>	<i>137</i>
6.1.4	<i>Black-Bodies</i>	<i>141</i>
6.1.5	<i>VISCAL System</i>	<i>145</i>
6.1.6	<i>IR Channels</i>	<i>146</i>
6.1.7	<i>VIS/SWIR Channels</i>	<i>151</i>
6.2	L1 PRODUCTS PERFORMANCES	162
6.2.1	<i>TIR Channel Calibration</i>	<i>162</i>
6.2.2	<i>VIS/SWIR Channel Calibration</i>	<i>162</i>
6.2.3	<i>Geometric Calibration</i>	<i>173</i>
6.2.4	<i>Cloud Screening</i>	<i>176</i>
6.2.5	<i>References</i>	<i>180</i>
6.3	L2 PRODUCT PERFORMANCES.....	181
6.3.1	<i>Land Surface Temperature (LST)</i>	<i>181</i>
6.3.2	<i>Fire Radiative Power (FRP)</i>	<i>189</i>
7	SUMMARY OF PERFORMANCES – SYN	198
7.1	L1 PRODUCTS PERFORMANCES	198
7.2	L2 PRODUCT PERFORMANCES.....	198
7.2.1	<i>SYN L2 quality assessment: inter-comparisons with ground-based measurements and MODIS</i>	<i>198</i>
7.2.2	<i>SY_2_VGP, SY_2_VG1, SY_2_V10: consistency checks with PROBA-V</i>	<i>202</i>
8	PROBLEMS ENCOUNTERED IN THE REPORTING PERIOD.....	210
8.1	PRODUCT NOTICES REPORTS	210
8.1.1	<i>OLCI</i>	<i>210</i>
8.1.2	<i>SLSTR</i>	<i>210</i>
8.1.3	<i>SYN</i>	<i>210</i>
8.2	INSTRUMENT ANOMALIES.....	211
8.2.1	<i>OLCI</i>	<i>211</i>
8.2.2	<i>SLSTR</i>	<i>211</i>
8.2.3	<i>SYN</i>	<i>212</i>

List of Figures

Figure 1: Daytime combined SLSTR-A and SLSTR-B Level-1 image for visible channels on 23rd January 2021. ----- 25

Figure 2: Evolution of VGT-S product after inclusion of improved composite method.----- 26

Figure 3: long term monitoring of CCD temperatures using minimum value (top), time averaged values (middle), and maximum value (bottom) provided in the annotations of the Radiometric Calibration Level 1 products, for the Shutter frames, all radiometric calibrations so far. ----- 32

Figure 4: long term monitoring of OLCI-B CCD temperatures using minimum value (top), time averaged values (middle), and maximum value (bottom) provided in the annotations of the Radiometric Calibration Level 1 products, for the Shutter frames, all radiometric calibrations so far except the first one (absolute orbit 167) for which the instrument was not yet thermally stable. ----- 33

Figure 5: OLCI-A Signal to Noise ratio as a function of the spectral band for the 5 cameras. These results have been computed from radiometric calibration data. All calibrations except first one (orbit 183) are present with the colours corresponding to the orbit number (see legend). The SNR is very stable with time: the curves for all orbits are almost superimposed. The dashed curve is the ESA requirement. ----- 34

Figure 6: OLCI-A long-term stability of the SNR estimates from Calibration data, example of channel Oa01. ----- 35

Figure 7: OLCI-B Signal to Noise ratio as a function of the spectral band for the 5 cameras. These results have been computed from radiometric calibration data. All calibrations except first one (orbit 167) are presents with the colours corresponding to the orbit number (see legend). The SNR is very stable with time: the curves for all orbits are almost superimposed. The dashed curve is the ESA requirement. ---- 37

Figure 8: OLCI-A camera averaged spectral calibration evolution as a function of absolute orbit number (all spectral S02/S03 calibrations since the beginning of the mission are included except the very first one (1st March 2016, orbit 195)).The data are normalized with the first Spectral Calibration of the plot, which is from 18 April 2016 (orbit 881). The last spectral Calibration is from 12 December 2020 (orbit 25107). ----- 40

Figure 9: OLCI-A line-averaged spectral calibration relative to the one acquired on 4th May 2016 (orbit 1107), as a function of time derived from all S09 sequences. The last calibration is from 12 December 2020 (orbit 25105). For each camera, the spectral evolution derived from spectral lines at 485 nm, 656 nm, 770 nm and 854 nm have been averaged. ----- 40

Figure 10: OLCI-B across track spectral calibration from all S02/S03 sequences since the beginning of the mission. Left top plot is spectral line 1; Right top plot is spectral line 2 and bottom plot spectral line 3. On-ground spectral characterisation is in red. ----- 41

Figure 11: OLCI-B camera averaged spectral calibration evolution as a function of absolute orbit number (all spectral S02/S03 calibrations since the beginning of the mission are included). The data are normalized with the first Spectral Calibration. The first (reference) calibration is from 8 May 2018 (orbit 182), the last from 22 Dec. 2020 (orbit 13856).----- 42

	Sentinel-3 MPC S3MPC OPT Annual Performance Report - Year 2020	Ref.: S3MPC.ACR.APR.007 Issue: 1.1 Date: 28/04/2021 Page: vii
---	---	--

Figure 12: OLCI-B camera averaged spectral calibration evolution as a function of absolute orbit number from S09 calibrations since the beginning of the mission. The last calibration for S09 is from 22 December 2020 (orbit 13854). For each camera, the spectral evolution corresponding derived from spectral lines at 485 nm, 656 nm, 770 nm and 854 nm have been averaged. The data are normalized with the first Spectral Calibration. ----- 42

Figure 13: OLCI-A camera-averaged instrument evolution since channel programming change (25/04/2016) and up to most recent calibration (25/01/2021) versus wavelength.----- 43

Figure 14: OLCI-A camera averaged gain relative evolution with respect to calibration of 25/04/2016 (change of OLCI channel settings), as a function of elapsed time since launch; one curve for each band (see colour code on plots), one plot for each module. The diffuser ageing has been taken into account. Early mission data (16 Feb. to 25 April) is not available due to missing information required for accurate gain computation. ----- 44

Figure 15: OLCI-A gain relative evolution with respect to “best geometry” calibration (22/11/2016), as a function of elapsed time since launch (x axis) and spatial pixel (y axis) for Channel Oa2 (412.5 nm), Camera 1. ----- 45

Figure 16: OLCI-B camera-averaged instrument evolution since channel programming change (18/06/2018) and up to most recent calibration (27/01/2021) versus wavelength.----- 46

Figure 17: OLCI-B camera averaged gain relative evolution with respect to first calibration after channel programming change (18/06/2018), as a function of elapsed time since the beginning of the mission; one curve for each band (see colour code on plots), one plot for each module. The diffuser ageing has been taken into account.----- 47

Figure 18: OLCI-A Diffuser 1 ageing as a function of wavelength (or spectral band). Ageing is clearly visible in spectral band #1 to #6.----- 48

Figure 19: Slope of ageing fit (% of loss per exposure) vs wavelengths, using all the available ageing sequence at the time of the current cycle (#67 = red curve), and at the time of the fifteen previous cycles with an aging sequence (see legend below the curves).----- 49

Figure 20: OLCI-B Diffuser 1 ageing as a function of wavelength (spectral bands). ----- 50

Figure 21: OLCI-B: Slope of ageing fit (% of loss per exposure) vs wavelengths, using all the available ageing sequence at the time of the current cycle (red curve) and at the time of previous cycle for which an ageing sequence was measured (see legend within the figure). ----- 51

Figure 22: overall OLCI-A georeferencing RMS performance time series over the whole monitoring period (left) and number of validated control points corresponding to the performance time series (right) ---- 52

Figure 23: across-track (left) and along-track (right) georeferencing biases time series for Camera 1 (starting 01/03/2018).----- 52

Figure 24: same as Figure 23 for Camera 2.----- 53

Figure 25: same as Figure 23 for Camera 3.----- 53

Figure 26: same as Figure 23 for Camera 4.----- 53



Figure 27: same as Figure 23 for Camera 5.----- 54

Figure 28: OLCI-A spatial across-track misregistration at each camera transition (left) and maximum amplitude of the across-track error within each camera (left).----- 54

Figure 29: OLCI-A spatial along-track misregistration at each camera transition (left) and maximum amplitude of the along-track error within each camera (left).----- 54

Figure 30: overall OLCI-B georeferencing RMS performance time series (left) and number of validated control points corresponding to the performance time series (right) over the whole monitoring period.----- 55

Figure 31: across-track (left) and along-track (right) georeferencing biases time series for Camera 1.--- 56

Figure 32: same as Figure 31 for Camera 2.----- 56

Figure 33: same as Figure 31 for Camera 3.----- 56

Figure 34: same as Figure 31 for Camera 4.----- 57

Figure 35: same as Figure 31 for Camera 5.----- 57

Figure 36: OLCI-B spatial across-track misregistration at each camera transition (left) and maximum amplitude of the across-track error within each camera (left).----- 57

Figure 37: OLCI-B spatial along-track misregistration at each camera transition (left) and maximum amplitude of the along-track error within each camera (left).----- 58

Figure 38: RMS performance of the Gain Model of current Processing Baseline as a function of orbit.-- 59

Figure 39: For the 5 cameras: Evolution model performance, as camera-average and standard deviation of ratio of Model over Data vs. wavelength, for each orbit of the test dataset, including 11 calibrations in extrapolation, with a colour code for each calibration from blue (oldest) to red (most recent).----- 60

Figure 40: RMS performance of the OLCI-B Gain Model of the current processing baseline as a function of orbit.----- 61

Figure 41: For the 5 cameras: Evolution model performance, as camera-average and standard deviation of ratio of Model over Data vs. wavelength, for each orbit of the test dataset, including 11 calibrations in extrapolation, with a colour code for each calibration from blue (oldest) to red (most recent).----- 62

Figure 42: comparison of OSCAR and DIMITRI results for the various methods.----- 63

Figure 43: Time-series of the elementary ratios (observed/simulated) signal from S3A/OLCI for (top to bottom) Band Oa03 and band Oa17 respectively, over Six PICS Cal/Val sites. Dashed-green and orange lines indicate the 2% and 5% biases respectively. Error bars indicate the desert methodology uncertainty.----- 64

Figure 44: Time-series of the elementary ratios (observed/simulated) signal from S3B/OLCI for (top to bottom) Band Oa03 and band Oa17 respectively over Six PICS Cal/Val sites. Dashed-green and orange lines indicate the 2% and 5% biases respectively. Error bars indicate the desert methodology uncertainty.-- 65

Figure 45: The estimated gain values for (top) S3A/OLCI and (bottom) S3B/OLCI from Glint, Rayleigh and PICS methods as a function of wavelength. We use the gain value of Oa8 from PICS method as reference



gain for Sunlint method. Dashed-green and orange lines indicate the 2% and 5% respectively. Error bars indicate the methods uncertainties. ----- 68

Figure-46 : Ratio of observed TOA reflectance to simulated one for MSI-A, MSI-B, OLCI-A and OLCI-B averaged over the six PICS test sites as a function of wavelength.----- 69

Figure 47. New CHL climatology for the Rayleigh calibration sites based CMEMS GlobColour products- 70

Figure 48: OSCAR Rayleigh S3A and S3B Calibration results for 2020 as a function of wavelength. ----- 71

Figure 49: OSCAR Rayleigh OLCI-A Calibration results 2019 and 2020 as a function of wavelength. ----- 71

Figure 50: OSCAR Rayleigh OLCI-B Calibration results for 2019 and 2020 as a function of wavelength. - 72

Figure 51: OSCAR Glitter S3A and S3B Calibration results (adapted to Rayleigh result at 665 nm) for 2019 as a function of wavelength.----- 73

Figure 52: Cloud top height rough estimate for cloud screening and cloud shadow calculation ----- 81

Figure 53: PixBox collection (2019) OLCI-A and OLCI-B ----- 82

Figure 54: Results from 2017 PixBox validation on OLCI-A ----- 83

Figure 55: Validation results of OLCI-A and OLCI-B data using PixBox collection of 2019 ----- 83

Figure 56: Validation results of OLCI-A only (left) and OLCI-B only (right) using PixBox collection of 2019 ----- 84

Figure 57: Laquim et al. (2020) table 2 ----- 84

Figure 58: Validation results of OLCI-A/B (left) and OLCI-A/B flat-fielded and aligned (right) using PixBox collection of 2019----- 85

Figure 59: Validation results of flat-fielded and aligned OLCI-A only (left) and OLCI-B only (right) using PixBox collection of 2019 ----- 85

Figure 60: Upper left: Scatter plot of the IWV products, derived from OLCI A above land and from SUOMI NET GNSS measurements. Upper right: Histogram of the difference between OLCI and GNSS (blue: original OLCI, orange: bias corrected OLCI). Lower left: Temporal evolution of different quality measures (from top to bottom: systematic deviation factor, bias, root mean squared difference (with and without bias correction), explained variance (number in boxes are the numbers of matchups)). Lower right: Positions of the GNSS stations (grey: no valid matchup) ----- 87

Figure 61: Upper left: Scatter plot of the IWV products, derived from OLCI A above land and from AMR MWR. Upper right: Histogram of the difference between OLCI and ARM (blue: original OLCI, orange: bias corrected OLCI). Lower left: Temporal evolution of different quality measures (from top to bottom: systematic deviation factor, bias, root mean squared difference (with and without bias correction), explained variance (number in boxes are the numbers of matchups)). Lower right: Position of ARM SGP. ----- 88

Figure 62: Left: Scatter plot of the IWV products, derived from OLCI A above land and from GRUAN radiosonde measurements. Right: Histogram of the difference between OLCI and GRUAN (blue: original OLCI, orange: bias corrected OLCI). ----- 89

Figure 63: Upper left: Scatter plot of the IWV products, derived from OLCI A above land and from AERONET. Upper right: Histogram of the difference between OLCI and AERONET (blue: original OLCI, orange: bias corrected OLCI). Lower: Positions of the used AERONET stations (grey: no valid matchup). 90

Figure 64: Scatter plot of the IWV products, derived from OLCI B above land and from SUOMI NET GNSS measurements (upper left), from ARM MWR (upper right) and AERONET (lower)----- 91

Figure 65: Time-series OGVI and OTCI and corresponding scatterplot of monthly mean for site IT-Lison, Italy, land cover Cropland. A and C represent S3A; B and D represent S3B. ----- 96

Figure 66: Time-series OGVI and OTCI and corresponding scatterplot of monthly mean for site DE-Hainich, Deutschland, land cover Broadleaved, deciduous, closed. A and C represent S3A; B and D represent S3B.----- 97

Figure 67: Time-series OGVI and OTCI and corresponding scatterplot of monthly mean for site US-Central-Plains, United States, land cover Shrub, closed-open, deciduous. A and C represent S3A; B and D represent S3B.----- 98

Figure 68: Time-series OGVI and OTCI and corresponding scatterplot of monthly mean for site AU-Litchfield, Australia, land cover Broadleaved, evergreen. A and C represent S3A; B and D represent S3B. ----- 99

Figure 69: Time-series OGVI and OTCI and corresponding scatterplot of monthly mean for site BE-Brasschaat, Belgium, land cover Needle-leaved, evergreen. A and C represent S3A; B and D represent S3B. ----- 100

Figure 70: Comparison of OTCI-MTCI (a) and OGVI-MGVI (b). Points in the scatterplot represent the monthly mean of all available S3A and MERIS archive over 42 validation sites. Red and grey lines represent the modelled and 1:1 lines respectively. The scatterplots are updated to include extractions from cycle S3A 67. ----- 101

Figure 71: Global composites of Sentinel-3 OTCI (mean of 2016 to 2019) and Envisat MTCI (mean of 2002 to 2012) values for summer—i.e. Jun, Jul, Aug (a,b)—and spatial distribution of differences (c). Index value frequency distribution (d), density scatterplot of agreement between the two products (e), and frequency distribution of differences (f). For (c) and (f), difference is expressed in percentage computed as the ratio of per pixel absolute difference to the mean. Blue indicates areas where the Sentinel-3 OTCI is greater than the Envisat MTCI, conversely, red indicates areas where the Envisat MTCI is greater than the Sentinel-3 OTCI. Grey pixels are areas where the difference between the Envisat MTCI and Sentinel-3 OTCI is within $\pm 5\%$ ----- 102

Figure 72: Scatterplot of monthly mean for S3A and S3B for site DE-Hainich, land cover – broadleaved deciduous forest. (left: OGVI, right: OTCI) ----- 103

Figure 73: Scatterplot of monthly mean for S3A and S3B for site FR-Aurade, land cover – cropland. (left: OGVI, right: OTCI)----- 104

Figure 74: FR scatter plot of OLCI versus in situ measurements. ----- 108

Figure 75: Band ratio validation between in situ and OLCI A. ----- 108

Figure 76: FR scatter plot of OLCI versus in situ measurements without Annot_DROUT flags----- 111

Figure 77: Taylor diagram, comparison between standard flag extraction (blue) and Annot_DROUT flag not considered (red).----- 112

Figure 78: OLCI camera geometry. ----- 113

Figure 79: Statistics comparison between OLCI 5 cameras without the Annot_DROUT consider (column left) and with all the fleg considers (column right). ----- 116

Figure 80: Validation scatter plot for OLCI B. ----- 118

Figure 81: Band ratio validation between in situ and OLCI B.----- 119

Figure 82: Chlorophyll statistics with HPLC (a), Fluorometric (b) data and Spectrophotometry (c). -- 120

Figure 83 TSM scatter plot comparison with in-situ Turbidity at Warp Cefas SmartBuoy in situ data, conc_tsmv.2 old and new conv were processed with C2RCC within SNAP; TSM_NN v1 and v2 were processed with the Ground Segment----- 122

Figure 84 TSM scatterplot comparisons with TSM in-situ data form the Belgian Monitoring Programme , courtesy of RBINS----- 123

Figure 85: Demonstration of the improvements in resolving chlorophyll changes in clear water condition, due to the changes of the water model in the ongoing work of improving the neural nets. It also shows the improved performance in sun glint conditions.----- 124

Figure 86: Upper left: OLCI aerosol optical thickness at 865nm against AERONET at 870nm, upper right: OLCIs Angström exponent at 865nm against the AERONET Angström exponent at 865nm-440nm. Lower left: Temporal evolution of different quality measures of the optical thickness comparison (from top to bottom: systematic deviation factor, bias, root mean squared difference (with and without bias correction), explained variance (number in boxes are the numbers of matchups)). Lower right: positions of the used AERONET stations.----- 126

Figure 87: Upper left: OLCI aerosol optical thickness at 865nm against Maritime AERONET at 870nm, upper right: OLCIs Angström exponent at 865nm against the Maritime AERONET Angström exponent at 865nm-440nm. Lower right: positions of the used cruises. ----- 127

Figure 88: Upper left: OLCI aerosol optical thickness at 865nm against AERONET v3 L1.5 AOT at 870nm, upper right: OLCIs Angström exponent at 865nm against the AERONET v3 L1.5 Angström exponent at 865nm-440nm. Lower: positions of the used AERONET stations. ----- 129

Figure 89: Baffle temperature trends for SLSTR-A (left) and SLSTR-B (right) from 1st Feb 2020 to end of Jan 2021. The vertical dashed lines indicate the start and end of each cycle.----- 131

Figure 90: OME temperature trends for SLSTR-A (left) and SLSTR-B (right) from 1st Feb 2020 to end of Jan 2021, showing the paraboloid stops and flip baffle (top two plots) and optical bench and scanner and flip assembly (lower two plots). The vertical dashed lines indicate the start and end of each cycle.----- 132

Figure 91: SLSTR-A detector temperatures for each channel from 1st Feb 2020 to end of January 2021. Discontinuities occur for the infrared channels where the FPA was heated for decontamination, and on 14th October when the cold tip temperature was increased. The vertical dashed lines indicate the start and end of each cycle.----- 133

Figure 92: SLSTR-B detector temperatures for each channel from 1st Feb 2020 to end of January 2021. The discontinuity occurs for the infrared channels where the cold tip temperature was increased on 30th March and when the FPA was heated for decontamination in November. The vertical dashed lines indicate the start and end of each cycle. ----- 134

Figure 93: The increase in S8 temperature for SLSTR-A (top) and SLSTR-B (bottom) following recent decontaminations.----- 135

Figure 94: The increase in cooler drive amplitude following recent decontaminations on SLSTR-A (top) and SLSTR-B (bottom). Note that the step in the blue and magenta lines for SLSTR-A and the orange line for SLSTR-B correspond to the points at which the cooler cold tip temperature was increased (the increased temperature requires a lower drive amplitude). ----- 136

Figure 95: SLSTR-A histogram of standard deviation with respect to the linear control law of the scanners and flip mirror in each orbit from February 2020 to February 2021 for nadir view (left) and oblique view (right). ----- 138

Figure 96: SLSTR-A scanner and flip jitter from February 2020 to February 2021, showing mean (red) and stddev (blue) compared to the expected one for the nadir view (left) and oblique view (right). The vertical dashed lines indicate the start and end of each cycle. ----- 138

Figure 97: SLSTR-B histogram of standard deviation with respect to the linear control law of the scanners and flip mirror from February 2020 to February 2021.----- 139

Figure 98: SLSTR-B scanner and flip jitter, showing mean (red) and stddev (blue) compared to the expected one for the oblique view for February 2020 to February 2021. The vertical dashed lines indicate the start and end of each cycle. ----- 140

Figure 99: SLSTR-A blackbody temperature and baseplate gradient trends for Feb 2020 to Jan 2021. The vertical dashed lines indicate the start and end of each cycle. Discontinuities are caused by the decontaminations, and a black-body crossover test. ----- 141

Figure 100: SLSTR-B blackbody temperature and baseplate gradient trends for Feb 2020 to Jan 2021. The vertical dashed lines indicate the start and end of each cycle. Discontinuities are caused by the decontaminations, and a black-body crossover test. ----- 142

Figure 101: SLSTR-A detector counts vs. temperatures at the blackbody cross-over points for the BB cross-over test on 1st and 2nd October 2020. Part 1 of the test is shown on the left and part 2 on the right. -- 144

Figure 102: SLSTR-B detector counts vs. temperatures at the blackbody cross-over points for the BB cross-over test on 28th and 29th September 2020. Part 1 of the test is shown on the left and part 2 on the right. ----- 144

Figure 103: BT differences vs time for all of the blackbody cross-over tests performed to date (including pre-launch measurements) for SLSTR-A (left) and SLSTR-B (right). The part 1 crossover is shown in the top plots, and part 2 in the lower plots. Different symbols indicate different channels (S7: square, S8: triangle, S9: diamond) and different colours indicate nadir (red) and oblique (blue) views. Error bars are derived from the blackbody temperature gradients and standard deviations of the BB signals during the cross-over.----- 145



Figure 104: Variation of the SLSTR-A and SLSTR-B VISCAL peak width during the last two years of operations for the nadir (black/green) and oblique (red/blue) views. ----- 146

Figure 105: SLSTR-A gain (left) and offset (right) trends for the TIR channels in nadir view. The different colour symbols show the response for each of the detector elements and integrators in the channels. The discontinuities are due to the decontamination (February and May 2020) and the cold tip temperature increase (October 2020).----- 147

Figure 106: SLSTR-B gain (left) and offset (right) trends for the TIR channels in nadir view. The different colour symbols show the response for each of the detector elements and integrators in the channels. The discontinuities are due to the cold tip temperature increase (March 2020), the decontamination (November 2020), and in the offset plot only, for the update of dynamic range in August 2020. ----- 147

Figure 107: Ratio between nadir and oblique view gains for TIR channels for SLSTR-A (left) and SLSTR-B (right). The different colour symbols show each of the detector elements and integrators in the channels. ----- 148

Figure 108: NEDT trend for the thermal channels for SLSTR-A (left) and SLSTR-B (right). Blue points were calculated from the cold blackbody signal and red points from the hot blackbody.----- 149

Figure 109: Gain trend for VIS channels (nadir view) for SLSTR-A. The data have been adjusted to allow for the variation of the solar intensity. The oscillations in the signal are due to the build-up of a thin condensation layer causing a thin film interference effect. The different colour symbols show the response for each of the 4 detector elements in the VIS channels.----- 152

Figure 110: Gain trend for SWIR channels (nadir view) for SLSTR-A. Outliers in the plots are due to gaps in LO data or decontamination cycles. The different colour symbols show the response for each of the 8 detector elements of the A and B stripes of the SWIR channels.----- 153

Figure 111: Gain trend for VIS channels (nadir view) for SLSTR-B. The data have been adjusted to allow for the variation of the solar intensity. The oscillations in the signal are due to the build-up of a thin condensation layer causing a thin film interference effect. The different colour symbols show the response for each of the 4 detector elements in the VIS channels.----- 154

Figure 112: Gain trend for SWIR channels (nadir view) for SLSTR-B. Outliers in the plots are due to gaps in LO data or decontamination cycles. The different colour symbols show the response for each of the 8 detector elements of the A and B stripes of the SWIR channels.----- 155

Figure 113: Dark signal trend for VIS channels (nadir view) for SLSTR-A. The different colour symbols show the signal for each of the 4 detector elements in the VIS channels. The gaps in February and May are due to the decontaminations.----- 156

Figure 114: Dark signal trend for SWIR channels (nadir view) for SLSTR-A. The different colour symbols show the signal for each of the 8 detector elements of the A and B stripes of the SWIR channels. The gaps in February and May are due to decontaminations and the step in October is due to the cooler cold tip temperature increase.----- 157

Figure 115: Dark signal trend for VIS channels (nadir view) for SLSTR-B. The different colour symbols show the signal for each of the 4 detector elements in the VIS channels. ----- 158



Figure 116: Dark signal trend for SWIR channels (nadir view) for SLSTR-B. The different colour symbols show the signal for each of the 8 detector elements in the SWIR channels. The step on 30th March is due to the cooler cold tip temperature increase and the discontinuity in November is due to the decontamination.----- 159

Figure 117: SLSTR-A VIS and SWIR channel signal-to-noise. Different colours indicate different detectors. ----- 160

Figure 118: SLSTR-B VIS and SWIR channel signal-to-noise. Different colours indicate different detectors. ----- 160

Figure 119 Condensation layer thickness throughout the mission for SLSTR-A (blue) and SLSTR-B (red) ----- 161

Figure 120: Comparisons of SLSTR-A S1-S3 and S5a and S5b channels vs. the corresponding channels for AATSR over desert sites. ----- 164

Figure 121: Inter-comparisons between SLSTR-A and OLCI VIS channels for all desert sites in nadir view. ----- 165

Figure 122: Inter-comparisons between SLSTR-A and MODIS NIR and SWIR channels in nadir view.---- 166

Figure 123: Comparisons of SLSTR-B S1-S3 and S5a and S5b channels vs. the corresponding channels for AATSR over desert sites. ----- 167

Figure 124: Inter-comparisons between SLSTR-B and OLCI VIS channels for all desert sites in nadir view. ----- 168

Figure 125: Inter-comparisons between SLSTR-B and MODIS VIS and SWIR channels in nadir view. ---- 169

Figure 126: SLSTR-A measured radiance with respect to the computed radiance over sun-glints using radiative transfer models for the Nadir view. ----- 170

Figure 127: SLSTR-B measured radiance with respect to the computed radiance over sun-glints using radiative transfer models for the Nadir view. ----- 170

Figure 128: Summary of comparisons of SLSTR VIS/SWIR channel reflectances vs. Reference methods used to provide vicarious correction factors.----- 172

Figure 129: Daily offset results from the GEOCAL Tool analysis for Nadir view along and across track (top two plots) and Oblique view along and across track (bottom two plots) for SLSTR-A. ----- 174

Figure 130: Daily offset results from the GEOCAL Tool analysis for Nadir view along and across track (top two plots) and Oblique view along and across track (bottom two plots) for SLSTR-B. ----- 175

Figure 131: S3A cloud identification confusion matrices for matchups. Left shows daytime data and right shows night-time data.----- 178

Figure 132: S3B cloud identification confusion matrices for matchups. Left shows daytime data and right shows night-time data.----- 179

Figure 133: A time series of the total number of matchups indicated to be 'clear-sky' by the Basic and Bayesian masks for each of the 4 SST algorithms for SLSTR-A. The number of matchups with an SST bias > 3K is also plotted, as this can be indicative of unidentified cloud. ----- 180

	Sentinel-3 MPC S3MPC OPT Annual Performance Report - Year 2020	Ref.: S3MPC.ACR.APR.007 Issue: 1.1 Date: 28/04/2021 Page: xv
---	---	---

Figure 134: In situ validation of S3A SL_2_LST product at twelve “Gold Standard” stations for the period 1st February 2020 to 31st January 2021.----- 183

Figure 135: In situ validation of S3B SL_2_LST product at twelve “Gold Standard” stations for the period 1st February 2020 to 31st January 2021.----- 184

Figure 136: Monthly daytime LST difference between S3A SL_2_LST and operational SEVIRI from LSA SAF for each month from February 2020 to January 2021. Top row from left to right: Feb 2020, Mar 2020, Apr 2020, May 2020, Jun 2020, Jul 2020. Bottom row from left to right: Aug 2020, Sep 2020, Oct 2020, Nov 2020, Dec 2020, Jan 2021.----- 187

Figure 137: Monthly night-time LST difference between S3A SL_2_LST and operational SEVIRI from LSA SAF for each month from February 2020 to January 2021. Top row from left to right: Feb 2020, Mar 2020, Apr 2020, May 2020, Jun 2020, Jul 2020. Bottom row from left to right: Aug 2020, Sep 2020, Oct 2020, Nov 2020, Dec 2020, Jan 2021.----- 187

Figure 138: Monthly daytime LST difference between S3B SL_2_LST and operational SEVIRI from LSA SAF for each month from February 2020 to January 2021. Top row from left to right: Feb 2020, Mar 2020, Apr 2020, May 2020, Jun 2020, Jul 2020. Bottom row from left to right: Aug 2020, Sep 2020, Oct 2020, Nov 2020, Dec 2020, Jan 2021.----- 188

Figure 139: Monthly night-time LST difference between S3B SL_2_LST and operational SEVIRI from LSA SAF for each month from February 2020 to January 2021. Top row from left to right: Feb 2020, Mar 2020, Apr 2020, May 2020, Jun 2020, Jul 2020. Bottom row from left to right: Aug 2020, Sep 2020, Oct 2020, Nov 2020, Dec 2020, Jan 2021.----- 188

Figure 140: Comparison of fire clusters FRP [MW] between MODIS MOD14 and SLSTR with F1_ON (circles) and F1_OFF (crosses) options. The lines represent robust linear regressions (RLM) with 0.05 confidence intervals (CI).----- 192

Figure 141: Comparison of fire clusters with FRP lower than 1000 MW between MODIS MOD14 and SLSTR with F1_ON (circles) and F1_OFF (crosses) options. The lines represent robust linear regressions (RLM) with the corresponding Standard Deviation (SD) intervals.----- 194

Figure 142: Summary of Omissions and Commissions errors (top), and fire pixels detected by both sensors (bottom) with the F1_OFF option.----- 195

Figure 143: Summary of Omissions and Commissions errors (top), and fire pixels detected by both sensors (bottom) with the F1_ON option. ----- 196

Figure 144: Comparison of the distribution of fire clusters FRP for MODIS and SLSTR F1_ON (top) and F1_OFF (bottom). The line represent estimations kernel densities underlying the observed distributions. ----- 197

Figure 145 : AOD (550nm) matchups between SYNERGY L2 data and AERONET in-situ measurements for (a) S3A and (b) S3B. ----- 199

Figure 146: NDVI value obtained for the 8 scenes included in the dataset used for the SYN L2 quality assessment. This NDVI value is computed using OLCI NIR and RED top of atmosphere radiance normalized by the solar irradiance. Colorbars are the same for all scenes, from 0 to 0.8. ----- 200

Figure 147: Inter-comparison between normalized SYN SDR (Oa17) products and normalized SDR MODIS (b2) products over the 8 reference scenes. ----- 201

Figure 148: Number of pairwise TOA observations used in the intercomparison between SY_VGP and PROBA-V L2A from 01/07/2020 – 30/09/2020. ----- 203

Figure 149: Sentinel-3 SYN VGT tiles over Europe and Africa (green), PROBA-V coverage since July 2020 (yellow), 10°x10° tiles considered in the intercomparison (red) ----- 204

Figure 150: Temporal evolution of the occurrence frequency of quality flags for SY_VG1 S3A (left) and S3B (middle) in comparison to PROBA-V S1 (right) over a 10°x10° tile located in Western Europe (01-10/10/2020)----- 206

Figure 151: Systematic difference (left) and mean bias (right) between SY_VGP and PROBA-V L2A per band and per S3 sensor (01-10/10/2020)----- 206

Figure 152: Systematic difference (left) and mean bias (right) between SY_V10 and PROBA-V S10 per band and per S3 sensor (01/07/2020 – 30/09/2020) ----- 207

Figure 153: Statistical consistency of SY_V10 NDVI vs. PROBA-V S10 NDVI: scatter density plots and GM regression (left), bias frequency plots (right)----- 208

Figure 154: OLCI anomalies/events in 2020----- 211

Figure 155: SLSTR anomalies/events in 2020----- 212

Figure 156: SYN anomalies/events in 2020----- 213

List of Tables

Table 1: OLCI Processing Baseline ----- 27

Table 2: SLSTR Processing Baseline----- 28

Table 3: SYN Processing Baseline ----- 29

Table 4: OLCI-A SNR figures as derived from Radiometric Calibration data. Figures are given for each camera (time average and standard deviation), and for the whole instrument. The requirement and its reference radiance level are recalled (in $\text{mW}\cdot\text{sr}^{-1}\cdot\text{m}^{-2}\cdot\text{nm}^{-1}$).----- 36

Table 5: OLCI-B SNR figures as derived from Radiometric Calibration data. Figures are given for each camera (time average and standard deviation), and for the whole instrument. The requirement and its reference radiance level are recalled (in $\text{mW}\cdot\text{sr}^{-1}\cdot\text{m}^{-2}\cdot\text{nm}^{-1}$).----- 38

Table 6: Synthesis of the DIMITRI results: estimated gain values for S3A/OLCI from Glint, Rayleigh and PICS over the period January 2020- January 2021. ----- 65

Table 7: Synthesis of the DIMITRI results: estimated gain values for S3B/OLCI from Glint, Rayleigh and PICS over the period January 2020- January 2021. ----- 66

Table 8: S3ETRAC Rayleigh Calibration sites ----- 69



Table 9: Overview of the OSCAR Rayleigh and Glitter calibration results for S3A and S3B for 2019-----	74
Table 10: Validation sites analysed in report S3A 67/S3B 48. Land cover data from GLC2000 grouped according to the International Geosphere-Biosphere Programme (IGBP) designations. -----	94
Table 11: Comparison statistics between monthly S3A/B OLCI land products and MERIS archive data. -	95
Table 12: Comparison statistics between monthly S3A/B OLCI land products. -----	103
Table 13: Summary of OLCI-A FR statistics. -----	108
Table 14: Summary of OLCI FR statistics without Annot_DROUT flags. -----	111
Table 15: FR statistics over April 2016 - June 2020 FR data for camera 1.-----	114
Table 16: FR statistics over April 2016 - June 2020 FR data for camera 2.-----	114
Table 17: FR statistics over April 2016 - June 2020 FR data for camera 3.-----	114
Table 18: FR statistics over April 2016 - June 2020 FR data for camera 4.-----	114
Table 19: FR statistics over April 2016 - June 2020 FR data for camera 5.-----	115
Table 20: OCLI B Validation Statistics -----	119
Table 21: SLSTR-A scanner and flip mirror jitter statistics (each year runs from February to February). 137	
Table 22: SLSTR-B scanner and flip mirror jitter statistics (each year runs from February to February). 139	
Table 23: NEDT for SLSTR-A in cycles 054-067 averaged over all detectors for both Earth views towards the hot +YBB (top) and the cold -YBB (bottom). -----	149
Table 24: NEDT for SLSTR-B in cycles 035-048 averaged over all detectors for both Earth views towards the hot +YBB (top) and the cold -YBB (bottom) -----	150
Table 25: The list of these sites and their geographical limits -----	163
Table 26: Summary of Vicarious Radiometric Calibration Results performed by all groups. Comparisons are performed by comparing the measured reflectance vs. reference reflectance. Results presented here are the ratios R_{meas}/R_{ref} . -----	171
Table 27: Proposed VIS-SWIR Calibration Adjustments Based on Vicarious Calibration analysis. Note S4 is not included because the vicarious calibration techniques do not extend to this band. -----	173
Table 28: Statistics of In situ validation for S3A SL_2_LST product at twelve “Gold Standard” stations for the period 1 st February 2020 to 31 st January 2021 -----	185
Table 29: Statistics of In situ validation for SL_2_LST product at twelve “Gold Standard” stations for the period 1 st February 2020 to 31 st January 2021 -----	186
Table 30: Statistics of monthly LST difference between SLSTR-A and SLSTR-B SL_2_LST and operational SEVIRI from LSA SAF over Africa for each month from February 2020 to January 2021 -----	189
Table 31: Comparison of FRP retrieval between MODIS and SLSTR using the F1_ON and F1_OFF option. -----	191
Table 32: Statistical indicators between AERONET and SYN L2 Aerosol Optical Thickness-----	199

	Sentinel-3 MPC S3MPC OPT Annual Performance Report - Year 2020	Ref.: S3MPC.ACR.APR.007 Issue: 1.1 Date: 28/04/2021 Page: xviii
---	---	--

Table 33: Correlation and unbiased root mean square error for the reference normalised SDR. ----- 202

Table 34: Occurrence frequency of quality flags over land pixels for SY_VG1 derived from S3A and S3B in comparison to PROBA-V S1, over 6 10°x10° tiles (01-10/10/2020) ----- 205

Table 35: Occurrence frequency of quality flags over land pixels for SY_V10 derived from S3A and S3B in comparison to PROBA-V S10, over 6 10°x10° tiles, 01/07/2020 – 30/09/2020 ----- 206

Table 36: List of OLCI Product Notices issued in 2020 ----- 210

Table 37: List of SLSTR Product Notices issued in 2020 ----- 210

Table 38: List of SYN Product Notices issued in 2020 ----- 210



1 Introduction

This document is the Year 3 (year 2019) Annual Performance Report version of the MPC Optical report prepared by the ACRI-ST consortium for the realisation of the “Preparation and Operations of the Mission Performance Centre (MPC) for the Copernicus Sentinel-3 Mission”, ESA contract 4000111836/14/I-LG.

1.1 Scope of the document

This document provides a summary of the end-to-end mission performance from the 1st of January 2020 until the 31st of December 2020 carried out by the S3 Mission Performance Centre during the fourth year of the routine operations phase.

It addresses more specifically activities related to the Optical mission (an equivalent report – S3MPC.CLS.APR.008 – is issued to address STM activities).

1.2 Applicable documents

The full Applicable Documents (AD) ID correspondence is provided in the Configuration Item Data List (S3MPC.ACR.LST.002).

1.3 Reference documents

The full Reference Documents (RD) ID correspondence is provided in Configuration Item Data List (S3MPC.ACR.LST.002).

1.4 Acronyms and abbreviations

The definition of the acronyms and abbreviations used in this document is provided in the List of Acronyms and Definitions (S3MPC.ACR.LST.003).

2 Executive Summary

2.1 OLCI

Instrument performance

The OLCI-A and OLCI-B **instrument health is excellent**. The sensors temperatures are perfectly well controlled. The nominal radiometric diffusers ageing shows the expected magnitude and spectral behaviours: around 0.5% after 5 years for OLCI-A at 400 nm (Oa01), down to 0.1% at 560 nm (Oa06) and undetectable above; below 0.35% for OLCI-B. The **instrument sensitivity evolution so far is limited to less than 3% (OLCI-A)** and no evidence of severe degradation can be demonstrated: the variation of the instrument sensitivity seems more correlated with a potential spectral evolution of the correcting filters – inside the spectrometers – than to darkening of the optics or loss of sensitivity of the CCD sensors. Sensitivity **evolution of OLCI-B is similar to that of OLCI-A**, and maybe with a slightly higher magnitude for the 400 nm channel (up to 4%). The regularly monitored instrument **SNR performance is well within requirement**.

Spectral Calibration is monitored thanks to dedicated acquisition campaigns. The in-flight spectral campaigns reveal a **high agreement of the in-flight characterisation with the pre-flight** spectral calibration for both A and B sensors, with differences of the OLCI channels centre **smaller than 0.1 nm**, except for channels Oa01 (400 nm) and Oa21 (1020 nm), with up to 0.2 nm. A **small temporal evolution** is observed, different for each camera but approximately identical at all wavelengths; the **observed changes for OLCI-A after 4 years are smaller than 0.15 nm** (except camera 5 at 0.23 nm); observed changes for OLCI-B are within 0.25 nm for all cameras.

Level 1 products performance

The **geometric performance** is monitored using the ESA GeoCal tool CFI. It is currently **fully compliant for OLCI-A and OLCI-B** to the 0.5 pixel RMS requirement. However, a **significant along-track drift of OLCI-B cameras has been assessed, requiring frequent geometric re-calibration**.

The **OLCI-A and OLCI-B Radiometric Gain Models** (gain at reference date + time drift) are used to calibrate Earth Observation data at any date. Their current **performance is better than 0.1% RMS** (0.12 for OLCI-B channel Oa01).

Absolute and inter-band calibration performance is monitored by indirect methods over natural targets. Three methods are used within S3-MPC: the “Rayleigh” method (molecular atmospheric backscattering over clear sky off-glinc open ocean) provides absolute calibration in the blue-to-red spectral domain; the “Glinc” method (spectral dependency of the Sun specular reflection over ocean) provides inter-band calibration; and the PICS method (Pseudo-Invariant Calibration Sites, temporally stable desert areas) provides absolute calibration over the whole spectral domain as well as cross-mission comparisons for sensors with comparable channels. Two of these methods, Rayleigh and Glinc, are undertaken by two different implementations providing very consistent results.



All methods point out an excess of brightness for OLCI-A radiances. Results are in pretty close agreement **around 2-3%** between 560 and 900 nm (Oa06 to Oa19). Rayleigh gives higher biases in the blue-green (about 6 % while PICS remains around 2%) but this method is suspected to overestimate the simulated signal at those wavelengths so PICS are considered more reliable. Channel Oa21 (1020 nm) is only addressed by the Glint interband method and the results are much worse: 3 to 7%, depending on the reference band. **Radiometric validation for OLCI-B indicates performance within the 2% requirement** for all bands from 560 nm (Oa05) to 940 nm (Oa20). As for OLCI-A, the PICS method shows compliance also in the blue region (Oa1 to Oa4, 400 to 510 nm) while the Rayleigh method shows biases of about 3 to 5%, depending on implementation. The OLCI-B 1020 nm (Oa21) has a similar performance than its OLCI-A counterpart.

Level 2 products performance

Integrated Water Vapour

Integrated Water Vapour has been validated against available in-situ data, according to the surface type: GNSS and AERONET networks over Land, AERONET (coastal stations), AERONET-OC and AERONET Maritime networks over water.

Validation demonstrates that the product is of high quality (bias corrected RMS difference of ~ 0.8 to 1.5 kg/m²) for retrievals above land surfaces, but there is a systematic overestimation of 9% to 13%. Validation for OLCI-B gives similar results.

The comparison with GNSS stations close to water shows a larger wet bias for the ocean retrievals (up to 25%), and in particular in transition zones between glint and off glint.

Land Products

OLCI Global Vegetation Index (O-GVI, a.k.a. FAPAR)

Quantitative validation against in-situ data is not possible so far, as no in-situ station provides directly comparable products. Several specific campaigns have been conducted however, and significant efforts are undertaken to generate adequate in-situ data. In the meantime, **OLCI FAPAR is regularly compared to MERIS 10-years climatology. There is a fairly good agreement**, accounting for the methodology limitations, with **high correlation, > 0.9** (when sufficient dynamics are present) **and good RMSD (<0.1)**.

OLCI Terrestrial Chlorophyll Index (O-TCI)

For the same reason as for O-GVI, no quantitative validation against in-situ data is available and **comparison with MERIS TCI (M-TCI) climatology** has been done over a number of sites, **showing high correlation, > 0.9** (when sufficient dynamics are present) **and good RMSD (<0.1)**.



Marine Products

Water-Leaving reflectances

OLCI-A Level 2 product **validation against in situ measurements shows very good results up to 560 nm**. 665nm band shows poor statistics, longer wavelengths are not validated due to the lack of in situ data.

OLCI-B Level 2 product validation show much more performance, as expected since System Vicarious Calibration has not been applied yet.

Case 1 Chlorophyll product (CHL_OC4Me)

In situ chlorophyll concentration derived from HPLC analysis shows slight overestimation for higher values. Chlorophyll-a measurement shows some estimation errors, however this bias could be due to the low variability for in the HPLC in situ values (0.1-1 mg.m⁻³). More measurement needs to be gathered in order to have a better insight of OLCI estimation on oligotrophic waters.

OLCI-B Level 2 product validation is not available due to lack of in-situ data.

Aerosol Optical Thickness and Angstrom Exponent (T865 and A865)

The validation of OLCI-A aerosol products shows a **high agreement for the aerosol optical thickness** ($r^2 = 0.7$, $rmsd < 0.02$), if the systematic overestimation of around 40% is corrected. The **Angstrom Exponent agrees with less accuracy** ($r^2 = 0.2$) but the order of magnitude (1.6) is almost met (bias = -0.2).

OLCI B shows the same pattern as for OLCI A. However, the number of matchups with maritime AERONET is still too low to reach valid quantitative results.

2.2 SLSTR

2.2.1 SLSTR-A

Instrument performance

The SLSTR-A instrument has performed exceptionally well for another year, with all parameters within safe limits. There have been no major anomalies, and only short gaps in data coverage due to ground station issues, manoeuvres or calibration observations.

The cooler has been performing well, with the IR detectors maintained at a stable temperature. The cooler cold tip temperature was increased by 1K in October 2020, and this should increase the time between decontaminations.

Radiometric noise levels for the TIR and VIS/SWIR channels have remained stable throughout at pre-launch values. NEDT for the S8 and S9 channels are below 20 mK with no indication of degradation.



Blackbody temperatures have shown a seasonal cycle on top of the daily/orbital temperature cycles, with the highest temperatures reached during December. The maximum temperature has increased only slightly compared to the previous year, and will be monitored carefully to prevent it reaching the limit of 305 K necessary to avoid the S7 saturation level.

The VISCAL system is illuminated by the Sun once per orbit and Vicarious calibration results suggest that the system is not degrading significantly over time. The stability is much better than that observed for AATSR on ENVISAT.

The scanners continue to perform well, with orbital mean deviation from the expected position for both nadir and oblique scanners less than 1.5", and a standard deviation less than 7". The flip mirror orbital mean deviation is less than 1" with a standard deviation <8" in the nadir position and <14" in oblique position. The worst instantaneous jitter encountered is as good, or better, than previous years.

Level 1 products performance

Validation of the absolute radiometric calibration of the IR channels has been carried out at EUMETSAT using comparisons against IASI-A and B in 2018. The stability of the flight gains, radiometric noise and instrument temperatures suggest that the calibration has not drifted significantly since then.

The VIS and SWIR channels are calibrated via an on-board Solar diffuser-based calibration system. Evaluation of the radiometric calibration has used the techniques developed for AATSR and MERIS and show that the calibration system is stable. Assessment of the VIS channels S1-S3 show good agreement with OLCI and AATSR. At the SWIR wavelengths, there is a significant discrepancy between SLSTR and AATSR and MODIS that must be taken into account in any L2 processing. An adjustment to the L1 processing to correct the main calibration difference is foreseen. The root cause of the anomaly has not been found and is still under investigation.

Geometric calibration is monitored using the GEOCAL tool. Average absolute geometric offsets <0.1 km are achieved for the nadir view and oblique view across-track and <0.2 km for the oblique view along-track.

Level 2 products performance

Land Products

The SLSTR-A SL_2_LST product from SLSTR went operational in the Sentinel 3 PDGS on 5th July 2017 with PB 2.16. No additional updates to the retrieval algorithm have been implemented in the IPF since. However, Processing Baseline 2.29 released on 4th April 2018 included the new Probabilistic Cloud Mask implemented in the IPF at Level-1 and carried through to Level-2. Furthermore, from 26th February 2019 an updated ADF of retrieval coefficients has been implemented in PB 2.47, IPF 06.14. An updated probabilistic cloud coefficients ADF was applied on 23rd October 2020 in PB 2.73. Matchups against twelve "Gold Standard" in situ stations show that the overall absolute daytime accuracy is 0.98 K and the absolute night-time accuracy is 0.56 K, both of which are within the mission requirements for LST. Comparisons with respect to the operational LSA SAF LST product are within the uncertainty range when considering



the uncertainties from the reference products, and thus the products can be interpreted as consistent with each other. Overall, the SL_2_LST product is performing in line with the 1 K mission requirement for LST.

The **SLSTR FRP NTC** product (both SLSTR-A and SLSTR-B) has been released to the public on the 19th August 2020. The current processing baseline for SLSTR-A FRP products is v2.70 and for SLSTR-B is v1.46. The baseline was deployed in the Land processing centres on 28th July 2020 for SLSTR-A and for SLSTR-B. At present, the algorithm is predominantly delivering active fire detections and FRP data from night-time (ascending node) S3A and S3B overpasses, as the S7 (middle infrared) channel saturates frequently over warm surfaces during day-time. The current configuration makes use of the F1_ON option for the processing, contrary to the NRT product which uses the F1_OFF option. An inter-comparison with MODIS MOD14 products, matched with similar overpass time and restricted to the central portion of the swath, has shown good agreement for the overall FRP distribution and active fire detection. SLSTR appears to detect consistently more small fires than MODIS, i.e. fires with very low FRP, and exhibits 7% and 35% rates of errors of omission and commission, respectively. The comparison of fire clusters detected by both sensors (MODIS and SLSTR) shows agreement in their distribution, although SLSTR exhibits a negative bias of 18.2 MW per cluster, possibly affected by the different overpass time, by the IFOV value, and by the position of fire pixels in the swath. A second inter-comparison performed using the F1_OFF option, showed similar results, although the performance with the F1_ON option is more in line with the detections from MODIS.

2.2.2 SLSTR-B

Instrument performance

Instrument and blackbody temperatures for SLSTR-B have been stable on top of the daily/orbital and seasonal trends, and consistent with those for SLSTR-A. The cooler has been performing well, with the IR detectors maintained at a stable temperature. The cooler cold tip temperature was increased by 2K in March 2020, and this should increase the time between decontaminations.

The visible channel radiometric gain shows a variation from orbit to orbit especially in channels S1 and S2. The reason for this behaviour is thought to be due to partial motional chopping of the VIS detectors by an internal aperture in the VIS FPA. If this is correct, the effect will be present on the earth scene data for S1 and S2.

The NEDT levels are roughly consistent between SLSTR-A and SLSTR-B, except for F1, which shows more orbit-to-orbit variation and higher noise values. This may be caused by motional chopping of the SLSTR-B F1 detectors, which are known to be close to edge of the aperture for SLSTR-B.

The SLSTR-B scanner and flip mean and standard deviations from their expected positions are broadly consistent with SLSTR-A, although the oblique scanner has a slightly larger mean deviation of <3".

Level 1 products performance

Initial validation of the absolute radiometric calibration of the IR channels has been carried out by EUMETSAT using comparisons against IASI-A and B. Analysis from the tandem phase comparisons show that the in-flight calibration of SLSTR-B is consistent with that of SLSTR-A.

The S3A and S3B satellites are configured to be 140 degrees out of phase in order to observe complimentary portions of the earth. Figure 1 shows an example combined Level-1 SLSTR-A/SLSTR-B image (daytime only) to show the combined daily SLSTR coverage.

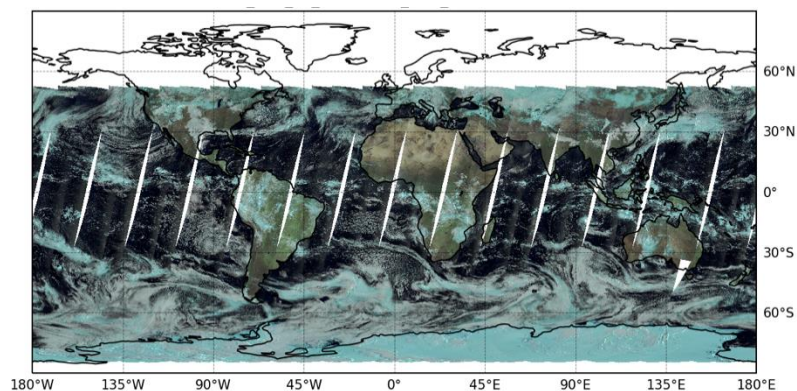


Figure 1: Daytime combined SLSTR-A and SLSTR-B Level-1 image for visible channels on 23rd January 2021.

Level 2 products performance

Land Products

The S3B SL_2_LST product from SLSTR went operational in the Sentinel 3 PDGS on 26th February 2019 with PB 1.19 IPF 06.14. An updated probabilistic cloud coefficients ADF was applied on 23rd October 2020 in PB 1.50. Matchups against ten "Gold Standard" in situ stations show that the overall absolute daytime accuracy is 0.90 K and the absolute night-time accuracy is 0.50 K, both of which are within the mission requirements for LST. As for SLSTR-A, comparisons with respect to the operational LSA SAF LST product are within the uncertainty range when considering the uncertainties from the reference products, and thus the products can be interpreted as consistent with each other. Overall, the SL_2_LST product is performing in line with the 1 K mission requirement for LST.

Regarding the **SLSTR FRP NTC** products, please refer to the SLSTR-A section.

2.3 SYN

Following the evolutions implemented in the SYNERGY L2 and VGS softwares, quality assessments have been re-conducted at the end of year 2018 and confirmed **the clear improvement of the SYN L2 and SYN VGT-P like products**. In particular, the correlation between the Aerosol Optical Thickness data provided by SYN L2 and provided by AERONET stations are close and, despite a bias of 0.2 due to remaining cloud contamination, a regression slope of 1.12 can be drawn comparing these two datasets. Similarly, we

observe a **high correspondence between TOA reflectances provided by SYN VGT-like products and the ones provided by PROBA-V products**. A regression slope close to 1 is observed on the BLUE, Red and NIR radiometric measurements. For SWIR measurements however, systematic large differences are observed and could be linked to the SLSTR calibration of SWIR channels.

Several major improvements have been progressively brought to the SYN L2 products during the year 2018. Besides several bugs corrected on the cloud handling and on the handling of Sun Zenith Angles, the global quality of the SYN L2 and SYN VGT like products have been increased as a result of:

1. **A reduction of cloud contamination** with a more appropriate filtering of the cloudy pixels
2. **A discarding of the pixels flagged as affected by snow** from the aerosol retrieval section
3. An inclusion of the **CAMS reanalysis for climatologically filled pixels**
4. **The alignment between SYN VGT-like processing module and PROBA-V processing module** in terms of projection on the 1 km Plate-Carrée grid and in terms of VGT-S composite method

The composite method has been improved by the addition of relevant selection rules before the “maximum-NDVI” selection. Similarly, the projection on the 1 km Plate-Carrée is no longer performed through the duplication of the nearest neighbor but by a stretched bi-cubic interpolation. These two evolutions improve the handling of border pixels in the VGT-like products, decrease the level of noise and provide smoother visual aspect as well as better geographical details in composite products.

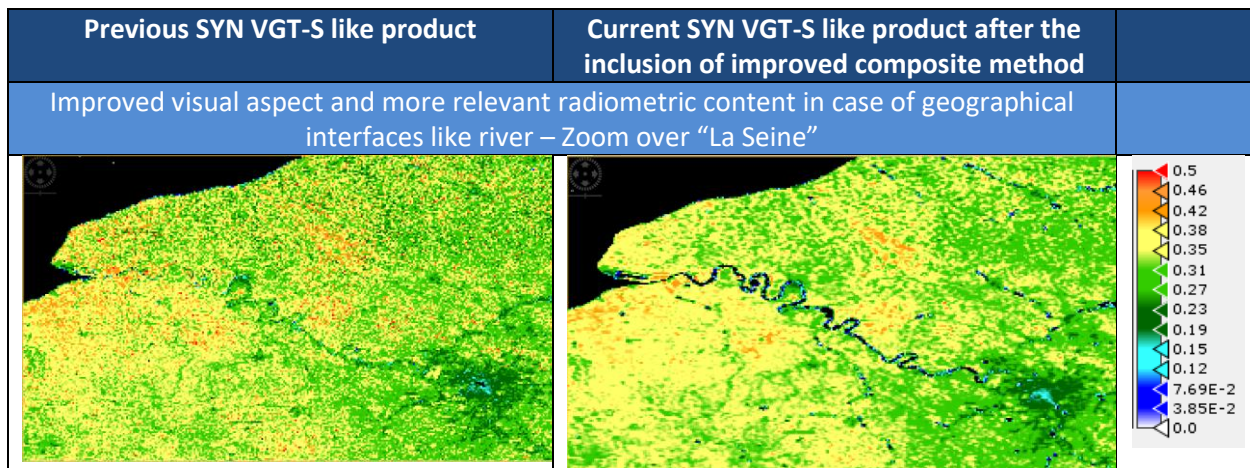


Figure 2: Evolution of VGT-S product after inclusion of improved composite method.

3 Processing baseline description

This section lists all processing baselines that have been delivered between the 1st of February 2017 and the 31st of December 2019, corresponding to year 1, year 2 and year 3 of the routine phase of the MPC contract.

3.1 OLCI

All OLCI processing baselines are listed in Table 1.

Table 1: OLCI Processing Baseline

Processing Baseline	Delivered to PDGS	Deployed in Land PDGS	Changes
S3B: 1.38	01/04/2020	16/04/2020	<ul style="list-style-type: none"> ▪ S3B OLCI Level 1 ADF update <ul style="list-style-type: none"> ○ Dark correction LUT ▪ Geometric calibration
S3A: 2.71 S3B: 1.48	24/09/2020	15/10/2020	<ul style="list-style-type: none"> ▪ S3A OL_1 <ul style="list-style-type: none"> ○ Gain model ○ Dark correction LUT ▪ S3B OL_1 <ul style="list-style-type: none"> ○ Gain model ▪ Dark correction LUT
S3A: 2.74 S3B: 1.51	06/11/2020	10/12/2020	<ul style="list-style-type: none"> ▪ OLCI L1 EO v06.09 ▪ SIIIMPC-4717: OLCI Dark Correction Source and inclusion of IPPVMs in OL_1_CAL_AX
S3B: 1.52	20/11/2020	10/12/2020	<ul style="list-style-type: none"> ▪ S3B OLCI Level 1 ADF update ▪ Geometric calibration

3.2 SLSTR

All SLSTR processing baselines are listed in Table 2.

Table 2: SLSTR Processing Baseline

Processing Baseline	Delivered to PDGS	Deployed in Land PDGS	Changes
2.59 / 1.31	11-Oct-2019	15-Jan-2020	<ul style="list-style-type: none"> ▪ Revised ortho-regridding of all channels and revised geo-referencing of SLSTR F1 fire channel ▪ Improved geometric calibration for the oblique view ▪ Improved S7 BT upper limit, temporal ▪ Interpolation of ECMWF meteorological fields ▪ Improved quality checks during decontamination and black body crossover tests ▪ Removal of the c stripe (time domain integrated) from product, improved flags, and update of several NetCDF variable attributes. ▪ Baseline collection (parameter within the filename) has been incremented from 003 to 004 due to the implementation of the new regridding and the change in the product format.
2.61 / 1.33	22-Nov-2019	15-Jan-2020	<ul style="list-style-type: none"> ▪ Disable SLSTR c-stripe images ▪ SLSTR L1/L2 Products Baseline Collection (BC) set to 004 ▪ Correction of incorrect IPF implementation of probabilistic cloud mask
1.40-B	30-Apr-2020	9-Jun-2020	<ul style="list-style-type: none"> ▪ This version corrects the upper BT limit for the SLSTR-B S7 oblique view channel.
2.70 / 1.46	10-Jul-2020	19-Aug-2020	<ul style="list-style-type: none"> ▪ New SLSTR FRP delivered in NTC timeliness
2.73 / 1.50	23-Oct-2020	12-Nov-2020	<ul style="list-style-type: none"> ▪ Update the SLSTR L1 probabilistic cloud mask ADF

3.3 SYN

All SYN processing baselines are listed in Table 3.

Table 3: SYN Processing Baseline

Processing Baseline	Delivered to PDGS	Deployed in Land PDGS	Changes
S3A: 2.40 S3B: 1.11	06/09/2018	13/09/2018	<ul style="list-style-type: none"> ▪ First public version
S3A: 2.44 S3B: 1.16	13/12/2018	16/01/2019 (SY2) 21/01/2019 (SY2_VGS)	<ul style="list-style-type: none"> ▪ New IDEPIX cloud flags now used in VGT-P/K products ▪ Correction of AG variable (T550) over ocean set to zero instead of fill value ▪ Correction of NDVI set to 0 instead of _FillValue over ocean in VG products ▪ Improving VGS composite method
S3A: 2.51 S3B: 1.23	24/05/2019	06/06/2019	<ul style="list-style-type: none"> ▪ Corrections of <ul style="list-style-type: none"> ○ Synergy wrong generation of time.nc values ○ Typo in some SYN VGT-P /VGT-S attributes ○ SY_2_SYN products missing SLSTR oblique scans ○ SY_2_VGK products with wrong footprint

4 Calibration and characterisation changes

4.1 OLCI

4.1.1 Instrument settings

There has been no change to the OLCI-A or OLCI-B instrument setting during the reporting period.

4.1.2 Evolutions in Radiometric Calibration of EO data

4.1.2.1 OLCI-A

The following evolutions of the EO radiometric calibration auxiliary data have been implemented since beginning of 2020:

- ❖ 15/10/2020: PB S3A-2.71 updated the Radiometric Gain Models and Dark Correction tables
- ❖ 10/12/2020: PB S3A-2.74 updated the Source of the Dark Correction Tables through an IPF update.

4.1.2.2 OLCI-B

The following evolutions of the EO radiometric calibration auxiliary data have been implemented since beginning of 2020:

- ❖ 16/04/2020: PB S3B-1.38 updated Dark Correction tables
- ❖ 15/10/2020: PB S3B-1.48 updated the Radiometric Gain Models and Dark Correction tables
- ❖ 10/12/2020: PB S3B-1.51/1.52 updated the Source of the Dark Correction Tables through an IPF update.

4.2 SLSTR

4.2.1 Instrument settings

4.2.1.1 SLSTR-A

The SLSTR-A cooler cold tip temperature was increased by 1K on 14th October 2020. This increased the temperature of the SWIR and TIR detectors accordingly (see Section 6.1.2). A subsequent adjustment was made to the S8 detector offset voltage to correct the lower limit of the dynamic range on 26th January 2021.



4.2.1.2 SLSTR-B

The SLSTR-B cooler cold tip temperature was increased by 2K on 30th March 2020. This increased the temperature of the SWIR and TIR detectors accordingly (see Section 6.1.2). A subsequent adjustment was made to the S8 and S9 detector offset voltages to correct the lower limit of the dynamic range on 5th August 2020.

4.2.2 Evolutions in Radiometric Calibration of EO data

No updates to the SLSTR-A or SLSTR-B radiometric calibration parameters have been applied in the reporting period.

5 Summary of performances – OLCI

5.1 Instrument performances

5.1.1 Temperature stability

5.1.1.1 OLCI-A

CCD temperatures are monitored on the long-term using data from Radiometric Calibration acquisitions (see Figure 3). Variations are very small (0.09 C peak-to-peak) and no trend can be identified.

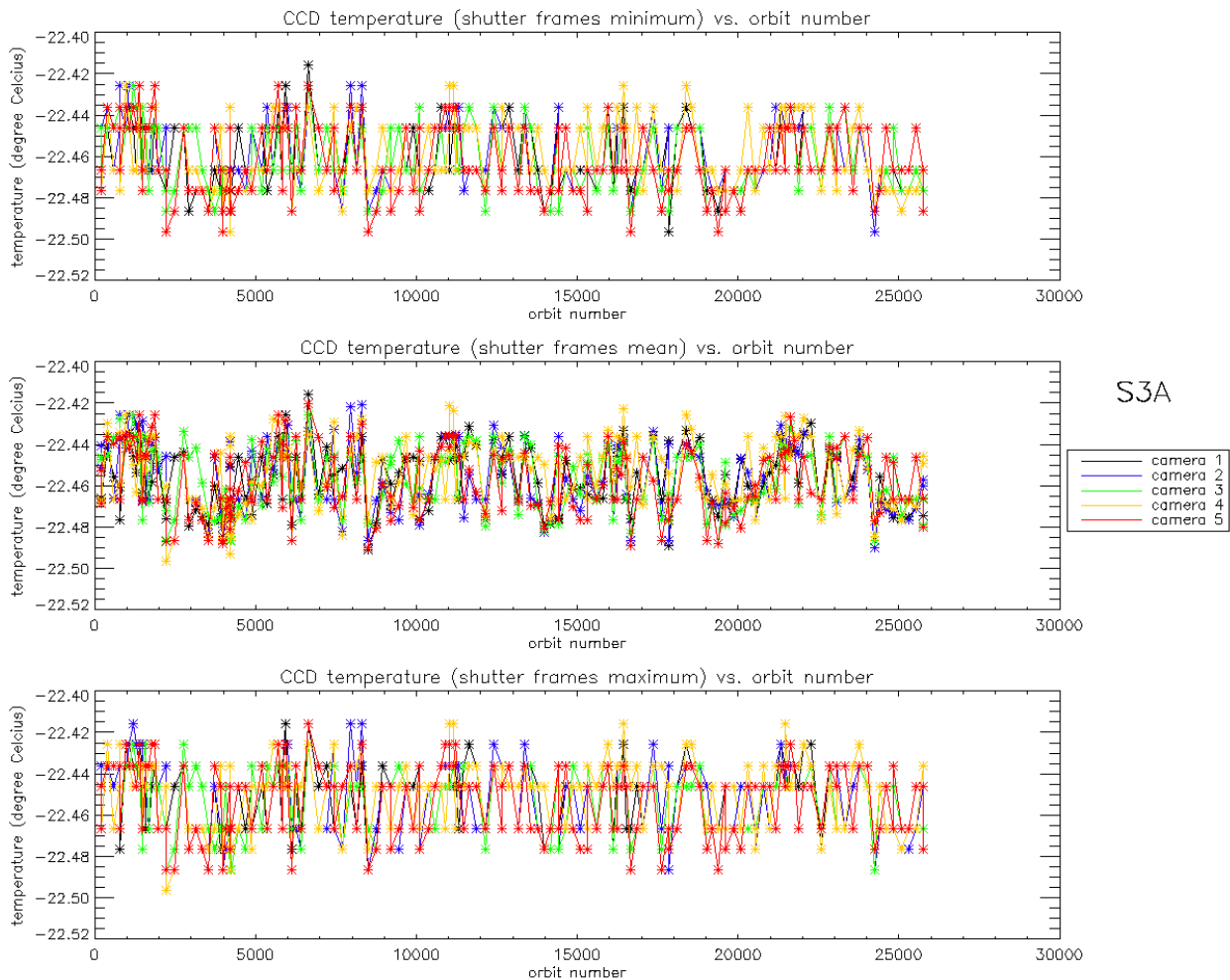


Figure 3: long term monitoring of CCD temperatures using minimum value (top), time averaged values (middle), and maximum value (bottom) provided in the annotations of the Radiometric Calibration Level 1 products, for the Shutter frames, all radiometric calibrations so far.

5.1.1.2 OLCI-B

As for OLCI-A, the variations of CCD temperature are very small (0.08 C peak-to-peak) and no trend can be identified.

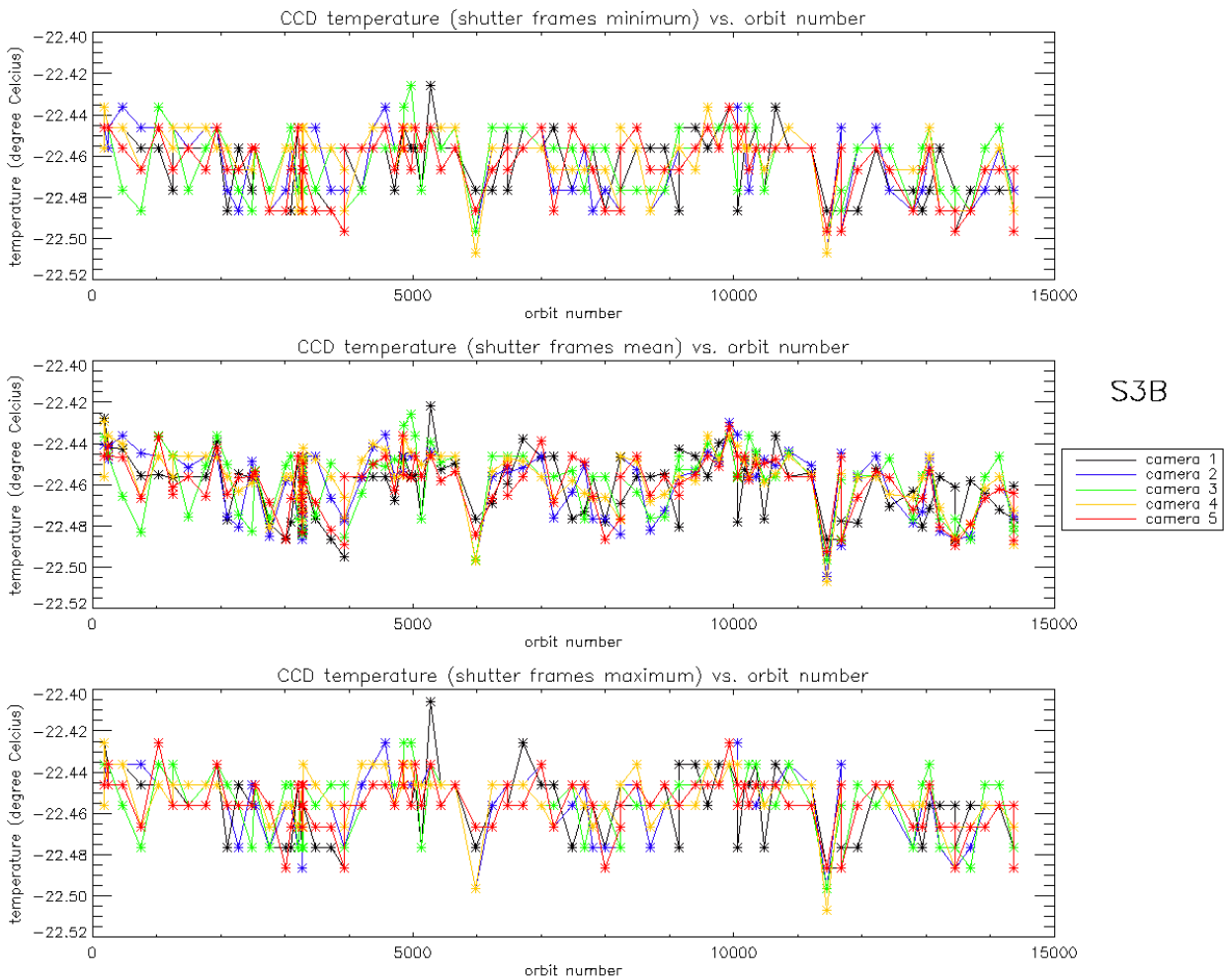


Figure 4: long term monitoring of OLCI-B CCD temperatures using minimum value (top), time averaged values (middle), and maximum value (bottom) provided in the annotations of the Radiometric Calibration Level 1 products, for the Shutter frames, all radiometric calibrations so far except the first one (absolute orbit 167) for which the instrument was not yet thermally stable.

5.1.2 Signal to noise ratio

5.1.2.1 OLCI-A

OLCI signal to noise ratio (SNR) is monitored using Radiometric Calibration data acquired on the radiometric diffuser that provides a signal smoothly varying with time. After correction for the variation due to the variation of the illumination with illumination geometry during the 24 seconds of acquisitions, variability is assessed and SNR is derived, as the incoming radiance is known. SNR values obtained at the

Calibration signal level are then downscaled to a typical clear sky ocean signal level, as defined in the mission requirements.

SNR computed for all radiometric calibration data is presented on Figure 5 as a function of band number. Stability with time is shown on Figure 6: SNR of band Oa01 (400nm, the most varying) is plotted against orbit number.

There is no significant evolution of this parameter over the mission and the ESA requirement is fulfilled for all bands.

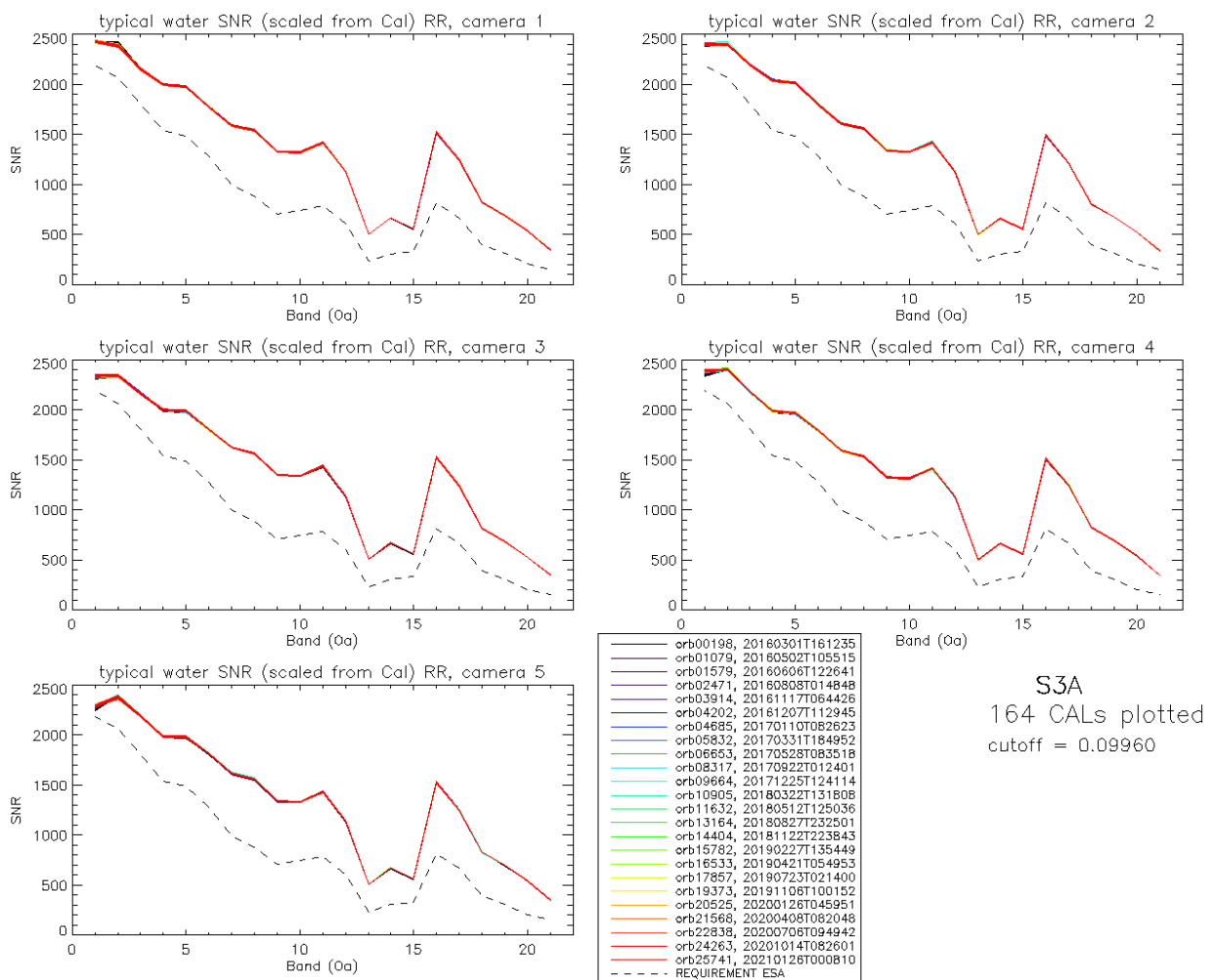


Figure 5: OLCI-A Signal to Noise ratio as a function of the spectral band for the 5 cameras. These results have been computed from radiometric calibration data. All calibrations except first one (orbit 183) are present with the colours corresponding to the orbit number (see legend). The SNR is very stable with time: the curves for all orbits are almost superimposed. The dashed curve is the ESA requirement.

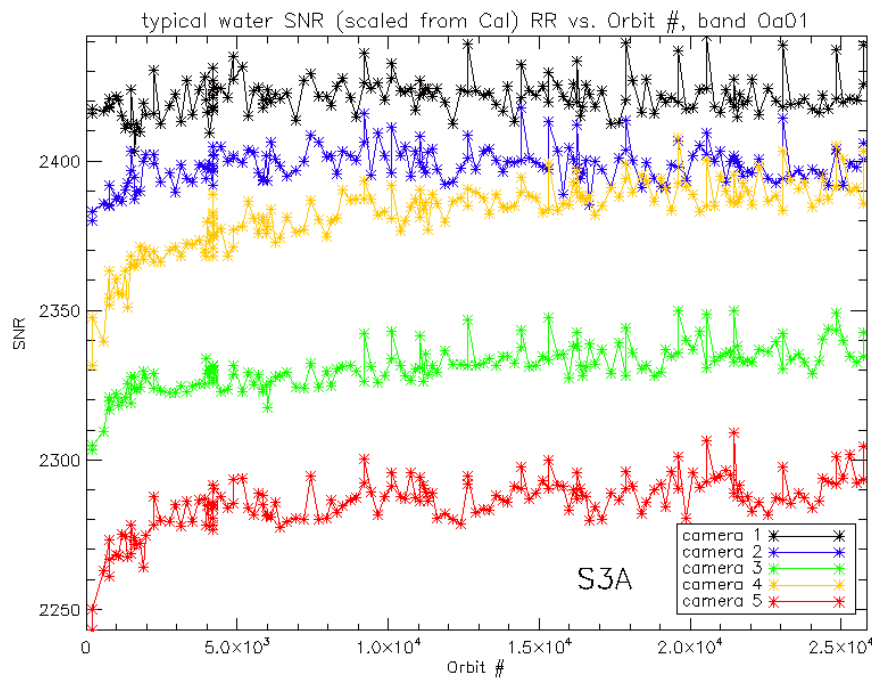


Figure 6: OLCI-A long-term stability of the SNR estimates from Calibration data, example of channel Oa01.

The mission averaged SNR figures are provided in Table 4, together with their radiance reference level. According to the OLCI SNR requirements, these figures are valid at these radiance levels and at Reduced Resolution (RR, 1.2 km). They can be scaled to other radiance levels assuming shot noise (CCD sensor noise) is the dominating term, i.e. radiometric noise can be considered Gaussian with its standard deviation varying as the square root of the signal: $SNR(L) = SNR(L_{ref}) \cdot \sqrt{\frac{L}{L_{ref}}}$. Following the same assumption, values at Full Resolution (300 m) can be derived from RR ones as 4 times smaller.

Table 4: OLCI-A SNR figures as derived from Radiometric Calibration data. Figures are given for each camera (time average and standard deviation), and for the whole instrument. The requirement and its reference radiance level are recalled (in $mW.sr^{-1}.m^{-2}.nm^{-1}$).

nm	L _{ref} LU	SNR RQT	C1		C2		C3		C4		C5		All	
			avg	std	avg	std	avg	std	avg	std	avg	std	avg	std
400.000	63.0	2188	2421	6.3	2398	6.3	2331	7.6	2381	12.1	2285	9.3	2363	7.0
412.000	74.1	2061	2389	9.0	2405	6.3	2339	4.8	2401	5.0	2381	8.8	2383	5.2
442.000	65.6	1811	2159	5.6	2197	5.9	2164	4.9	2185	4.1	2194	5.5	2180	3.9
490.000	51.2	1541	2000	4.6	2036	5.0	1997	4.2	1984	4.4	1988	4.7	2001	3.3
510.000	44.4	1488	1979	5.3	2014	4.8	1985	4.6	1967	4.5	1985	4.4	1986	3.6
560.000	31.5	1280	1776	4.5	1802	4.1	1803	4.8	1794	3.9	1819	3.4	1799	3.0
620.000	21.1	997	1591	4.0	1609	4.2	1624	3.2	1593	3.2	1615	3.5	1606	2.6
665.000	16.4	883	1546	4.2	1557	4.4	1567	3.8	1533	3.6	1561	3.8	1553	3.1
674.000	15.7	707	1328	3.4	1337	3.6	1350	2.8	1323	3.2	1342	3.6	1336	2.5
681.000	15.1	745	1319	3.7	1326	3.1	1338	2.7	1314	2.5	1333	3.5	1326	2.2
709.000	12.7	785	1420	4.2	1420	4.0	1435	3.4	1414	3.4	1431	3.1	1424	2.8
754.000	10.3	605	1127	3.1	1121	2.9	1135	3.3	1125	2.5	1139	2.8	1129	2.3
761.000	6.1	232	502	1.1	498	1.1	505	1.2	500	1.1	508	1.4	503	0.9
764.000	7.1	305	663	1.6	658	1.6	668	2.1	661	1.5	670	2.1	664	1.4
768.000	7.6	330	558	1.5	554	1.3	562	1.3	557	1.4	564	1.3	559	1.0
779.000	9.2	812	1516	4.8	1498	4.7	1526	5.2	1511	5.0	1526	5.1	1515	4.2
865.000	6.2	666	1244	3.5	1213	3.5	1239	4.0	1246	3.5	1250	2.8	1238	2.8
885.000	6.0	395	823	1.7	801	1.6	814	1.9	824	1.5	831	1.7	819	1.1
900.000	4.7	308	691	1.6	673	1.3	683	1.6	693	1.5	698	1.5	688	1.0
940.000	2.4	203	534	1.2	522	1.1	525	0.9	539	1.1	542	1.3	532	0.7
1020.000	3.9	152	345	0.9	337	0.8	348	0.7	345	0.8	351	0.8	345	0.5

5.1.2.2 OLCI-B

As for OLCI-A there is no significant evolution of the SNR over the mission and the ESA requirement is fulfilled for all bands.

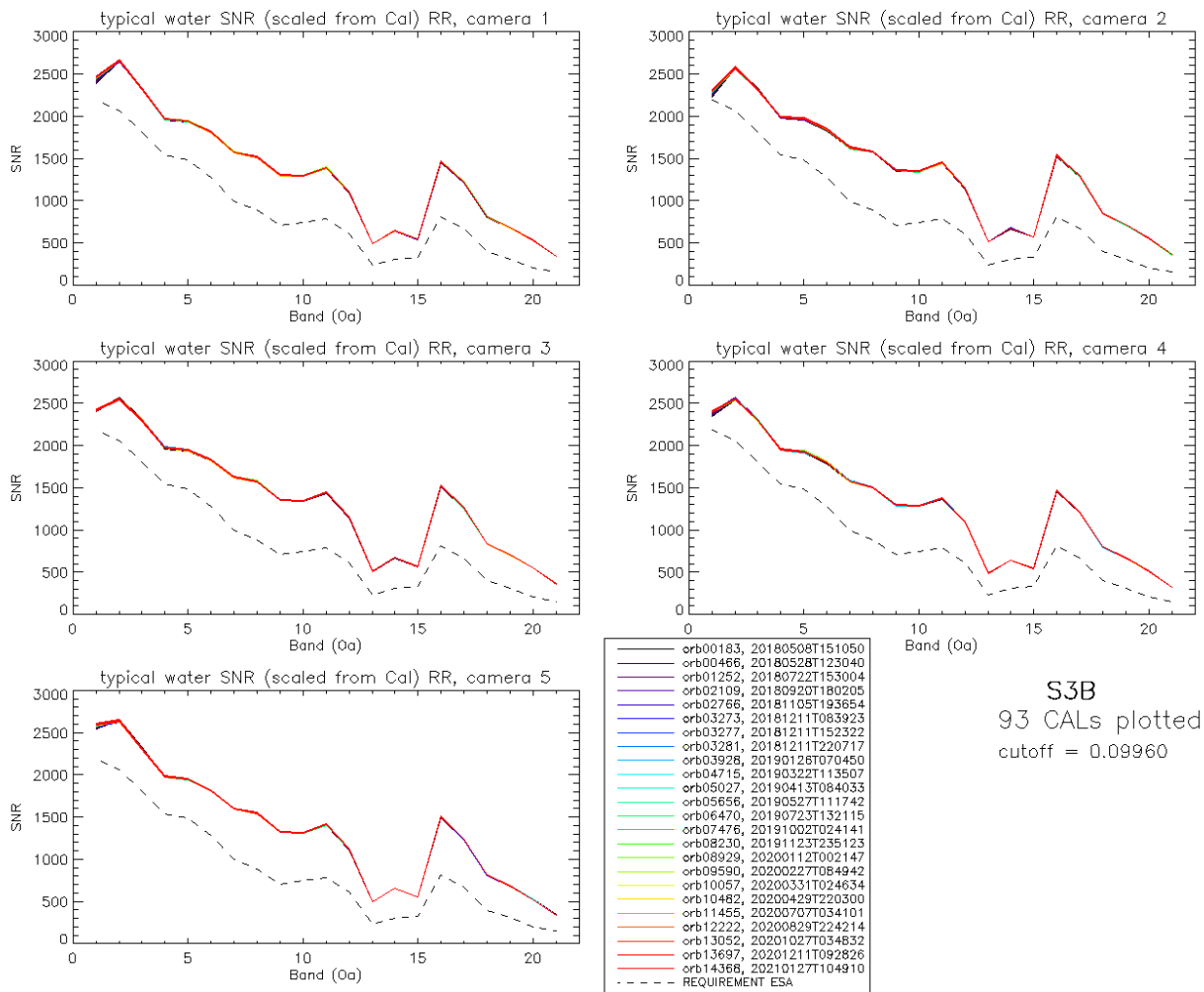


Figure 7: OLCI-B Signal to Noise ratio as a function of the spectral band for the 5 cameras. These results have been computed from radiometric calibration data. All calibrations except first one (orbit 167) are presents with the colours corresponding to the orbit number (see legend). The SNR is very stable with time: the curves for all orbits are almost superimposed. The dashed curve is the ESA requirement.

As for OLCI-A, the mission averaged SNR figures are provided in Table 5 below, together with their radiance reference level.

Table 5: OLCI-B SNR figures as derived from Radiometric Calibration data. Figures are given for each camera (time average and standard deviation), and for the whole instrument. The requirement and its reference radiance level are recalled (in $mW.sr^{-1}.m^{-2}.nm^{-1}$).

nm	L _{ref}	SNR	C1		C2		C3		C4		C5		All	
	LU	RQT	avg	std	avg	std	avg	std	avg	std	avg	std	avg	std
400.000	63.0	2188	2449	20.0	2289	17.1	2418	6.0	2392	13.7	2581	13.6	2426	13.0
412.000	74.1	2061	2655	6.6	2570	6.0	2546	8.4	2550	6.0	2639	7.0	2592	5.0
442.000	65.6	1811	2325	6.3	2318	5.8	2301	6.3	2304	6.2	2310	6.1	2312	5.1
490.000	51.2	1541	1966	4.6	1989	5.6	1972	4.8	1952	4.7	1979	4.8	1971	3.8
510.000	44.4	1488	1938	4.9	1967	5.8	1943	4.9	1923	5.1	1952	4.8	1944	4.1
560.000	31.5	1280	1813	5.0	1847	5.4	1829	4.7	1804	5.1	1817	4.3	1822	3.9
620.000	21.1	997	1573	4.2	1626	4.7	1625	3.9	1576	3.8	1601	3.3	1600	2.9
665.000	16.4	883	1513	4.2	1579	3.8	1574	4.0	1501	3.2	1546	4.0	1543	2.9
674.000	15.7	707	1301	3.8	1358	3.8	1353	3.4	1292	2.7	1328	3.1	1327	2.4
681.000	15.1	745	1293	3.7	1347	3.3	1343	3.0	1285	2.8	1316	2.8	1317	2.2
709.000	12.7	785	1390	4.2	1447	4.3	1443	4.3	1373	3.0	1412	4.0	1413	3.2
754.000	10.3	605	1096	4.0	1142	3.9	1142	3.8	1089	2.9	1116	3.5	1117	3.2
761.000	6.1	232	487	1.3	509	1.3	508	1.4	485	1.2	497	1.5	497	1.1
764.000	7.1	305	643	1.7	672	2.0	672	1.9	641	1.6	657	1.9	657	1.5
768.000	7.6	330	541	1.6	567	1.5	564	1.4	541	1.4	554	1.7	553	1.2
779.000	9.2	812	1467	4.5	1534	4.9	1526	5.7	1466	4.1	1506	4.7	1500	4.1
865.000	6.2	666	1221	3.7	1287	3.8	1258	3.8	1205	3.8	1238	3.0	1242	3.0
885.000	6.0	395	808	2.4	847	1.9	834	2.0	799	1.8	814	2.2	820	1.6
900.000	4.7	308	679	1.5	714	2.0	704	1.7	669	1.5	683	1.5	690	1.2
940.000	2.4	203	527	1.3	549	1.6	551	1.3	510	1.2	522	1.3	532	0.9
1020.000	3.9	152	336	0.8	358	1.1	358	0.8	318	0.8	339	1.0	342	0.6

5.1.3 Spectral Calibration

5.1.3.1 OLCI-A

OLCI's spectral characteristics are regularly monitored in-flight by different spectral campaigns, which are shortly outlined in the following. A detailed description is given in *S3-TN-ESA-OL-660*. The procedures use the programming capability of OLCI to define 45 bands around stable spectral features, to characterize

the spectral dispersion of each camera system with respect to the spectral dimension and the spatial (across track) dimension. Simulations of OLCI measurements in the 45 bands are optimized for best agreement with the spectral features, as a function of individual bandwidth and band centre wavelength. Depending on the used spectral feature the achieved accuracy for the centre wavelength is in the order of 0.1-0.2 nm, the precision (repeatability) is better than 0.05 nm.

Three different calibration sequences **S0*** are used regularly:

- ❖ **S09**: The 45 bands are grouped around the atmospheric oxygen absorption band at 770 nm and around distinct solar Fraunhofer lines at 485 nm, 656 nm and 854 nm. To increase the feature stability, the same few hundred frames are acquired at the same orbit cycle (number 24), belonging to Libyan Desert. Since the end of the commissioning phase in June 2016, four S09 campaigns have been performed.
- ❖ **S02/S03**: The 45 bands are grouped around three spectral features of the on-board spectral diffusor at 405 nm, 520 nm and 800 nm. 500 frames are acquired on the white diffusor (**S02**) as reference and on the spectral (so called pink) diffusor (**S03**). Since the end of the commissioning phase in June 2016 three **S02/S03** campaigns have been performed.
- ❖ **S02 solar**: Solely the white diffusor data is used to identify and utilize solar Fraunhofer lines and to provide therewith a spectral characterization independent from the on-board spectral diffusor.

The spectral campaigns performed during and after the commissioning phase reveal a high agreement of the in-flight characterisation with the pre-flight spectral calibration. The resulting differences of the centre wavelengths of the nominal OLCI bands between pre- and in-flight calibration are smaller than 0.1 nm, despite of band 1 and 21, where differences ≤ 0.2 nm have been detected.

A small temporal evolution can be observed since the first in-flight characterisation. This is shown in Figure 8 (S02/S03) and Figure 9 (S09), where the camera mean spectral distance to its value since respectively orbit 881 (April 2016) and orbit 1107 (May 2016) is plotted.

The evolution of the centre wavelength is different for each camera but approximately the same for all wavelengths. Since the end of the commissioning phase (June 2016, \sim orbit 1800) the observed changes are smaller than 0.15 nm (0.23 nm for camera 5).

We see that the long-term evolution of the spectral calibration obtained with sequence S09 is in rather good agreement with the one obtained with sequence S02/S03.

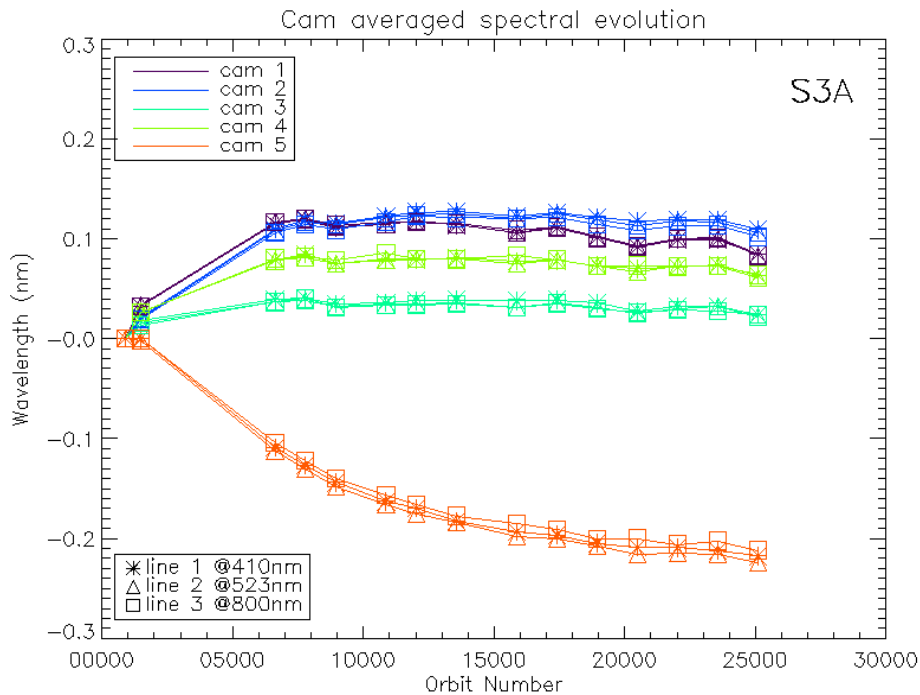


Figure 8: OLCI-A camera averaged spectral calibration evolution as a function of absolute orbit number (all spectral S02/S03 calibrations since the beginning of the mission are included except the very first one (1st March 2016, orbit 195)). The data are normalized with the first Spectral Calibration of the plot, which is from 18 April 2016 (orbit 881). The last spectral Calibration is from 12 December 2020 (orbit 25107).

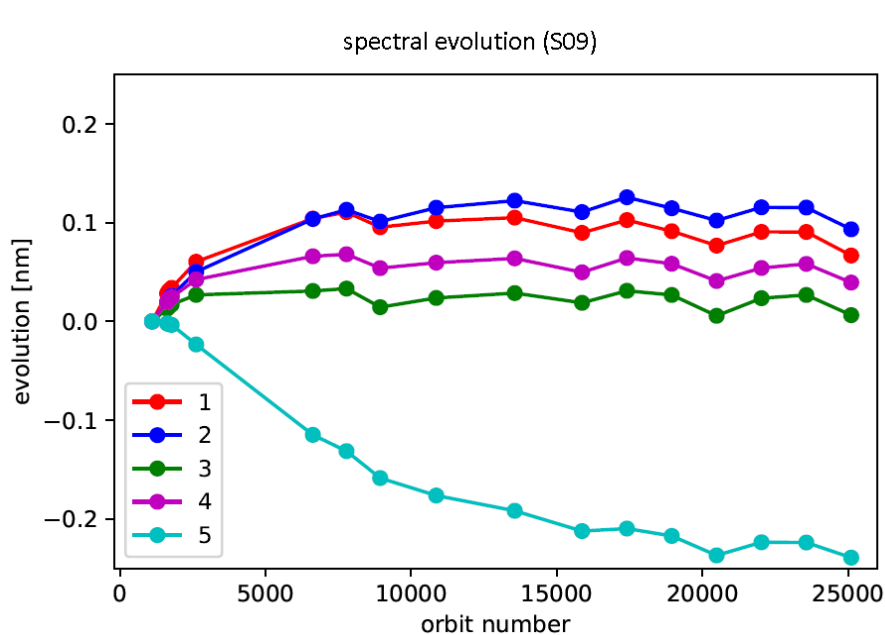


Figure 9: OLCI-A line-averaged spectral calibration relative to the one acquired on 4th May 2016 (orbit 1107), as a function of time derived from all S09 sequences. The last calibration is from 12 December 2020 (orbit 25105). For each camera, the spectral evolution derived from spectral lines at 485 nm, 656 nm, 770 nm and 854 nm have been averaged.

5.1.3.2 OLCI-B

ACT profiles of absolute spectral calibration obtained with all S02/S03 sequences, including comparison with on-ground characterisation, are plotted in Figure 10 showing the very good agreement between pre-flight and in-flight spectral calibrations. Differences are roughly < 0.2 nm except for line 3 camera 2, which is < 0.3 nm.

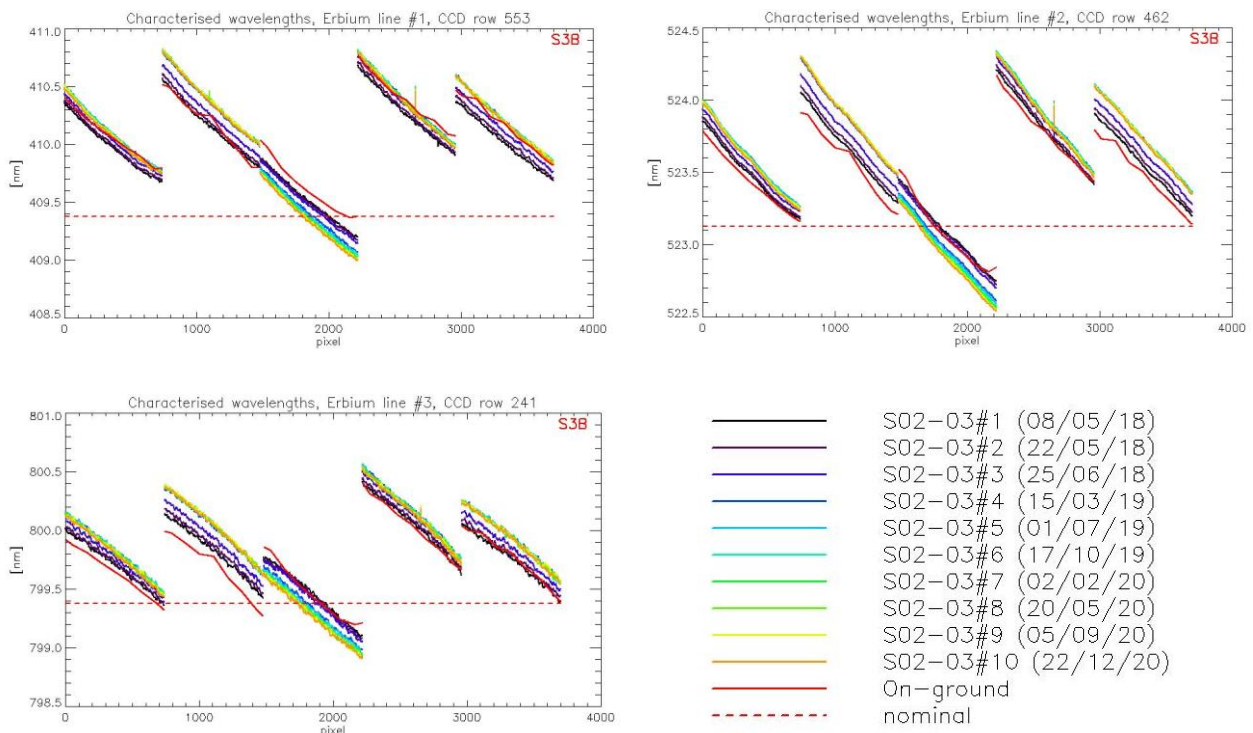


Figure 10: OLCI-B cross track spectral calibration from all S02/S03 sequences since the beginning of the mission. Left top plot is spectral line 1; Right top plot is spectral line 2 and bottom plot spectral line 3. On-ground spectral characterisation is in red.

Figure 11 shows the temporal evolution of the spectral calibration obtained with all S02/S03 sequences since the beginning of the mission. As for OLCI-A a small drift is observed. For OLCI-B, this drift is positive for camera 1, 2, 4 and 5 and negative for camera 3.

Evolution derived from the S09 calibration sequence (spectral calibration using O₂ absorption and Fraunhofer lines) is presented in Figure 12. As for OLCI-A, we see that the long-term evolution of the spectral calibration obtained with sequence S09 is in rather good agreement with the one obtained with sequence S02/S03.

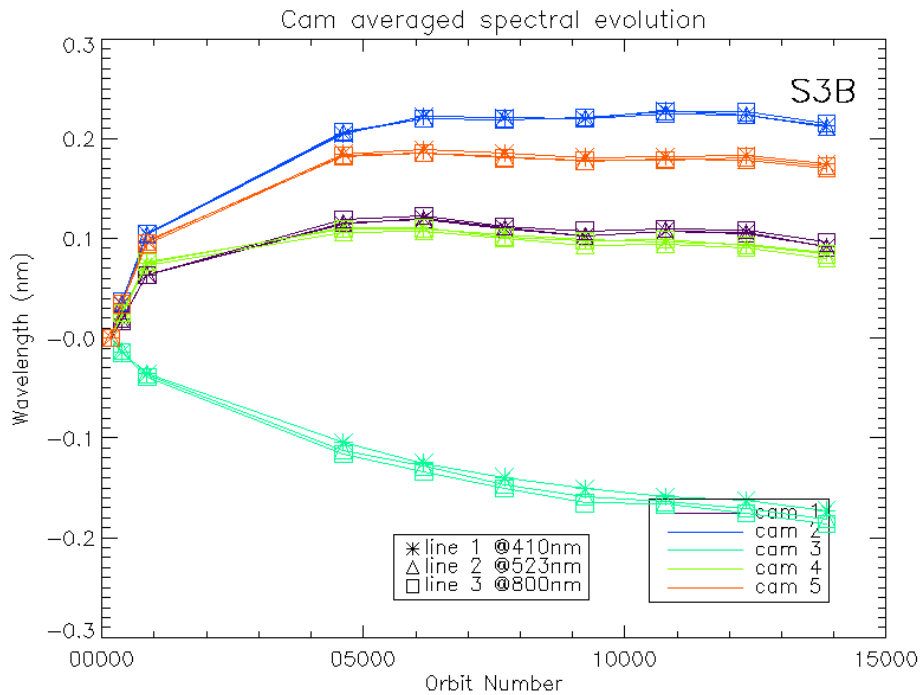


Figure 11: OLCI-B camera averaged spectral calibration evolution as a function of absolute orbit number (all spectral S02/S03 calibrations since the beginning of the mission are included). The data are normalized with the first Spectral Calibration. The first (reference) calibration is from 8 May 2018 (orbit 182), the last from 22 Dec. 2020 (orbit 13856).

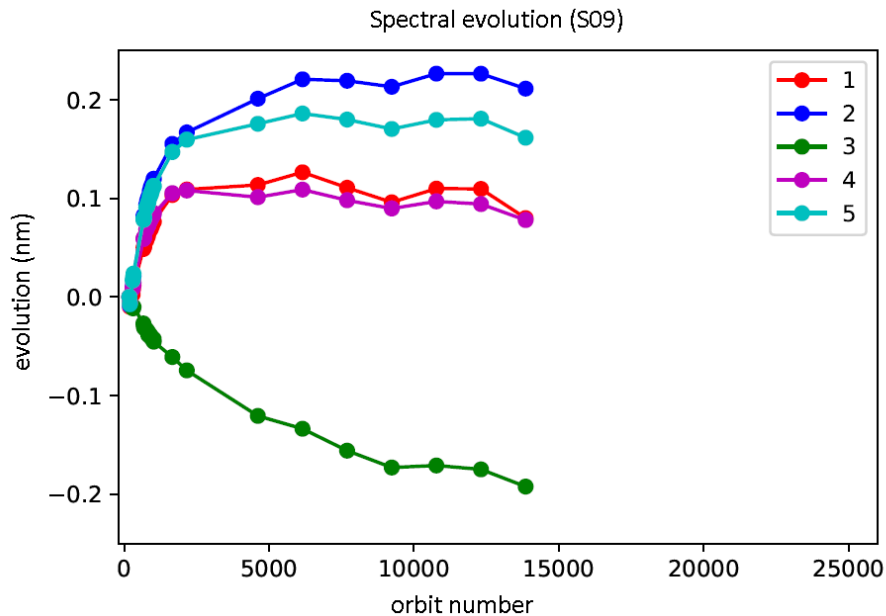


Figure 12: OLCI-B camera averaged spectral calibration evolution as a function of absolute orbit number from S09 calibrations since the beginning of the mission. The last calibration for S09 is from 22 December 2020 (orbit 13854). For each camera, the spectral evolution corresponding derived from spectral lines at 485 nm, 656 nm, 770 nm and 854 nm have been averaged. The data are normalized with the first Spectral Calibration.

5.1.4 Radiometric stability

5.1.4.1 OLCI-A

The stability with time of the instrument sensitivity is monitored through the radiometric calibration processing results: time series of radiometric gains normalised to a given date are analysed. This is done at the full spatial resolution before being summarised by spatial averaging over each camera: if there is some variability of the sensitivity evolution for a given channel inside a given camera, it remains limited with respect to camera-to-camera variability.

The overall instrument evolution (since channel programming change, 25/04/2016 to 25/01/2021) is shown on Figure 13: a maximum of about 2.8% is reached at 400 nm, with a high inter-camera variability, while other bands show much lower values, within $\pm 1\%$. The spectral behaviour of the 5 cameras is very similar, to the exception of camera 1 at the blue edge (bands Oa1 and Oa2, 400 & 412 nm), and camera 5 in the red to NIR spectral range.

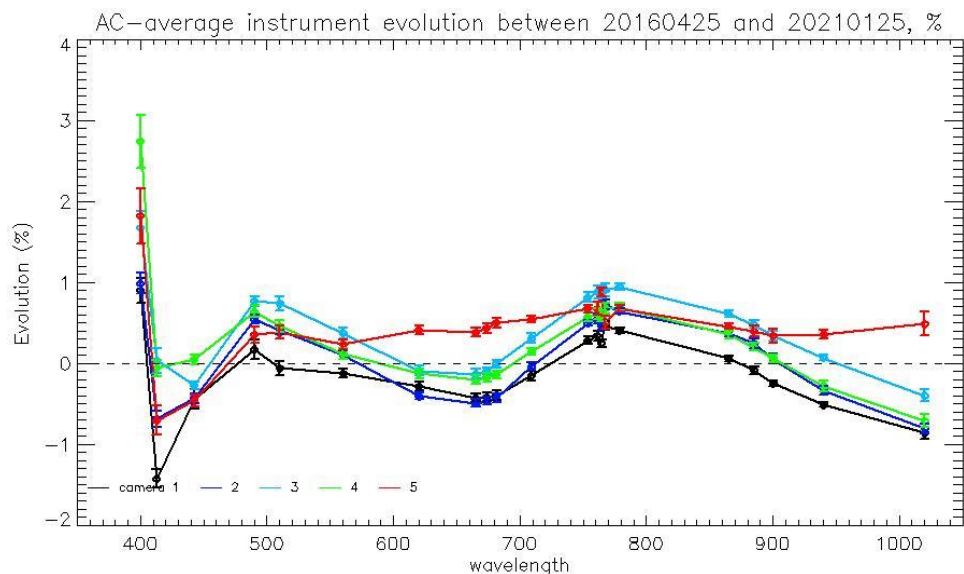


Figure 13: OLCI-A camera-averaged instrument evolution since channel programming change (25/04/2016) and up to most recent calibration (25/01/2021) versus wavelength.

Time series of sensitivity evolution are shown on Figure 14 one plot per camera, as a function of elapsed time since launch. It shows that, if a significant evolution occurred during the early mission, the trends tend to stabilize, with the notable exception of band 1 in particular for camera 4. An example of an evolution surface for channel Oa2 (412 nm) is given below for Camera 1 (Figure 15), justifying the use of spatial averages for long-term monitoring.

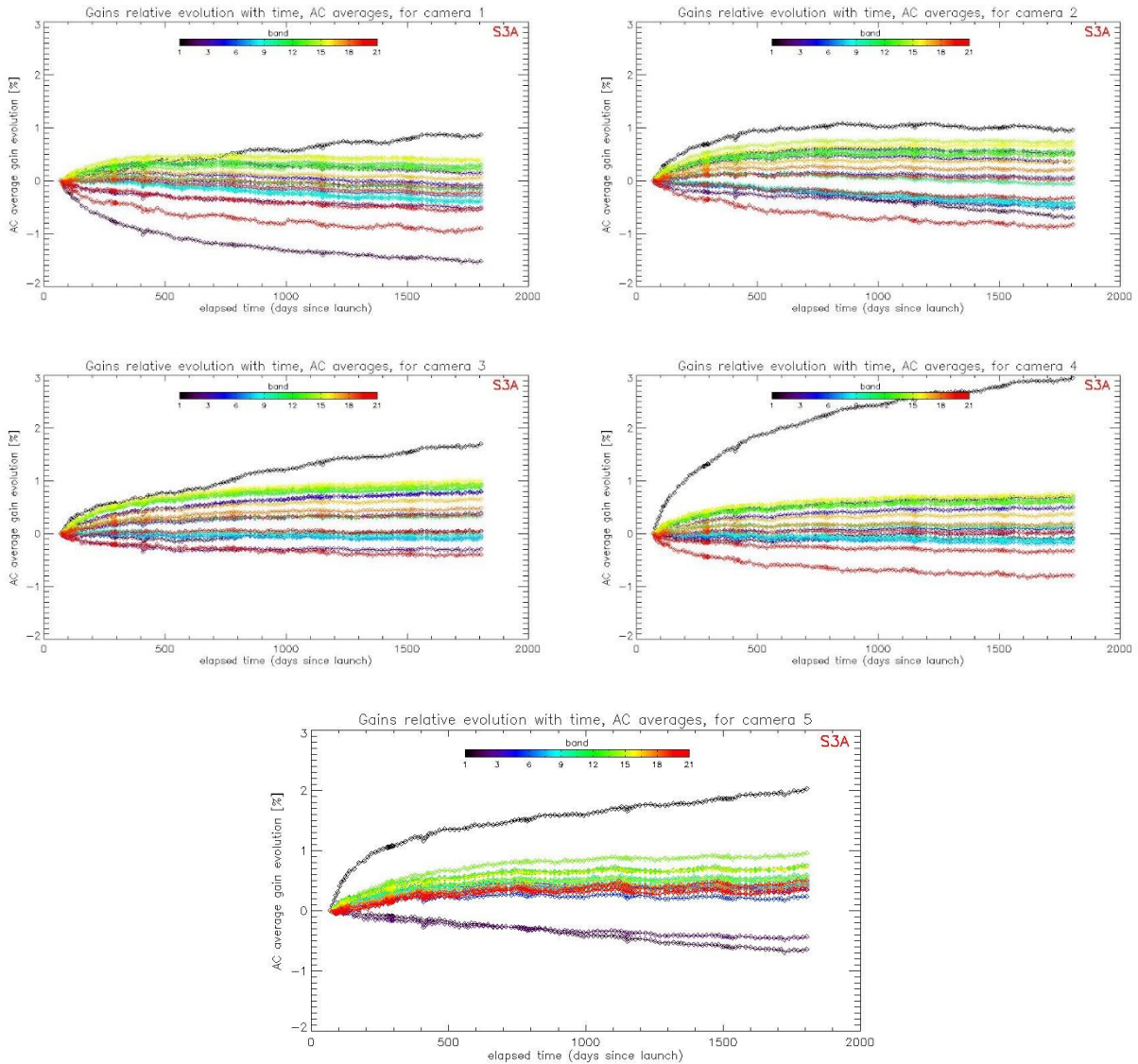


Figure 14: OLCI-A camera averaged gain relative evolution with respect to calibration of 25/04/2016 (change of OLCI channel settings), as a function of elapsed time since launch; one curve for each band (see colour code on plots), one plot for each module. The diffuser ageing has been taken into account. Early mission data (16 Feb. to 25 April) is not available due to missing information required for accurate gain computation.

Gain evolution, band Oa2, Camera 1

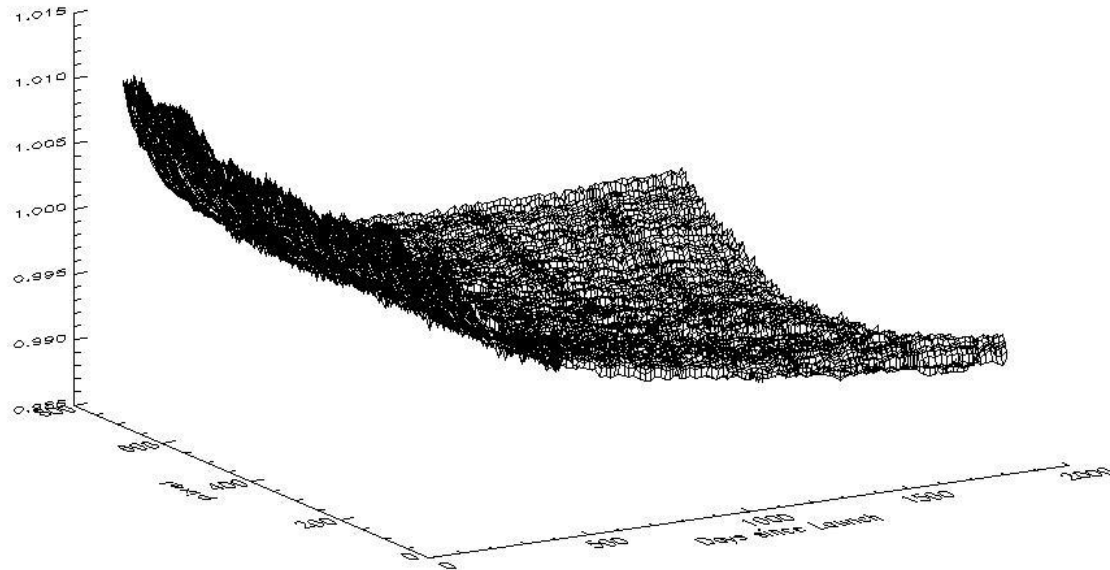


Figure 15: OLCI-A gain relative evolution with respect to “best geometry” calibration (22/11/2016), as a function of elapsed time since launch (x axis) and spatial pixel (y axis) for Channel Oa2 (412.5 nm), Camera 1.

5.1.4.2 OLCI-B

The overall instrument evolution (18/06/2018 to 14/02/2020) is shown on Figure 16: a maximum of about 4% is reached at 400 nm, while other bands show lower values, within $\pm 1.5\%$. The spectral behaviour of the 5 cameras is very similar, to the exception of camera 3 at both edges (bands Oa1 and Oa21, 400 & 1020 nm).

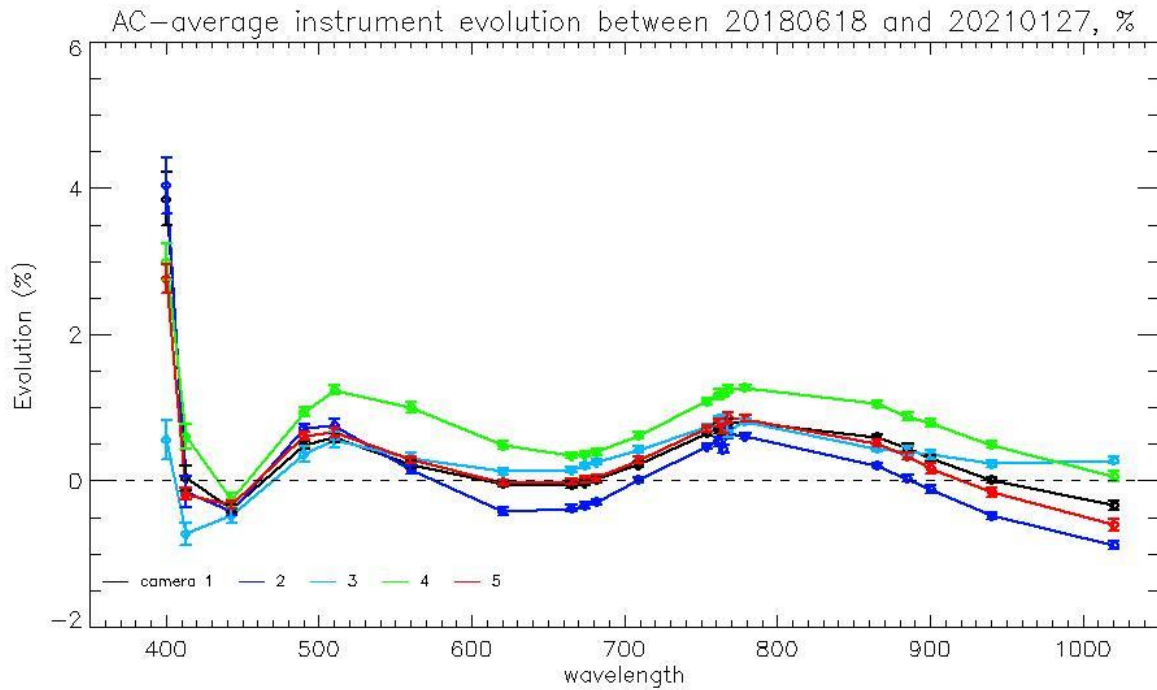


Figure 16: OLCI-B camera-averaged instrument evolution since channel programming change (18/06/2018) and up to most recent calibration (27/01/2021) versus wavelength.

Time series of sensitivity evolution are shown on Figure 17, one plot per camera, as a function of elapsed time since launch. It shows that, if a significant evolution occurred during the early mission, the trends tend to stabilize.

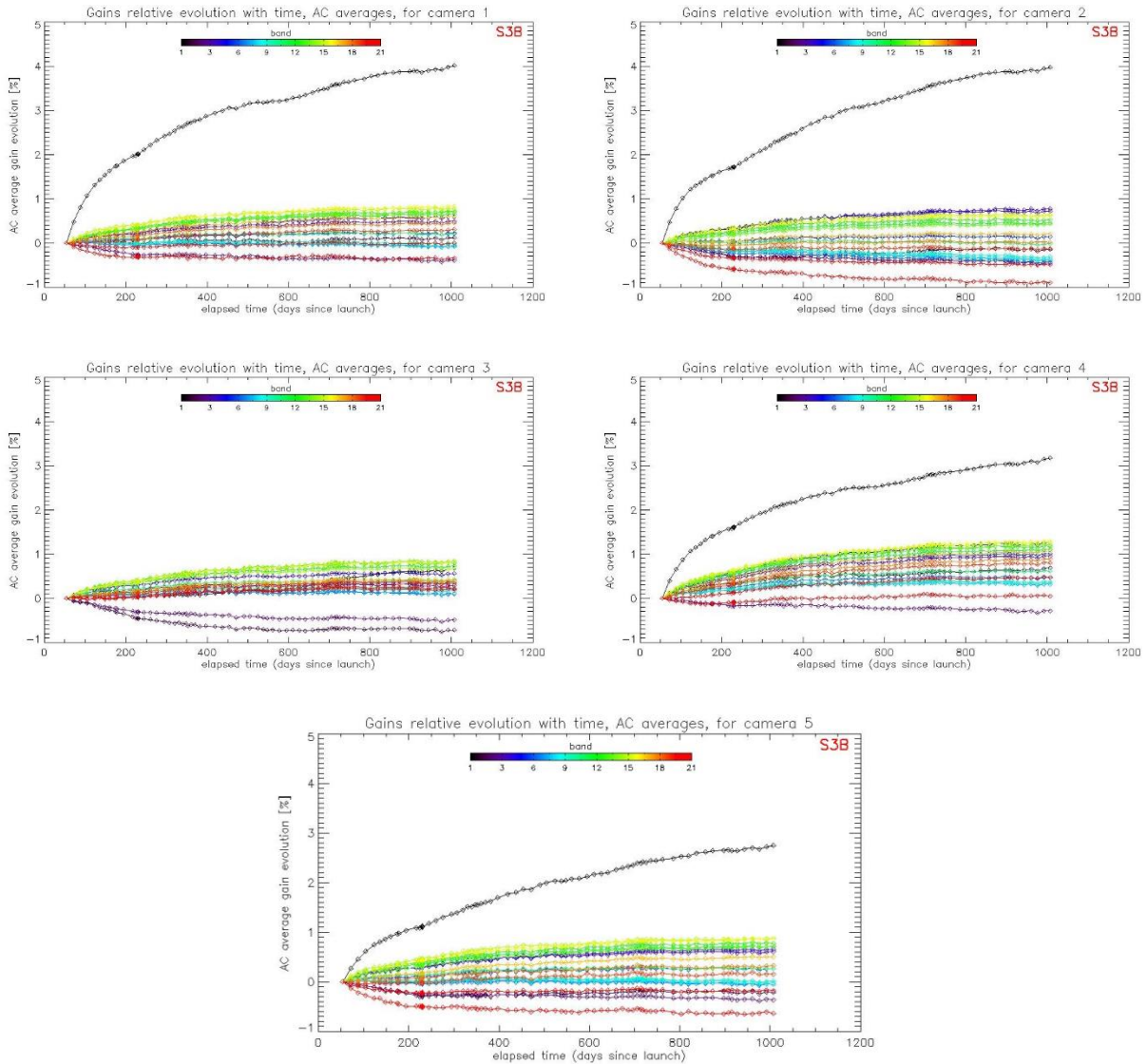


Figure 17: OLCI-B camera averaged gain relative evolution with respect to first calibration after channel programming change (18/06/2018), as a function of elapsed time since the beginning of the mission; one curve for each band (see colour code on plots), one plot for each module. The diffuser ageing has been taken into account.

5.1.5 Ageing of radiometric diffuser

5.1.5.1 OLCI-A

The ageing of the nominal radiometric solar diffuser is monitored using a second, or reference, radiometric diffuser. The relative darkening of the solar diffuser, expected to be measurable after significant cumulated exposure to UV light, is assessed at every channel through the evolution with time of the relative response of the nominal diffuser with respect to that of the reference one acquired under

almost identical illumination conditions one orbit after the nominal one; the first pair of measurements is used as the reference point. Ageing is first assessed at every spatial pixel and then averaged over the field-of-view (FOV) as independent of the instrument itself.

FOV-averaged ageing as a function of wavelength is represented in Figure 18 for all available ageing acquisition (21 so far, excluding the first sequence used as the reference). As expected, ageing is rather low (<0.53% after about 5 years) and stronger for the ‘bluest’ spectral bands (short wavelengths). At present, ageing is clearly visible for wavelengths up to about 650 nm.

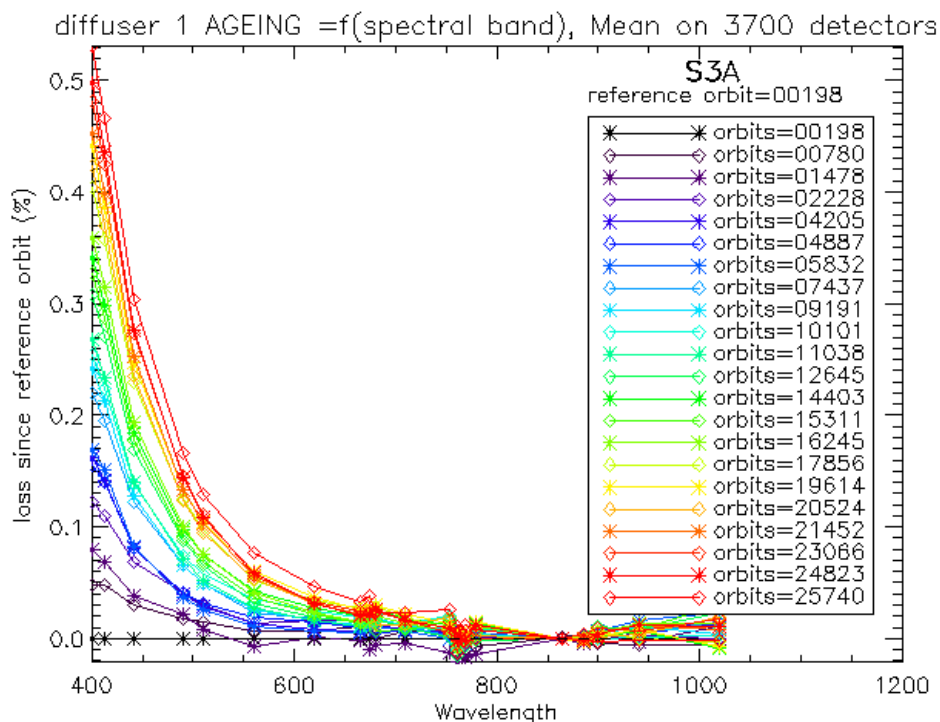


Figure 18: OLCI-A Diffuser 1 ageing as a function of wavelength (or spectral band). Ageing is clearly visible in spectral band #1 to #6.

A model of the nominal diffuser ageing is derived by fitting the measured ageing against cumulated exposure to light, so that it can be used to accurately predict (or model) the nominal diffuser reflectance at any time. This model is used to derive the OLCI Radiometric Gain Model (see section 5.2.1.2). The slope of this ageing model (% of reflectance loss per exposure) as a function of wavelength is presented in Figure 19 for sixteen consecutive estimations (during orbit cycles 20, 24, 27, 29, 33, 38, 40, 43, 47, 52, 54, 56, 58, 60, 65 and 67 i.e. between July 2017 and January 2021), the first one being that used to build the current Radiometric Gain Model. It shows that the stability is excellent.

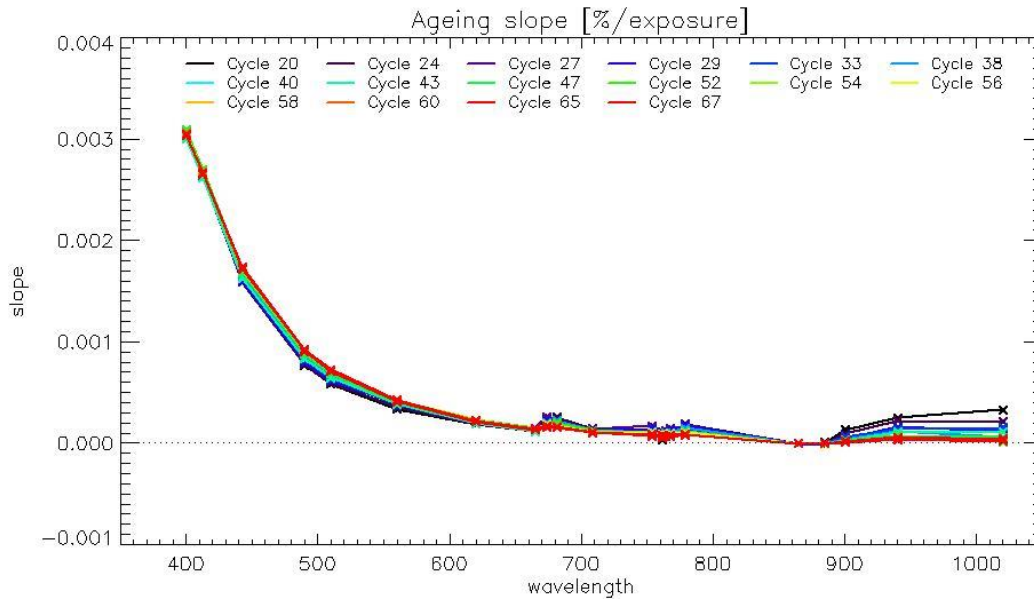


Figure 19: Slope of ageing fit (% of loss per exposure) vs wavelengths, using all the available ageing sequence at the time of the current cycle (#67 = red curve), and at the time of the fifteen previous cycles with an aging sequence (see legend below the curves).

5.1.5.2 OLCI-B

OLCI-B FOV-averaged ageing as a function of wavelength is represented in Figure 20 for all available ageing acquisition (13 so far, excluding the first sequence used as the reference). The ageing is clearly visible in spectral band Oa01 to Oa05, with the expected spectral shape and order of magnitude. However, we also observe some ageing in bands Oa06 to Oa11; such an unexpected behaviour is under investigation and prevents further use of the nominal ageing assessment method until fully understood.

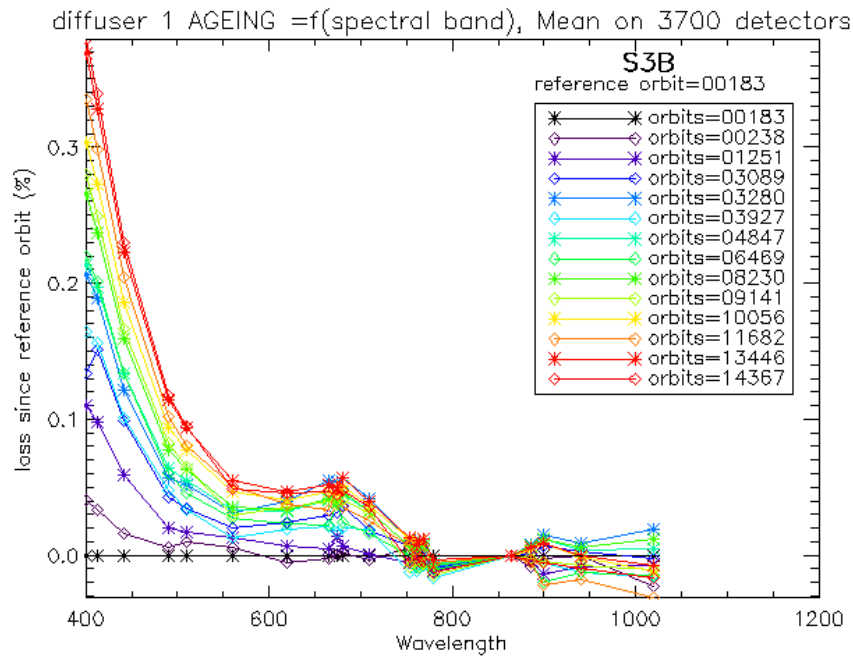


Figure 20: OLCI-B Diffuser 1 ageing as a function of wavelength (spectral bands).

As for OLCI-A, the OLCI-B Diffuser Ageing has been modelled as a function of cumulated exposure time (i.e. number of acquisition sequence on nominal diffuser, regardless of the band setting). The OLCI-A modelling methodology has been applied to OLCI-B. The results of this modelling, iterated at each new Ageing Sequence acquisition, expressed as the rate of ageing (% of loss per exposure) as a function of wavelength is presented in Figure 21. The unexpected bump near 650-700 nm mentioned in the previous annual report seems to decrease with time (i.e with the quantity of data used for modelling the ageing) which is a good point since there is no expected significant ageing at these wavelengths.

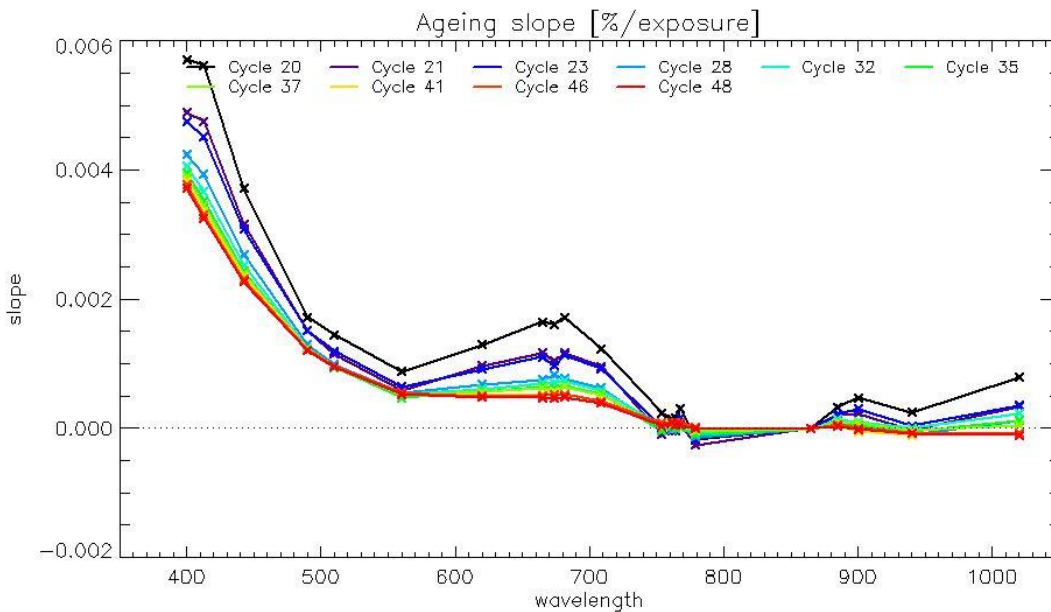


Figure 21: OLCI-B: Slope of ageing fit (% of loss per exposure) vs wavelengths, using all the available ageing sequence at the time of the current cycle (red curve) and at the time of previous cycle for which an ageing sequence was measured (see legend within the figure).

An alternative assessment method, based on direct comparison of nominal diffuser observations during the same day (as part of a specific campaign referred to as the Yaw Manoeuvres) has provided reliable results very close to those of the nominal method for channels Oa01 to Oa05 and negligible ageing at higher wavelengths, as expected. An exposure time dependent ageing model based on this alternative method has been established and is used to derive the Gain Model (see section 5.2.2.2).

5.2 L1 products performances

5.2.1 Geometric Performance

Regular monitoring of the geolocation performance by correlation with GCP (Ground Control Points) imagettes using the so-called GeoCal Tool is done continuously.

5.2.1.1 OLCI-A

The good performance of OLCI-A georeferencing since the introduction of the upgraded Geometric Calibration on 14/03/2018 is confirmed. It has however significantly improved after its last full revision of GCMs (Geometric Calibration Models, or platform to instrument alignment quaternions) and IPPVMs (Instrument Pixels Pointing Vectors) both derived using the GeoCal Tool and put in production on 30/07/2019. The following figures show time series of the overall RMS performance (Figure 22, requirement criterion) and of the across-track and along-track biases for each camera (Figure 23 to Figure 27). Figure 28 and Figure 29 address the monitoring of the performance homogeneity within the field of view: georeferencing errors in each direction at camera transitions (difference between last pixel of

camera N and first pixel of camera N+1) and within a given camera (maximum bias minus minimum inside each camera).

The performance improvement since the 30/07/2019 is significant on most figures: the global RMS value decreases from around 0.35 to about 0.2 and remains below 0.3 since then (Figure 22), the across-track biases decrease significantly for all cameras (Figure 23 to Figure 27), the along-track bias reduces where it was significant (camera 3, Figure 25) and the field of view homogeneity improves drastically (Figure 28 and Figure 29). It is also worth to mention a reduction of the dispersion – distance between the ± 1 sigma lines – in Figure 23 to Figure 27). Along-track biases of cameras 3 to 5 are however still slightly drifting, resulting in slowly degrading RMS performance (Figure 22), but this is closely monitored so that appropriate actions can be taken.

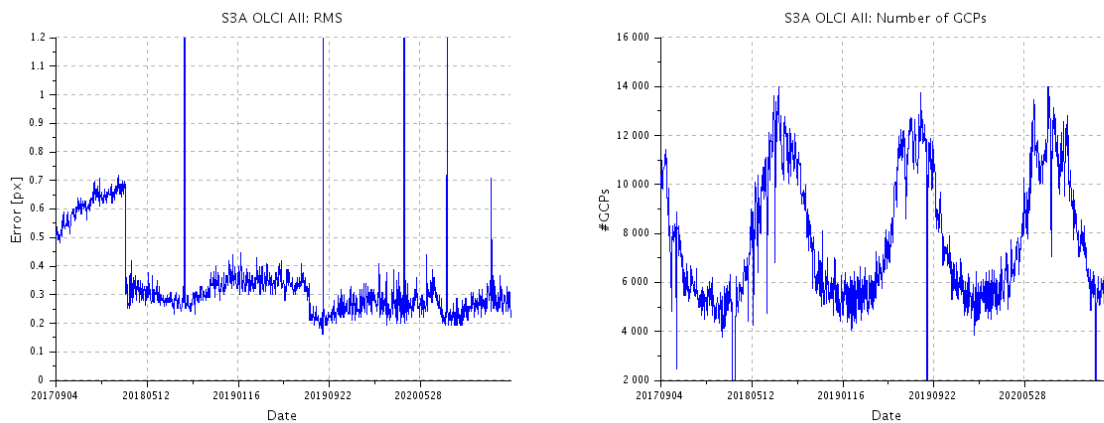


Figure 22: overall OLCI-A georeferencing RMS performance time series over the whole monitoring period (left) and number of validated control points corresponding to the performance time series (right)

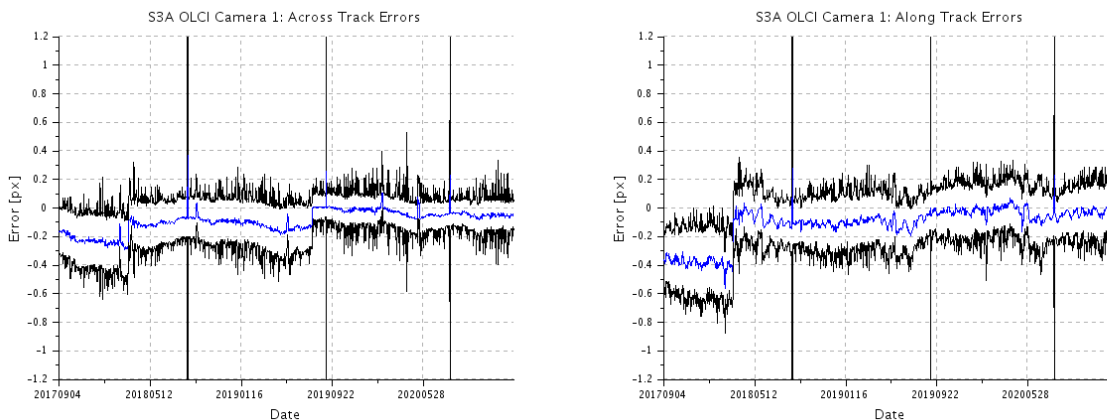


Figure 23: across-track (left) and along-track (right) georeferencing biases time series for Camera 1 (starting 01/03/2018).

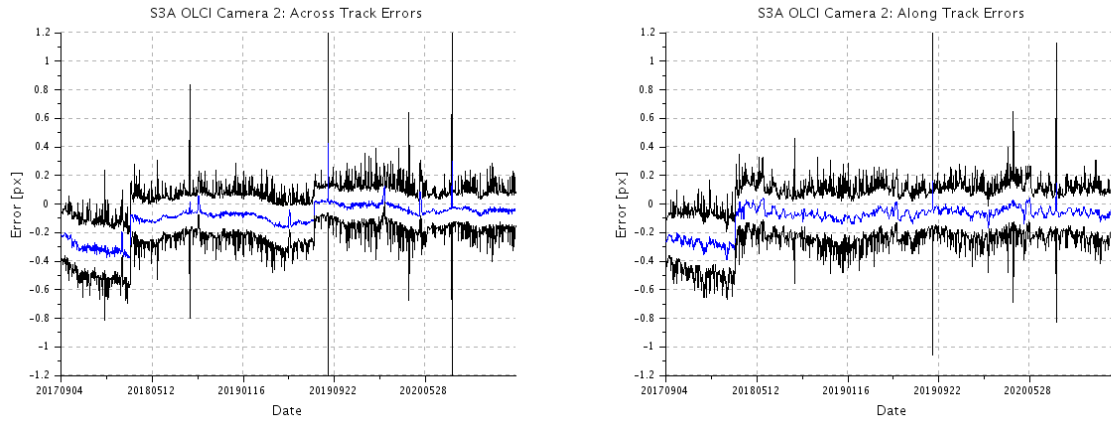


Figure 24: same as Figure 23 for Camera 2.

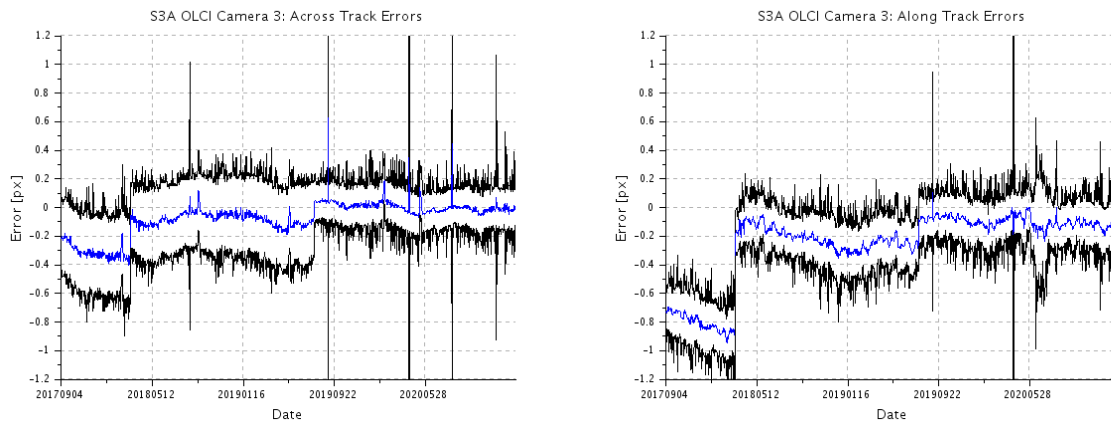


Figure 25: same as Figure 23 for Camera 3.

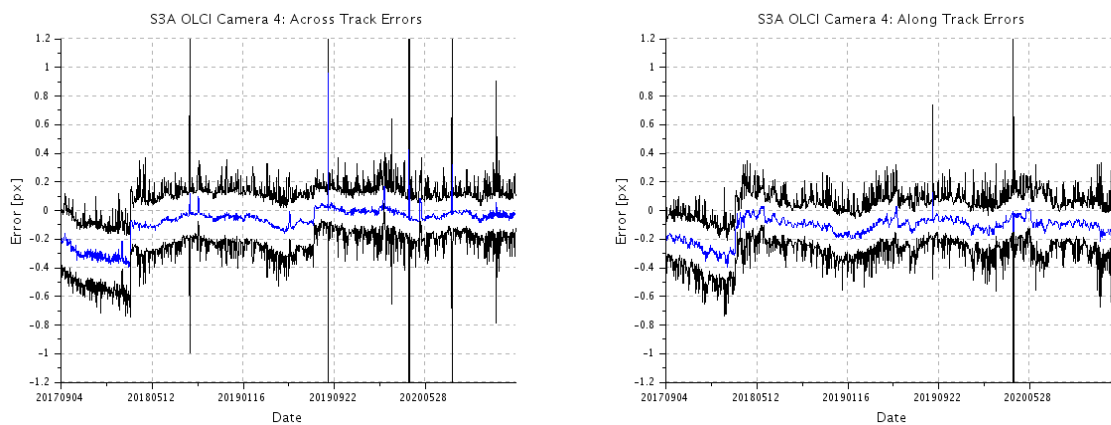


Figure 26: same as Figure 23 for Camera 4.

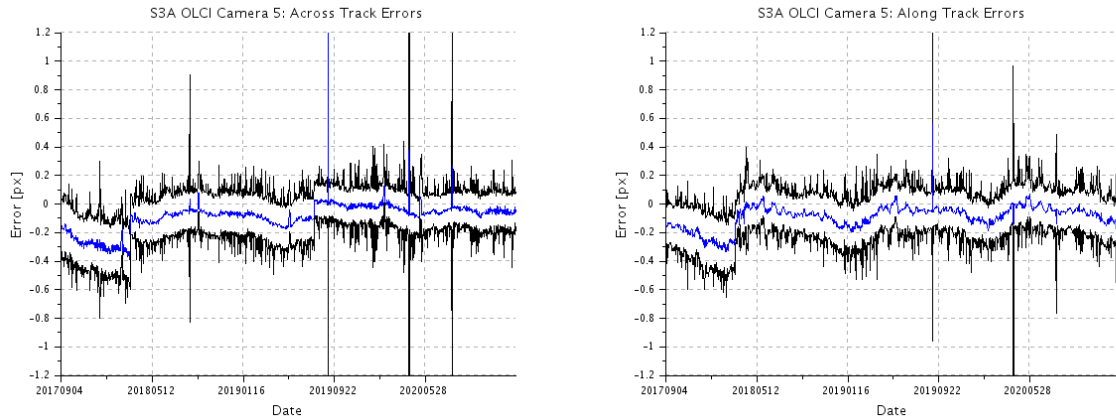


Figure 27: same as Figure 23 for Camera 5.

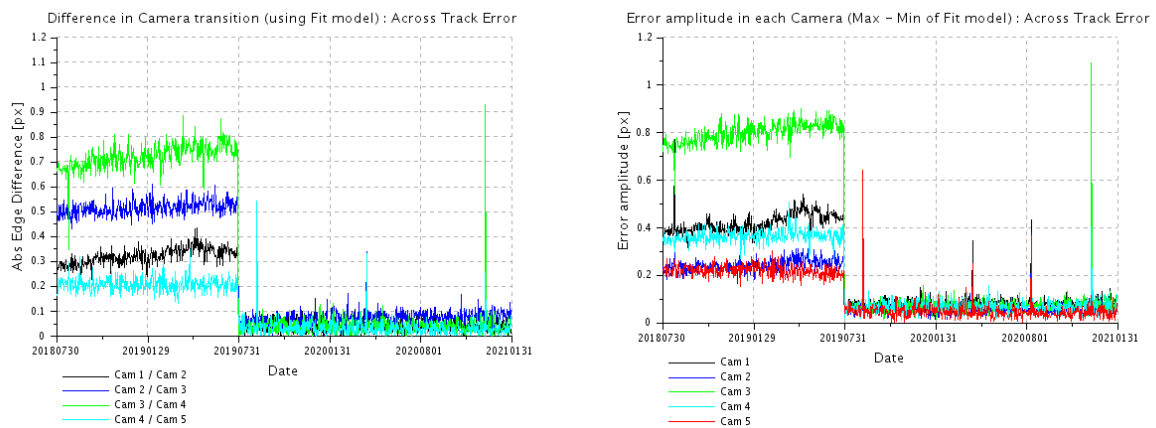


Figure 28: OLCI-A spatial across-track misregistration at each camera transition (left) and maximum amplitude of the across-track error within each camera (left).

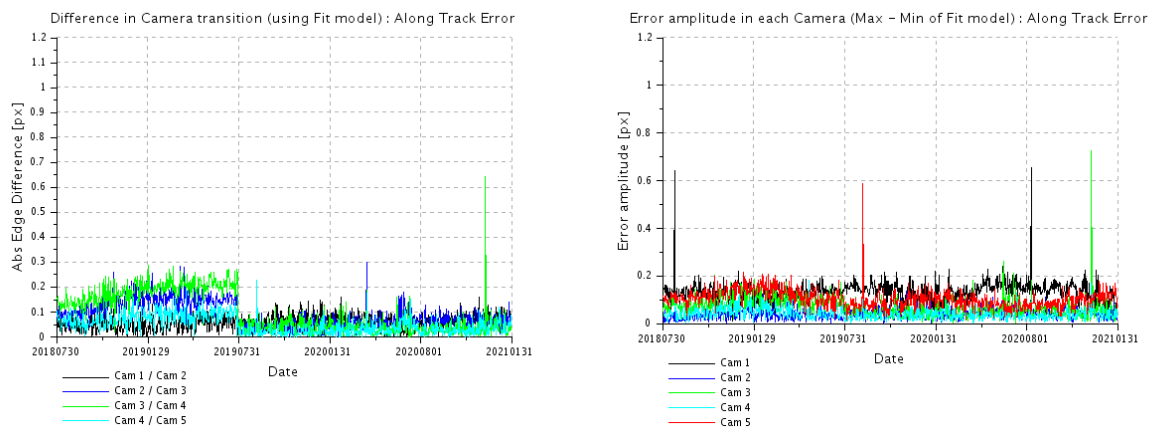


Figure 29: OLCI-A spatial along-track misregistration at each camera transition (left) and maximum amplitude of the along-track error within each camera (left).

5.2.1.2 OLCI-B

The performance of OLCI-B georeferencing is within requirements since the introduction of the 3rd Geometric Calibration on 12/12/2018. Significant persistent along-track depointing drifts required several re-calibration since the: a major upgrade was introduced on 30/07/2019, followed by further adjustments, the most recent being that of 10/12/2020. The following figures show time series of the overall RMS performance (Figure 30, requirement criterion), the across-track and along-track biases for each camera (Figure 31 to Figure 35), as well as pointing homogeneity across the field of view (bias differences at camera interfaces and bias amplitudes within each camera, Figure 36 and Figure 37).

As for OLCI-A, despite compliance to the RMS requirement of 0.5 pixel, OLCI-B showed significant heterogeneity of the performance within the field of view, with discrepancies at camera transitions of up to 1 pixel. Introduction of upgraded pointing vectors (first occurrence 30/07/2019) greatly improved many performance indicators: the global RMS value decreases from around 0.4 to about 0.3 (Figure 30), the across-track biases decrease significantly for all cameras (Figure 31 to Figure 35) and the field of view homogeneity improves drastically (Figure 36 and Figure 37, but also reduction of the dispersion – distance between the ± 1 sigma lines – in Figure 31 to Figure 35).

The global RMS performance as well as the along and across-track average biases are quite stable since then, however in-FOV across-track pointing homogeneity slowly degrades continuously (Figure 36) and frequent re-calibrations were necessary to maintain the performance.

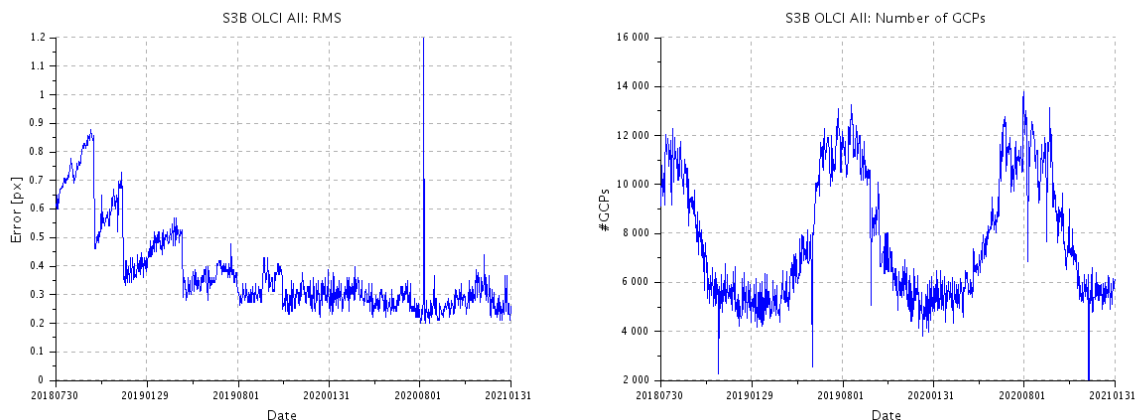


Figure 30: overall OLCI-B georeferencing RMS performance time series (left) and number of validated control points corresponding to the performance time series (right) over the whole monitoring period.

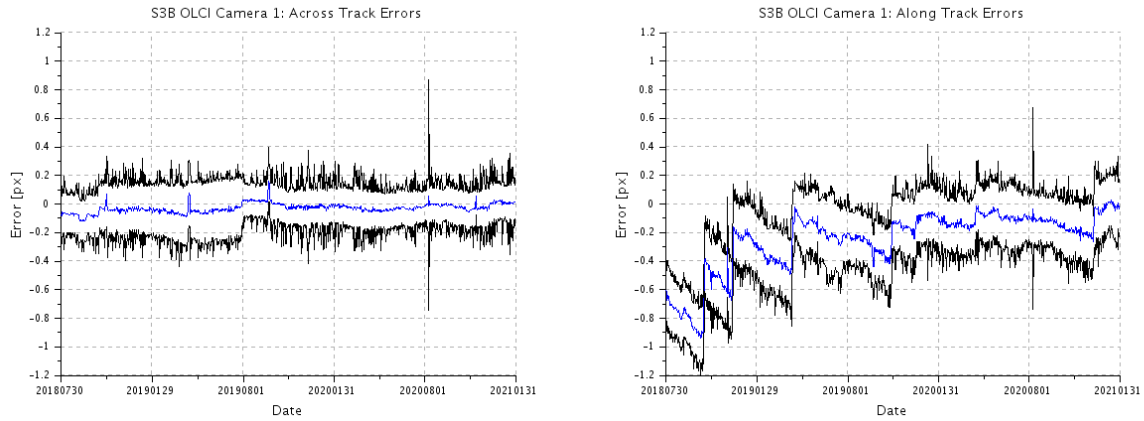


Figure 31: across-track (left) and along-track (right) georeferencing biases time series for Camera 1.

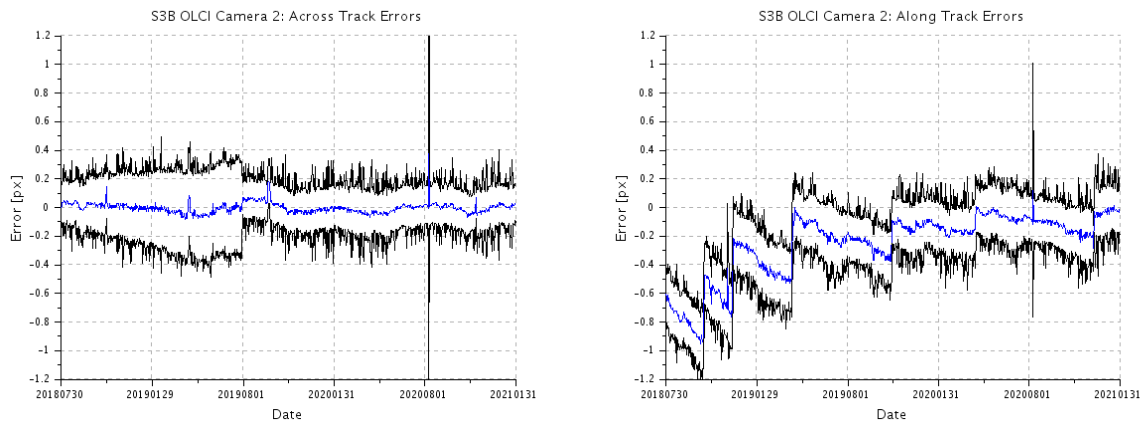


Figure 32: same as Figure 31 for Camera 2.

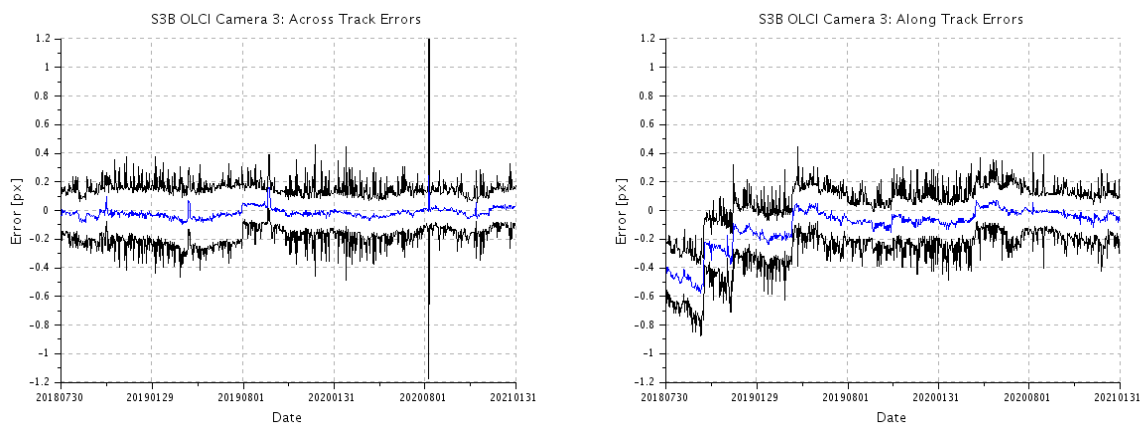


Figure 33: same as Figure 31 for Camera 3.

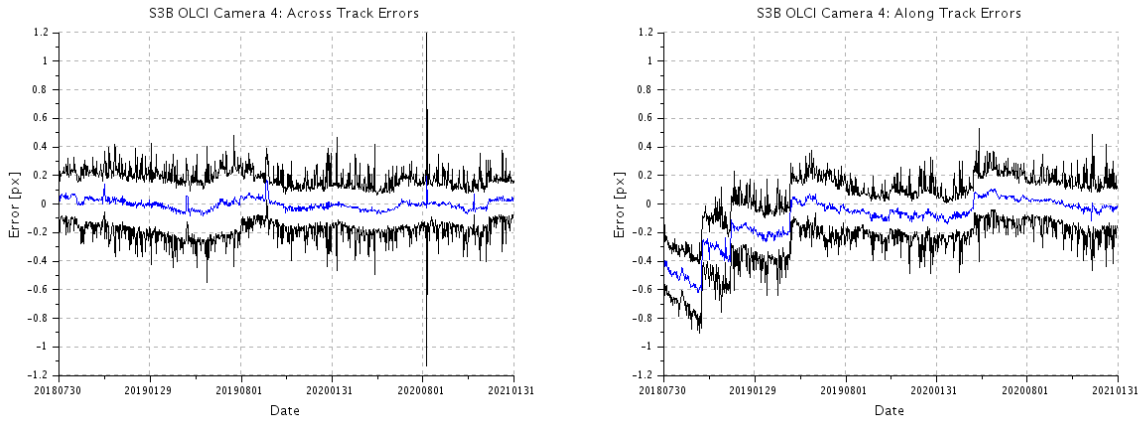


Figure 34: same as Figure 31 for Camera 4.

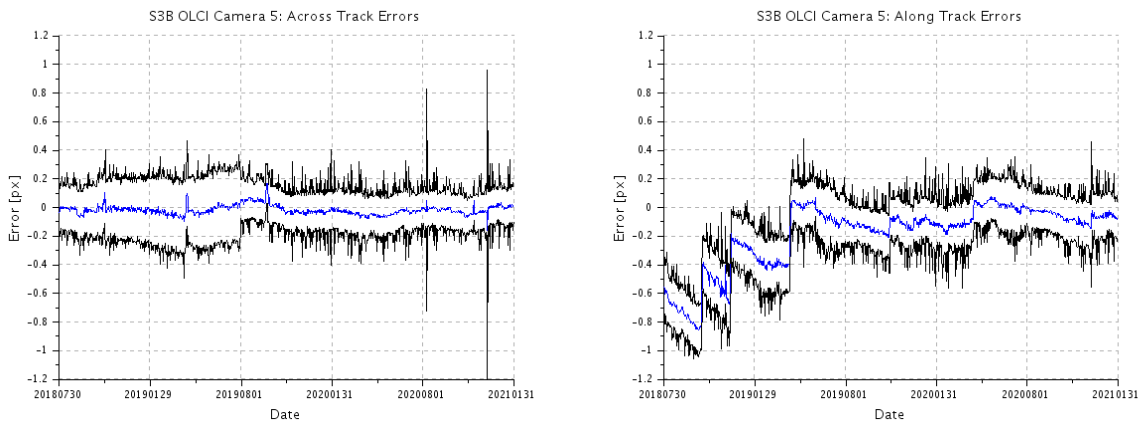


Figure 35: same as Figure 31 for Camera 5.

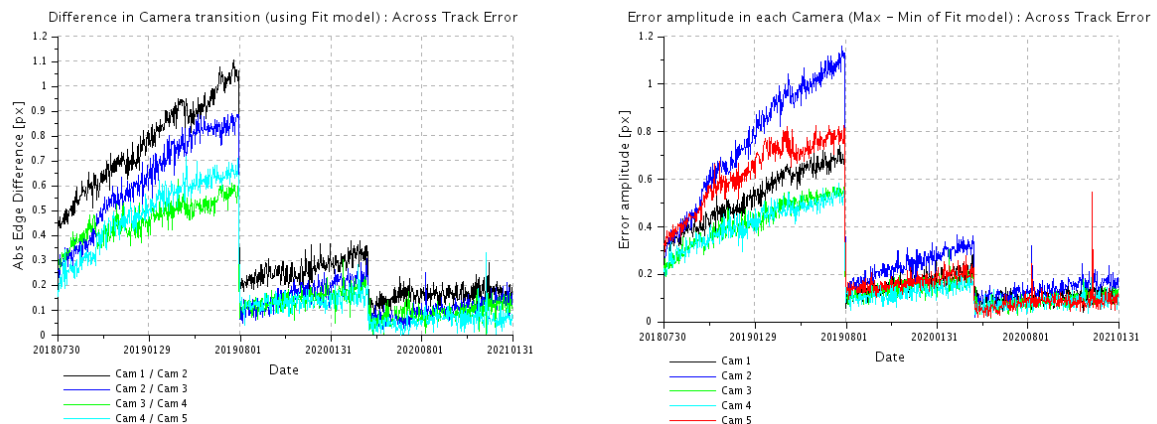


Figure 36: OLCI-B spatial cross-track misregistration at each camera transition (left) and maximum amplitude of the across-track error within each camera (left).

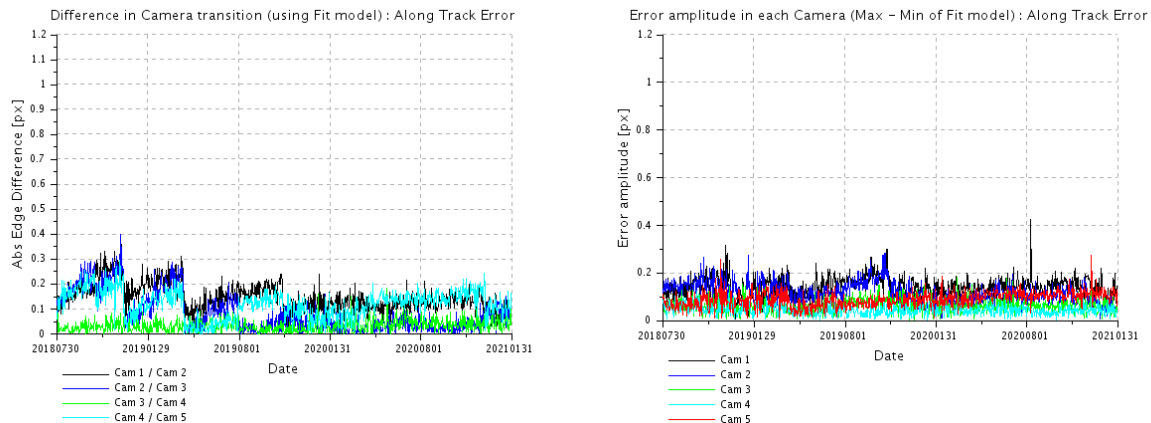


Figure 37: OLCI-B spatial along-track misregistration at each camera transition (left) and maximum amplitude of the along-track error within each camera (left).

5.2.2 Radiometric Gain Model Performance

5.2.2.1 OLCI-A

OLCI radiometric Calibration is based on its on-board calibration system: a carefully characterised solar diffuser is used as a secondary radiometric standard to derive instantaneous radiometric gains from diffuser measurements and computation of the incoming radiance, by use of diffuser characterisation, illumination and viewing geometry as well as spectral response functions.

OLCI Level 1 data processing to calibrate measured radiances using a Radiometric Gain Model (RGM) includes a long term drift correction, in order to avoid radiometric discontinuities between successive gain estimates as well as simplifying maintenance of operational processing configuration. The model is expressed as a bounded exponential time evolution applied onto the gain at a reference date. The time evolution model is fitted, on a per band and per pixel basis, on the evolution data presented above (section 5.1.4.1); the Gain at the reference date is obtained by time averaging after correction of the evolution. Diffuser ageing (see section 5.1.5) is of course accounted for during this process.

Consequently, the model is always used in extrapolation for routine production, as derived from already acquired data; it can only be used in interpolation for data reprocessing. Its performance is thus continuously monitored against new radiometric calibration, regularly acquired. The current operational RGM has been derived from data spanning 08/08/2016 to 08/08/2020 and put in operations the 15/10/2020 (processing baseline 2.71). It includes the correction of the diffuser ageing for the six bluest bands (Oa1 to Oa6) for which it is clearly measurable.

The model RMS performance over the complete dataset (including the 11 calibrations in extrapolation over about 6 months) remains better than 0.08% – except for channels Oa1 (400 nm) that reaches 0.09% for the earliest calibration – when averaged over the whole field of view (Figure 38) even if a small drift of the model with respect to most recent data is now visible in most channels.

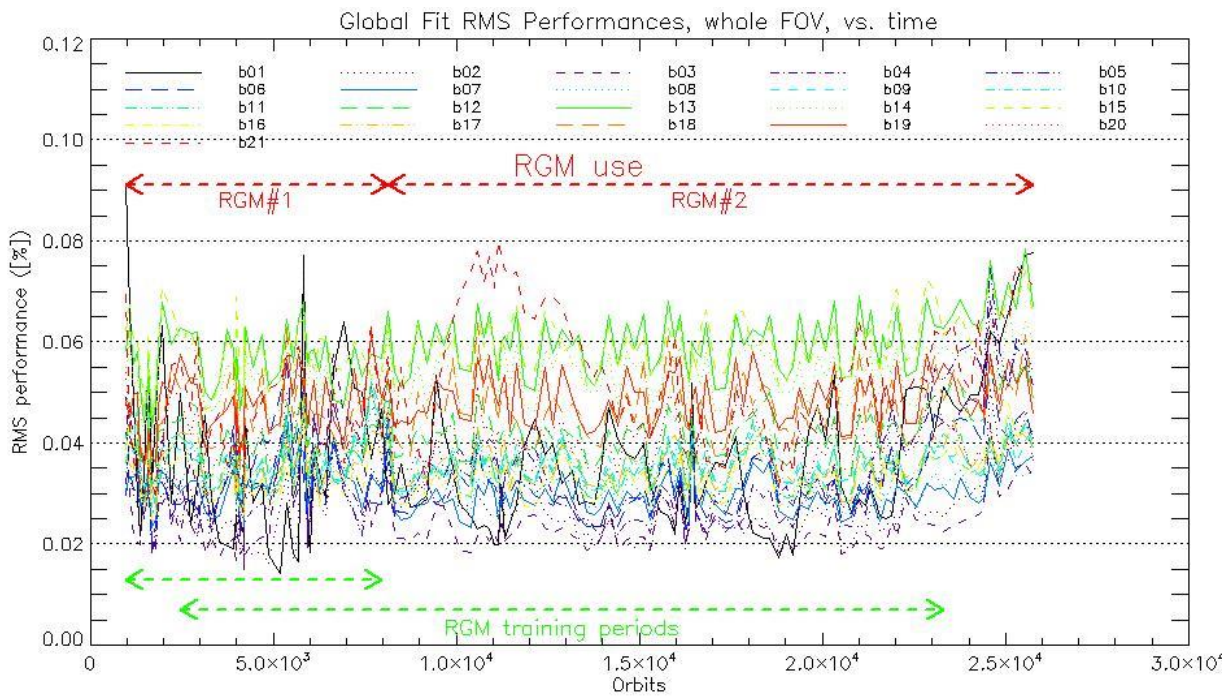


Figure 38: RMS performance of the Gain Model of current Processing Baseline as a function of orbit.

More details are provided on Figure 39 on which per camera mean and standard deviation of Model over Data ratios are plotted against wavelength for each orbit. Conclusions are however the same with performances within 0.1% ($1-\sigma$) but for Oa1 and Oa21, the former reaching 0.15% in cameras 4, while the latter has a larger dispersion (up to 0.2%) in camera 5, due to a group of pixels with an anomalous behaviour that cannot be fully captured by the model mathematical expression.

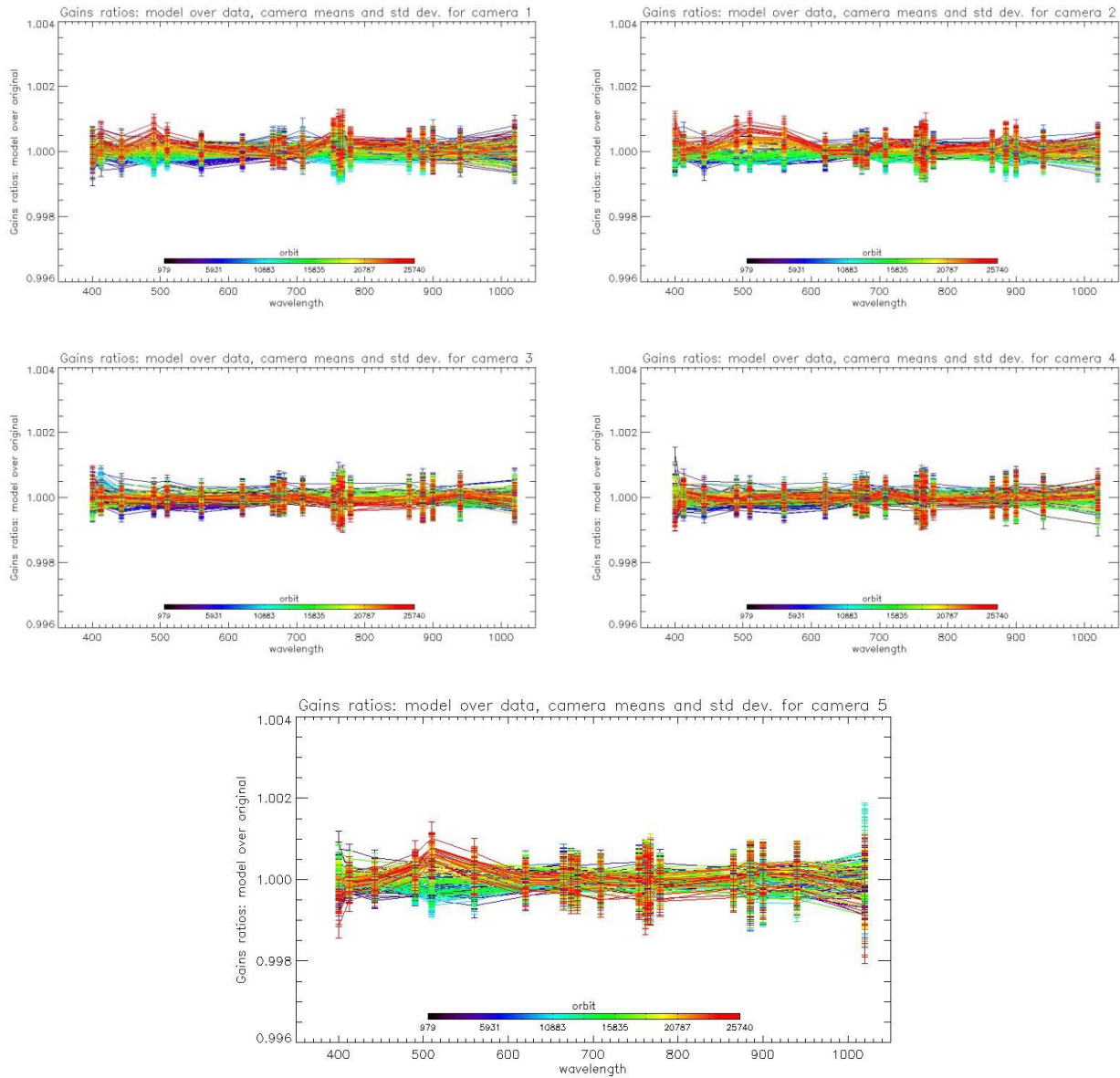


Figure 39: For the 5 cameras: Evolution model performance, as camera-average and standard deviation of ratio of Model over Data vs. wavelength, for each orbit of the test dataset, including 11 calibrations in extrapolation, with a colour code for each calibration from blue (oldest) to red (most recent).

5.2.2.2 OLCI-B

Instrument response and degradation modelling for OLCI-B, including the use of the in-flight BRDF model (based on 11th December 2018 Yaw Manoeuvres), has been refreshed and deployed at PDGS on 15th October 2020 (Processing Baseline 1.48). The model has been derived on the basis of an extended Radiometric Calibration dataset (from 05/11/2018 to 09/08/2020). It includes the correction of the diffuser ageing for the five bluest bands (Oa1 to Oa5) for which it is clearly measurable. The model performance over the complete dataset (including the 11 calibrations in extrapolation over about 6 months) is illustrated in Figure 40. It remains better than 0.07% when averaged over the whole field of view for all band except Oa01 (< 0.13%) which starts to show a significant drift compared to the other bands.

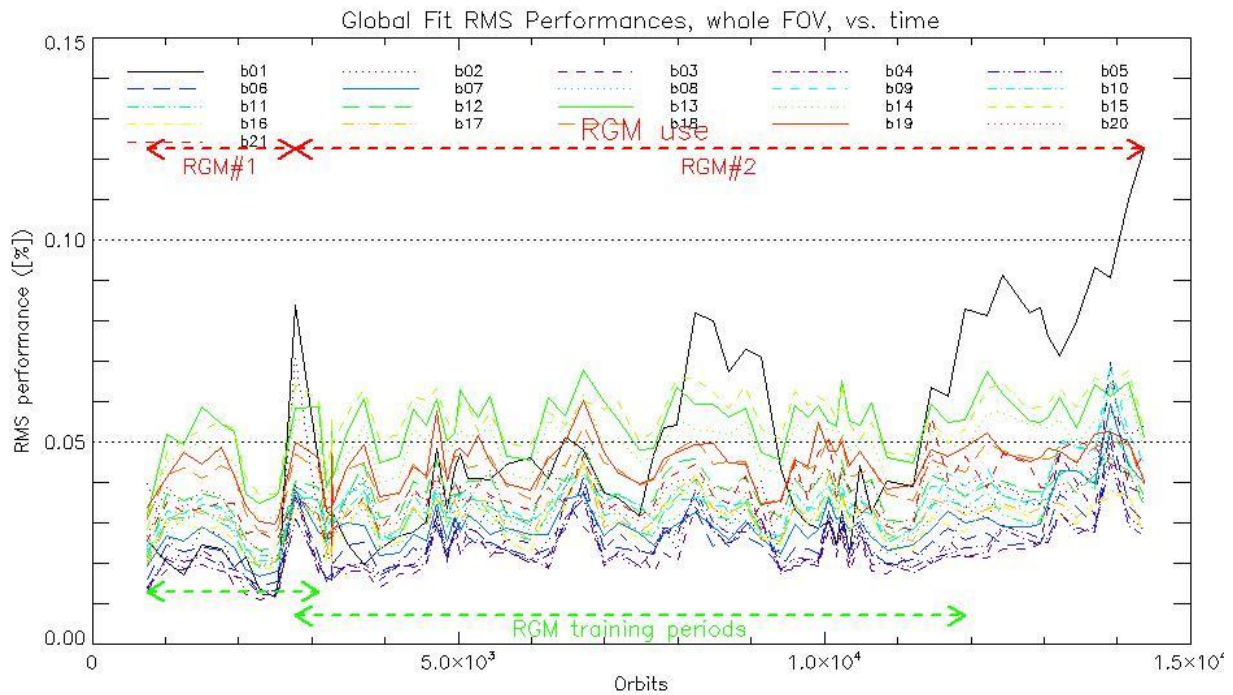


Figure 40: RMS performance of the OLCI-B Gain Model of the current processing baseline as a function of orbit.

More details are provided on Figure 41 on which per camera mean and standard deviation of Model over Data ratios are plotted against wavelength for each orbit.

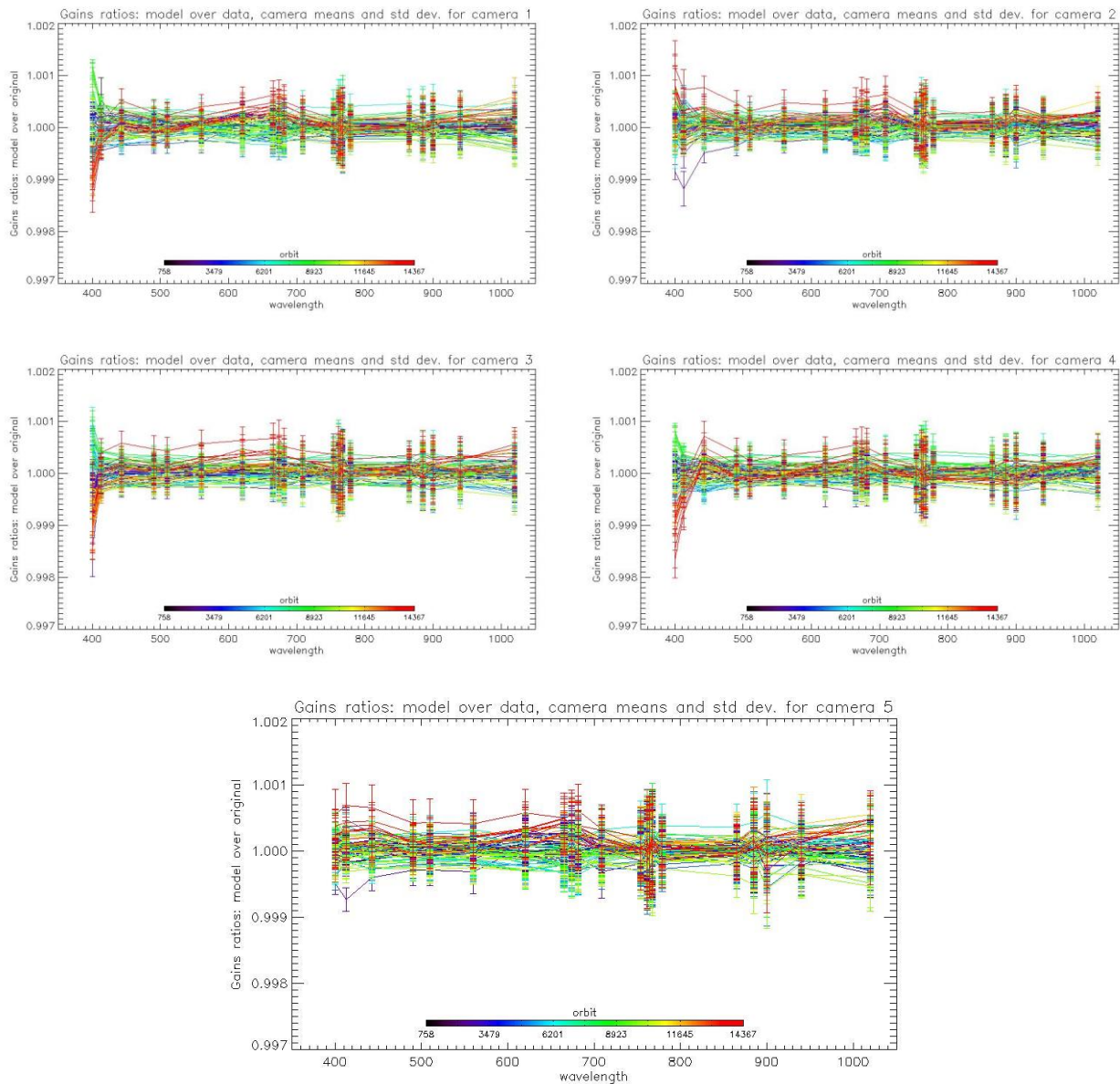


Figure 41: For the 5 cameras: Evolution model performance, as camera-average and standard deviation of ratio of Model over Data vs. wavelength, for each orbit of the test dataset, including 11 calibrations in extrapolation, with a colour code for each calibration from blue (oldest) to red (most recent).

5.2.3 Radiometric Validation

Radiometric Validation is performed at S3-MPC using three indirect methods, comparing simulated TOA radiances to that measured by the OLCI instrument.

- ❖ The “Rayleigh” method: measurement of the Rayleigh atmospheric backscattering over open ocean sites in clear sky off-glint conditions with low aerosol load to provide absolute calibration in the blue-to-red spectral domain.

- ❖ The “Glint” method: using the specular reflection of the sun (i.e. sun glint) on the open ocean surface and its known spectral dependency to assess inter-band calibration in the red-to-NIR spectral range.
- ❖ The PICS method: measurement over well characterized, temporally stable desert areas (Pseudo-Invariant Calibration Sites or PICS) to provide absolute calibration over the whole spectral domain. This method also allows cross-mission intercomparison with other sensors providing comparable spectral channels (e.g. Aqua/MODIS, S2A/MSI and MERIS/3REP).

The first two methods are undertaken by two different implementations: DIMITRI operated by ARGANS, and OSCAR operated by VITO.

Despite their discrepancies, more or less within their claimed accuracies, all methods do point out an excess of brightness for OLCI-A radiances (Figure 42, Figure 43, Figure 48 and Figure 51 and Table 9). Results are in pretty close agreement around 2-3% between 560 and 900 nm, except at 709 nm, likely because of the H₂O absorption correction accuracy. Biases are a bit worse in the blue, but the different methods (Rayleigh and PICS) do not agree in that spectral range: Rayleigh gives about 5-6 % while PICS remains around 2%. The Rayleigh method is however suspected to underestimate the simulated signal in the blue region whatever the sensor and the implementation, so that the 2-3% estimate of the PICS method is more reliable. Results for 1020 nm are much worse (5 to 6%, depending on the reference band).

The same figures for OLCI-B show current performance within the 2% requirement for all bands from 510 nm (Oa04) to 940 nm (Oa20) with remarkable agreement for all methods but DIMITRI Rayleigh. As for OLCI-A, the two Rayleigh methods indicate excess of brightness for the 4 bluest channels, between 2 and 4 %, while the PICS results provide very good performance estimates.

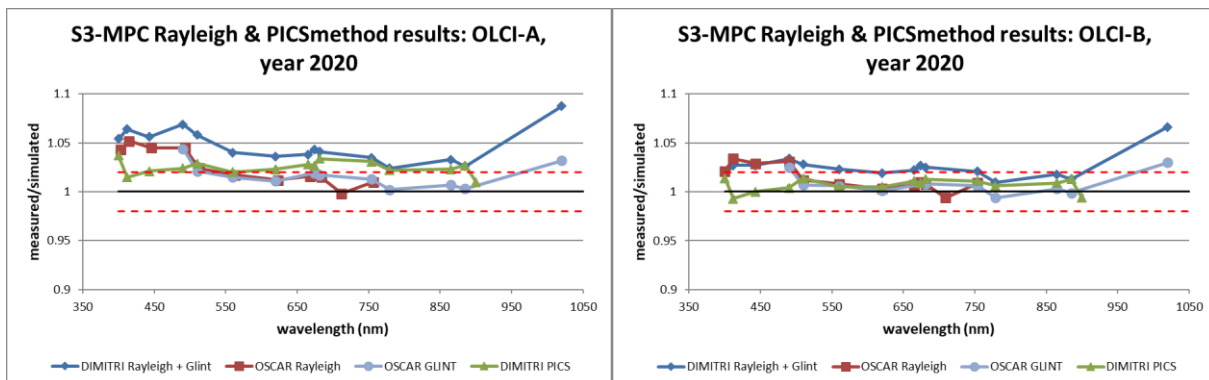


Figure 42: comparison of OSCAR and DIMITRI results for the various methods.

5.2.3.1 DIMITRI results

The time-series from the PICS method over the operational products display a good consistency over all the used CalVal sites (Figure 43 and Figure 44) and highlights a good stability of both sensors (OLCI-A and OLCI-B) over the analysed period.

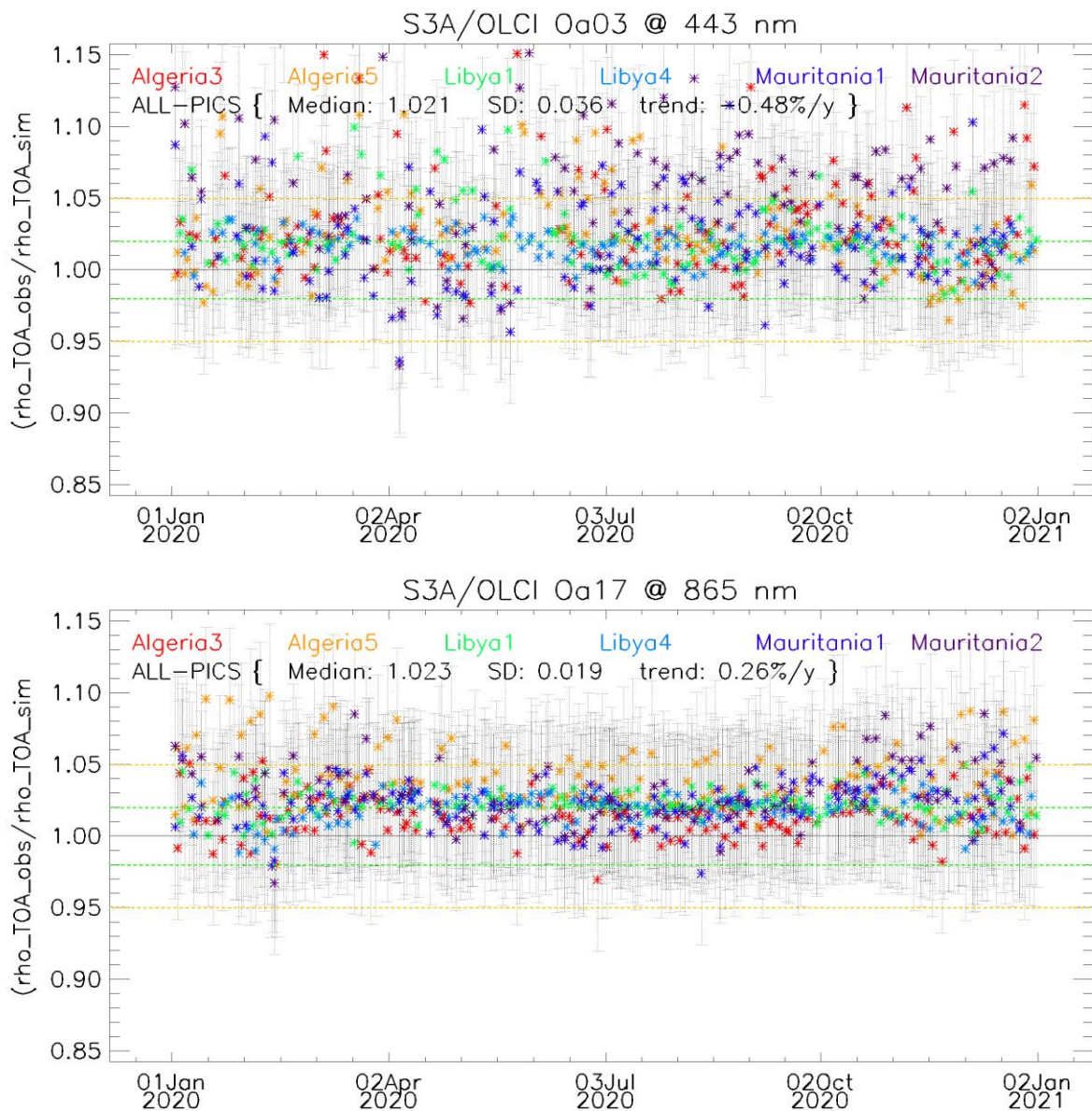


Figure 43: Time-series of the elementary ratios (observed/simulated) signal from S3A/OLCI for (top to bottom) Band Oa03 and band Oa17 respectively, over Six PICS Cal/Val sites. Dashed-green and orange lines indicate the 2% and 5% biases respectively. Error bars indicate the desert methodology uncertainty.

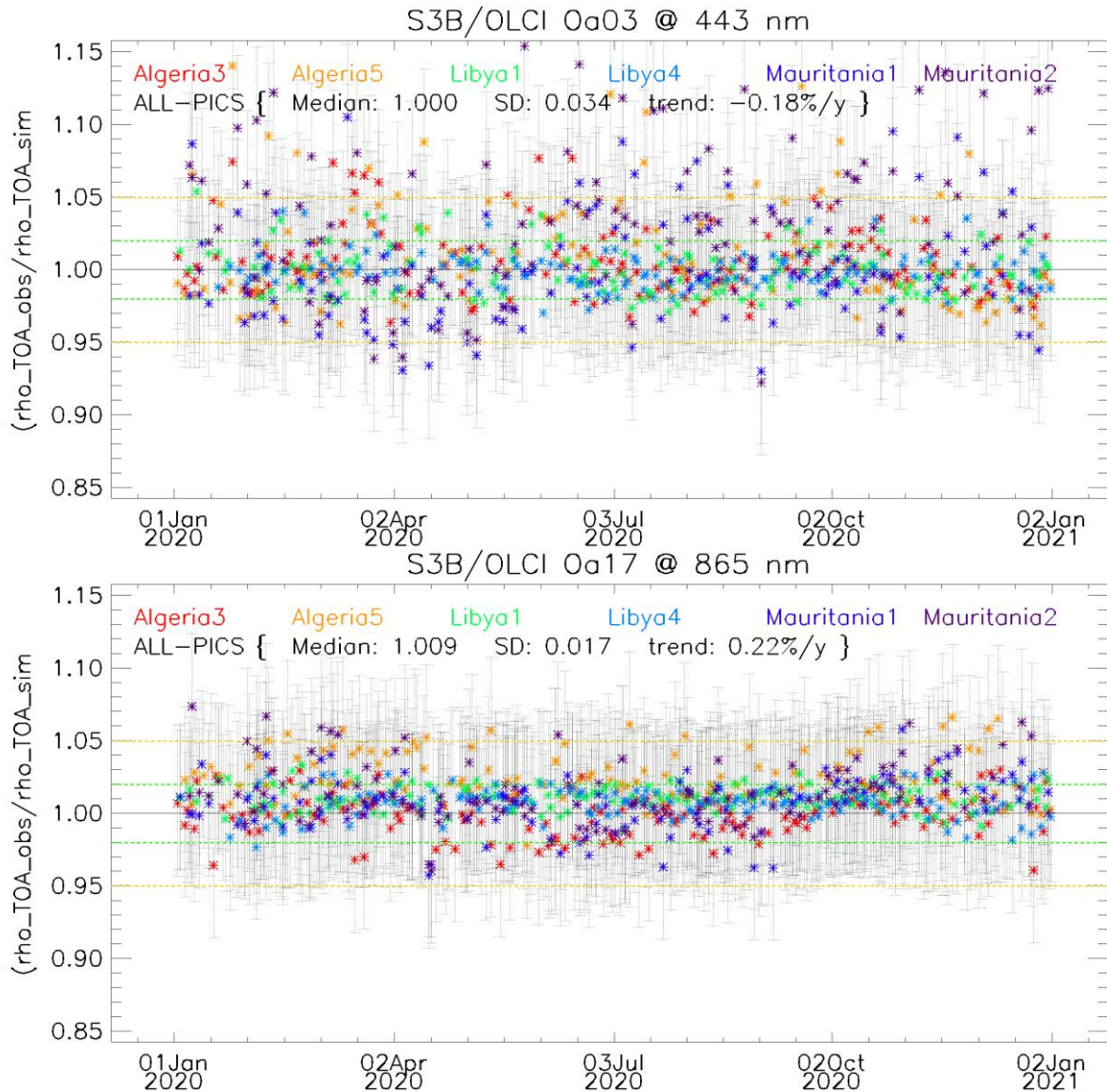


Figure 44: Time-series of the elementary ratios (observed/simulated) signal from S3B/OLCI for (top to bottom) Band Oa03 and band Oa17 respectively over Six PICS Cal/Val sites. Dashed-green and orange lines indicate the 2% and 5% biases respectively. Error bars indicate the desert methodology uncertainty.

The synthesis of the results shows a good consistency over Rayleigh, Glint and PICS methods (Table 6, Table 7 and Figure 45) from OLCI-A and OLCI-B over the period January 2020- January 2021.

Table 6: Synthesis of the DIMITRI results: estimated gain values for S3A/OLCI from Glint, Rayleigh and PICS over the period January 2020- January 2021.



Sentinel-3 MPC
S3MPC OPT Annual Performance
Report - Year 2020

Ref.: S3MPC.ACR.APR.007
 Issue: 1.1
 Date: 28/04/2021
 Page: 66

S3A-OLCI		Rayleigh Over Jan'20-Dec'20		Glint Over Jan'20-Dec'20		PICS Over Jan'20-Dec'20	
S3A-OLCI Bands	Wave length (nm)	Rayleigh Gain Coefficient	Standard deviation	Glint Gain Coefficient	Standard deviation	PICS Gain Coefficient	Standard deviation
Oa01	400	1.054	0.033	NA	NA	1.037*	0.051
Oa02	412	1.064	0.037	NA	NA	1.015	0.029
Oa03	443	1.056	0.040	NA	NA	1.021	0.036
Oa04	490	1.069	0.041	NA	NA	1.024	0.044
Oa05	510	1.058	0.036	NA	NA	1.029	0.043
Oa06	560	1.040	0.032	1.029	0.011	1.020	0.037
Oa07	620	1.036	0.030	1.025	0.003	1.023	0.021
Oa08	665	1.038	0.027	1.028	0.000	1.028	0.022
Oa09	674	1.040	0.027	1.033	0.002	1.027	0.019
Oa10	681	NA	NA	1.031	0.002	1.034	0.023
Oa11	709	NA	NA	NA	NA	NA	NA
Oa12	754	NA	NA	1.025	0.007	1.031	0.018
Oa13	761	NA	NA	NA	NA	NA	NA
Oa14	764	NA	NA	NA	NA	NA	NA
Oa15	768	NA	NA	NA	NA	NA	NA
Oa16	779	NA	NA	1.014	0.009	1.022	0.020
Oa17	865	NA	NA	1.023	0.010	1.023	0.019
Oa18	885	NA	NA	1.016	0.015	1.027	0.017
Oa19	900	NA	NA	NA	NA	1.010*	0.031
Oa20	940	NA	NA	NA	NA	NA	NA
Oa21	1020	NA	NA	1.077	0.026	NA	NA

Table 7: Synthesis of the DIMITRI results: estimated gain values for S3B/OLCI from Glint, Rayleigh and PICS over the period January 2020- January 2021.



Sentinel-3 MPC
S3MPC OPT Annual Performance
Report - Year 2020

Ref.: S3MPC.ACR.APR.007
 Issue: 1.1
 Date: 28/04/2021
 Page: 67

S3B-OLCI		Rayleigh Over Jan'20-Dec'20		Glint Over Jan'20-Dec'20		PICS Over Jan'20-Dec'20	
S3B-OLCI Bands	Wave length (nm)	Rayleigh Gain Coefficient	Standard deviation	Glint Gain Coefficient	Standard deviation	PICS Gain Coefficient	Standard deviation
Oa01	400	1.018	0.032	NA	NA	1.014*	0.049
Oa02	412	1.027	0.033	NA	NA	0.993	0.028
Oa03	443	1.027	0.032	NA	NA	1.000	0.034
Oa04	490	1.034	0.031	NA	NA	1.004	0.045
Oa05	510	1.028	0.029	NA	NA	1.014	0.042
Oa06	560	1.023	0.028	1.013	0.010	1.005	0.035
Oa07	620	1.019	0.026	1.009	0.003	1.005	0.020
Oa08	665	1.022	0.025	1.011	0.000	1.011	0.023
Oa09	674	1.027	0.027	1.017	0.002	1.009	0.020
Oa10	681	NA	NA	1.015	0.001	1.013	0.022
Oa11	709	NA	NA	NA	NA	NA	NA
Oa12	754	NA	NA	1.011	0.004	1.011	0.018
Oa13	761	NA	NA	NA	NA	NA	NA
Oa14	764	NA	NA	NA	NA	NA	NA
Oa15	768	NA	NA	NA	NA	NA	NA
Oa16	779	NA	NA	1.000	0.005	1.006	0.019
Oa17	865	NA	NA	1.008	0.008	1.009	0.017
Oa18	885	NA	NA	1.003	0.010	1.013	0.017
Oa19	900	NA	NA	NA	NA	0.994*	0.032
Oa20	940	NA	NA	NA	NA	NA	NA
Oa21	1020	NA	NA	1.056	0.018	NA	NA

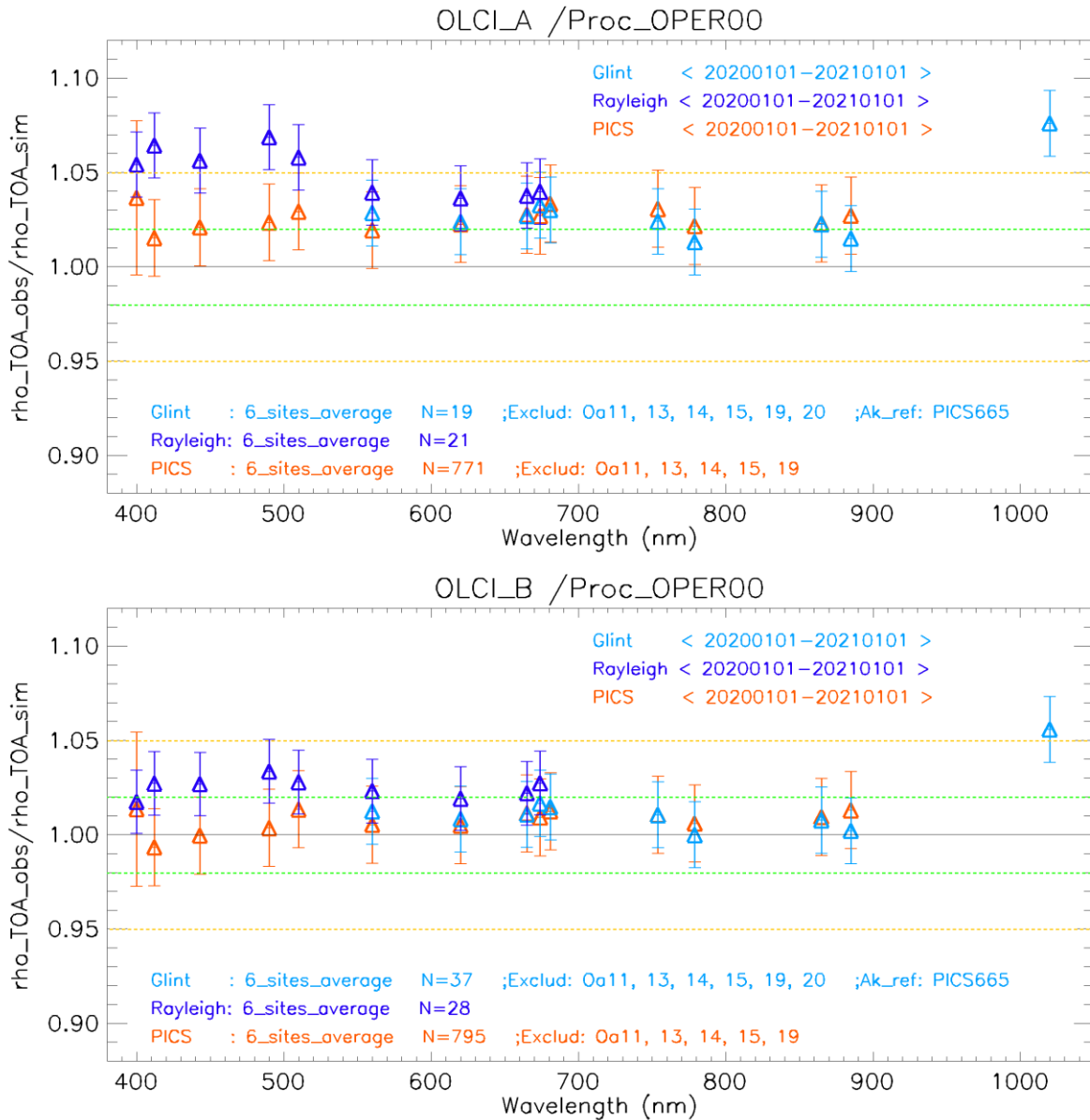


Figure 45: The estimated gain values for (top) S3A/OLCI and (bottom) S3B/OLCI from Glint, Rayleigh and PICS methods as a function of wavelength. We use the gain value of Oa8 from PICS method as reference gain for Sunlint method. Dashed-green and orange lines indicate the 2% and 5% respectively. Error bars indicate the methods uncertainties.

Cross-mission Intercomparison with MSI-A, MSI-B has been performed over January 2020 until January 2021. Figure-46 shows the estimated gain over different time-series for different sensors over PICS. The spectral bands with significant absorption from water vapor and O₂ are excluded. OLCI-A seems to have higher gain wrt the other sensors, and about 1-2% higher gain wrt to OLCI-B over VNIR spectral range.

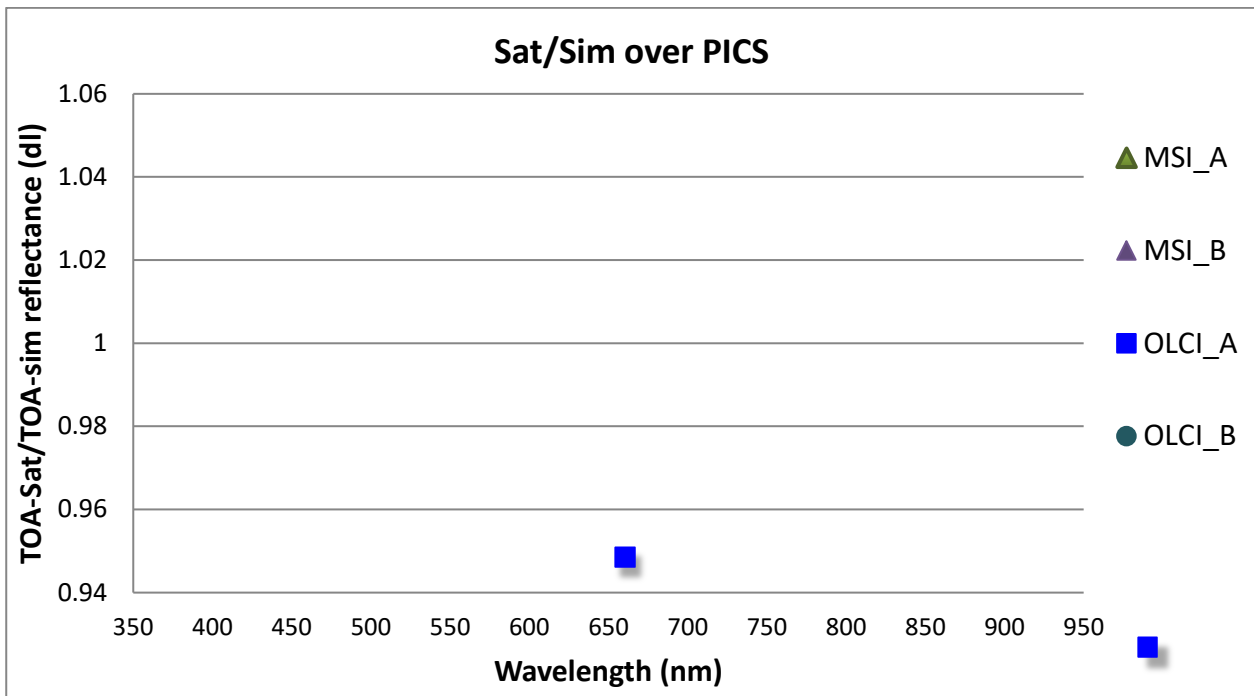


Figure-46 : Ratio of observed TOA reflectance to simulated one for MSI-A, MSI-B, OLCI-A and OLCI-B averaged over the six PICS test sites as a function of wavelength.

5.2.3.2 OSCAR results

The OSCAR Rayleigh and Glint methods have been applied to the S3A and S3B S3ETRAC data from the 6 oceanic calibration sites listed in Table 8. The OSCAR Rayleigh method has been improved by the use of a new chlorophyll climatology, described below.

Table 8: S3ETRAC Rayleigh Calibration sites

Site Name	Ocean	North Latitude	South Latitude	East Longitude	West Longitude
PacSE	South-East of Pacific	-20.7	-44.9	-89	-130.2
PacNW	North-West of Pacific	22.7	10	165.6	139.5
PacN	North of Pacific	23.5	15	200.6	179.4
AtIN	North of Atlantic	27	17	-44.2	-62.5
AtIS	South of Atlantic	-9.9	-19.9	-11	-32.3
IndS	South of Indian	-21.2	-29.9	100.1	89.5

Updates to the OSCAR Rayleigh method

A new CHL climatology (Figure 47) has been derived from the CMEMS GlobColour chlorophyll products which are publicly available on the CMEMS web portal. The climatology has been derived from the CMEMS OLCI monthly CHL products with a 4 km spatial resolution (i.e., dataset-oc-glo-chl-olci_a-l4-av_4km_monthly-rt-v02 products) considering the years 2017, 2018 and 2019. To impact of the climatology on the OSCAR Rayleigh results was assessed by reprocessing S3ETRAC data from the year 2019 with the new climatology. Overall, the new OLCI derived CHL climatology had a small effect on the OSCAR Rayleigh results with a slight decrease in the calibration results (i.e. smaller bias between modelled and measured values).

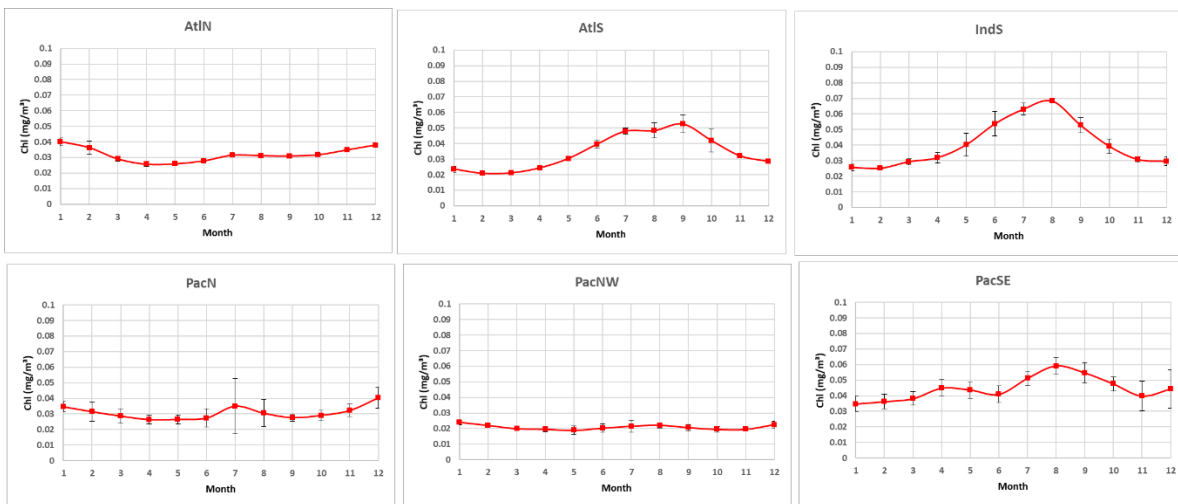


Figure 47. New CHL climatology for the Rayleigh calibration sites based CMEMS GlobColour products

OSCAR Rayleigh results

The OSCAR Rayleigh have been applied to the OLCI-A and OLCI-B S3ETRAC data from the 6 oceanic calibration sites using the new chlorophyll climatology. In Figure 48, the average OSCAR OLCI-A and OLCI-B Rayleigh results for the year 2020 are given. This average is obtained from 344 OLCI-A and 362 OLCI-B scenes from 2020 with valid results. A bias is observed between OLCI-A and OLCI-B, with OLCI-A being about 2 % brighter than OLCI-B in blue bands (i.e. Oa1 to Oa3). This bias seems to decrease with wavelength to about 1% in green bands and about 0.7% in red bands .

In Figure 49 and Figure 50 the average results of 2020 are compared with the average results of 2019 for respectively OLCI-A and OLCI-B. The results are very consistent between the years, both for OLCI-A and OLCI-B.

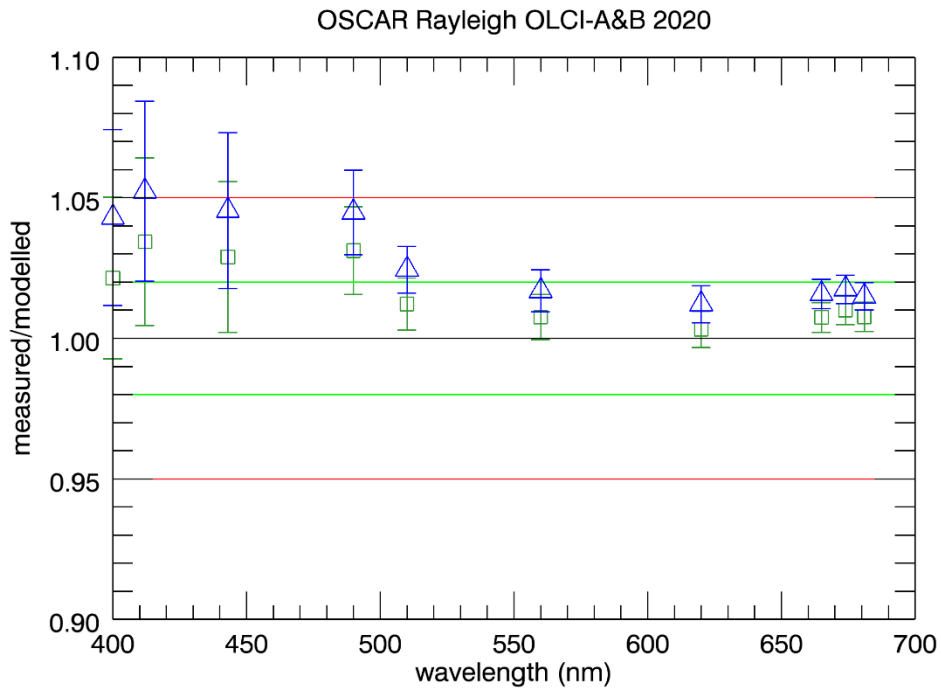


Figure 48: OSCAR Rayleigh S3A and S3B Calibration results for 2020 as a function of wavelength.

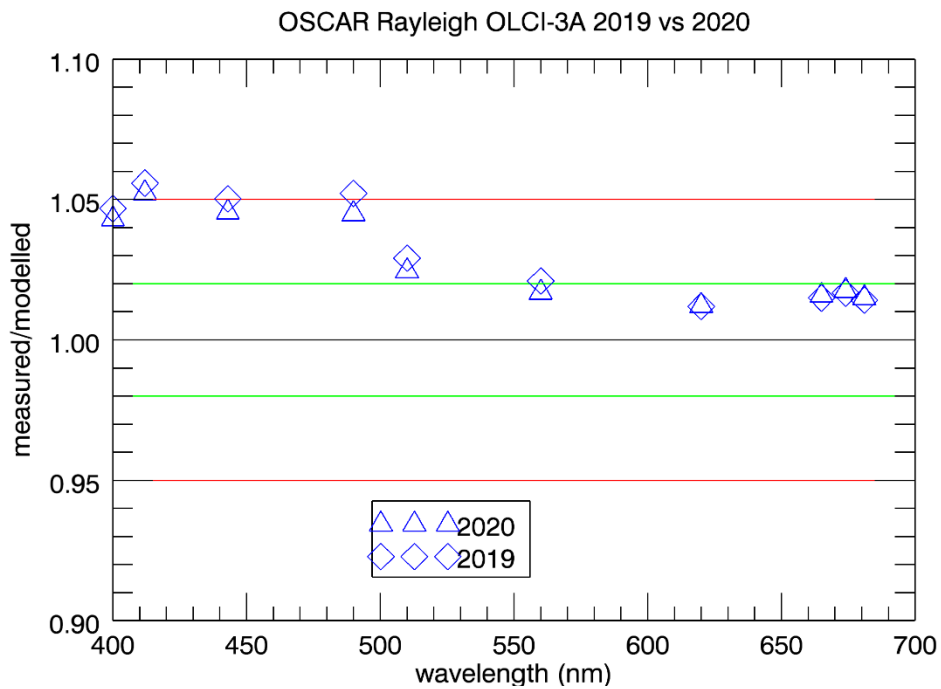


Figure 49: OSCAR Rayleigh OLCI-A Calibration results 2019 and 2020 as a function of wavelength.

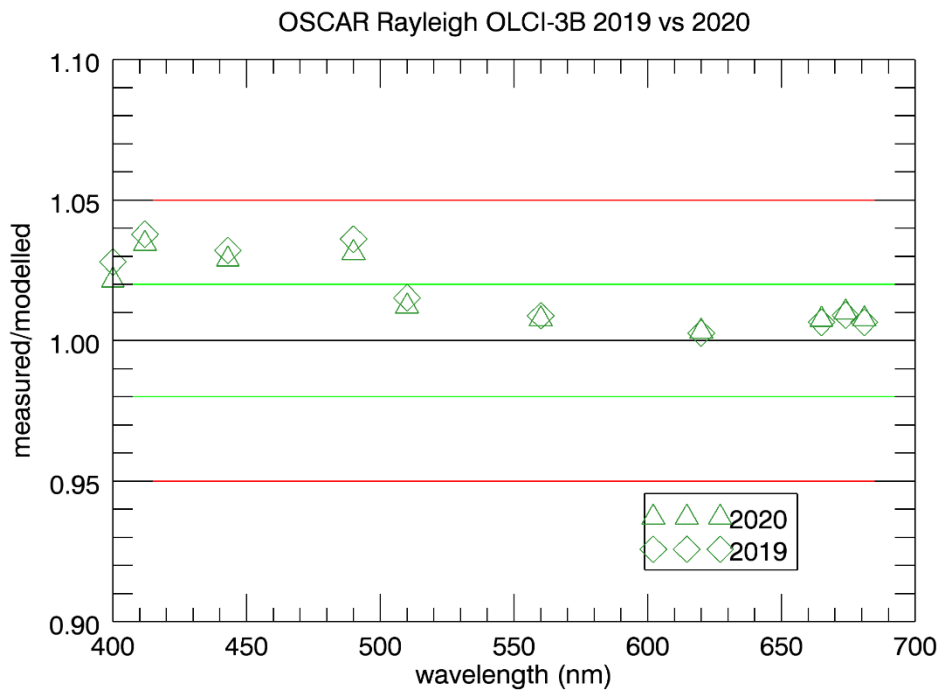


Figure 50: OSCAR Rayleigh OLCI-B Calibration results for 2019 and 2020 as a function of wavelength.

OSCAR Glitter results

In Figure 51, the average OSCAR OLCI-A and OLCI-B Glitter results, adapted to the Rayleigh result at 665 nm, are given for the year 2020. Similarly, as as for the Rayleigh results, a bias is observed between OLCI-A and OLCI-B, with OLCI-A being slightly brighter than OLCI-B with a bias decreasing with wavelength. Inter-band differences are small (< 1%) and well within the requirements except for the bands Oa21 (i.e. 1020 nm) and Oa4.

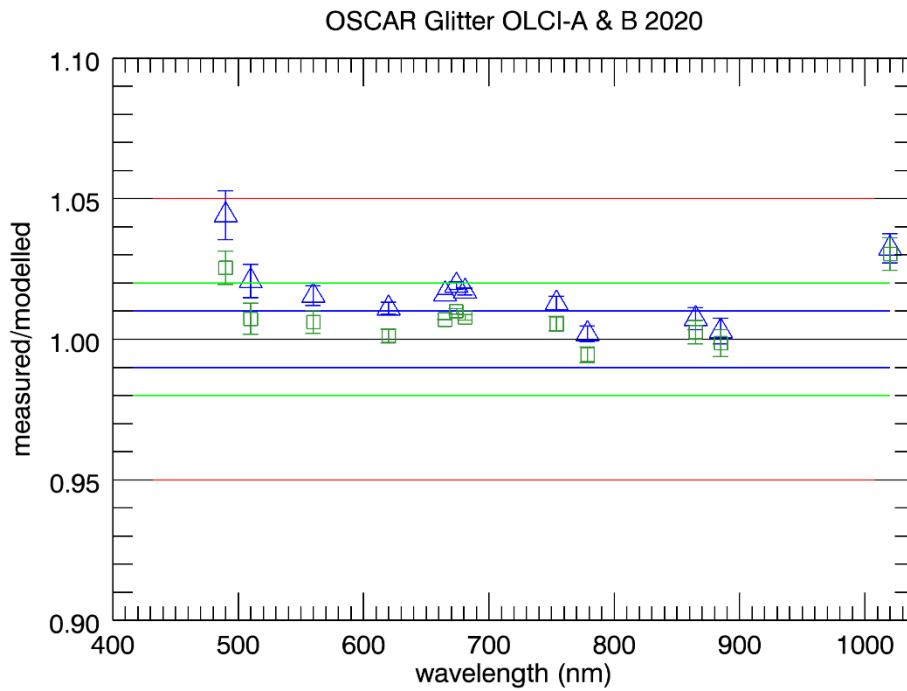


Figure 51: OSCAR Glitter S3A and S3B Calibration results (adapted to Rayleigh result at 665 nm) for 2019 as a function of wavelength.

Synthesis OSCAR Results

The synthesis of the OSCAR results is given in Table 9 below. This table shows a good consistency between the Rayleigh and Glitter results.

Table 9. Overview of the OSCAR Rayleigh and Glitter calibration results for S3A and S3B for 2019

OLCI band	Wavelength	Oscar Rayleigh S3A		Oscar Glint S3A		Oscar Rayleigh S3B		Oscar Glint S3B	
		2020		2020		2020		2020	
	(nm)	avg	stdev	avg	stdev	avg	stdev	avg	stdev
Oa01	400	1.043	0.031	NA	NA	1.021	0.029	NA	NA
Oa02	412	1.052	0.032	NA	NA	1.034	0.030	NA	NA
Oa03	443	1.045	0.028	NA	NA	1.029	0.027	NA	NA
Oa04	490	1.045	0.015	1.044	0.009	1.031	0.016	1.025	0.006
Oa05	510	1.024	0.008	1.021	0.006	1.012	0.009	1.007	0.006
Oa06	560	1.017	0.007	1.015	0.003	1.008	0.008	1.006	0.004
Oa07	620	1.012	0.007	1.011	0.002	1.003	0.006	1.001	0.002
Oa08	665	1.016	0.005	NA	NA	1.007	0.005	NA	NA
Oa09	674	1.017	0.005	1.019	0.001	1.010	0.005	1.010	0.001
Oa10	681	1.015	0.005	1.017	0.001	1.008	0.005	1.008	0.001
Oa11	709	0.998	0.008	NA	NA	0.994	0.008	NA	NA
Oa12	754	1.010	0.002	1.013	0.002	1.009	0.002	1.006	0.003
Oa13	761.25	NA	NA	NA	NA	NA	NA	NA	NA
Oa14	764.375	NA	NA	NA	NA	NA	NA	NA	NA
Oa15	767.5	NA	NA	NA	NA	NA	NA	NA	NA
Oa16	778.75	NA	NA	1.002	0.003	NA	NA	0.994	0.003
Oa17	865	NA	NA	1.007	0.004	NA	NA	1.003	0.004
Oa18	885	NA	NA	1.003	0.004	NA	NA	0.999	0.005
Oa19	900	NA	NA	NA	NA	NA	NA	NA	NA
Oa20	940	NA	NA	NA	NA	NA	NA	NA	NA
Oa21	1020	NA	NA	1.032	0.005	NA	NA	1.030	0.006

*OSCAR Rayleigh results for band Oa01 have to be considered with care due to larger uncertainty in the radiative transfer calculation

5.3 L2 product performances

5.3.1 Level 2 cloud screening

5.3.1.1 Introduction

Providing clear sky conditions for production of Sentinel-3 OLCI Level 2 products is essential to ensure a good and reliable Level 2 product quality for the users. After issues with the cloud screening in the initial processing baseline, a big effort was made by the Sentinel-3 MPC to improve the level 2 cloud flagging algorithms. Since 2017 a new cloud flagging is implemented in the current operational and reprocessed products. This had been extensively validated during 2019 and is documented in the Annual Report 2019. In brief summary, the overall accuracy is 86%, and the user accuracy for clear sky conditions which is the most relevant criteria for users, is 92.1%. To complement cloud screening validation against expert supervised classification, an innovative approach has been started: a validation exercise using data from the MicroWave Radiometer (MWR) on-board Sentinel-3. It is described in section

The work in the year 2020 focussed on improving the limitations which are still in the cloud screening. The achievements are summarized below. Since these improvements do not depend on the platform (S-3A or B) we do not differentiate.

5.3.1.2 Cloud screening validation with MWR

5.3.1.2.1 Introduction and summary

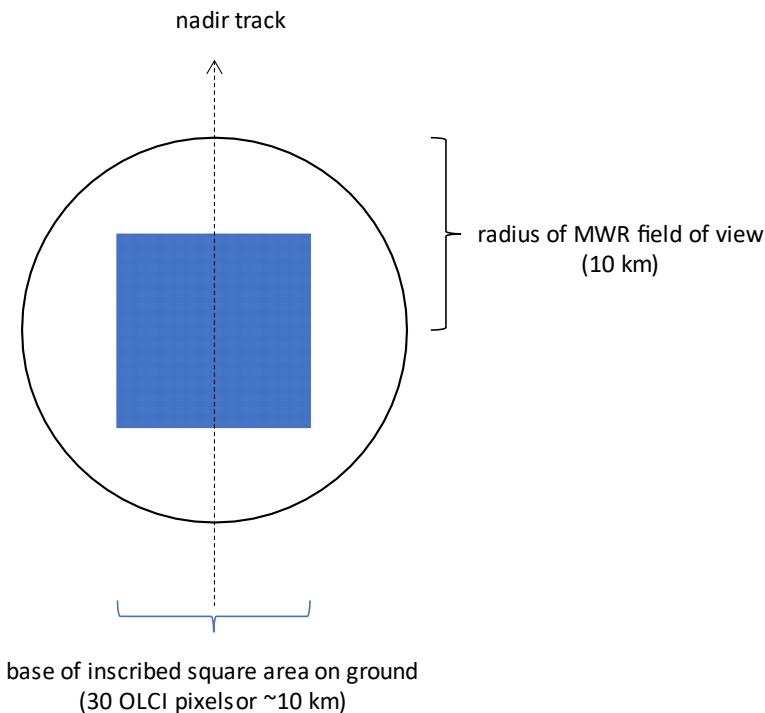
A statistical analysis of the liquid water path (LWP) signal from the MWR instrument and the corresponding cloud response from OLCI was conducted. The OLCI/SLSTR cloud response has been defined in terms of the fraction of cloudy pixels (as flagged by an OLCI or SLSTR cloud masks) within a square inscribed into the circular MWR field of view. A Technical Concept Note has been drafted and presented to the S3MPC OLCI-SYN ESL. Data products from MWR and OLCI have been acquired for four separate months. This dataset has been used to demonstrate the feasibility of an algorithm for routine cloud mask validation over water. To derive an ATBD, the LWP detection threshold and the associated level of confidence have been investigated and determined. A corresponding cloud fraction (CF) response threshold has been derived. A statistical test to indicate success or failure of the validation exercise has been defined and applied to the collected datasets. Method and results were presented at the OLCI-SYN QWG#6 meeting. Processing algorithms for MWR and OLCI have been prototyped. Software for conducting the cloud mask validation and for visualising the validation results was prototyped.

5.3.1.2.2 Processing

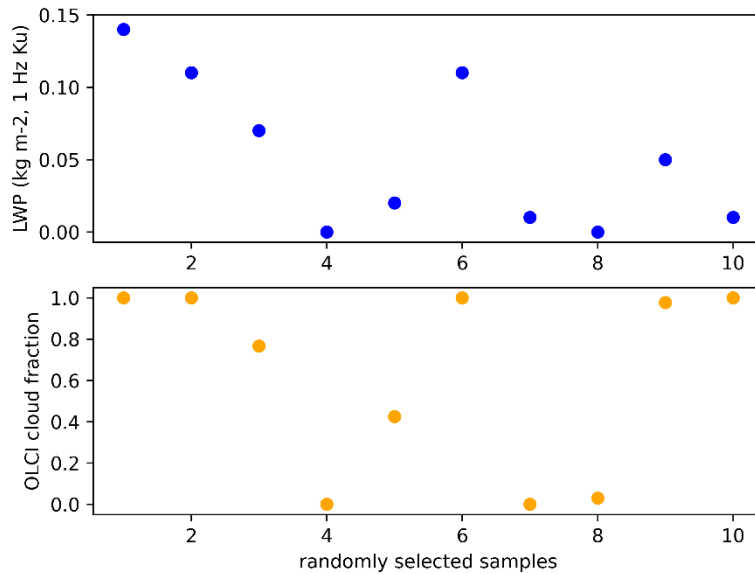
Preamble. The MWR instrument provides measurements of the liquid water path (LWP) which can be used to verify the cloud masks of OLCI and SLSTR under a few restrictions and limitations: Firstly, LWP measurements are conducted over water and do require a certain distance (let's say 50 km) to the coast and sea ice. LWP measurements over land are not feasible. Secondly, LWP measures the amount of liquid

water contained in a vertical column of “air” above a base area of 1 square meter on ground. These LWP measurements are sensitive to water droplets within clouds but not sensitive to ice particles. Thus, pure ice clouds cannot be detected by MWR measurements. Thirdly, the MWR LWP measurements do not constitute a fiducial reference. The LWP signal is affected by detection noise and even measurements above the nominal LWP detection threshold may include false detections. Thus, LWP measurements identify cases (apart from false detections) where any OLCI or SLSTR cloud test (which is sensitive to water clouds) must necessarily not indicate clear sky. LWP measurements are feasible to verify (i.e., falsify) the clear-sky hypothesis but are not suited to verify (i.e., falsify) the cloudy sky claim of an OLCI or SLSTR cloud mask. Though the WO is titled “cloud screening validation with MWR” only the clear-sky result of a cloud mask can be verified (i.e., falsified) in a mere statistical sense (because the LWP signal includes false detections) and based on a statistical test.

Signal analysis. Activities conducted within the signal analysis task of the WO included the collection of four months (Jun 2019, Oct 2019, Jan 2020, Apr 2020) of MWR Level-2 water products and corresponding OLCI Level-1 and Level-2 products. The collected data include about 1.7 million MWR fields of view, each of which is associated with a single LWP measurement. Corresponding OLCI pixels within a 30 x 30 pixels square (in the following referred to as macro pixel) inscribed into the MWR fields of view were extracted and merged with the MWR measurements (see Figure below).



For each field of view, the fraction of cloudy OLCI pixels within a macro pixel was computed and associated with the corresponding LWP measurement. Typical associations are depicted in the figure below.



The analysis of these associations showed that there is a statistical correlation between both signals, which can be used to formulate a statistical test to falsify the clear sky claim of a cloud test.

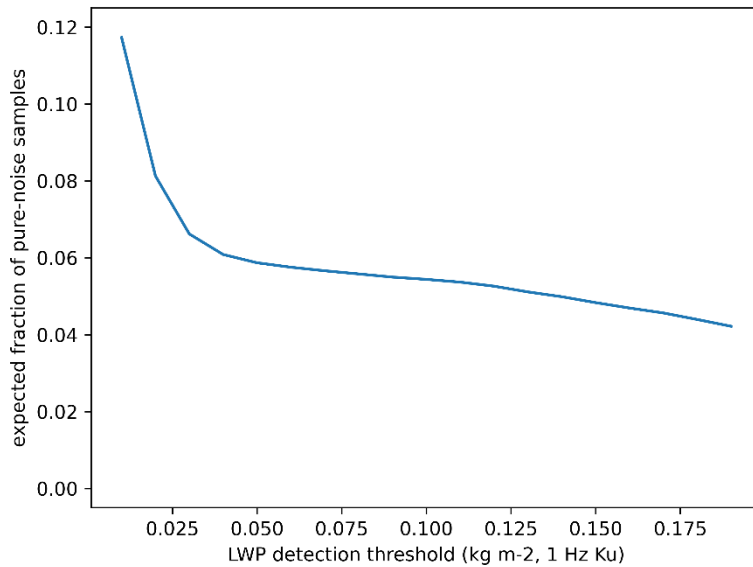
Let T_{LWP} denote the LWP detection threshold and let T_{CF} denote the cloud fraction response threshold below which an OLCI macro pixel is considered as clear sky area. Further let X_{LWP} and X_{CF} denote an LWP measurement and its associated cloud fraction. Then the clear sky claim $X_{CF} < T_{CF}$ of a cloud test is falsified, if $X_{LWP} > T_{LWP}$.

Though scientific literature suggested an LWP detection threshold between 30 g m⁻² and 40 g m⁻² the association of this estimate with a confidence level C_{LWP} and with a concrete number of clouds in terms of cloud fraction T_{CF} remained unclear from the signal correlation analysis.

Algorithm development. Activities conducted within the algorithm development task focused on the determination of the LWP detection threshold, its associated level of confidence C_{LWP} and a reasonable cloud fraction response threshold.

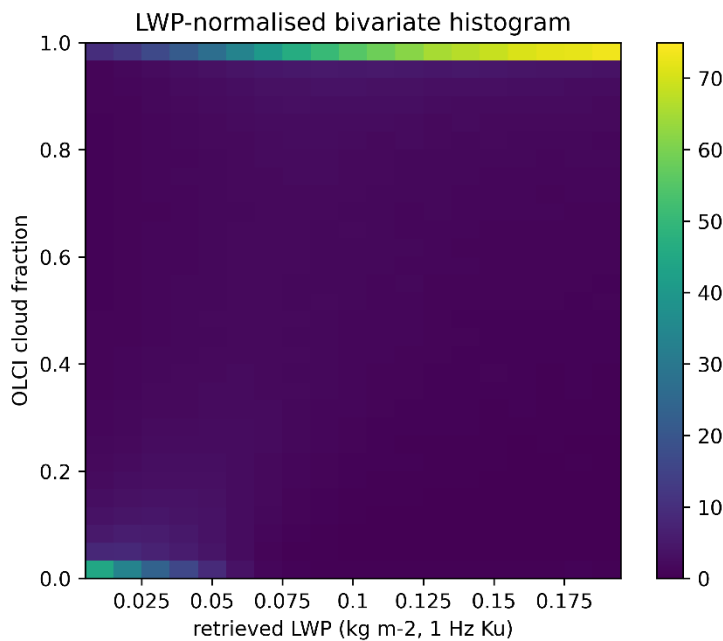
The statistical distribution of LWP measurements revealed that a considerable percentage of LWP measurements yielded negative values. These negative values are distributed rather homogeneously over open ocean but tend to avoid polar regions, where clouds are most frequent.

We interpreted these negative LWP values as (one half of) a pure and presumably clear-sky retrieval noise. Assuming that this noise is symmetric, we derived the expected fraction of pure-noise LWP measurements as a function of an assumed LWP detection threshold (shown in the figure below).

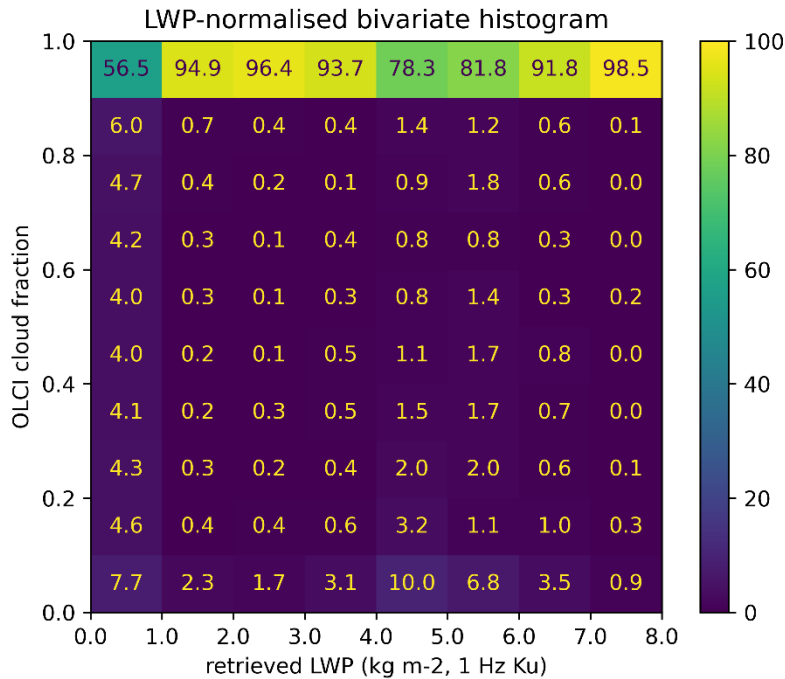


Based on this relation, we determined an LWP detection threshold of $T_{LWP} = 40 \text{ g m}^{-2}$ which is associated with a confidence level of $C_{LWP} \approx 0.95$. This means, that the chance of having detected a true LWP signal is 95%, if $X_{LWP} > T_{LWP}$ (and the chance of having a false signal is 5%).

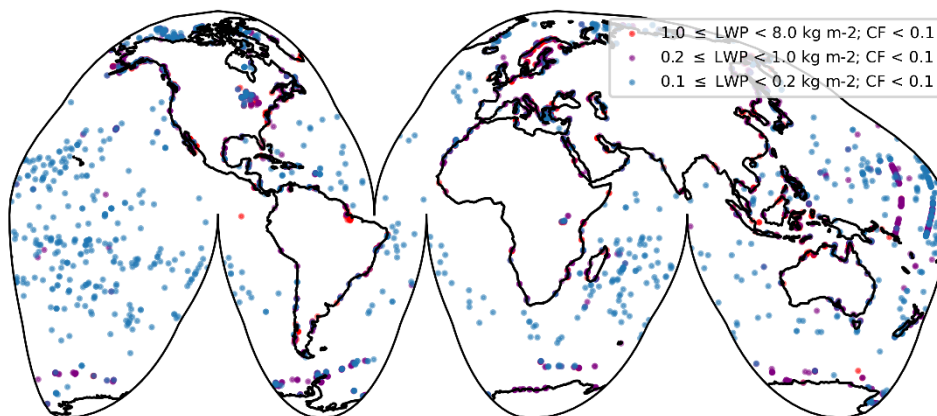
The bivariate distribution of LWP and CF values within the dataset collected during the signal analysis task was further analysed. The analysis supported a detection threshold of $T_{LWP} = 40 \text{ g m}^{-2}$ and revealed that the CF response to LWP is rather abrupt (and thus highly sensitive) once the LWP signal exceeds the detection threshold (shown in the figure below).



A further activity was the search of evidence of undetected clouds. The full range of the bivariate distribution of LWP and CF values was investigated and revealed possibly undetected clouds in the range $X_{LWP} > 0.04 \text{ g m}^{-2}$ and $X_{CF} < 0.10$ (see figure below).



An analysis of the geographic distribution of the fields of view corresponding to these cases, however, revealed that almost all cases where $X_{LWP} > 200 \text{ g m}^{-2}$ correspond to situations where the field of view is located at inland waters, or close to the coast or sea ice region, where a measurement of LWP is not feasible (red and purple dots in the figure below).



The suspicious cases where $X_{LWP} > 100 \text{ g m}^{-2}$ and $X_{CF} < 0.10$ amount to merely 0.5% of the total 916,000 cases where LWP exceeds the detection threshold, an amount which is negligible.

Other suspicious cases where $X_{LWP} > 40 \text{ g m}^{-2}$ and $X_{CF} < 0.10$ (or $X_{CF} < 0.05$) amount to non-negligible 7% (or 5%) of total cases. These amounts, however, are consistent with the expected fraction of false LWP detections, which is about 5%. Thus, we did not find evidence of undetected clouds.

The results of this activity were presented at the OLCI-SYN QWG#6 meeting.

Application of the method to SLSTR will be conducted in the next period.

Prototype software. Prototype software was developed for conducting the signal analysis and algorithm development tasks. The software includes downloading of products from public data hubs, collocation of MWR and OLCI observations, and statistical analysis. Corresponding developments for SLSTR are in progress.

Method testing and refinement. The method has been tested and refined iteratively, during conduction of the signal analysis and algorithm development tasks.

5.3.1.3 On-going improvements

5.3.1.3.1 Improvements due to usage of O2 bands

The oxygen absorption bands of OLCI (Oa13, Oa14 and Oa15) are sensitive to the absorption of oxygen in the atmosphere which scales with the air mass between the sensor and scattering target (= height of cloud) and thus is an indicator for clouds, in general. The usage is limited by the spectral differences per detector, and if this is not taken into account properly, the usability is rather limited.

As described in last year's (2019) report, thanks to R. Preusker (Spectral Earth) a method to harmonise the wavelength per detector for the O2 bands was developed, called O2 harmonisation. It has been implemented as a SNAP processor and made available publicly.

During 2020, the O2 bands harmonization was also adapted to OLCI-B. It requires time-dependent mode of central wavelength. In December 2020 it was already implementation in SNAP. The documentation will be updated early 2021. Documentation and code will be transferred to ACRI when ready.

Once the bands are harmonised they can be used much better for cloud screening purpose, e.g. for the separation between snow and ice, and likewise for distinction between glint and clouds.

R. Preusker also calculated a large number of TOA spectra for the O2 bands for the nominal wavelengths, and covering a large number of cloud and surface conditions. With these simulations we calculated a neural net which provides an estimate of the cloud top height (CTH, example see figure below). The method has been optimised to be fast and robust, but it is not very precise. The purpose it to use this as one information for cloud screening, and also use it for the calculation of cloud shadow (see next paragraph).

5.3.1.3.2 Cloud Shadow

Background:

Already during 2019 R. Preusker calculated a large number of TOA spectra for the O2 bands for the nominal wavelengths, and covering a large number of cloud and surface conditions. With these simulations we calculated a neural net which provides an estimate of the cloud top height (CTH, example see Figure 52).

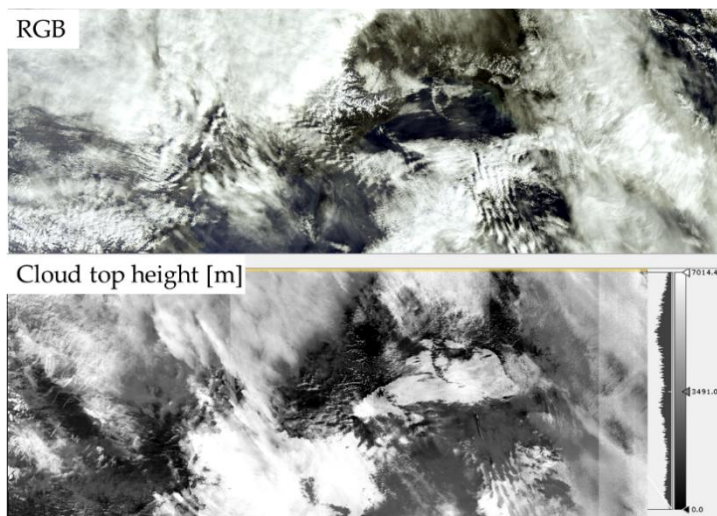


Figure 52: Cloud top height rough estimate for cloud screening and cloud shadow calculation

The method has been optimised to be fast and robust, but it is not very precise. The purpose is to use this as one information for cloud screening, but also use it for the calculation of cloud shadow.

Improvements 2020:

The improvement made during 2020 is the adaption of the O2 harmonization to OLCI B, thus the CTH can now also be estimated for OLCI B.

The technical note (TN) on the cloud shadow algorithm, sent to ACRI end of 2019, was analysed for feasibility to be implemented in the IPF. A study based on TN was done by ACRI and presented at the S3MPC ESL council in June 2020. A few questions/remarks have been raised by ACRI afterwards. Additionally, an issue with finding the correct direction of shadow in observation plain was identified by Brockmann Consult (BC). An updated version of the TN was provided to ACRI in November 2020. Nevertheless, there was still one open issue with shadows at scene borders, leading to strange behaviour, which was investigated in December 2020 and will presumably be fixed early 2021.

5.3.1.3.3 Snow/Cloud

The new approach for detecting snow using transmission in Oa13 (761nm) was implemented in SNAP/Idepix during 2020. Verification extended to more scenes for both OLCI-A and OLCI-B. Further studies are needed before potential implementation in IPF can be discussed.

5.3.1.3.4 Analysis on NN for OLCI-A/B using pixel collection.

The new pixel collection (2019) comprising OLCI-A and OLCI-B L1 data was used to analyse the performance of the current cloud screening NN, as the current NN was only trained on OLCI-A data. As OLCI-A and OLCI-B have slight spectral differences, it was expected that the current NN performs not as good on OLCI-B as on OLCI-A. If there is a big difference/influence, the next step was to see, if the use of the S3-TC A2B alignment coefficients (tandem phase) and flat fielding, allow the usage of a single NN based on OLCI-A or OLCI-B?

The new OLCI-A/B PixBox collection comprises 20,202 pixels and is nearly even distributed between OLCI-A and OLCI-B (see figure below)

Total pixel number: 20202, A: 51% (78 files), B: 49% (125 files)

Land (total 48%)

- Land 39%
- Town 4%
- Desert 5%
- dry/salt lake 0.4%

Water (total 51%)

- coastal waters 22%
- open ocean 22%
- Lake 3.0%
- River 1.6%

Others 2.7%

sun glint 2.8%

Clouds

- Clear 48%
- Cloudy 52%
 - opaque 18%
 - Oversaturated 1.8%
 - semi-transparent total 32%
 - Thick 8%
 - Average 11%
 - Thin 10%
 - spatially mixed 3.3%
 - over sun glint 0.8%

Snow / Ice

- land/mountain ice 11%
- floating ice 5%

Shadow

- over land 1%
- over water 0.3%

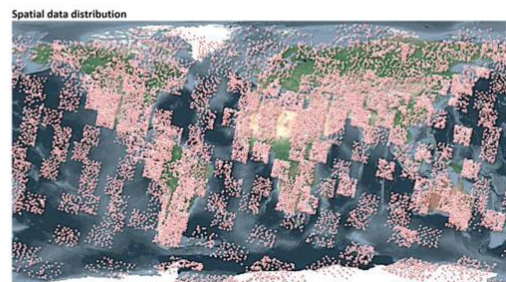


Figure 53: PixBox collection (2019) OLCI-A and OLCI-B

The last validation for OLCI cloud flagging was done in 2017 on a collection of OLCI-A data from 2017. The results had shown an overall accuracy (OA) of 86.09%. Now the main two question were. How is the overall performance now? Is there a difference between the performance of OLCI-A and OLCI-B?

As a recap, the validation results of 2017 are shown in the figure below.

OLCI LFR cloud val. - all surface (Insitu 1-5 vs CLD Flags)
 In-Situ Database

		Clear	Cloud	Sum	U A	E
OLCI FR	Class					
	CLEAR	3856	330	4186	92.1	7.9
	CLOUD	900	3756	4656	80.7	19.3
	Sum	4756	4086	8842		
P A		81.1	91.9		OAA:	86.09
E		18.9	8.1			

Scotts Pi: 0.721
 Krippendorfs alpha: 0.721
 Cohens kappa: 0.722

Figure 54: Results from 2017 PixBox validation on OLCI-A

Validation of cloud screening NN (IdePix) on OLCI-A/B data based on the 2019 PixBox collection shows that the overall performance is still the same, with 86.75% OA (figure below). Even though, data of both sensors is used.

OLCI-A & OLCI-B

In-Situ Database

		Clear	Cloud	Sum	U A	E
OLCI FR IdePix	Class					
	CLEAR	6662	714	7376	90.3	9.7
	CLOUD	1416	7280	8696	83.7	16.3
	Sum	8078	7994	16072		
P A		82.5	91.1		OAA:	86.75
E		17.5	8.9			

Scotts Pi: 0.734
 Krippendorfs alpha: 0.734
 Cohens kappa: 0.735

Figure 55: Validation results of OLCI-A and OLCI-B data using PixBox collection of 2019

This already leads to the expectation that the NN is performing equally on OLCI-A and OLCI-B. And exactly this can be seen when analysing the two sensors separately (see figure below). OLCI-A and OLCI-B have both OAs above 86%. Interestingly, OLCI-B performs even a bit better compared to OLCI-A.

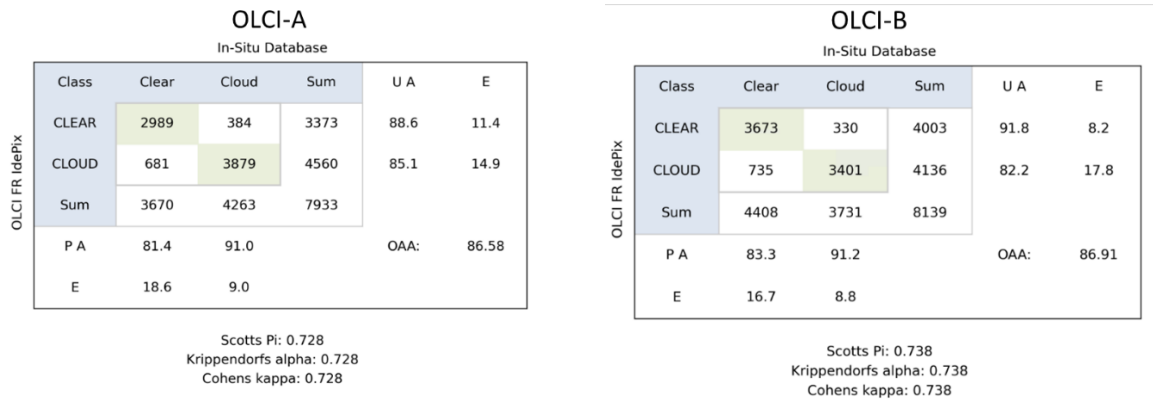


Figure 56: Validation results of OLCI-A only (left) and OLCI-B only (right) using PixBox collection of 2019

In conclusion this means, the NN based on OLCI-A is robust against the slight spectral differences between the two sensors. Therefore, a single NN can be used for the two sensors. Additionally, the analysis had shown that the performance of the cloud screening NN is stable since 2017.

Nevertheless, we wanted to know what flat-fielding and sensor alignment could do to the performance of the NN. A SNAP based tool was developed based on [Lamquin et al. (2020)] (<https://doi.org/10.3390/rs12111804>). It applies the values of Table 2 individually to each OLCI sensor (i.e., flat-fielding to achieve inter-camera harmonization) and then apply a linear regression to align the radiometry of both sensors (i.e. to achieve inter-sensor homogenization).

	Cam 1	Cam 2	Cam 3	Cam 4	Cam 5
OLCI-A	0.992	0.997	1.000	0.998	0.988
OLCI-B	0.991	0.997	1.000	0.996	0.983

Figure 57: Laquim et al. (2020) table 2

The tool was used to be run in front of the cloud screening NN (IdePix). The results are shown in the right part of the figure below. The results with the standard OLCI products are shown in the left part of the figure for comparison.

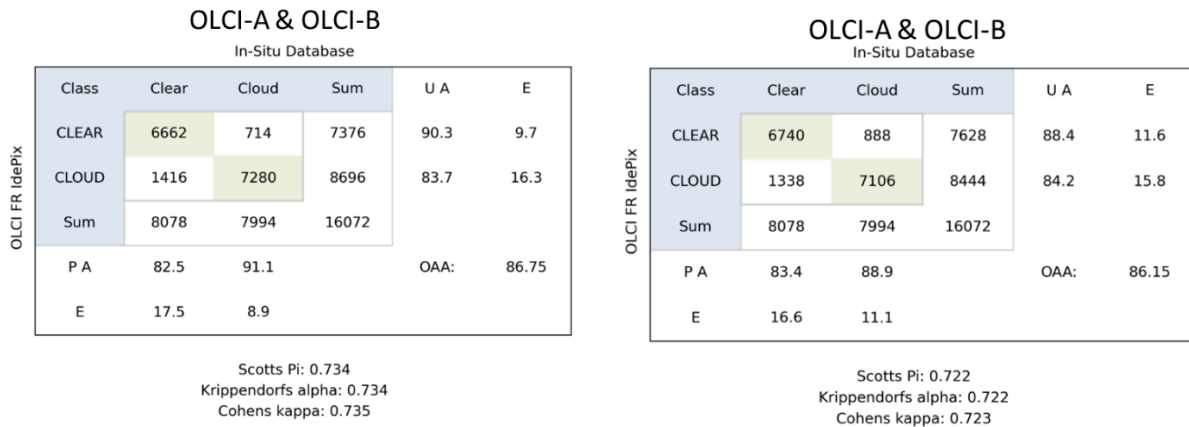


Figure 58: Validation results of OLCI-A/B (left) and OLCI-A/B flat-fielded and aligned (right) using PixBox collection of 2019

The results show that flat-fielding and harmonization do not have the expected effect on the cloud screening NN. In contrary, flat-fielding and harmonization seem to decrease the OA.

Flat-fielding and alignment also do not influence the relation of the validation results of OLCI-A and OLCI-B when done separately. Still OLCI-B is performing slightly better looking at the OA. Only user accuracies have changed slightly.

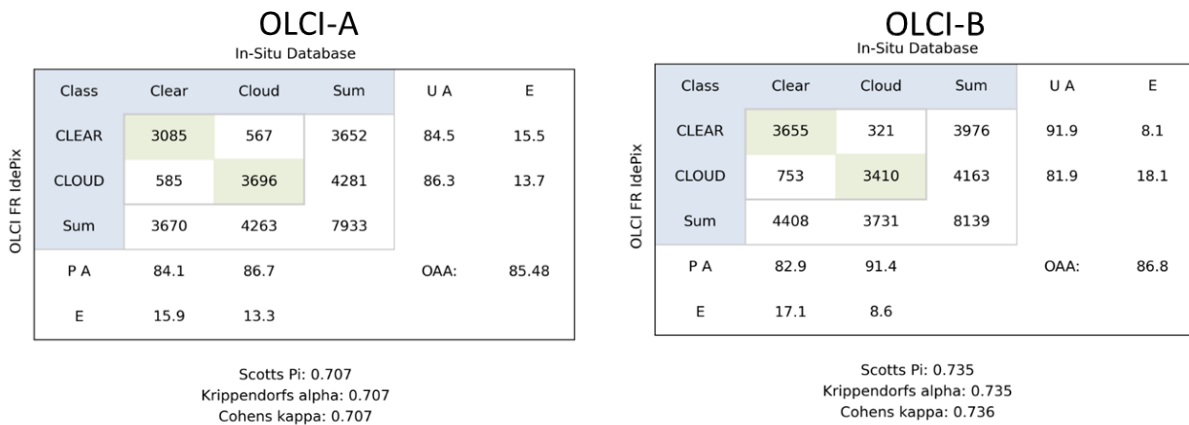


Figure 59: Validation results of flat-fielded and aligned OLCI-A only (left) and OLCI-B only (right) using PixBox collection of 2019

For this analysis flat-fielding and alignment have been applied. It might be valuable to validate with aligned data only (without flat fielding), to see the effects on OLCI-B.

5.3.2 Integrated Water Vapour (IWV)

The OLCI L2 IWV processor distinguishes between ocean and land surfaces and works very differently above the respective surfaces. The algorithm above water shows some serious flaws and therefore is under revision. OLCI's IWV above land surface is validated using the following ground truth data:

1. Global GNSS data, with a focus to north America (SUOMI NET, Ware et al. 2000)
2. Microwave radiometer measurements at the *Atmospheric Radiation Measurement (ARM) Climate Research Facility* of the US Department of Energy (Turner et al. 2003, Turner et al. 2007).
3. GRUAN radiosonde observations IWV (Immler et al 2010, Bodeker 2015)
4. AERONET (Holben et al 1998), using atmospheric transmission measurements at 0.9 μ m

All L2 product types have been validated: full resolution and reduced resolution, near real time and non-time critical, Ocean Colour (*wrr*, *wfr*) and Land Colour (*lrr*, *lfr*). The found results for all product types are identical, as expected, since the used processor is the same. The following quantitative comparisons are hence restricted to *wrr NT* (Ocean Colour Product, reduced resolution, non-time critical). Since the ocean colour product and the land colour product provide water vapour above land and water surfaces, the comparison is comprehensive. OLCI A data partly belong to reprocessed data if processed before Nov/2017. The ocean colour products from OLCI A have been taken from EUMETSATs rolling archive CODA (Copernicus Online Data Access, <https://coda.eumetsat.int/#/home>) or reprocessed OLCI A CODAREP (<https://codarep.eumetsat.int/#/home>) websites. All OLCI B data is from EUMETSATs CODA.

Integrated water vapour above land

5.3.2.1.1 Validation of OLCI A IWV using GNSS

490,000 potential matchups within the period of June 2016 to January 2021 have been analysed yet. The scenes cover high and low elevations; however, the majority of the used SUOMI-NET ground stations are in North and Central America. Only OLCI measurements are taken for the validation which are above land and are cloud-free in an area of about 10x10 km² around the GNSS stations. For the cloud detection, the standard L2 cloud-mask has been applied (including the cloud ambiguous and cloud margin flags). The comparison of OLCI and GNSS shows a very high agreement (Figure 60). The correlation between both quantities is 0.98 The root-mean-squared-difference is 2.2 kg/m². The systematic overestimation by OLCI is 12%. The bias corrected *rmsd* is 1.3 kg/m². Interesting is the strong seasonal pattern of the bias. It is also partly visible in the systematic overestimation swinging between 7 and 12 %. This clearly belongs to the seasonality of water vapor in North Amerika, with lower (better) values during winter. This could be an artefact of the retrieval inherent spectral extrapolation of the surface reflectance from window bands to the absorption band.

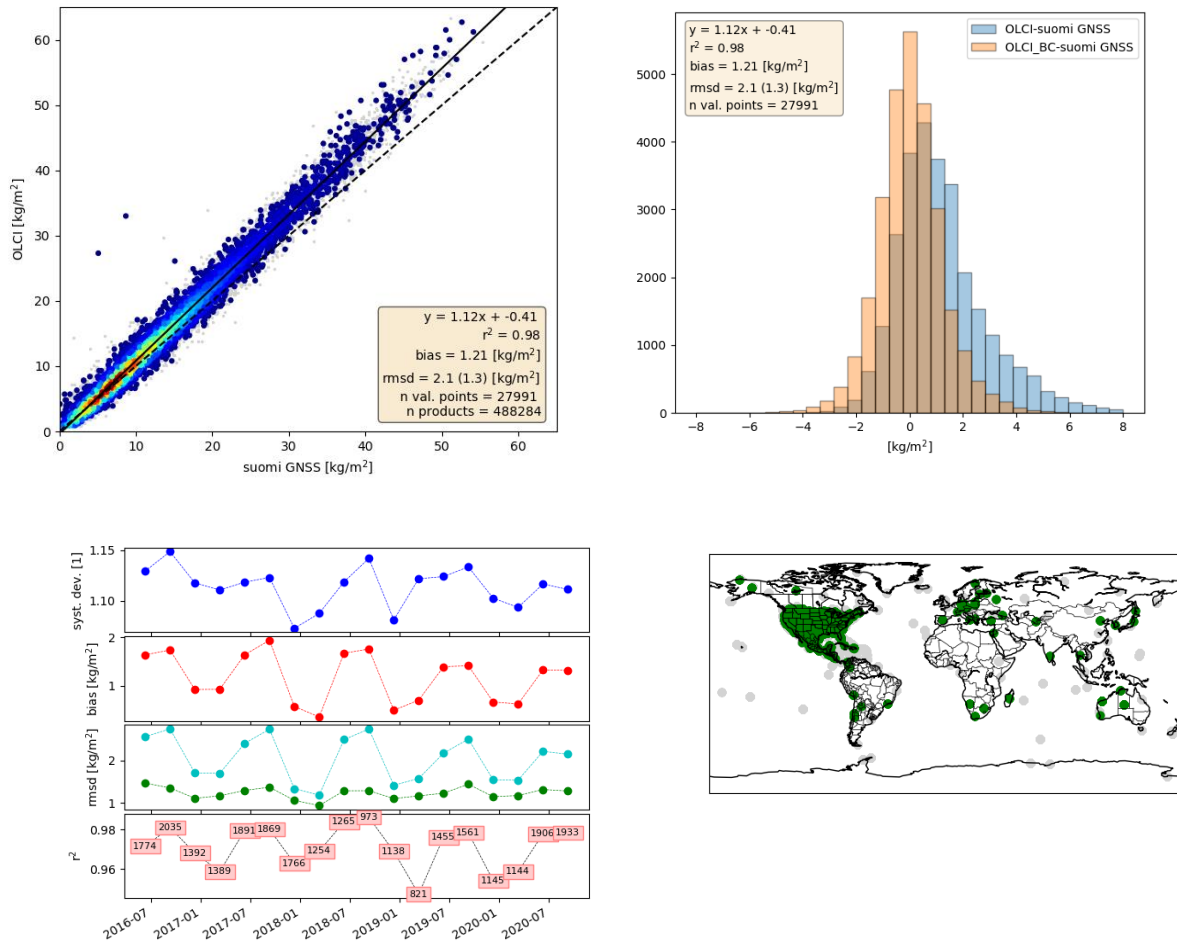


Figure 60: Upper left: Scatter plot of the IWV products, derived from OLCI A above land and from SUOMI NET GNSS measurements. Upper right: Histogram of the difference between OLCI and GNSS (blue: original OLCI, orange: bias corrected OLCI). Lower left: Temporal evolution of different quality measures (from top to bottom: systematic deviation factor, bias, root mean squared difference (with and without bias correction), explained variance (number in boxes are the numbers of matchups)). Lower right: Positions of the GNSS stations (grey: no valid matchup)

5.3.2.1.2 Validation of OLCI A IWV using passive microwave radiometer at ARM sites

Microwave radiometer measurements at the *Atmospheric Radiation Measurement (ARM) Climate Research Facility* of the US Department of Energy provides the ground truth with the highest accuracy (0.6 kg/m²). Currently 3 ARM sites are operated continuously, only the SGP (southern great planes) site provided cloud free measurements. 3200 potential matchups within the period of June 2016 to October 2020 have been analysed yet. Only OLCI measurements are taken for the validation which are above land and are cloud-free in an area of about 10x10 km² around SGP. For the cloud detection, the standard L2

cloud-mask has been applied (including the cloud ambiguous and cloud margin flags), resulting in 149 valid matchups. The comparison shows a very high agreement (Figure 61). The correlation between both quantities is 0.99. The root-mean-squared-difference is 1.4 kg/m². The systematic overestimation by OLCI is 8%. The bias corrected *rmsd* is 0.8 kg/m², close to the uncertainty of ARM. The investigation of the temporal evolution shows the same seasonal pattern as the GNSS comparisons, again belonging to the same seasonality of water vapor in North America.

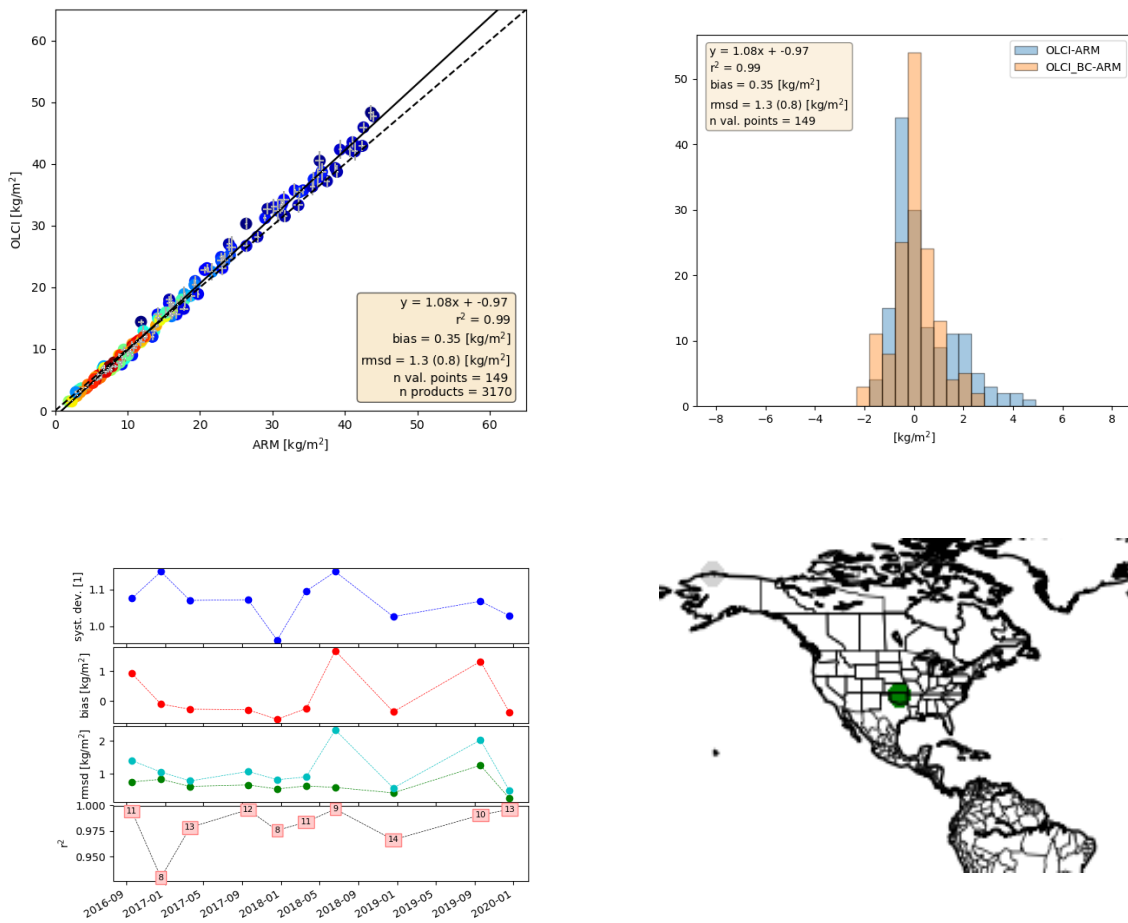


Figure 61: Upper left: Scatter plot of the IWV products, derived from OLCI A above land and from AMR MWR. Upper right: Histogram of the difference between OLCI and ARM (blue: original OLCI, orange: bias corrected OLCI). Lower left: Temporal evolution of different quality measures (from top to bottom: systematic deviation factor, bias, root mean squared difference (with and without bias correction), explained variance (number in boxes are the numbers of matchups)). Lower right: Position of ARM SGP.

5.3.2.1.3 Validation of OLCI A IWV using GRUAN radiosonde observations

Radiosonde observations of temperature, humidity and pressure allow a direct integration of water vapour. The emphasis of GRUAN is to provide long-term, highly accurate measurements of the atmospheric profile. This is achieved by a very rigid quality control and uncertainty quantification. From the 3300 potential matchups within the period of June 2016 to October 2020, only OLCI measurements are taken for the validation which are above land and are cloud-free in an area of about 10x10 km² around the radiosonde launch place. For the cloud detection, the standard L2 cloud-mask has been applied (including the cloud ambiguous and cloud margin flags). Eventually only 38 valid matchups could be used. This number is less than the number of valid matchups for the ARM site, since radiosondes launches are rare. That is why the time constraints have been relaxed to 6h. Still, the comparison shows a very high agreement (Figure 62). The correlation between both quantities is 0.99. The root-mean-squared-difference is 2.4 kg/m². The systematic overestimation by OLCI is 12%. The bias corrected *rmsd* is 1.3 kg/m². The number of valid matchups is currently too low to investigate a temporal evolution.

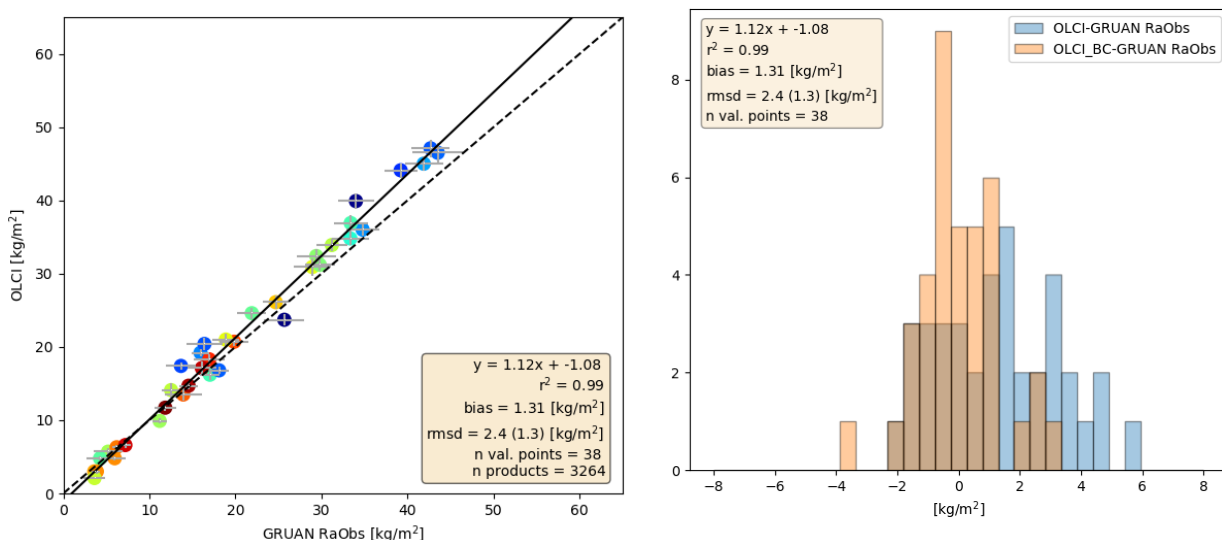


Figure 62: Left: Scatter plot of the IWV products, derived from OLCI A above land and from GRUAN radiosonde measurements. Right: Histogram of the difference between OLCI and GRUAN (blue: original OLCI, orange: bias corrected OLCI).

5.3.2.1.4 Validation of OLCI A IWV using AERONET observations

AERONET observations, regardless not primary made for water vapour, allow the direct estimation of the total column of water vapour by measuring the extinction of the direct solar irradiance at 900 nm. The used operational algorithm is quite simple and eventually relies on a logarithmic fit (incl. quadratic corrections). We are using AERONET for the IWV comparison, since AERONET data are better globally distributed, than ARM and SUOMINET, and are more frequent than GRUAN. Since the AERONET L2 is stringently quality controlled, it is published with a delay of up to 1 year, thus the latest AERONET data used here is from early Summer 2020. Only OLCI measurements are used for the validation which are

cloud-free (according to the standard cloud flags: *cloud*, *cloud margin* and *cloud ambiguous*) in an area of about 10x10 km² around the AERONET acquisition. From the 97000 potential matchups within the period of June 2016 to September 2020, 18500 valid matchups could be used. (Figure 63). The correlation between both quantities is 0.96. The root-mean-squared-difference is 3.7 kg/m². The systematic overestimation by OLCI is 19%. The bias corrected *rmsd* is 1.8 kg/m². The systematic deviation between OLCI and AERONET of 19% is significantly larger than the one found for GNSS, ARM and GRUAN (~10%). We think that this stems from a dry bias of AERONET and accordingly deficits in the operational algorithm, but we have not investigated it deeper.

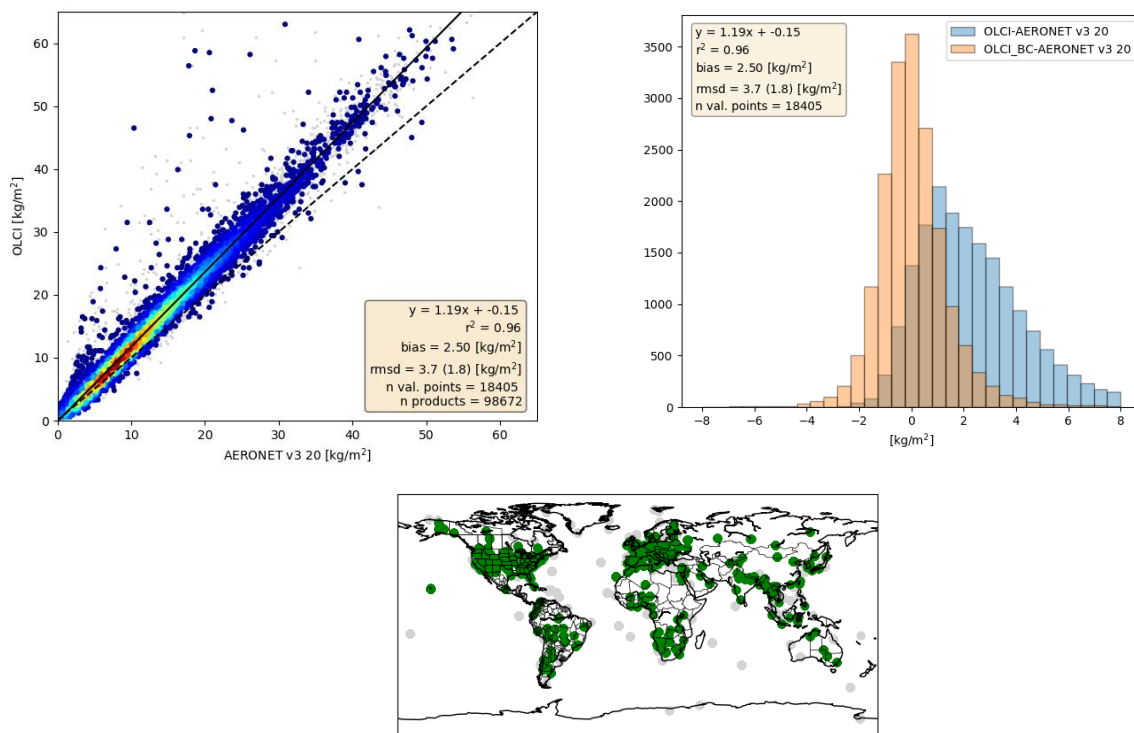


Figure 63: Upper left: Scatter plot of the IWV products, derived from OLCI A above land and from AERONET. Upper right: Histogram of the difference between OLCI and AERONET (blue: original OLCI, orange: bias corrected OLCI). Lower: Positions of the used AERONET stations (grey: no valid matchup).

5.3.2.1.5 Validation of OLCI B IWV

Within the period of June 2018 to January 2020 several 100000 scenes have been analysed yet. 11600 of them are valid for SUOMI-NET CONUS ground stations in North and Central America, 54 for ARM MWR and 13000 for AERONET. Contrary to OLCI A we are using AERONET V3 level 1.5 data. This data is faster published and allows much more matchups with data from the rolling archive CODA.

As for OLCI A, only measurements are taken for the validation which are above land and are cloud-free in an area of about 10x10 km² around the corresponding stations. For the cloud detection, the standard L2 cloud-mask has been applied (including the cloud ambiguous and cloud margin flags). The comparison of OLCI B shows almost identical results as for OLCI A (Figure 64).

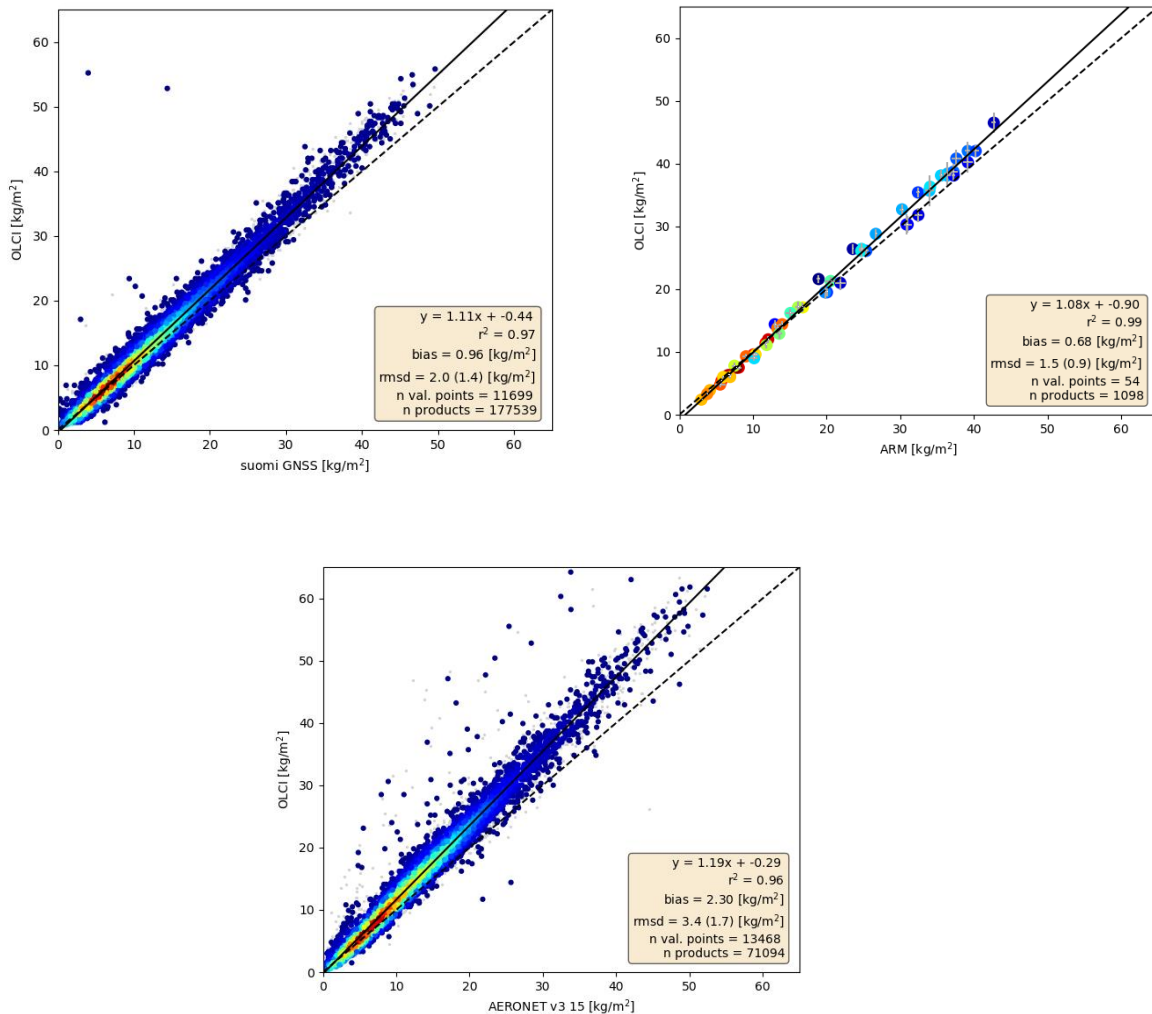


Figure 64: Scatter plot of the IWV products, derived from OLCI B above land and from SUOMI NET GNSS measurements (upper left), from ARM MWR (upper right) and AERONET (lower)

5.3.2.2 Summary

The validation exercise of the OLCI A IWV over land product using 4 different sources of ground truth showed consistently, that the product is of high quality (bias corrected root mean squared distance of down to 1.5 -0.8 kg/m²). However, there is a systematic overestimation of 9% to 13%. An equivalent validation of OLCI B shows the same results, no systematic differences between OLCI A and B have been

found. The validation with SUOMINET shows seasonal patterns of the overestimation with better values during winter seasons.

5.3.2.3 References

- ❖ Bodeker, G. E., Bojinski, S., Cimini, D., Dirksen, R. J., Haeffelin, M., Hannigan, J. W., Hurst, D. F., Leblanc, T., Madonna, F., Maturilli, M., Mikalsen, A. C., Philipona, R., Reale, T., Seidel, D. J., Tan, D. G. H., Thorne, P. W., Vömel, H., and Wang, J.: Reference upper-air observations for climate: From concept to reality, *B. Am. Meteorol. Soc.*, doi:10.1175/BAMS-D-14-00072.1, 2015.
- ❖ Holben, B. N., et al., AERONET—A federated instrument network and data archive for aerosol characterization, *Remote Sens. Environ.*, 66, 1–16, 1998.)
- ❖ Immler, F. J., Dykema, J., Gardiner, T., Whiteman, D. N., Thorne, P.W., and Vömel, H.: Reference Quality Upper-Air Measurements: guidance for developing GRUAN data products, *Atmos. Meas. Tech.*, 2, 1217–1231, doi:10.5194/amt-3-1217-2010, 2010.
- ❖ Pérez-Ramírez, D., D. N. Whiteman, A. Smirnov, H. Lyamani, B. N. Holben, R. Pinker, M. Andrade, and L. Alados- Arboledas (2014), Evaluation of AERONET precipitable water vapor versus microwave radiometry, GPS, and radiosondes at ARM sites, *J. Geophys. Res. Atmos.*, 119, 9596–9613, doi:10.1002/2014JD021730
- ❖ Smirnov, A., Holben, B.N., Slutsker, I., Giles, D.M., McClain, C.R., Eck, T.F., Sakerin, S.M., Macke, A., Croot, P., Zibordi, G., Quinn, P.K., Sciare, J., Kinne, S., Harvey, M., Smyth, T.J., Piketh, S., Zielinski, T., Proshutinsky, A., Goes, J.I., Nelson, N.B., Larouche, P., Radionov, V.F., Goloub, P., Krishna Moorthy, K., Matarrese, R., Robertson, E.J., Jourdin, F., 2009. Maritime aerosol network as a component of aerosol robotic network. *J. Geophys. Res.* 114, 1–10, <http://dx.doi.org/10.1029/2008JD011257>.
- ❖ Ware, R. H., D. W. Fulker, S. A. Stein, D. N. Anderson, S. K. Avery, R. D. Clark, K. K. Droegemeier, J. P. Kuettner, J. B. Minster, and S. Sorooshian (2000), SuomiNet: A real-time national GPS network for atmospheric research and education, *Bull. Am. Meteorol. Soc.*, 81(4), 677–694.
- ❖ Zibordi G., B. Holben, I. Slutsker, D. Giles, D. D'Alimonte, F. Mélin, J.-F. Berthon, D. Vandemark, H. Feng, G. Schuster, B. Fabbri, S. Kaitala, J. Seppälä. AERONET-OC: a network for the validation of Ocean Color primary radiometric products. *Journal of Atmospheric and Oceanic Technology*, 26, 1634-1651, 2009.

5.3.3 OLCI Global Vegetation Index (OGVI), a.k.a. FAPAR, and OLCI Terrestrial Chlorophyll Index (OTCI)

This section presents the performance of two Level 2 products routinely generated from OLCI: the OLCI Terrestrial Chlorophyll Index (OTCI) and OLCI Green Vegetation Index (OGVI). The former is a proxy of canopy chlorophyll content (CCC), whereas the latter is an estimation of the Green Instantaneous Fraction of Absorbed Photosynthetically Active Radiation (GIFAPAR). The performance evaluation activities over

the past year involve indirect verification efforts, a publication on an intercomparison activity performed between MTCI and OTCI and the continued development of an interactive MPC web application (https://s3mpc-soton.shinyapps.io/s3mpc_gui/). Additionally, a break down in the performance of the land products derived from the Sentinel-3 A and B units across different land covers is presented.

5.3.3.1 Indirect verification

The indirect verification consists of examining the annual evolution of OTCI and OGVI as well as the comparison with archive Medium Resolution Imaging Spectrometer (MERIS) Terrestrial Chlorophyll Index (MTCI) and MERIS Green Vegetation Index (MGVI). The MERIS archive is also referred to as MERIS climatology. The verification is carried out using 3x3 pixel extractions from >50 European Space Agency (ESA) core and Committee for Earth Observation Satellites (CEOS) Land Product Validation group (LPV) sites including a range of latitudes and land cover types (Table 10). The sites are scattered across 15 countries and are part of existing networks. Figure 65 to Figure 69 show the results of indirect verification on 5 unique land cover types: cropland, deciduous broadleaved forest, deciduous shrub, broadleaved evergreen forest and needle-leaved evergreen forest. The results correspond to S3A cycle 67, the last cycle that ended in 2020, are highlighted in red. The performance statistics between the monthly average OLCI and MERIS land products for every site is shown in Table 11. In general, OTCI and OGVI values are consistent with the MERIS archive with most of values falling within one standard deviation ($1\pm SD$) of MERIS climatology. The monthly mean extractions from all sites is shown in Figure 70. OTCI from S3B shows a strong agreement with the MERIS archive, $R^2 = 0.89$, $NRMSD < 0.11$ with very low bias, -0.01 . OGVI similarly shows a strong agreement with the MERIS archive, $R^2 = 0.89$, $NRMSD < 0.22$ with a slightly higher bias of 0.06.

Table 10: Validation sites analysed in report S3A 67/S3B 48. Land cover data from GLC2000 grouped according to the International Geosphere-Biosphere Programme (IGBP) designations.

Acronym	Country	Network	Lat	Lon	Land cover
AU-Cape-Tribulation	Australia	TERN-SuperSites, OzFlux	-16.106	145.378	EBF
AU-Cumberland	Australia	TERN-SuperSites, AusCover/OzFlux	-33.615	150.723	EBF
AU-Great-Western	Australia	TERN-SuperSites, AusCover/OzFlux	-30.192	120.654	DBF
AU-Litchfield	Australia	TERN-SuperSites, AusCover/OzFlux	-13.18	130.79	EBF
AU-Robson-Creek	Australia	TERN-SuperSites, AusCover/OzFlux	-17.117	145.63	EBF
AU-Rushworth	Australia	TERN-AusCover	-36.753	144.966	DBF
AU-Tumbarumba	Australia	TERN-SuperSites, AusCover/OzFlux	-35.657	148.152	EBF
AU-Warra-Tall	Australia	TERN-SuperSites, AusCover/OzFlux	-43.095	146.654	EBF
AU-Watts-Creek	Australia	TERN-AusCover	-37.689	145.685	EBF
AU-Wombat	Australia	TERN-SuperSites, AusCover/OzFlux	-37.422	144.094	EBF
BE-Brasschaat	Belgium	ICOS	51.308	4.52	ENF
BE-Vielsalm	Belgium	ICOS	50.305	5.998	ENF
BR-Mata-Seca	Brazil	ENVIRONET	-14.88	-43.973	non-forest
CA-Mer-Bleue	Canada	National Capitol Comission	45.4	-75.493	non-forest
CR-Santa-Rosa	Costa Rica	ENVIRONET	10.842	-85.616	EBF
CZ-Bili-Kriz	Czechia	ICOS	49.502	18.537	ENF
DE-Haininch	Deutschland	ICOS Associated	51.079	10.453	DBF
DE-Hones-Holz	Deutschland	ICOS	52.085	11.222	DBF
DE-Selhausen	Deutschland	ICOS	50.866	6.447	cultivated
DE-Tharandt	Deutschland	ICOS	50.964	13.567	ENF
FR-Aurade	France	ICOS	43.55	1.106	cultivated
FR-Estrees-Mons	France	ICOS Associated	49.872	3.021	cultivated
FR-Guayaflux	France	ICOS Associated	5.279	-52.925	EBF
FR-Hesse	France	ICOS	48.674	7.065	DBF
FR-Montiers	France	ICOS	48.538	5.312	DBF
FR-Puechabon	France	ICOS	43.741	3.596	ENF
IT-Casterporziano2	Italy	ICOS	41.704267	12.357293	DBF
IT-Collelongo	Italy	EFDC	41.849	13.588	DBF
IT-Lison	Italy	ICOS	45.74	12.75	cultivated
NE-Loobos	Netherlands	ICOS Associated	52.166	5.744	ENF
SE-Dahra	Senegal	KIT / UC	15.4	-15.43	cultivated
UK-Wytham-Woods	United Kingdom	ForestGeo - NPL	51.774	-1.338	DBF
US-Bartlett	United States	NEON, AERONET	44.064	-71.287	DBF
US-Central-Plains	United States	NEON, AERONET	40.816	-104.746	non-forest
US-Harvard	United States	NEON, AERONET	42.537	-72.173	DBF
US-Moab-Site	United States	NEON, AERONET	38.248	-109.388	non-forest
US-Mountain-Lake	United States	NEON, AERONET	37.378	-80.525	DBF
US-Oak-Rige	United States	NEON, AERONET	35.964	-84.283	DBF
US-Ordway-Swisher	United States	NEON, AERONET	29.689	-81.993	ENF
US-Smithsonian	United States	NEON, AERONET	38.893	-78.14	DBF
US-Steigerwarldt	United States	NEON	45.509	-89.586	DBF
US-Talladega	United States	NEON, AERONET	32.95	-87.393	ENF

Table 11: Comparison statistics between monthly S3A/B OLCI land products and MERIS archive data.

Site Acronym	S3A								S3B							
	OTCI vs MTCI				OGVI vs MGVI				OTCI vs MTCI				OGVI vs MGVI			
	n	R2	NRMSD	Bias	n	R2	NRMSD	Bias	n	R2	NRMSD	Bias	n	R2	NRMSD	Bias
AU-Cape-Tribulation	12	0.8	0.04	-0.11	12	0.27	0.06	0.15	11	0.75	0.04	-0.2	11	0.25	0.19	0.1
AU-Cumberland	12	0.9	0.02	0.01	12	0.46	0.07	0.08	12	0.46	0.05	0.02	12	0.45	0.13	0.09
AU-Great-Western	12	0.97	0.02	0.13	12	0.96	0	0.04	12	0.96	0.02	0.13	12	0.75	0.1	0.03
AU-Litchfield	12	0.93	0.02	-0.01	12	0.96	0.06	0.04	12	0.61	0.08	0.01	12	0.91	0.06	0.02
AU-Robson-Creek	12	0.93	0.03	-0.05	12	0.87	0.04	0.11	12	0.81	0.05	-0.17	12	0.65	0.13	0.12
AU-Rushworth	12	0.82	0.04	0.13	12	0.2	0.08	0.09	12	0.31	0.06	-0.14	12	0.33	0.08	0.04
AU-Tumbarumba	12	0.83	0.06	0.33	12	0.47	0.1	0.11	12	0.52	0.08	0.16	12	0.2	0.1	0.03
AU-Warra-Tall	12	0.64	0.07	-0.04	12	0.25	0.14	0.05	9	0.35	0.1	-0.33	9	0.22	0.35	0.01
AU-Watts-Creek	12	0.63	0.05	0.03	12	0.5	0.06	0.1	12	0.68	0.06	0.02	12	0.05	0.2	0.08
AU-Wombat	12	0.9	0.03	0.13	12	0.34	0.08	0.08	12	0.79	0.03	-0.1	12	0.04	0.11	0.04
BE-Brasschaat	11	0.99	0.03	-0.06	11	0.96	0.08	0.06	10	0.99	0.03	-0.07	10	0.93	0.08	0.02
BE-Vielsalm	11	0.95	0.03	0.08	11	0.98	0.06	0.1	10	0.77	0.07	0.03	10	0.83	0.17	0.1
BR-Mata-Seca	12	0.98	0.04	-0.01	12	0.99	0.05	0.02	12	0.92	0.08	0.02	12	0.98	0.07	0.04
CA-Mer-Bleue	10	0.95	0.06	-0.01	10	0.98	0.06	0.03	10	0.89	0.07	-0.04	10	0.96	0.08	0
CR-Santa-Rosa	12	0.98	0.04	0.1	12	0.59	0.21	0.12	12	0.93	0.08	-0.03	12	0.42	0.27	0.06
CZ-Bili-Kriz	10	0.85	0.04	0.04	10	0.96	0.07	0.07	8	0.92	0.04	-0.09	8	0.86	0.1	0.07
DE-Haininch	10	0.99	0.06	-0.05	10	0.99	0.05	0.06	9	0.97	0.09	-0.04	9	0.97	0.1	0.1
DE-Hones-Holz	10	0.99	0.03	0.06	10	0.99	0.05	0.05	10	0.97	0.08	-0.11	10	0.94	0.12	0.01
DE-Selhausen	12	0.88	0.09	-0.03	12	0.52	0.18	0.06	12	0.77	0.11	-0.18	12	0.22	0.3	0.02
DE-Tharandt	11	0.95	0.05	-0.04	11	0.96	0.09	0.09	10	0.99	0.02	-0.19	10	0.97	0.09	0.11
FR-Aurade	12	0.81	0.11	0.09	12	0.85	0.16	0.14	11	0.88	0.08	0.03	11	0.86	0.16	0.08
FR-Estrees-Mons	12	0.94	0.07	0.06	12	0.9	0.11	0.06	11	0.84	0.13	0.15	11	0.9	0.11	0.05
FR-Guayaflex	12	0.74	0.03	-0.17	12	0.11	0.1	0.17	11	0.72	0.03	-0.24	11	0	0.2	0.24
FR-Hesse	12	0.99	0.03	0.07	12	0.98	0.04	0.07	11	0.96	0.07	0.1	11	0.83	0.19	0.08
FR-Montiers	12	0.99	0.03	-0.12	12	0.98	0.06	0.04	11	0.95	0.09	-0.09	11	0.9	0.17	0.09
FR-Puechabon	12	0.84	0.03	-0.05	12	0.89	0.06	0.09	12	0.93	0.03	0.05	12	0.88	0.09	0.06
IT-Casterporziano2	12	0.97	0.02	-0.1	12	0.87	0.03	0.07	12	0.88	0.04	-0.07	12	0.54	0.1	0.05
IT-Collelongo	12	0.98	0.05	0	12	0.99	0.05	0.02	12	0.92	0.13	0.05	12	0.97	0.11	0.03
IT-Lison	12	0.98	0.03	-0.04	12	0.98	0.07	0.09	12	0.93	0.06	-0.05	12	0.94	0.1	0.08
NE-Loobos	12	0.71	0.07	0.06	12	0.89	0.1	0.04	12	0.57	0.07	0.04	12	0.88	0.1	0.03
SE-Dahra	12	0.76	0.04	-0.04	12	0.9	0.43	0.01	11	0.26	0.1	-0.07	11	0.88	0.52	0.02
US-Bartlett	12	0.97	0.04	-0.02	12	0.97	0.1	0.06	12	0.89	0.08	-0.05	12	0.95	0.12	0.04
US-Central-Plains	11	0.72	0.03	-0.05	11	0.89	0.21	0.01	10	0.47	0.05	-0.06	10	0.76	0.21	0
US-Harvard	12	0.99	0.03	-0.16	12	0.97	0.09	0.05	11	0.98	0.05	-0.22	11	0.95	0.14	0.02
US-Moab-Site	12	0.75	0.02	0.05	12	0.09	0.22	0.02	11	0.86	0.02	0.02	11	0.05	0.22	0.03
US-Mountain-Lake	12	0.99	0.04	-0.23	12	1	0.05	0.03	11	0.96	0.07	-0.41	11	0.99	0.05	0
US-Oak-Rige	12	0.99	0.03	-0.05	12	0.98	0.07	0.05	12	0.98	0.05	-0.07	12	0.99	0.05	0.05
US-Ordway-Swisher	12	0.51	0.03	0.02	12	0.94	0.03	0.09	12	0.12	0.04	0	12	0.7	0.07	0.06
US-Smithsonian	11	0.99	0.04	-0.2	11	0.99	0.07	0.04	9	0.99	0.06	-0.22	9	0.97	0.09	0.01
US-Steigerwardt	12	0.99	0.03	0.03	12	0.99	0.08	0	8	0.95	0.07	-0.03	8	0.99	0.05	0
US-Talladega	12	0.98	0.02	-0.12	12	0.98	0.05	0.07	12	0.92	0.04	-0.18	12	0.96	0.1	0.06

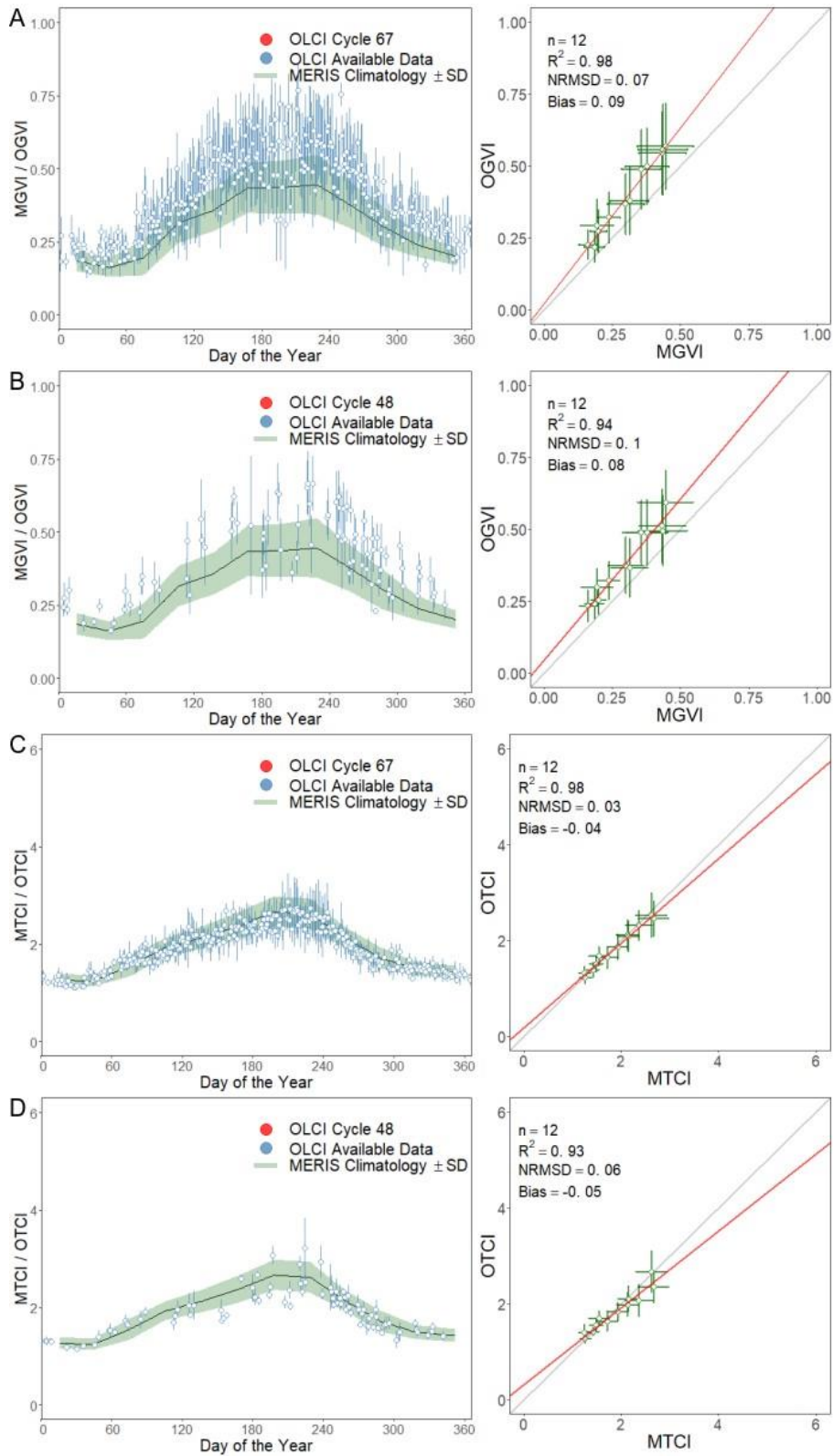


Figure 65: Time-series OGVI and OTCI and corresponding scatterplot of monthly mean for site IT-Lison, Italy, land cover Cropland. A and C represent S3A; B and D represent S3B.

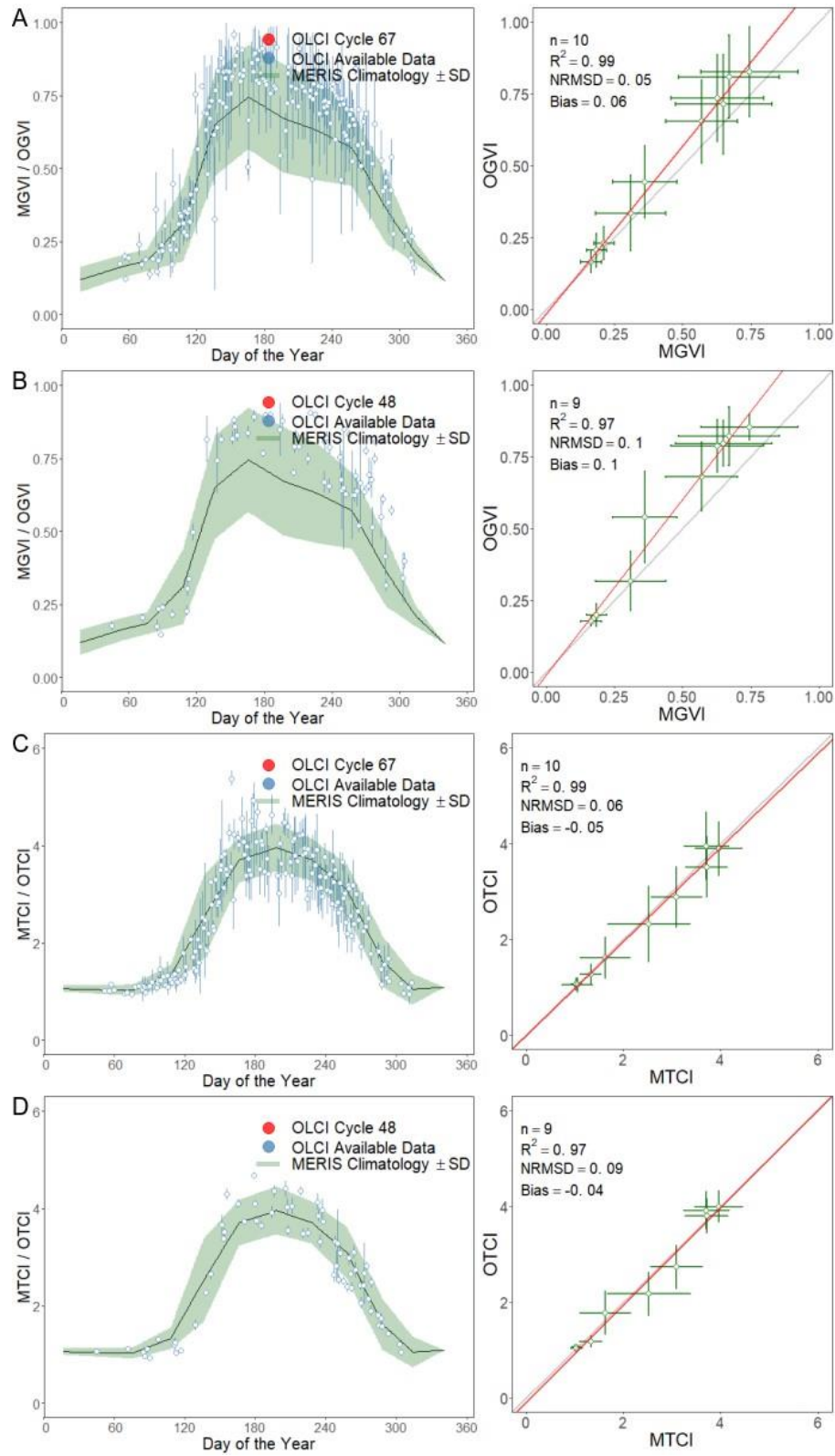


Figure 66: Time-series OGVI and OTCI and corresponding scatterplot of monthly mean for site DE-Haininch, Deutschland, land cover Broadleaved, deciduous, closed. A and C represent S3A; B and D represent S3B.

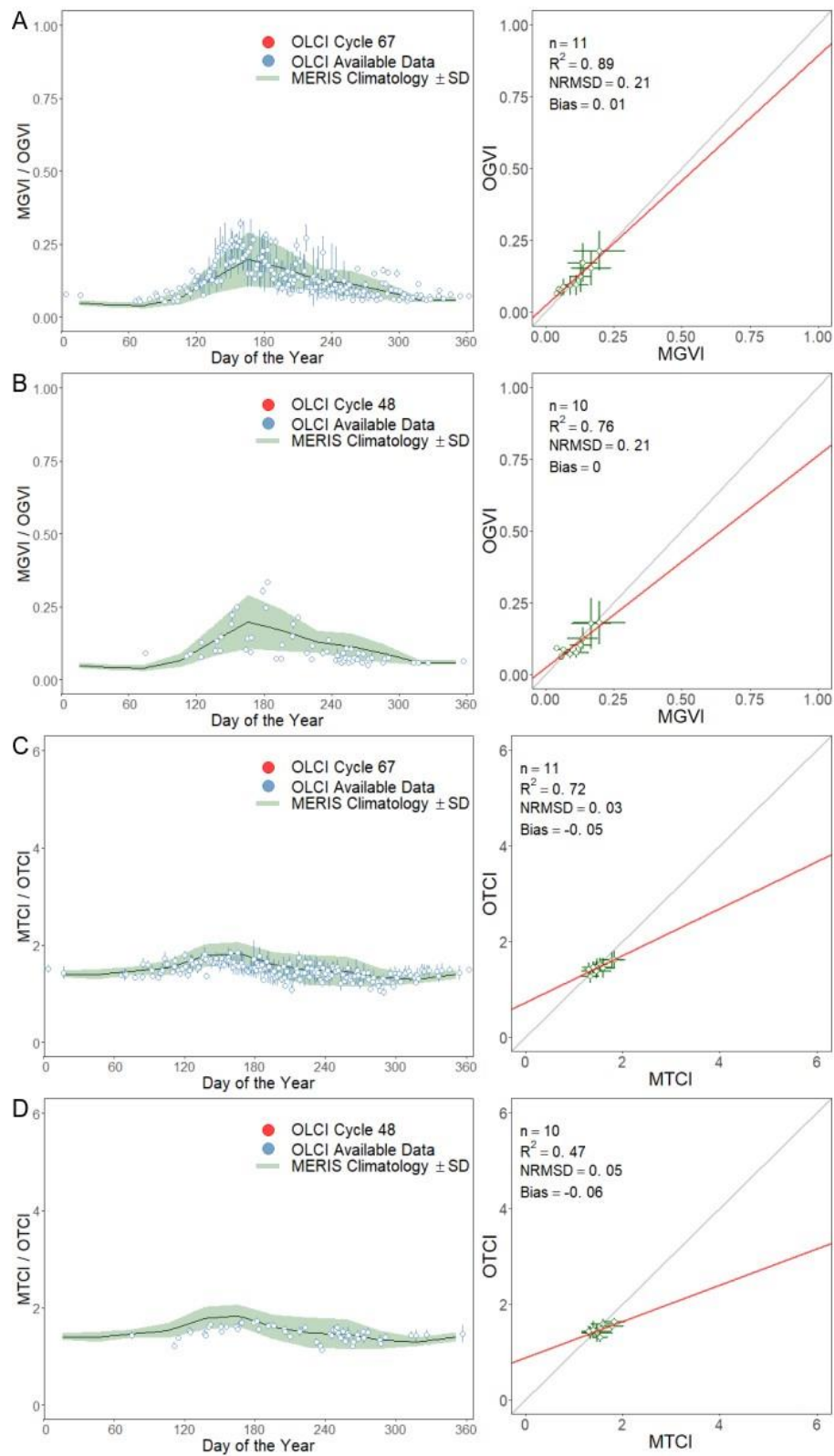


Figure 67: Time-series OGVI and OTCI and corresponding scatterplot of monthly mean for site US-Central-Plains, United States, land cover Shrub, closed-open, deciduous. A and C represent S3A; B and D represent S3B.

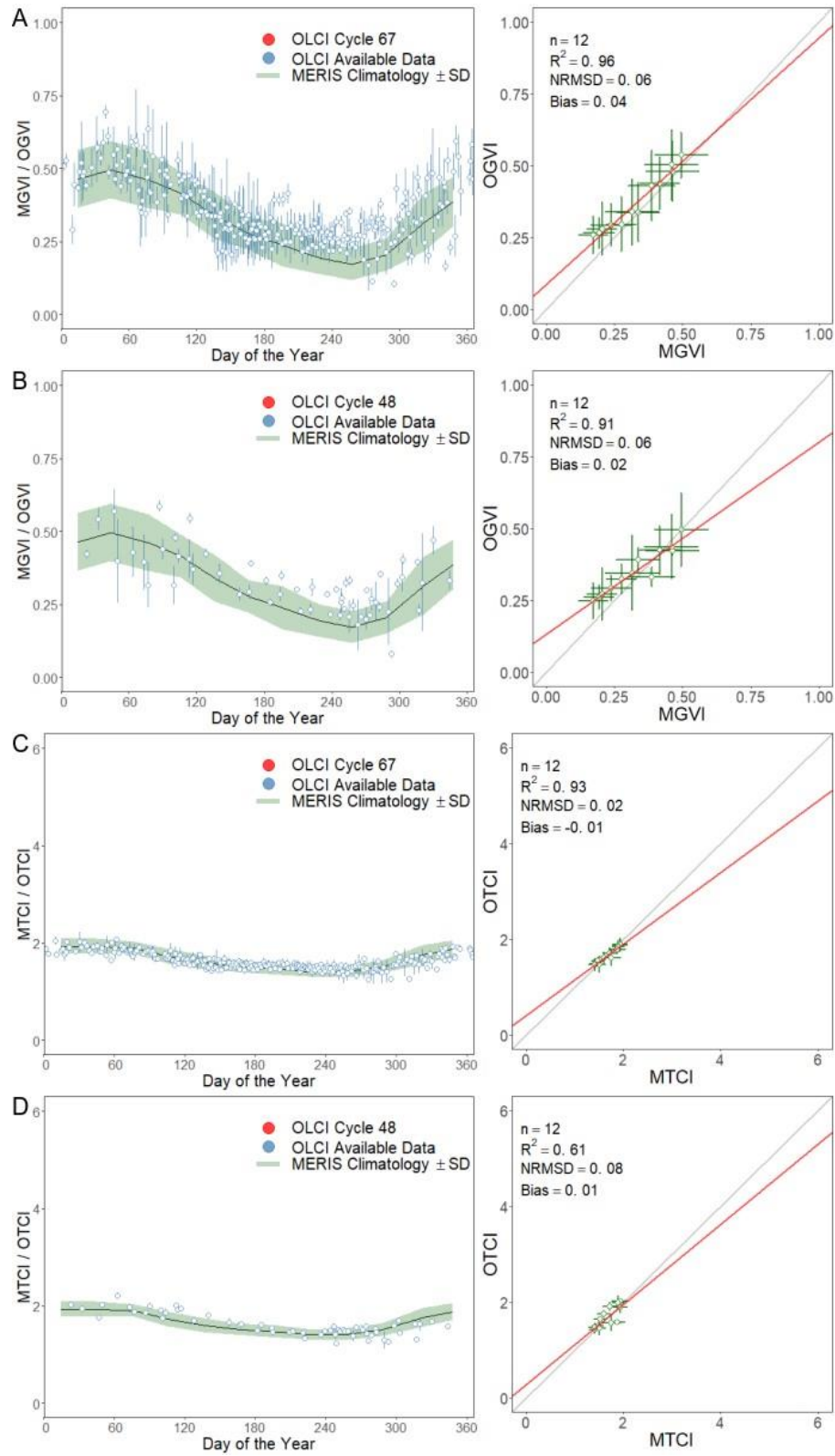


Figure 68: Time-series OGV and OTCI and corresponding scatterplot of monthly mean for site AU-Litchfield, Australia, land cover Broadleaved, evergreen. A and C represent S3A; B and D represent S3B.

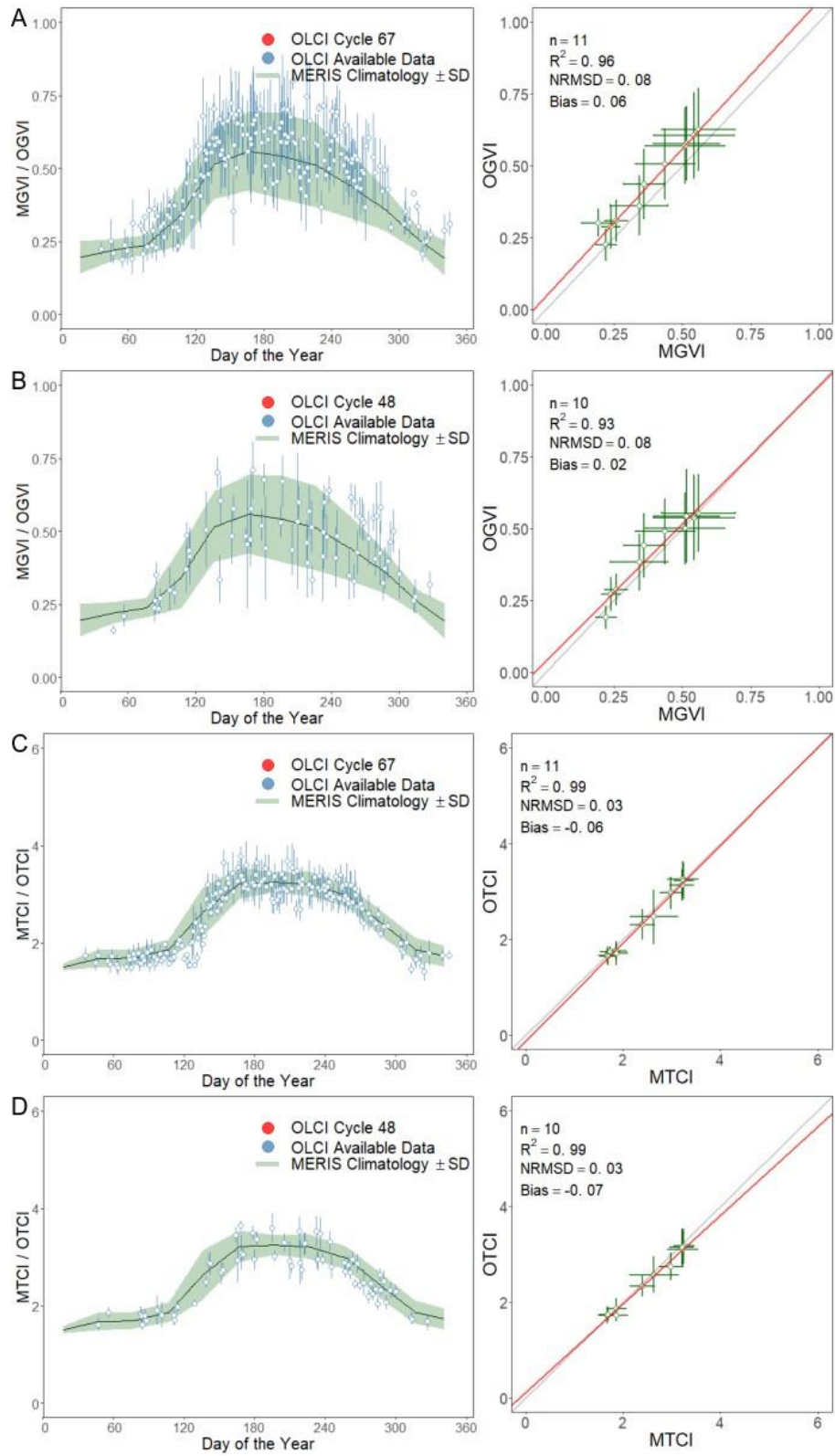


Figure 69: Time-series OGVI and OTCI and corresponding scatterplot of monthly mean for site BE-Brasschaat, Belgium, land cover Needle-leaved, evergreen. A and C represent S3A; B and D represent S3B.

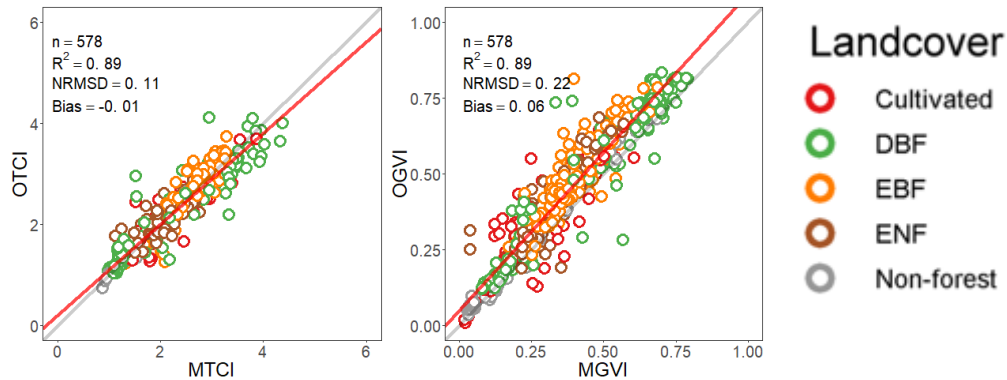


Figure 70: Comparison of OTCI-MTCI (a) and OGVI-MGVI (b). Points in the scatterplot represent the monthly mean of all available S3A and MERIS archive over 42 validation sites. Red and grey lines represent the modelled and 1:1 lines respectively. The scatterplots are updated to include extractions from cycle S3A 67.

A global analysis of the spatial consistency of the OTCI products has been published in the following paper “The Sentinel-3 OLCI Terrestrial Chlorophyll Index (OTCI): Algorithm Improvements, spatiotemporal Consistency and Continuity with the MERIS Archive” by Pastor-Guzman et al. (2020). Global composites of the different seasons were generated at 9.2 km resolution (Figure 71). Analysis on the overall distribution alongside the impact of latitudinal gradient on consistency was performed. Overall, the study found a strong correlation between the products ($R^2 > 0.88$), low global mean percentage difference (-1.86 to 0.61), low absolute bias (< 0.1), and minimal error (NRMSD ~ 0.1).

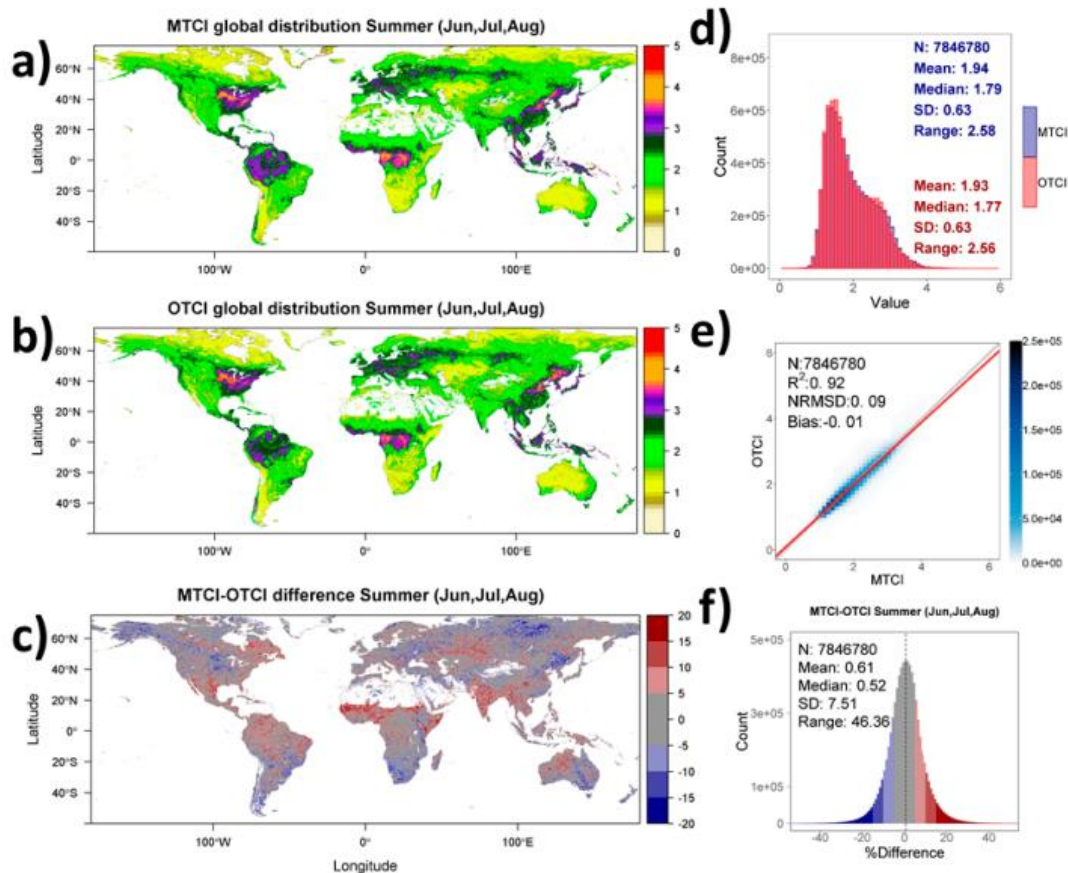


Figure 71: Global composites of Sentinel-3 OTCI (mean of 2016 to 2019) and Envisat MTCI (mean of 2002 to 2012) values for summer—i.e. Jun, Jul, Aug (a,b)—and spatial distribution of differences (c). Index value frequency distribution (d), density scatterplot of agreement between the two products (e), and frequency distribution of differences (f). For (c) and (f), difference is expressed in percentage computed as the ratio of per pixel absolute difference to the mean. Blue indicates areas where the Sentinel-3 OTCI is greater than the Envisat MTCI, conversely, red indicates areas where the Envisat MTCI is greater than the Sentinel-3 OTCI. Grey pixels are areas where the difference between the Envisat MTCI and Sentinel-3 OTCI is within $\pm 5\%$

5.3.3.2 Systematic Level-3 composite Production

Time and Space composite Level 3 products of OLCI's Terrestrial Chlorophyll Index and Global Vegetation Index (a.k.a. Instantaneous Green FAPAR) are now routinely generated by the S3MPC (by Brockmann Consult and University of Southampton) and are available from the FTP S3 MPC public website hosted by ACRI-ST (<ftp://ftp.acri-cwa.fr>)

The OLCI L3 vegetation products are separated into different directories, depending on the length of time period used to produce the products (8days/1month) and the platform (S3A/S3B). Inside these directories the products are split accordingly to the first day of observation data used to produce the product.

The data is stored in an integerized sinusoidal projection (ISIN), following the NASA definition for MODIS land data. Each global mosaic is available in separate tiles using a 10×10 degrees raster subset with a pixel ground resolution of 500m. The data format is a NetCDF-CF conforming NetCDF4 file.

5.3.3.3 Sentinel-3A and 3B biophysical variables inter-comparison results

The average monthly values for each site in Table 10 for both OTCI and OGVI have been calculated for the period where both S3A and S3B platforms are in orbit (September 2018 – present). An intercomparison between the monthly averages is conducted for all valid observations per land cover class. Only months where there are valid observations for both satellites are included in the analysis. As can be seen in Table 12, there is a strong relationship ($R^2 > 0.88$) between the monthly OTCI values from each platform across all the land covers. The analysis shows there is a consistent bias in the monthly average OTCI values obtained from S3B than S3A for all land cover classes. There are also strong relationships for the OGVI products between the different satellites ($R^2 > 0.84$) with a similar bias found in the OGVI product.

As shown in Figure 72 and Figure 73, both satellites capture the range of the products over different landcover types. At a cultivated site, there is a higher bias (0.08) in the OGVI values obtained by S3A in comparison to S3B. As the site is actively farmed, changes in the vegetation conditions between the observations taken by the different satellites could be influencing the values obtained. Further investigation into the impact of viewing angle and solar illumination is being performed.

Table 12: Comparison statistics between monthly S3A/B OLCI land products.

Landcover	N	OTCI			OGVI		
		R ²	Bias	NRMSE	R ²	Bias	NRMSE
EBF	281	0.96	-0.03	0.06	0.84	-0.01	0.08
Non-forest	125	0.96	-0.01	0.06	0.98	0.00	0.03
DBF	336	0.95	-0.01	0.09	0.91	-0.01	0.07
ENF	209	0.90	-0.04	0.07	0.84	-0.01	0.05
Cultivated	123	0.88	-0.03	0.10	0.84	-0.02	0.07

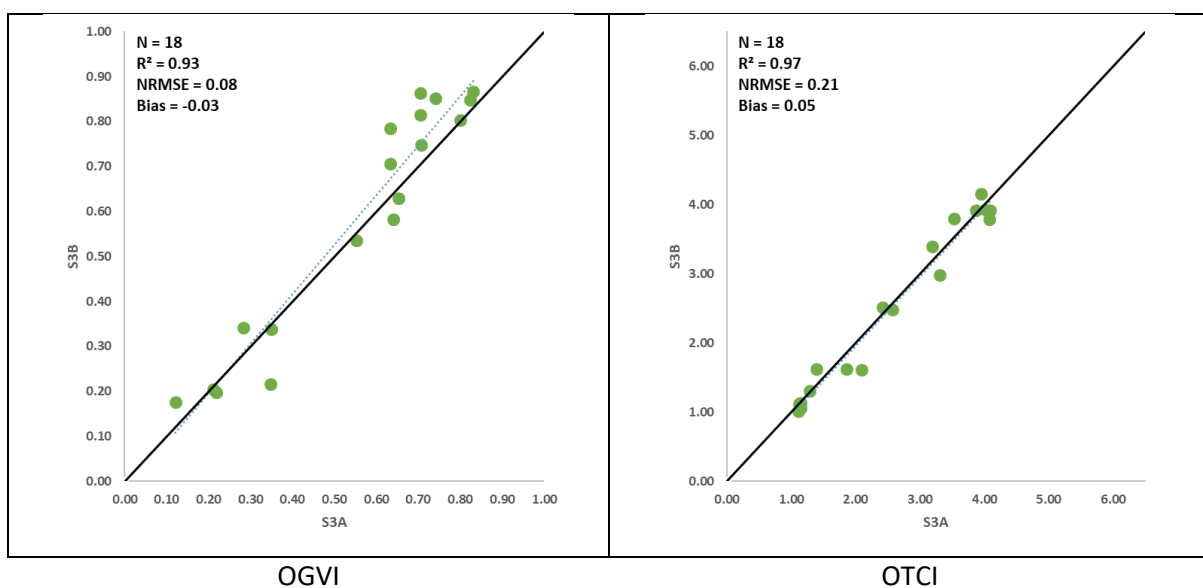


Figure 72: Scatterplot of monthly mean for S3A and S3B for site DE-Hainich, land cover – broadleaved deciduous forest. (left: OGVI, right: OTCI)

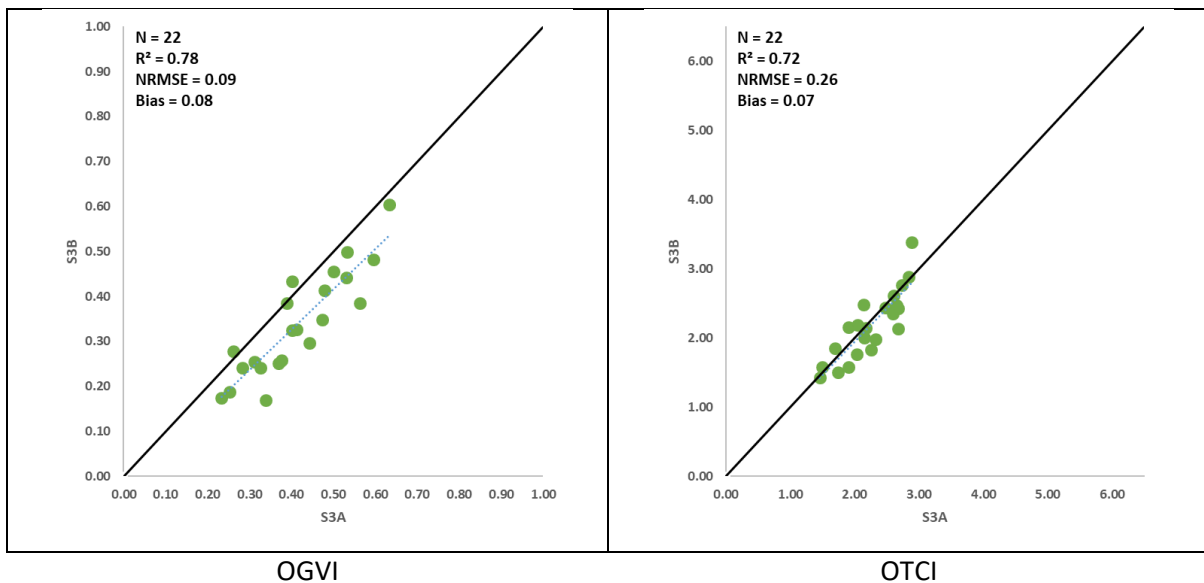


Figure 73: Scatterplot of monthly mean for S3A and S3B for site FR-Aurade, land cover – cropland. (left: OGVI, right: OTCI)

5.3.4 Water leaving Reflectance

The results presented in this section present the level-2 FR quantitative validation performed over the full OLCI time series against situ fiducial reference measurements. OLCI data used in these sections correspond to the last processing baseline (IPF version 6.11/6.13, PB 2.23 to 2.74/1.52). In situ data collected originate from the following stations or buoys:

- ❖ AERONET-OC https://aeronet.gsfc.nasa.gov/new_web/ocean_color.html
- ❖ BOUSSOLE <http://www.obs-vlfr.fr/Boussole/html/project/strategy.php>
- ❖ MOBY <https://www.star.nesdis.noaa.gov/sod/moby/gold/>
- ❖ SLGO <https://slgo.ca/en/>

5.3.4.1 Acknowledgements

S3-MPC acknowledges all PIs mentioned below and their respective institutions for their valuable contribution to the validation of OLCI L2 water products with a special emphasis on AERONET-OC PIs for their unique contribution to NRT data validation and a special mention to Giuseppe Zibordi maintaining and providing data over 5 ground stations. AERONET-OC is indeed from far the largest contributor of Fiducial Reference Measurements for routine quantitative data validation.

- ❖ AERONET-OC

- **AAOT, Galata, Gloria, GDT, HLH, Irbe Lighthouse:** Giuseppe Zibordi, Joint Research Centre of the European Commission
- **Ieodo, Socheongcho:** Young-Je Park & Hak-Yeol You, Korean Institute of Ocean Science and Technology & Korea Hydrographic and Oceanographic Administration
- **LISCO:** Sam Ahmed, Alex Gilerson, City College of New York
- **MVCO:** Hui Feng and Heidi Sosik, Ocean Process Analysis Laboratory (OPAL), Woods Hole Oceanographic Institution
- **Thornton:** Dimitry Van der Zande, RBINS/OD Nature
- **Lucinda:** Thomas Schroeder, Integrated Marine Observing System, IMOS
- **USC_SEAPRISM:** Burton Jones and Curtiss Davis, University Southern California | USC, Oregon State University
- **WaveCIS:** Alan Weidemann, Bill Gibson, Robert Arnone, University of Southern MS, Coastal Studies Inst – LSU, Naval Research Laboratory
- **Ariake tower:** Joji Ishizaka, Kohei Arai, Nagoya University & Saga University
- **Blyth NOAH:** Rodney Forster, University of Hull, UK
- **Casablanca platform:** Giuseppe Zibordi, Marco Talone, Joint Research Centre of the European Commission
- Grizzly bay, Lake Okeechobee, South Greenbay: NimaPahlevan, NASA
- **Lake Erie:** Tim Moore, Steve Ruberg, Menghua Wang, University of New Hampshire & NOAA
- ❖ BOUSSOLE
 - David Antoine, Enzo Vellucci (Curtin University, Perth & Laboratoire d’Oceanographie de Villefranche, CNRS)
- ❖ MOBY
 - Kenneth Voss & Carol Johnson (University of Miami & NIST)
- ❖ SLGO
 - Simon Belanger, Thomas Jaegler & Peter Galbraith (Arctus, Inc & Department of fisheries and Ocean Canada)
- ❖ AWI
 - Astrid Bracher (Alfred-Wegener-Institut)
- ❖ IMOS
 - Thomas Schroeder (Integrated Marine Observing System, IMOS)
- ❖ BSH
 - Holger Klein (Bundesamt für Seeschifffahrt und Hydrographie, BSH)
- ❖ Proval

- Edouard Leymarie (Laboratoire d’Oceanographie de Villefranche, CNRS)

5.3.4.2 Level-2 products filtering procedure

The flags used in the computations of the statistics over OLCI macropixels correspond to S3VT recommended flags and are listed below:

- ❖ INVALID, CLOUD, CLOUD_AMBIGUOUS, CLOUD_MARGIN, SNOW_ICE, SUSPECT, HISOLZEN, SATURATED, RISKGLINT, WHITECAPS, AC_FAIL, OC4ME_FAIL, ANNOT_TAU06, ANNOT_ABSO_D, ANNOT_DROUT, RWNEG_O2 to RWNEG_O8, ANNOT_MIXR1.

Additional filtering includes time difference between in situ measurement and satellite over path below 6 hours, wind speed lower than $9 \text{ m}\cdot\text{s}^{-1}$ and sun zenith angle lower than 60 degrees. Filtered mean and CV tests as described in Bailey and Werdell (2006) is also included in the filtering process.

Ref: W. Bailey and P.J. Werdell, "A multi-sensor approach for the on-orbit validation of ocean color satellite data products", Rem. Sens. Environ. 102, 12-23 (2006).

5.3.4.3 Results

5.3.4.3.1 OLCI-A

Figure 74 presented below represent the scatterplots and statistics of OLCI full resolution radiometric products against in situ data collected at AERONET-OC, BOUSSOLE, MOBY and SLGO from April 2016 to 9th of February 2020. The statistics are summarized in Table 13.

The total number of matchups varies from 29 to 955 depending on the wavelength. Most recent data of AERONET-OC have added new bands such as 400 nm, 620 nm, 665 nm.

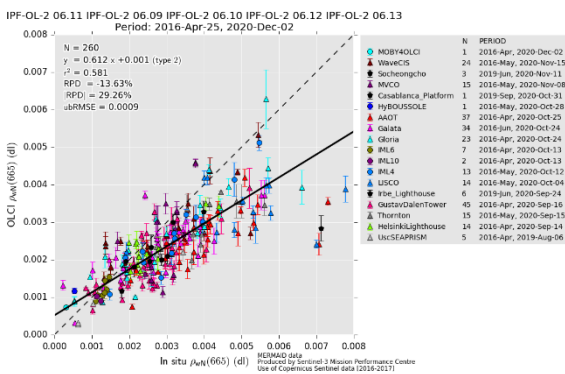
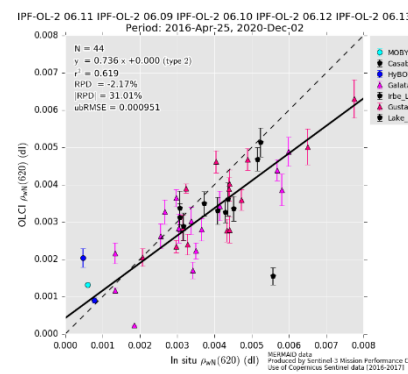
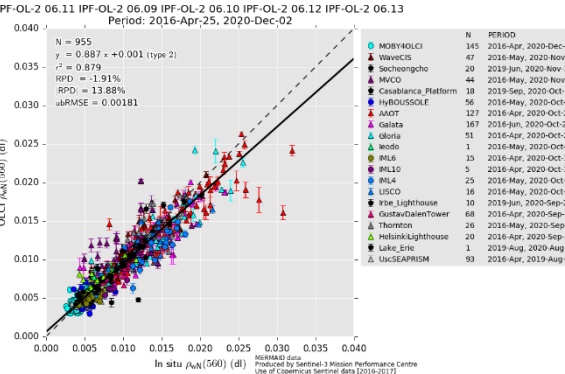
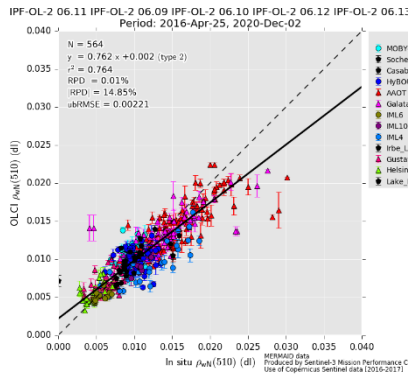
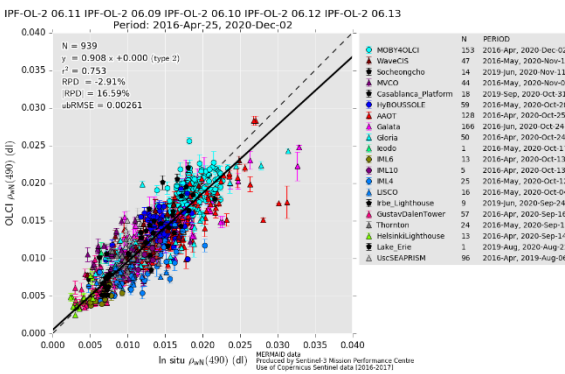
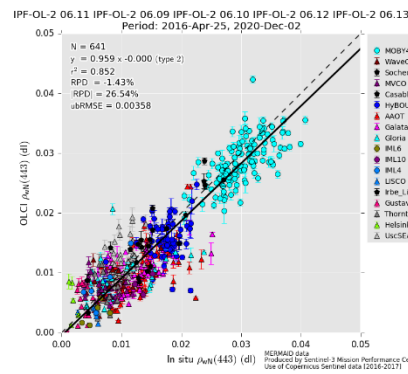
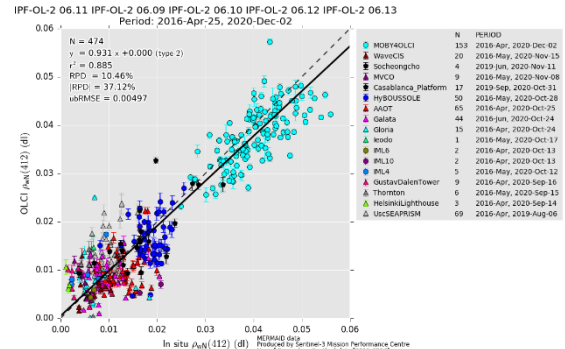
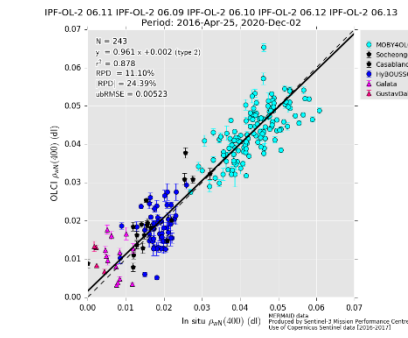
Regression statistics are very good up to 560 nm with slopes between 0.887 and 0.961 (with an exception at 510 nm with 0.762, but the dynamics for that band is very small) and r^2 mostly around 0.8. The 665 nm band is clearly the most critical one with poor slopes and r^2 (0.61 and 0.58 respectively). At this stage of the mission, there are still no clues for the poor performance of this band. OLCI products are almost within the requirements (5% accuracy in the blue/green bands) as demonstrated by the RPD values.



Sentinel-3 MPC

S3MPC OPT Annual Performance Report - Year 2020

Ref.: S3MPC.ACR.APR.007
 Issue: 1.1
 Date: 28/04/2021
 Page: 107



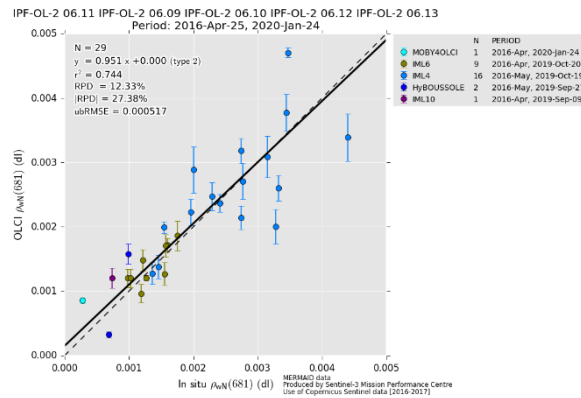


Figure 74: FR scatter plot of OLCI versus in situ measurements.

Table 13: Summary of OLCI-A FR statistics.

lambda	N	RPD	RPD	MAD	RMSE	slope	intercept	r2
400	243	11.10%	24.39%	0.0004	0.0052	0.9615	0.0016	0.88
412	474	10.46%	37.12%	-0.0009	0.0051	0.9312	0.0005	0.89
443	641	-1.43%	26.54%	-0.0011	0.0038	0.9595	-0.0005	0.85
490	939	-2.91%	16.59%	-0.0007	0.0027	0.9081	0.0005	0.75
510	564	0.01%	14.85%	-0.0005	0.0023	0.7623	0.0022	0.76
560	955	-1.91%	13.88%	-0.0005	0.0019	0.8871	0.0006	0.88
620	44	-2.17%	31.01%	-0.0005	0.0011	0.7356	0.0004	0.62
665	260	-13.63%	29.26%	-0.0007	0.0011	0.6123	0.0005	0.58
681	29	12.33%	27.38%	0.0001	0.0005	0.9508	0.0002	0.74

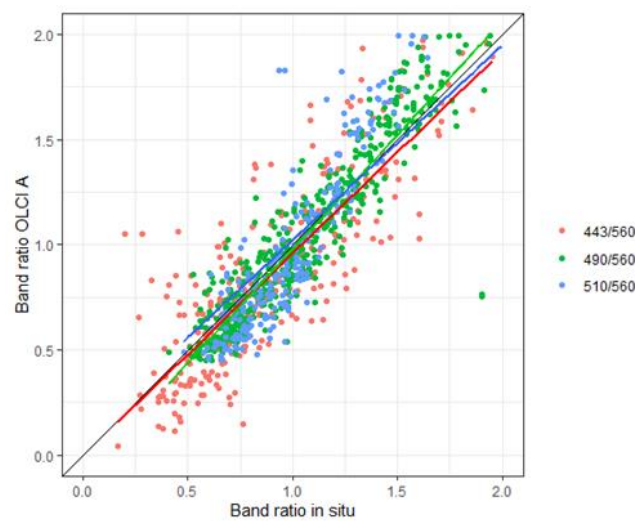


Figure 75: Band ratio validation between in situ and OLCI A.

Figure 75 shows the relationship between *in situ* blue-green and green band ratio and OLCI A band ratio. High correlation ($r = 98\%$, $p > 0.05$) between *in situ* and OLCI A data has been found. Biases are lower than 5% with a slight underestimation of the 443/560 nm ratio. Relative percentage differences are also around 5% for each band ratio.

Summary:

Level 2 product validation against in situ measurements shows very good results up to 560nm. Longer wavelength shows poor statistics with less in situ data.

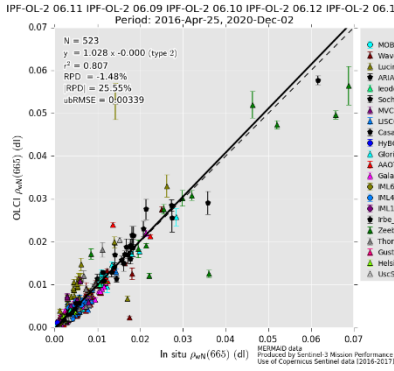
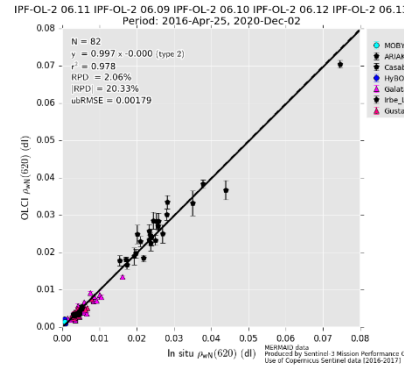
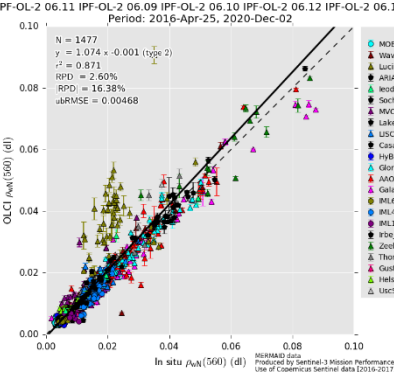
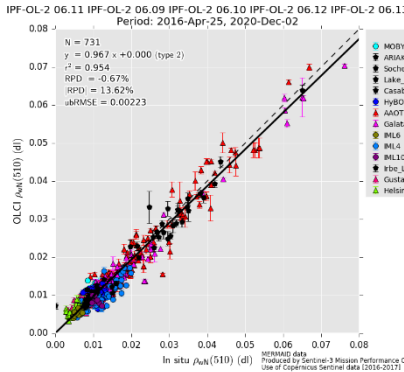
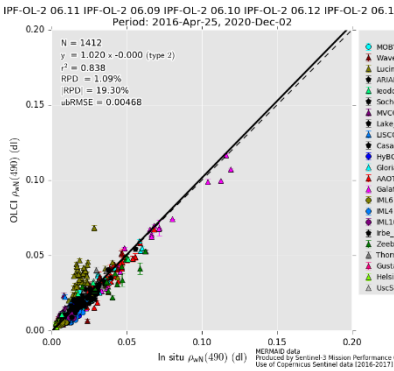
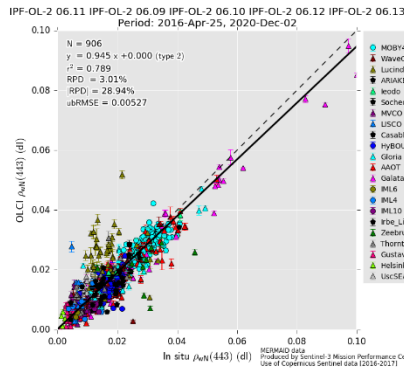
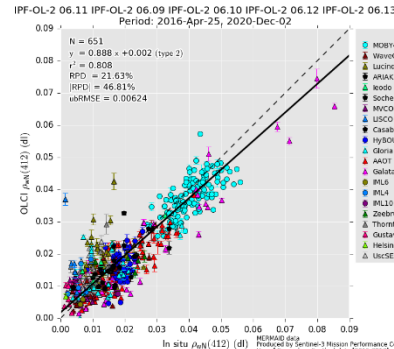
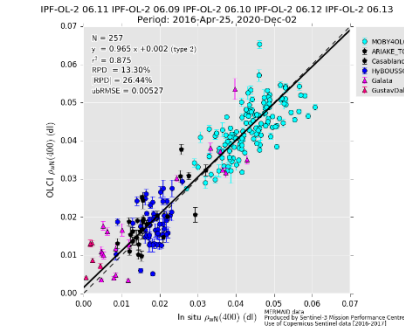
Due to lower signals and high variability for available data at 620 nm and to longer wavelengths, the performance of OLCI shows a percentage difference of -14% for 665 nm, with an underestimation of higher values (see Table 14).

5.3.4.3.2 Annot-Drout flag impact on level2 matchups

Sentinel 3 validation teams (S3VT) has shown the over flagging of coastal areas (where most in-situ data are available) of the Annot_Drout flag.

Figure 76 presented below represent the scatterplots and statistics of OLCI full resolution radiometric, without the flagging of Annot_Drout pixels, products against in situ data MERMAID database since April 2016 to December 2020. The statistics are summarized in Table 14.

The total number of matchups varies from 39 to 1477 depending on the wavelength. Regression statistics are very good with slopes between 0.88 and 1.02 (with an exception at 681 nm with 0.78, but the dynamics for that band are very small) and r^2 mostly around 0.8.



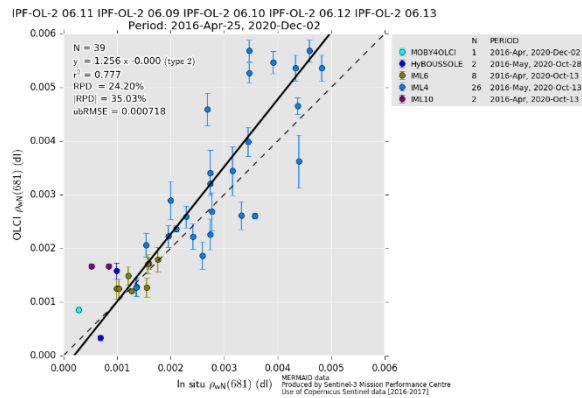


Figure 76: FR scatter plot of OLCI versus in situ measurements without Annot_DROUT flags

Table 14: Summary of OLCI FR statistics without Annot_DROUT flags.

lambda	N	RPD	RPD	MAD	RMSE	slope	intercept	r2
400	257	13.30%	26.44%	0.0004	0.0053	0.9645	0.0015	0.87
412	651	21.63%	46.81%	-0.0005	0.0063	0.8878	0.0018	0.81
443	906	3.01%	28.94%	-0.0007	0.0053	0.9446	0.0002	0.79
490	1412	1.09%	19.30%	-0.0001	0.0047	1.0202	-0.0005	0.84
510	731	-0.67%	13.62%	-0.0005	0.0023	0.9674	0.0000	0.95
560	1477	2.60%	16.38%	0.0003	0.0047	1.0742	-0.0007	0.87
620	82	2.06%	20.33%	-0.0002	0.0018	0.9972	-0.0001	0.98
665	523	-1.48%	25.55%	-0.0001	0.0034	1.0285	-0.0003	0.81
681	39	24.20%	35.03%	0.0004	0.0008	1.2560	-0.0002	0.78

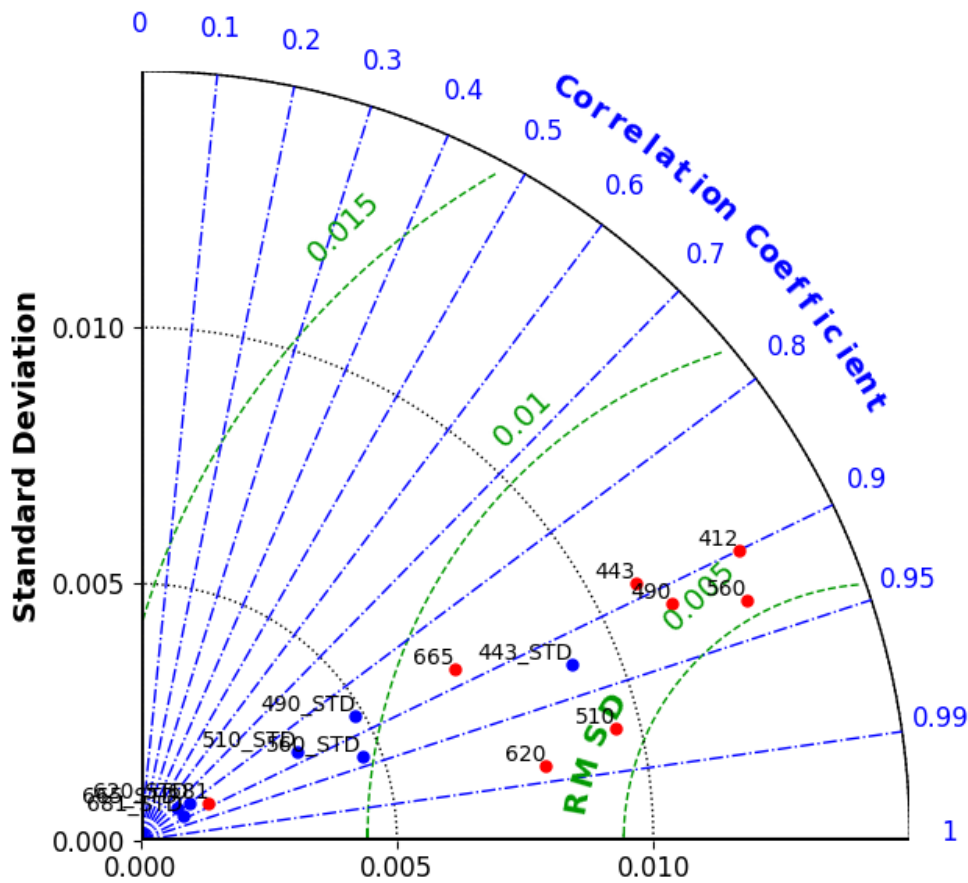


Figure 77: Taylor diagram, comparison between standard flag extraction (blue) and Annot_DROUT flag not considered (red).

Summary:

Annot_DroUT flag mainly coastal water reducing drastically the number of valid matchups with in-situ data.

More than 1400 matchup were found for 490 and 560 nm wavelength, for all bans r^2 increased to higher than 0.78. However, the relative percentage difference increases for most of the wavelength.

Without Annot_DROUT flags consider the matchup data shows higher standard deviation and variability than standard matchups methods.

5.3.4.3.3 Cameras sensitivity study to Level 2 reflectance products

5.3.4.3.4 On board camera comparison

This exercise was to evaluate the differences on the level 2 Marine product between different cameras onboard of OLCI. OLCI scans the Earth's surface using a push-broom method. CCD arrays provide spatial sampling in the across track direction, while the satellite's motion provides scanning in the along track direction. The instrument's 68.5° field of view, nadir pointing, covers a swath width of 1 270 km at altitude from SENTINEL-3 orbit (814.5 km). For the nominal orbit, at sub-satellite point, full spatial resolution (FR) of the OLCI instrument is approximately 300 m.

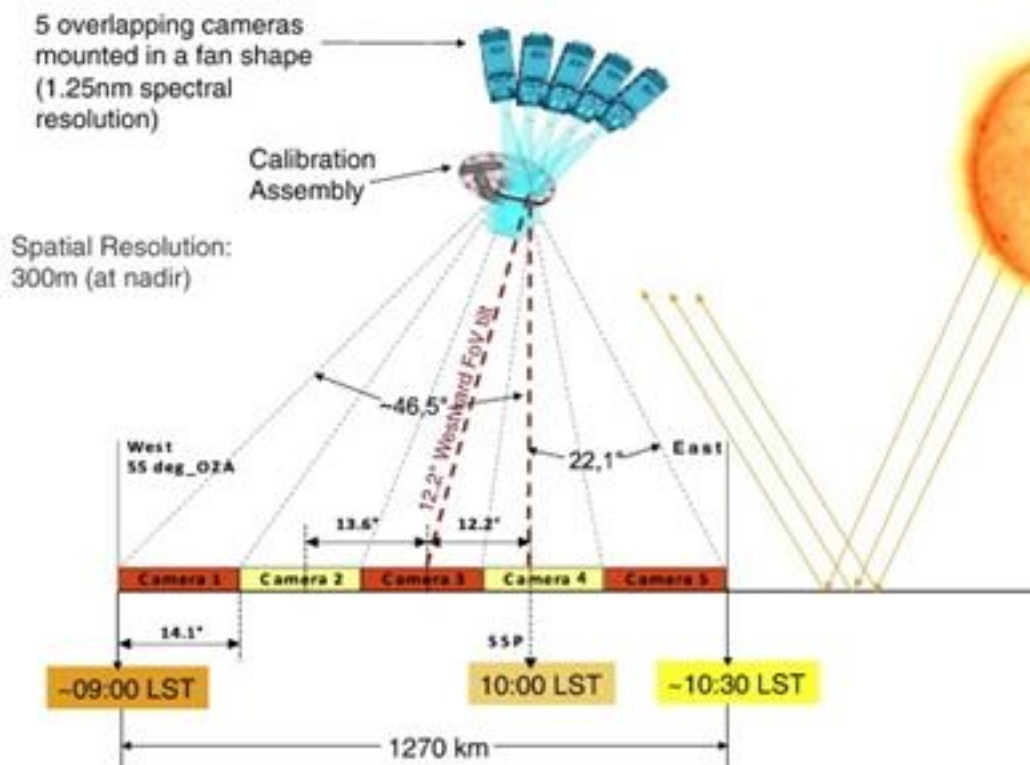


Figure 78: OLCI camera geometry.

Table 15: FR statistics over April 2016 - June 2020 FR data for camera 1.

Lambda	N	RPD	RPD	MAD	RMSE	slope	intercept	r2
400	91	-2.56%	14.59%	-0.0009	0.0055	1.0828	-0.0040	0.83
412	143	-7.37%	28.45%	-0.0025	0.0060	0.9721	-0.0018	0.87
443	191	-13.33%	24.50%	-0.0024	0.0047	1.0273	-0.0029	0.83
490	299	-8.02%	17.30%	-0.0015	0.0033	0.8752	0.0003	0.69
510	169	-2.73%	16.69%	-0.0010	0.0029	0.6420	0.0033	0.69
560	305	-3.93%	15.05%	-0.0008	0.0023	0.8424	0.0008	0.87
620	8	-5.15%	39.83%	-0.0010	0.0017	0.3515	0.0010	0.39
665	77	-13.58%	41.48%	-0.0009	0.0015	0.4873	0.0007	0.53
681	6	24.70%	56.02%	-0.0001	0.0006	0.8738	0.0002	0.69

Table 16: FR statistics over April 2016 - June 2020 FR data for camera 2.

lambda	N	RPD	RPD	MAD	RMSE	slope	intercept	r2
400	37	3.86%	19.01%	-0.0008	0.0054	0.9746	0.0002	0.85
412	72	3.24%	35.27%	-0.0019	0.0057	0.9430	-0.0006	0.88
443	117	-10.69%	24.63%	-0.0019	0.0037	1.0082	-0.0020	0.89
490	192	-8.09%	13.86%	-0.0012	0.0024	0.9875	-0.0010	0.85
510	122	-4.10%	12.57%	-0.0007	0.0019	0.8666	0.0008	0.85
560	197	-3.60%	12.56%	-0.0006	0.0016	0.9002	0.0004	0.92
620	9	19.19%	56.60%	-0.0007	0.0011	0.5647	0.0011	0.81
665	51	-21.44%	22.53%	-0.0007	0.0010	0.7132	0.0001	0.60
681	11	10.12%	19.06%	0.0001	0.0004	0.9306	0.0002	0.77

Table 17: FR statistics over April 2016 - June 2020 FR data for camera 3.

lambda	N	RPD	RPD	MAD	RMSE	slope	intercept	r2
400	53	3.65%	13.47%	0.0005	0.0044	0.9819	0.0011	0.89
412	116	6.86%	29.85%	-0.0004	0.0042	0.9467	0.0006	0.91
443	152	0.26%	23.72%	-0.0007	0.0031	0.9571	0.0000	0.88
490	200	1.82%	17.07%	-0.0001	0.0023	0.9553	0.0005	0.77
510	112	2.62%	13.62%	-0.0001	0.0016	0.8351	0.0017	0.84
560	205	0.17%	14.65%	-0.0003	0.0016	0.9087	0.0006	0.87
620	5	-10.55%	19.65%	-0.0007	0.0010	0.6630	0.0009	0.90
665	56	-12.30%	26.37%	-0.0007	0.0012	0.5980	0.0007	0.65
681	4	28.27%	28.27%	0.0006	0.0007	1.1847	0.0001	0.90

Table 18: FR statistics over April 2016 - June 2020 FR data for camera 4.



Sentinel-3 MPC
S3MPC OPT Annual Performance
Report - Year 2020

Ref.: S3MPC.ACR.APR.007
 Issue: 1.1
 Date: 28/04/2021
 Page: 115

lambda	N	RPD	RPD	MAD	RMSE	slope	intercept	r2
400	24	11.66%	16.53%	0.0015	0.0043	0.9422	0.0037	0.89
412	69	35.31%	49.30%	0.0001	0.0033	0.9508	0.0010	0.95
443	86	6.90%	20.28%	0.0000	0.0026	0.9388	0.0008	0.93
490	120	5.71%	16.29%	0.0000	0.0025	0.8702	0.0016	0.79
510	66	7.67%	17.44%	0.0001	0.0024	0.7292	0.0029	0.76
560	117	3.09%	12.14%	0.0001	0.0017	0.9725	0.0004	0.89
620	2	-3.95%	3.95%	-0.0002	0.0002	1.0883	-0.0006	1.00
665	39	0.21%	19.90%	-0.0002	0.0006	0.7332	0.0006	0.75
681	4	-2.90%	14.08%	-0.0002	0.0004	0.6145	0.0006	0.95

Table 19: FR statistics over April 2016 - June 2020 FR data for camera 5.

lambda	N	RPD	RPD	MAD	RMSE	slope	intercept	r2
400	12	50.10%	50.10%	0.0054	0.0064	0.7986	0.0093	0.92
412	41	167.37%	174.39%	0.0030	0.0048	0.8854	0.0042	0.78
443	47	42.75%	51.80%	0.0017	0.0032	0.9518	0.0022	0.78
490	70	3.07%	22.86%	0.0001	0.0024	1.2644	-0.0025	0.69
510	40	12.34%	22.10%	0.0007	0.0020	1.1310	-0.0004	0.67
560	71	-2.15%	16.73%	-0.0004	0.0017	0.8893	0.0005	0.76
620	5	1.98%	11.04%	0.0001	0.0004	-10.7730	0.0360	0.26
665	25	-17.30%	29.59%	-0.0008	0.0013	0.3918	0.0011	0.64
681	4	-0.87%	19.74%	-0.0002	0.0006	0.6299	0.0007	0.89

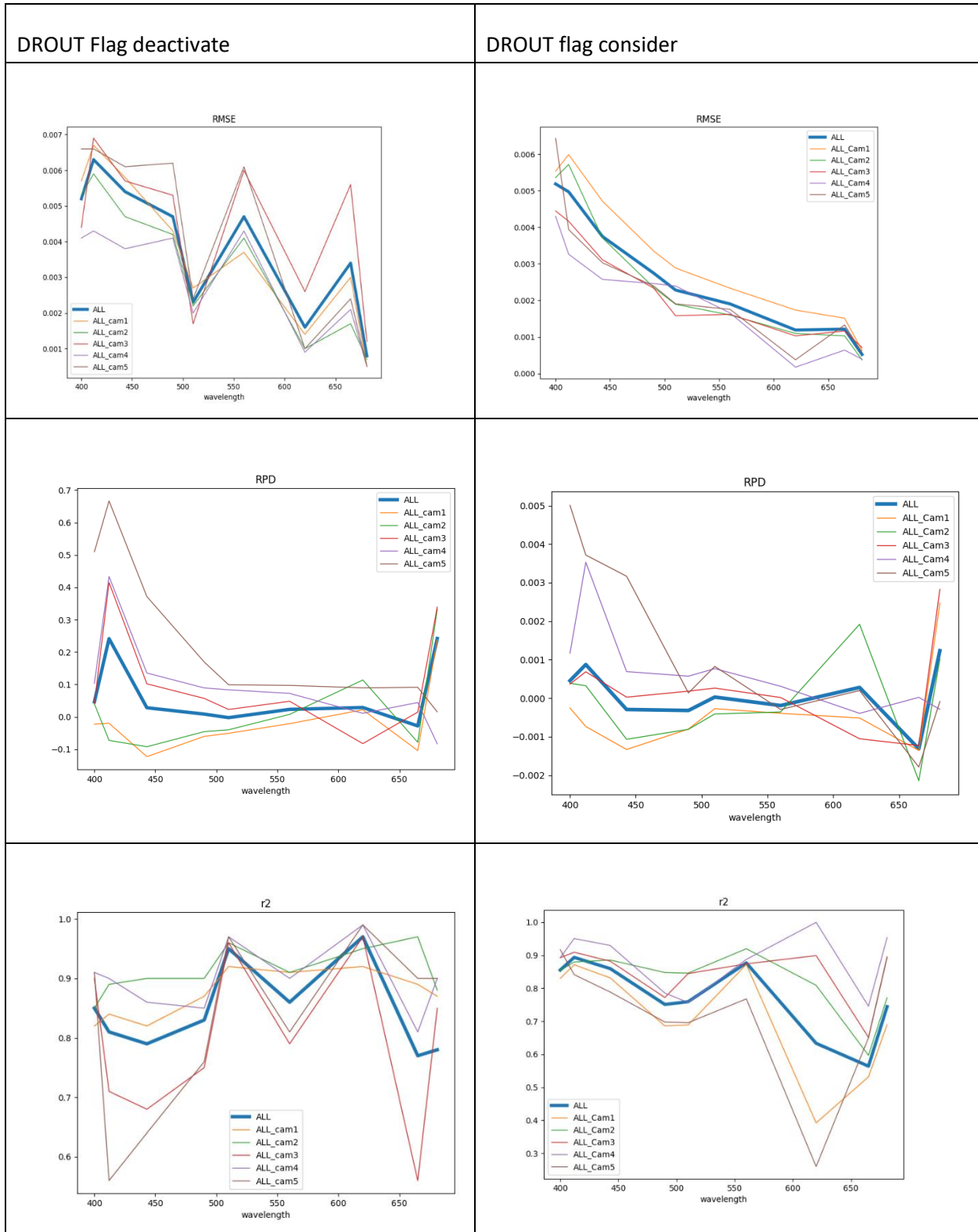


Figure 79: Statistics comparison between OLCI 5 cameras without the Annot_DROUT consider (column left) and with all the flag considers (column right).



Summary:

Camera 5 shows more inconsistency than the other camera mainly in the blue band for the matchup without *Annot_DROUT* flags. Due to the point of view of the Camera 5 the number of matchups is lower than the other camera. This camera may also be more affected by the glint.

5.3.4.3.5 OLCI-B

Analyses were performed on the entire archives of OLCI B data until the 27th of January 2021. OLCI B vicarious calibration activities are still ongoing, then the discrepancies between *in situ* data and satellite data may be due to the missing calibration (Figure 80). Even with the systematic shift in the blue wavelength, *in situ* data and satellite data are well correlated with a coefficient higher than 0.6 for the wavelength between 400 nm and 620 nm (Table 20).

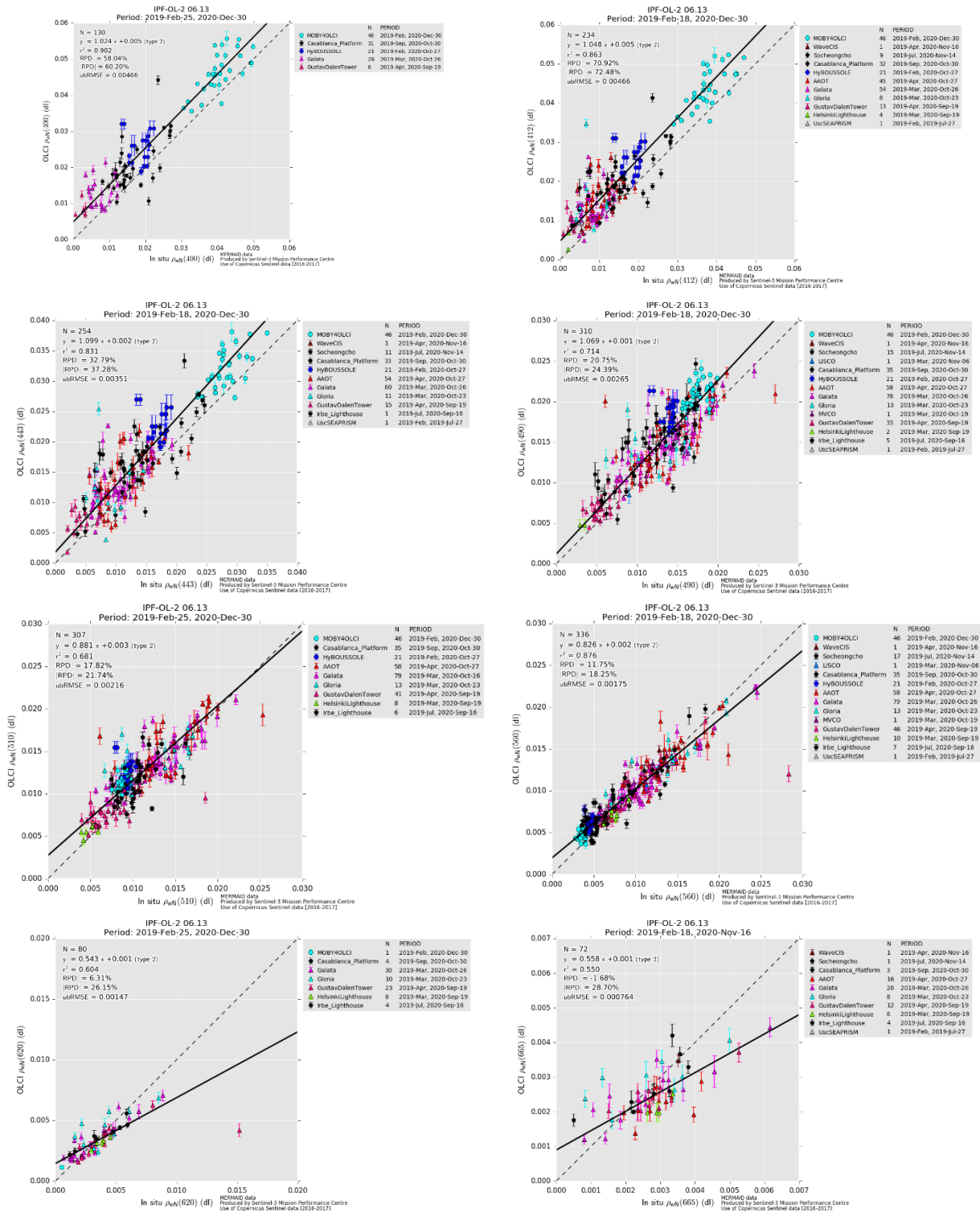


Figure 80: Validation scatter plot for OLCI B.

Table 20: OLCI B Validation Statistics

Lambda	N	RPD	RPD	MAD	RMSE	slope	intercept	r2
400	130	58.04%	60.20%	0.0054	0.0072	1.0242	0.0049	0.90
412	234	70.92%	72.48%	0.0055	0.0072	1.0477	0.0047	0.86
443	254	32.79%	37.28%	0.0032	0.0048	1.0988	0.0018	0.83
490	310	20.75%	24.39%	0.0021	0.0034	1.0690	0.0012	0.71
510	307	17.82%	21.74%	0.0014	0.0026	0.8814	0.0027	0.68
560	336	11.75%	18.25%	0.0004	0.0018	0.8258	0.0020	0.88
620	80	6.31%	26.15%	-0.0003	0.0015	0.5430	0.0014	0.60
665	72	-1.68%	28.70%	-0.0004	0.0008	0.5579	0.0009	0.55

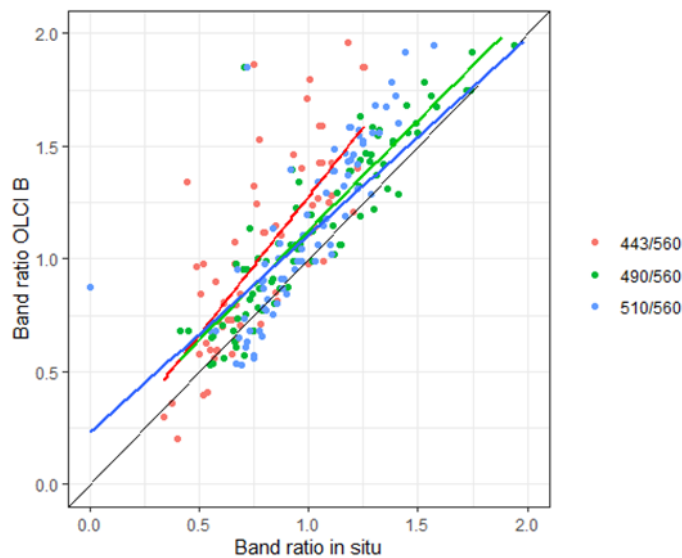


Figure 81: Band ratio validation between in situ and OLCI B.

Figure 81 shows the relationship between *in situ* blue-green and green band ratio and OLCI B band ratio. Biases are lower than 5% with a slight underestimation of the 443/560 nm ratio.

Summary:

S3B OLCI level 2 products have been released more recently and vicarious calibration activities are still on going. Therefore, only preliminary results are presented here. For the whole spectra, a high relative percentage difference (>15%) was found together with a systematic shift in the blue and blue-green (412, 443 and 490 nm) regions of the visible spectra.

5.3.5 Case 1 Chlorophyll product (OC4Me)

Figure 82 below present the statistics of OLCI OC4Me chlorophyll products against in situ measurements carried out at BOUSSOLE and on Bio-Argo floats. Please note that BOUSSOLE operations stopped in November 2017.

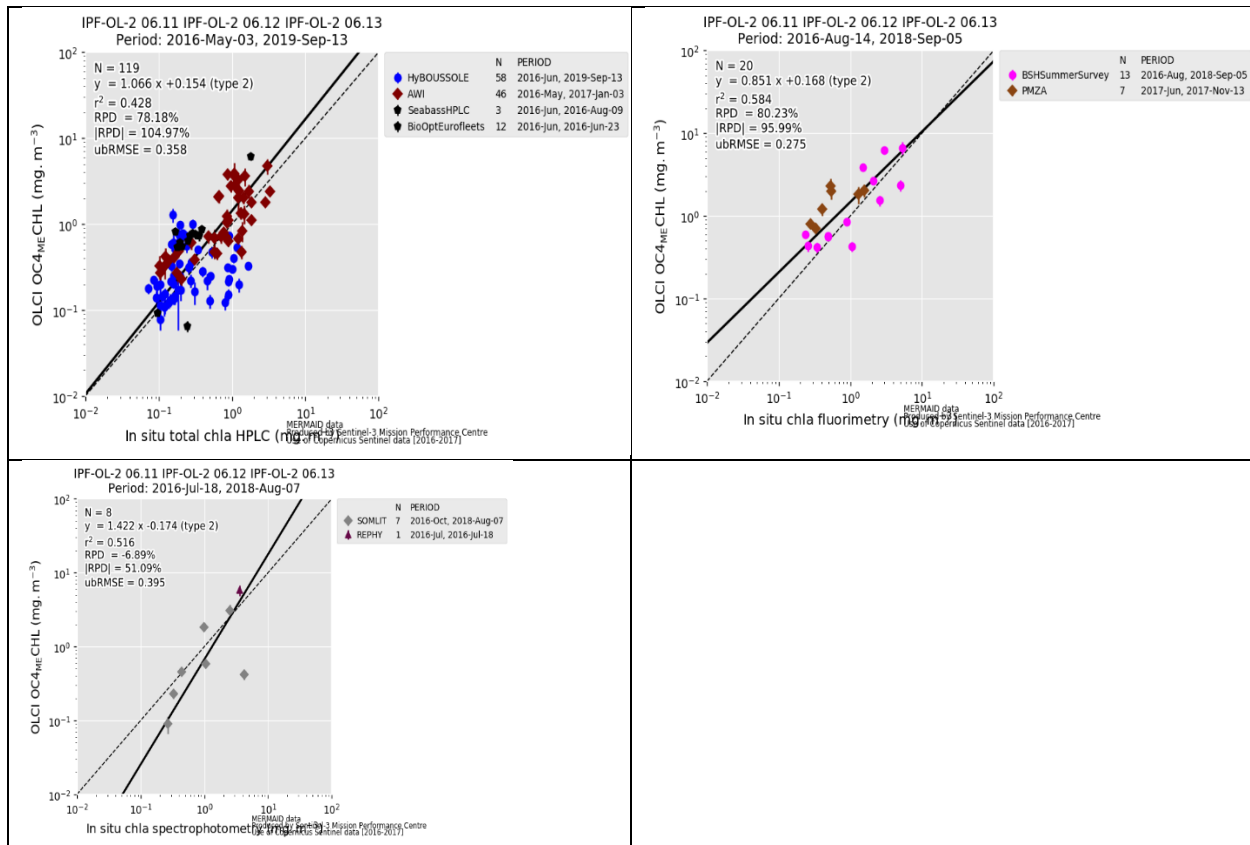


Figure 82: Chlorophyll statistics with HPLC (a), Fluorometric (b) data and Spectrophotometry (c).

The Chlorophyll-a algorithm validation was performed only on OLCI A data. Based only on HPLC Chlorophyll a value, OLCI OC4-Me products shows moderate positive correlation (r Pearson = 64%, p -value < 0.05 and RMSE = 0.38 $\text{mg}\cdot\text{m}^{-3}$) with scattered data (Figure 82). With a bias of -30%, OLCI OC4-Me algorithm tends to underestimate in situ values of HPLC chlorophyll-a.

Fluorometric chlorophyll also shows a better correlation (r Pearson = 76%, p -value < 0.05 and RMSE = 0.32 $\text{mg}\cdot\text{m}^{-3}$). These data are obviously of less quality but can nonetheless provide an indication of OLCI chlorophyll trends. In situ data shows low variability in the 0.1 to 1 mg/m^3 domain (mesotrophic water). No in situ measurement are in the oligotrophic domain.

Lambda	N	RPD	RPD	MAD	RMSE	slope	intercept	r2
CHL_OC4ME vs SPECT_chla_IS	8	-6.89%	51.09%	-0.1638	0.4275	1.4218	-0.1736	0.5163
CHL_OC4ME vs HPLC_chla_TOTAL_IS	119	78.18%	104.97%	0.1266	0.3795	1.0660	0.1544	0.4276
CHL_OC4ME vs Fluor_chla_IS	20	80.23%	95.99%	0.1767	0.3269	0.8515	0.1678	0.5843

Summary:

In situ chlorophyll concentration derived from HPLC analysis shows slight overestimation for higher values. Chlorophyll-a measurement shows some estimation errors, however this bias could be due to the low variability for in the HPLC in situ values (0.1-1 mg.m⁻³).

More measurement needs to be gathered in order to have a better insight of OLCI estimation on oligotrophic waters.

5.3.6 Alternative Atmospheric Correction and products for complex waters

The products for (optically) complex waters comprise chlorophyll-a concentration (CHL_NN), total suspended matter (TSM_NN) and absorption from Gelbstoff and Detritus (ADG443_NN), each with an associated error product. These products are derived from top-of-atmosphere radiance using the so-called Alternative Atmospheric Correction (AAC) which is coupled with the retrieval of the water products. Both, the AAC and the retrieval of water IOPs are performed by neural networks, based on a consistent set of water leaving and top-of-atmosphere reflectances. The concentrations are derived by empirical relationships between the IOPs and the concentrations.

The simulations and training range of the neural nets implemented in the Ground Segment processing of OLCI-A and B, the so-called version 1 set of nets, focussed on optically complex waters. Thus, it is recommended that these products are used in mesotrophic and eutrophic waters exceeding 0.1 mg/m³ in chlorophyll concentration. In 2018 a new set of neural nets was developed and has been tested extensively by the S3VT community. Following the recommendations from both the S3QWG and the S3VT, it was then decided late 2019/beginning of 2020 to implement the new AAC (NNv2) in the Ground Segment as well. This action occurred in the Summer of 2020 and after close interactions between Brockmann Consult and EUMETSAT's Ground Segment Team to confirm correctness, implementation was finalised at the end of 2020/beginning of 2021 for the planned L2 reprocessing early 2021.

The new NNs set includes improvements in both NNs:

- ❖ New water bio-optical model, including new exponent for detritus spectrum,
- ❖ Extended training range and co-variance ranges, including better coverage of high backscatter water such as river estuaries and lakes,
- ❖ Updated forward modelling: combining Hydrolight and CC atmosphere model,
- ❖ Increased number of training samples and more robust training to noise in data.

The extended training range used by NNv2 applies the following limits on IOPs at 442.5nm:

- ❖ apig = 0.001 – 6.0 (absorption by phytoplankton pigments)
- ❖ adetritus = 0.001 – 22.0 (absorption by humic and fulvic acid)
- ❖ ag = 0.001 – 22.0 (absorption by Gelbstoff)
- ❖ atot = 0.003 - 50.0 (total absorption, atot = adetritus + ag + apig)
- ❖ bp = 0.001 – 250.0 (backscattering by suspended matter)
- ❖ bwhite = 0.001 – 250.0 (backscattering by white particles such as coccolithophore and bubbles)
- ❖ btot = 0.0021 – 500.0 (total backscattering, btot = bp + bwhite)

In late 2019 a new IOP to TSM conversion was introduced following reports from the S3VT community that TSM was largely overestimating concentrations in many areas. The new TSM_NN conversion was based on re-analysis with OC-CCI in situ data and has been also implemented in the Ground Segment:

$$\text{TSM_NN [g m}^{-3}\text{]} = 1.06 \cdot (\text{iop_btot})^{0.942}, \text{ with } \text{iop_btot} = \text{iop_bp} + \text{iop_bw}$$

Validation efforts for NNv2 continued in 2020, also showing the improvement of the new TSM_NN compared to the old one. Figure 83 and Figure 84 show comparisons of the different TSM versions, both with NNv1 and NNv2 and with the old and new conversions and show the net improvement especially in the lower concentrations range from old to new.

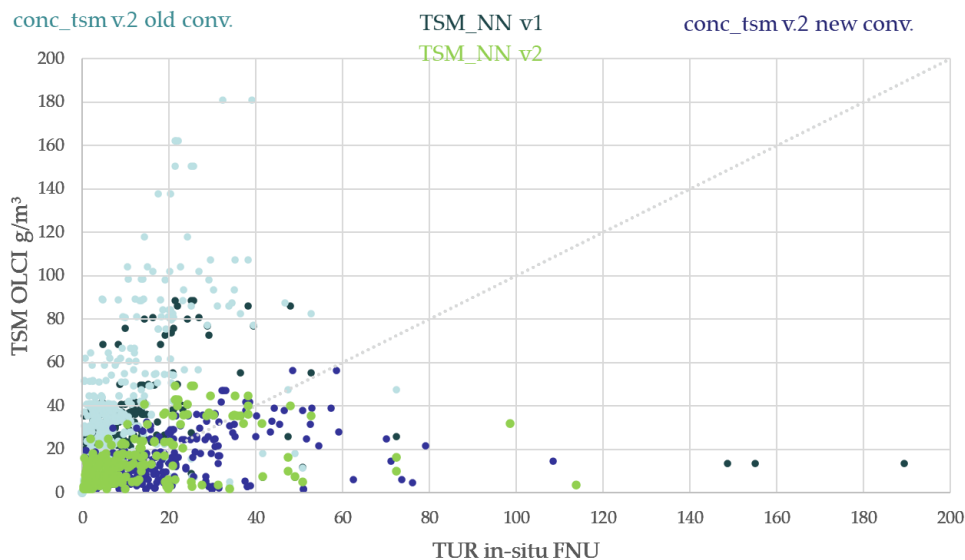


Figure 83 TSM scatter plot comparison with in-situ Turbidity at Warp Cefas SmartBuoy in situ data, conc_tsmv.2 old and new conv were processed with C2RCC within SNAP; TSM_NN v1 and v2 were processed with the Ground Segment

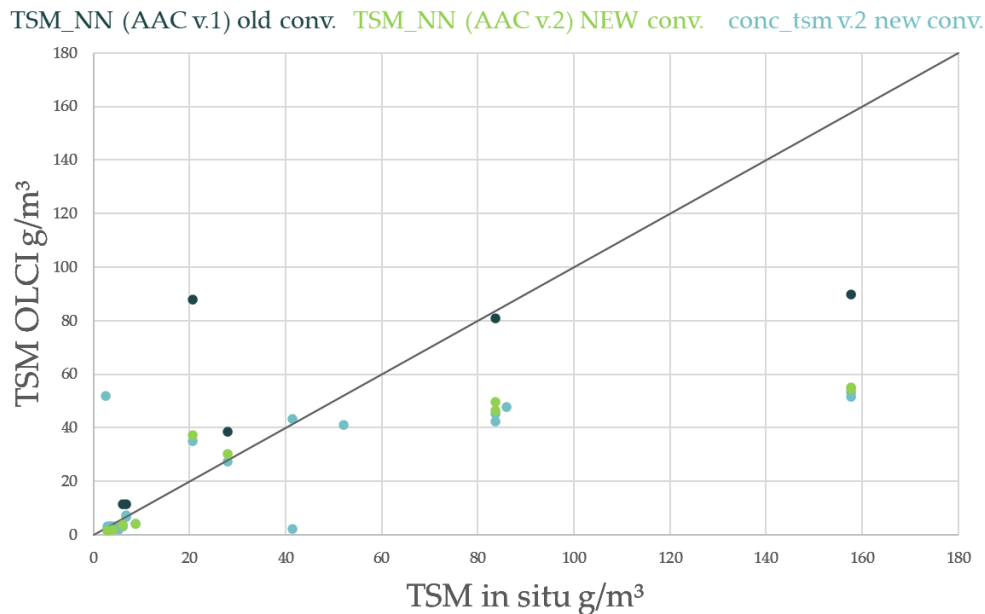


Figure 84 TSM scatterplot comparisons with TSM in-situ data form the Belgian Monitoring Programme , courtesy of RBINS

During validation, the TSM_NN maximum value was also found to not reflect the NNv2 training ranges and has been corrected to that effect. The maximum for TSM_NN is now set to 400 mg/mg³.

In parallel with the validation of the NNv2, and the implementation in the ground segment processor, the scientific improvements of the neural nets has continued. We are currently working towards version 3 of the nets by:

- ❖ Experimenting with fine tuning of Bio-optical model
 - Extended towards clear water
 - Modifying covariances
 - Linear vs. log neural nets
 - Modifying min-max training ranges
- ❖ Implementing a new pure water absorption model
 - Based on Mason et al 2016.
- ❖ Experimenting/Changing the Neural net architecture (Tensorflow / Keras)

The experimentations to improve retrieval in clear waters are so that the recommended cut at low Chl concentration can be removed or relaxed. First results show the improvements and demonstrate also that this change impacts the performance of the AAC in sun glint conditions.

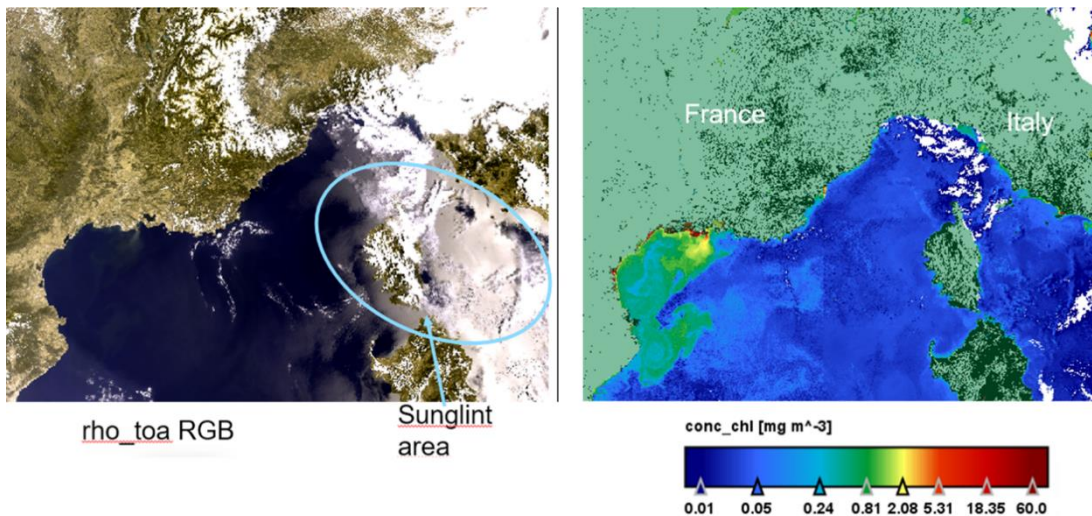


Figure 85: Demonstration of the improvements in resolving chlorophyll changes in clear water condition, due to the changes of the water model in the ongoing work of improving the neural nets. It also shows the improved performance in sun glint conditions.

5.3.7 Aerosol Optical Thickness and Angström Exponent

All OLCI-L2 ocean product types have been validated: full resolution and reduced resolution (*wrr*, *wfr*); near real time and non-time critical (*NR*, *NT*). The ocean colour products from OLCI A and B have been taken from EUMETSATs CODA (Copernicus Online Data Access, <https://codam.eumetsat.int/#/home>) or reprocessed OLCI A CODAREP (<https://codarep.eumetsat.int/#/home>) websites. Although the following quantitative comparisons are restricted to *full resolution non time critical*, the found results are valid for all product types.

To validate OLCI's Aerosol product (aerosol optical thickness and Angstrom coefficient at 865nm), we continuously compare it with data from AERONET (Holben et al 1998), AERONET-OC (Zibordi et al 2009) and MARITIME AERONET (Smirnow et al 2009). This is an ongoing process, where co-located data are collected and analysed, we are using AERONET **V3** data. Only quality assured level data are used for OLCI A. For OLCI B we used AERONET level 1.5 since it allows much more matchups. The background is as follows: It takes up to one year until AERONET level 2 data is released, but a period longer than one year is not covered by the rolling archive of CODA. CODAREP on the other hand does not provide all OLCI-B data, it is instead focussed on reprocessed OLCI-A.

5.3.7.1 AERONET comparisons with OLCI A

98000 OLCI A scenes within the period of June 2016 to January 2021 have been analysed so far. For a matchup, the temporal distance between the satellite overpass and the AERONET acquisition was less than 60 minutes. Since the AERONET L2 is expensively quality controlled, it is published with a delay of up to 1 year, thus the latest AERONET data is from early Summer 2020. Only OLCI measurements are used for the validation which are cloud-free (according to the standard cloud flags: *cloud*, *cloud margin* and

cloud ambiguous) in an area of about 10x10 km² around the AERONET acquisition. Further, all recommended flags from *Sentinel-3 OLCI Marine User Handbook* (EUM/OPS-SEN3/MAN/17/907205) have been applied. Eventually, to reduce the influence of undetected (sub pixel or sub visual) clouds, only matchups have been used, where the standard deviation of the aerosol optical thickness within the 10x10 km² area was less than 0.2. Due to the fact, that most of the AERONET stations are on land, the number of matchups reduced to 723 only. The results are summarised in

Figure 86. It becomes apparent, that:

- ❖ There is a highly linear relation between the AERONET and OLCI AOT, the explained variance is 0.75.
- ❖ The optical thickness of OLCI A is systematically overestimated by 20% - 50%, the majority of the cases is at around 32%.
- ❖ This leads to a systematic bias of 0.04.
- ❖ If the systematic overestimation is corrected, the root mean squared difference decreases from 0.05 to 0.03.
- ❖ There is only a weak ($r^2 = 0.2$) linear relation for the Angström exponent.
- ❖ The majority of AERONET has an Angström of 1.6, whereas OLCI gives 1.4, thus OLCI underestimates the spectral extinction by 0.2.

All investigated quality measures show no significant temporal evolution. There is a slight improvement of the systematic deviation from 1.5 to 1.1, but the significance is low.

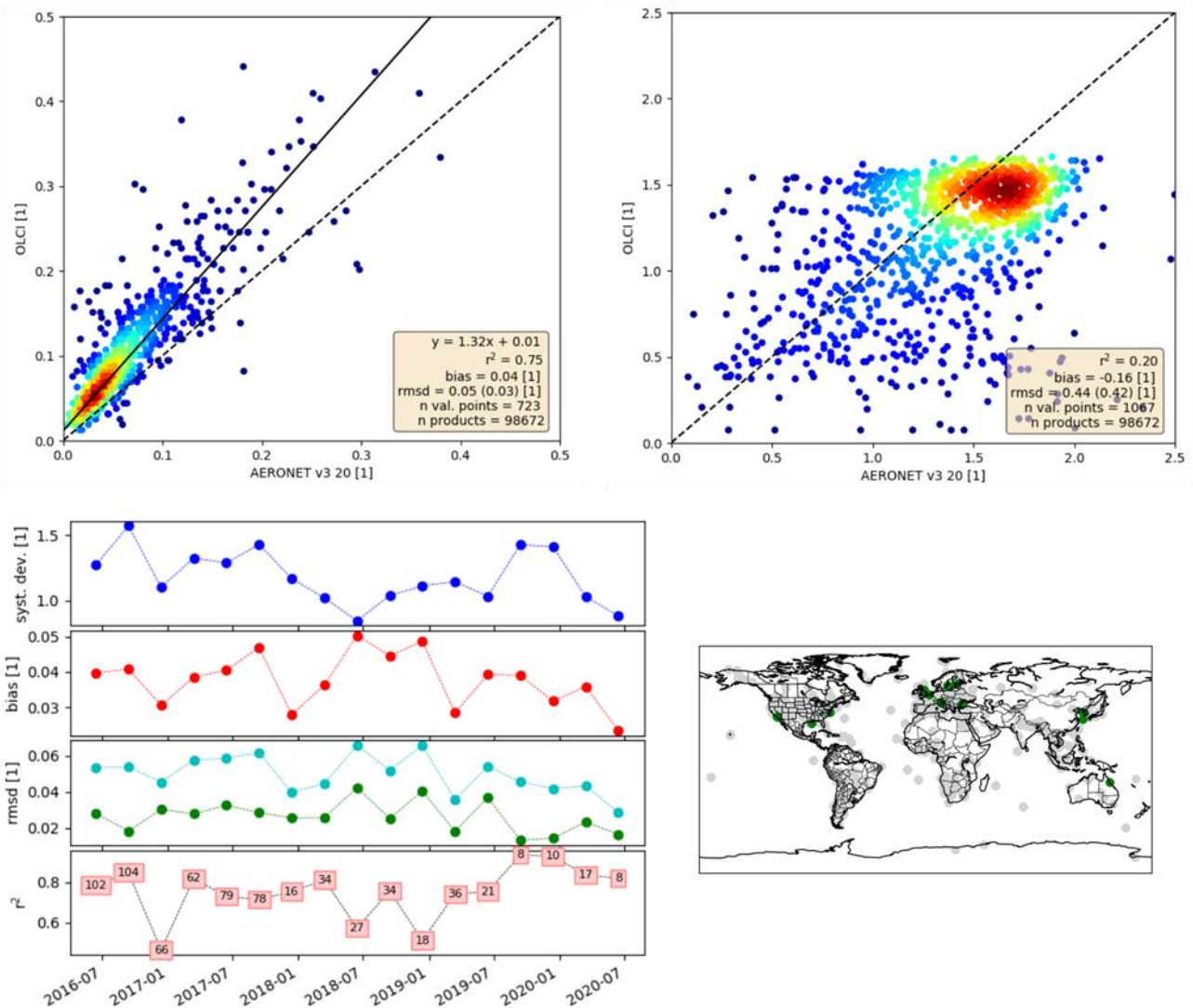


Figure 86: Upper left: OLCI aerosol optical thickness at 865nm against AERONET at 870nm, upper right: OLCI Angström exponent at 865nm against the AERONET Angström exponent at 865nm-440nm. Lower left: Temporal evolution of different quality measures of the optical thickness comparison (from top to bottom: systematic deviation factor, bias, root mean squared difference (with and without bias correction), explained variance (number in boxes are the numbers of matchups)). Lower right: positions of the used AERONET stations.

5.3.7.2 Marine AERONET comparisons with OLCI A

2300 OLCI A scenes within the period of June 2016 to January 2020 have been analysed so far. For a matchup, the temporal distance between the satellite overpass and the AERONET acquisition was less than 60 minutes. Since the maritime AERONET L2 is expensively quality controlled, it is published with a delay of up to 1 year, thus the latest data is from early Summer 2020. Only OLCI measurements are used for the validation which are cloud-free (according to the standard cloud flags: *cloud*, *cloud margin* and *cloud ambiguous*) in an area of about 10x10 km² around the AERONET acquisition. Further, all

recommended flags from *Sentinel-3 OLCI Marine User Handbook* (EUM/OPS-SEN3/MAN/17/907205) have been applied. Eventually, to reduce the influence of undetected (sub pixel or sub visual) clouds, only matchups have been used, where the standard deviation of the aerosol optical thickness within the 10x10 km² area was less than 0.2. After this rigid filtering only 61 leftovers remain. The results are summarized in Figure 87:

- ❖ There is a highly linear relation between the AERONET and OLCI AOT, the explained variance is 0.8.
- ❖ The data shows a systematic underestimation of 20%, contrary for the AERONET comparison. This is probably a sampling effect due to few points with high AOT.
- ❖ There is no linear relation for the Angström exponent.

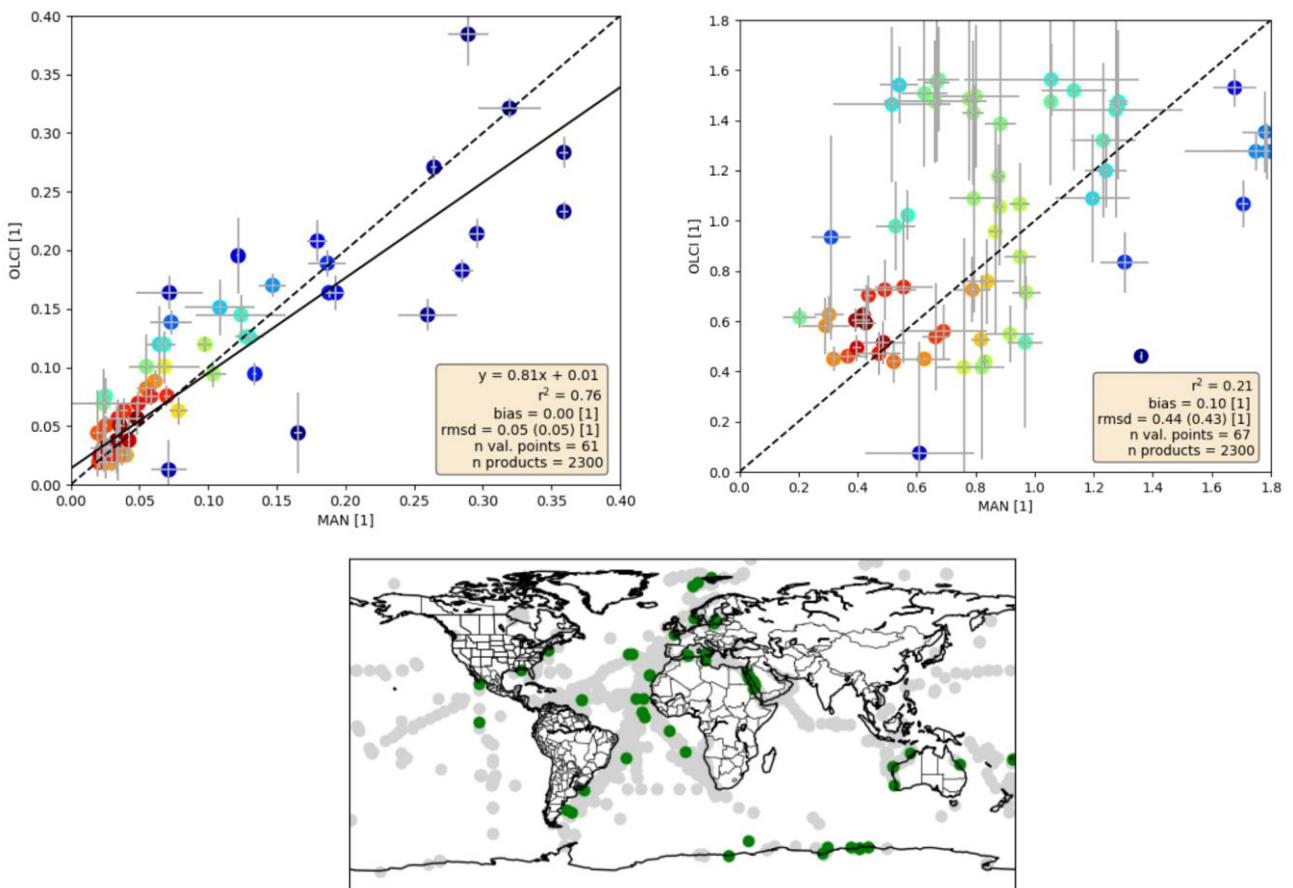


Figure 87: Upper left: OLCI aerosol optical thickness at 865nm against Maritime AERONET at 870nm, upper right: OLCIs Angström exponent at 865nm against the Maritime AERONET Angström exponent at 865nm-440nm. Lower right: positions of the used cruises.

5.3.7.3 AERONET comparisons with OLCI B

71000 OLCI B scenes within the period of June 2018 to January 2020 have been analysed so far. For a matchup, the temporal distance between the satellite overpass and the AERONET acquisition was less than 60 minutes. We used the AERONET L1.5, which is not is expensively quality controlled, but available in near time. Similarly to OLCI A, only measurements are used for the validation which are cloud-free (according to the standard cloud flags: *cloud*, *cloud margin* and *cloud ambiguous*) in an area of about 10x10 km² around the AERONET acquisition. Further, all recommended flags from *Sentinel-3 OLCI Marine User Handbook* (EUM/OPS-SEN3/MAN/17/907205) have been applied. Eventually, to reduce the influence of undetected (sub pixel or sub visual) clouds, only matchups have been used, where the standard deviation of the aerosol optical thickness within the 10x10 km² area was less than 0.2. Eventually the number of matchups reduced to 60 only. The results are summarised in Figure 88. It becomes apparent, that OLCI B behaves like OLCI A:

- ❖ There is a highly linear relation between the AERONET and OLCI AOT. The explained variance is 0.75.
- ❖ Similarly to OLCI A, OLCI B is systematically overestimated by 35%.
- ❖ The pattern of the Angström comparison is as for OLCI A; a weak relation, the majority around 1.4 and a systematic underestimates of OLCI by 0.3.

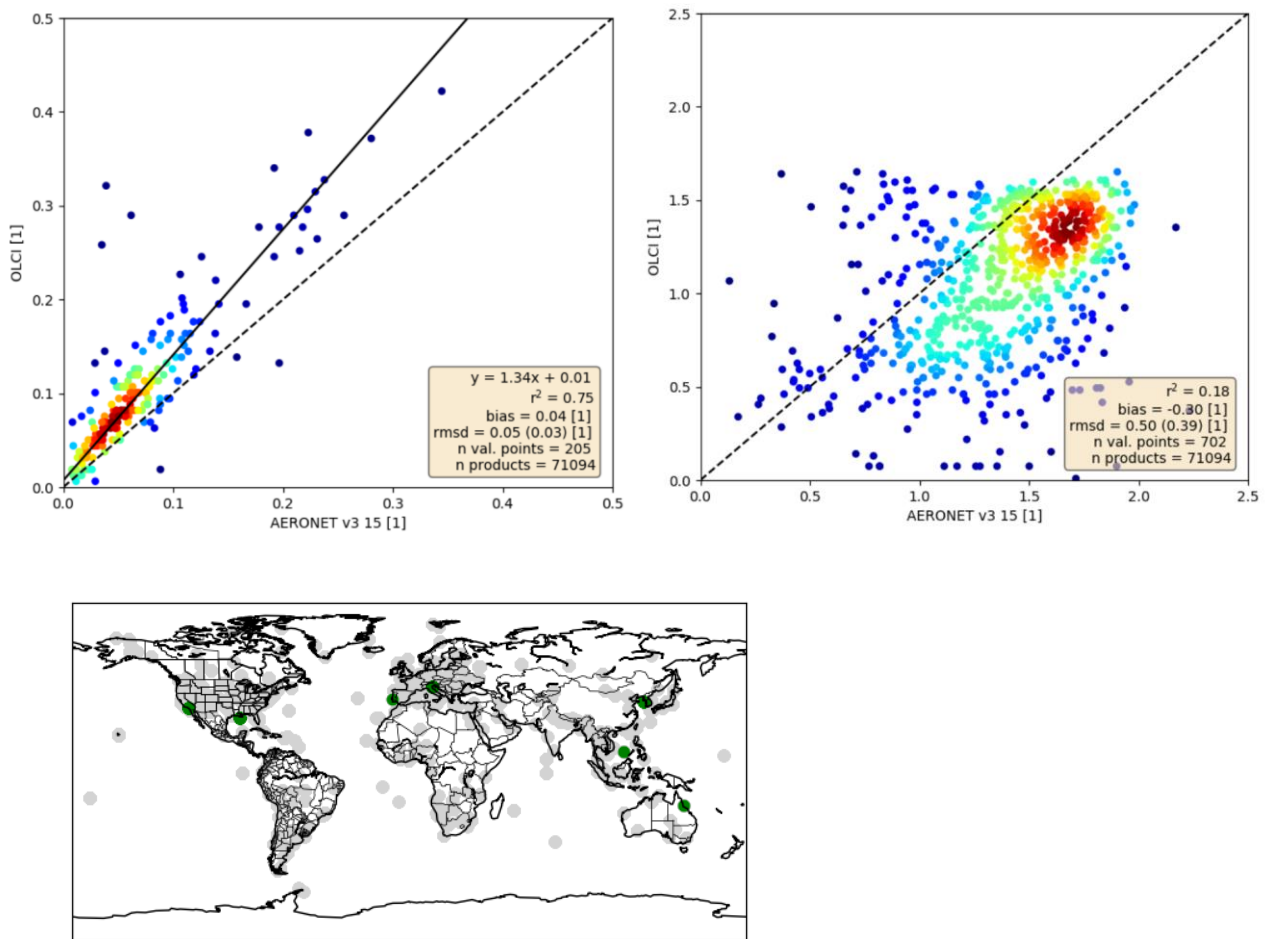


Figure 88: Upper left: OLCI aerosol optical thickness at 865nm against AERONET v3 L1.5 AOT at 870nm, upper right: OLCIs Angström exponent at 865nm against the AERONET v3 L1.5 Angström exponent at 865nm-440nm. Lower: positions of the used AERONET stations.

5.3.7.4 Summary

The validation of OLCI aerosols products shows a high agreement for the aerosol optical thickness ($rmsd \sim 0.02$); if a systematic overestimation of around 35-40 % is corrected. The Angström exponent agrees hardly ($r^2 = 0.2$), but the order of magnitude (1.6) is almost met (bias = -0.2). A validation of OLCI B using AERONET level 1.5 data, shows the same pattern as for OLCI A. The number of matchups with maritime AERONET and OLCI-A is still low, but the results are different. There is no systematic overestimation and the Angström exponent concentrates around 0.6.

5.3.7.5 References

- ❖ Holben, B. N., et al., AERONET—A federated instrument network and data archive for aerosol characterization, Remote Sens. Environ.,66, 1–16, 1998.)



- ❖ Smirnov, A., Holben, B.N., Slutsker, I., Giles, D.M., McClain, C.R., Eck, T.F., Sakerin, S.M., Macke, A., Croot, P., Zibordi, G., Quinn, P.K., Sciare, J., Kinne, S., Harvey, M., Smyth, T.J., Piketh, S., Zielinski, T., Proshutinsky, A., Goes, J.I., Nelson, N.B., Larouche, P., Radionov, V.F., Goloub, P., Krishna Moorthy, K., Matarrese, R., Robertson, E.J., Jourdin, F., 2009. Maritime aerosol network as a component of aerosol robotic network. *J. Geophys. Res.* 114, 1–10, <http://dx.doi.org/10.1029/2008JD011257>.
- ❖ Zibordi G., B.Holben, I.Slutsker, D.Giles, D.D'Alimonte, F.Mélin, J.-F. Berthon, D. Vandemark, H.Feng, G.Schuster, B.Fabbri, S.Kaitala, J.Seppälä. AERONET-OC: a network for the validation of Ocean Color primary radiometric products. *Journal of Atmospheric and Oceanic Technology* , 26, 1634-1651, 2009.

6 Summary of performances – SLSTR

6.1 Instrument performances

6.1.1 Instrument temperatures

As a thermal infrared instrument, thermal stability and uniformity of the optical mechanical enclosure, OME is critical to the radiometric calibration. During normal operations, temperatures have remained generally stable and consistent during the reporting period, with gradual changes due to the seasonal cycle, which are consistent with the first two years of operations for SLSTR-A. The exceptions are when the normal mode was disrupted by instrument operations or anomalies – for example, the decontaminations performed in February and May 2020 for SLSTR-A and in November 2020 for SLSTR-B.

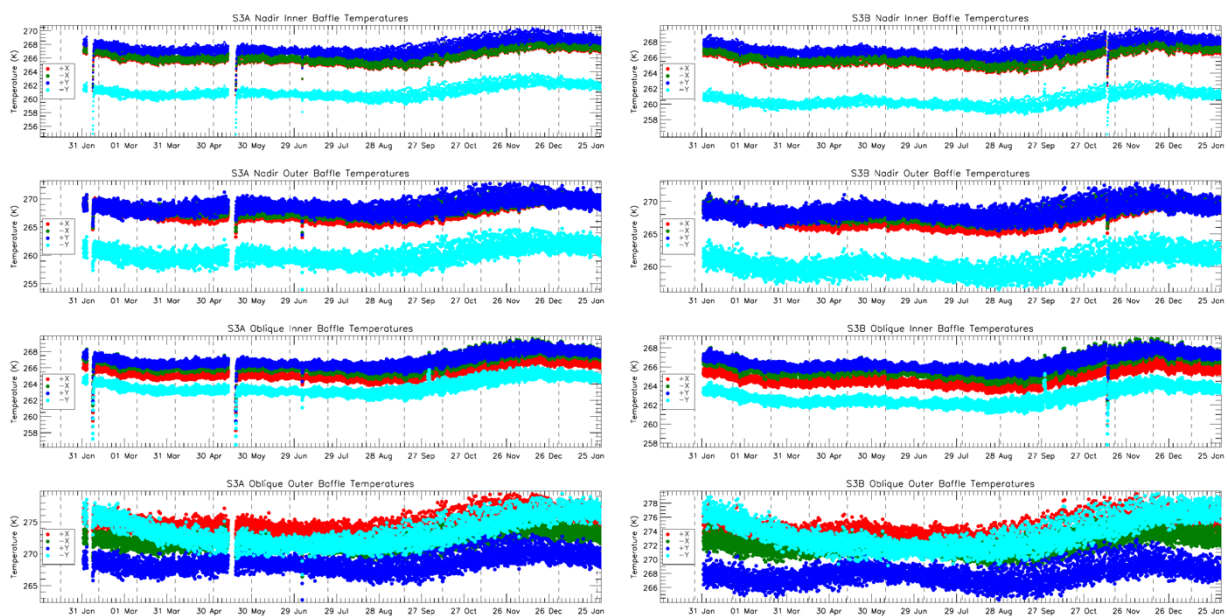


Figure 89: Baffle temperature trends for SLSTR-A (left) and SLSTR-B (right) from 1st Feb 2020 to end of Jan 2021. The vertical dashed lines indicate the start and end of each cycle.

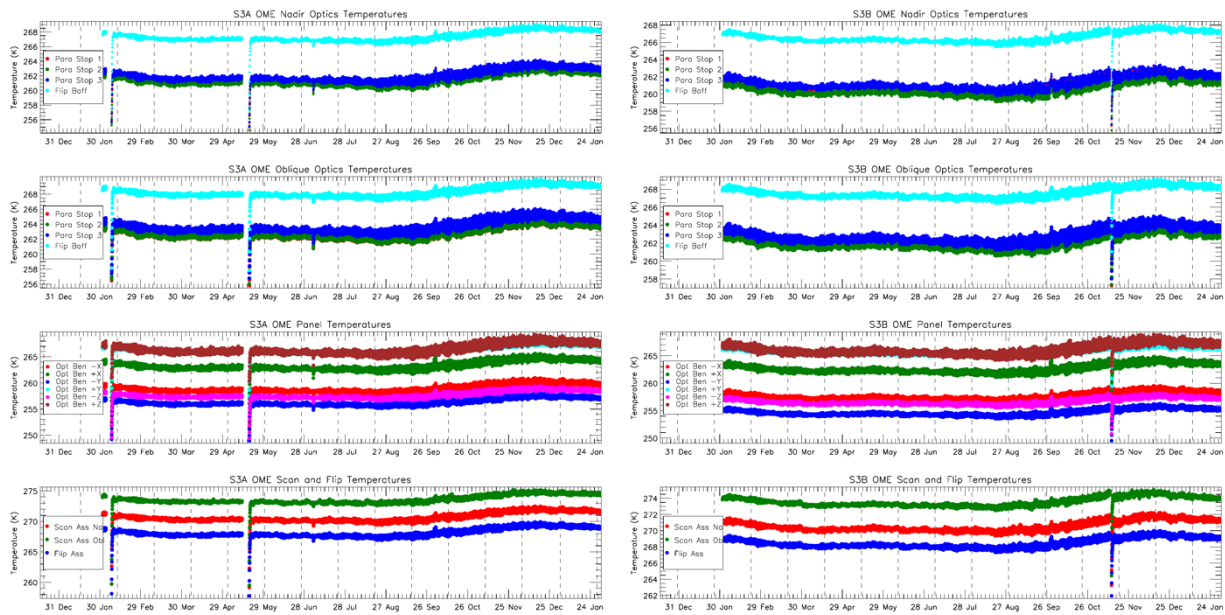


Figure 90: OME temperature trends for SLSTR-A (left) and SLSTR-B (right) from 1st Feb 2020 to end of Jan 2021, showing the paraboloid stops and flip baffle (top two plots) and optical bench and scanner and flip assembly (lower two plots). The vertical dashed lines indicate the start and end of each cycle.

6.1.2 Detector Temperatures

The cooler is performing well, maintaining the IR detectors between 84 and 89K – see Figure 91 and Figure 92. The IR FPA is affected by water ice contamination as is common for instruments with cryogenic optics, and was observed for all ATSR instruments. This affects the heat load on the IR FPA, which requires the cooler to run at increased drive levels and also affects the optical throughput of the channels. Therefore, periodic decontamination cycles are needed to remove the water ice from the cold surfaces. These were carried out in February and May 2020 for SLSTR-A and November 2020 for SLSTR-B.

The IR detector temperatures gradually increase following each decontamination as the ice layer builds up and the cooler drive amplitude increases. The rate of increase in S8 temperature following each SLSTR-A decontamination since the beginning of the mission is plotted in Figure 93, and the rate of increase in cooler drive amplitude in Figure 94. The rate of increase in temperature is reducing over time, consistent with the reduced water ice contamination rates (see Section 6.1.7.7). However, the change in slope of the cooler drive amplitude was lower than expected, in particular for SLSTR-B. In order to prolong the lifetime of the cooler, the cold tip temperature for SLSTR-B was increased by 2K on 30th March 2020. The cold tip temperature for SLSTR-A had already been increased by 1K on 18th July 2018, and was increased by a further 1K on 14th October 2020.

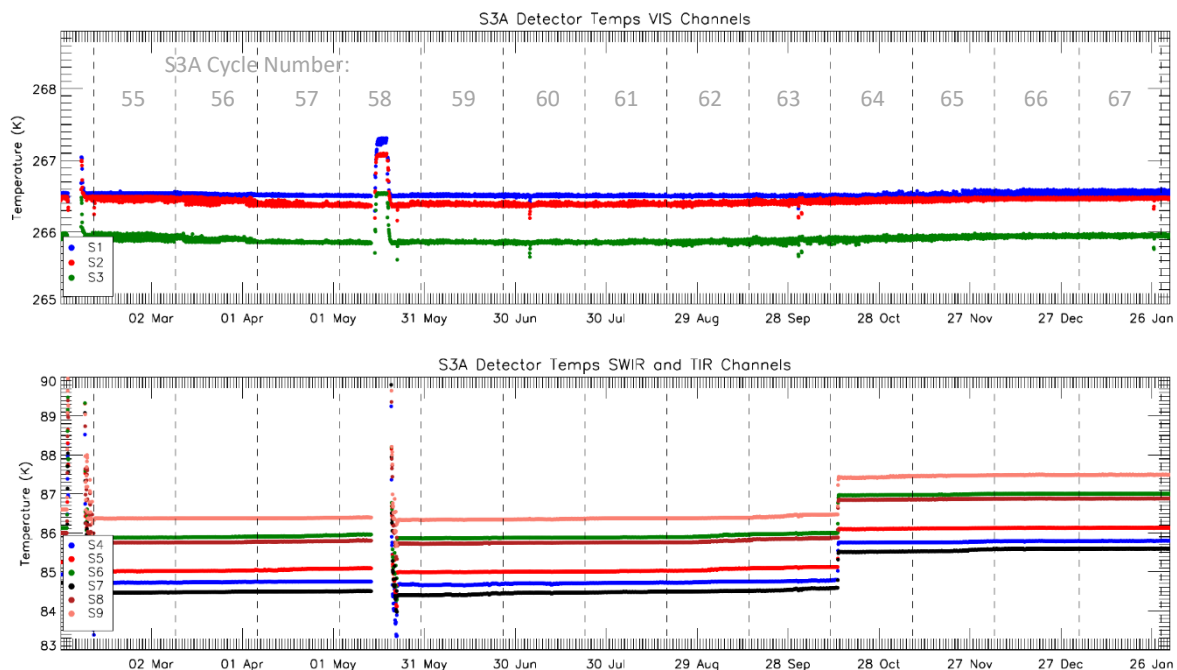


Figure 91: SLSTR-A detector temperatures for each channel from 1st Feb 2020 to end of January 2021. Discontinuities occur for the infrared channels where the FPA was heated for decontamination, and on 14th October when the cold tip temperature was increased. The vertical dashed lines indicate the start and end of each cycle.

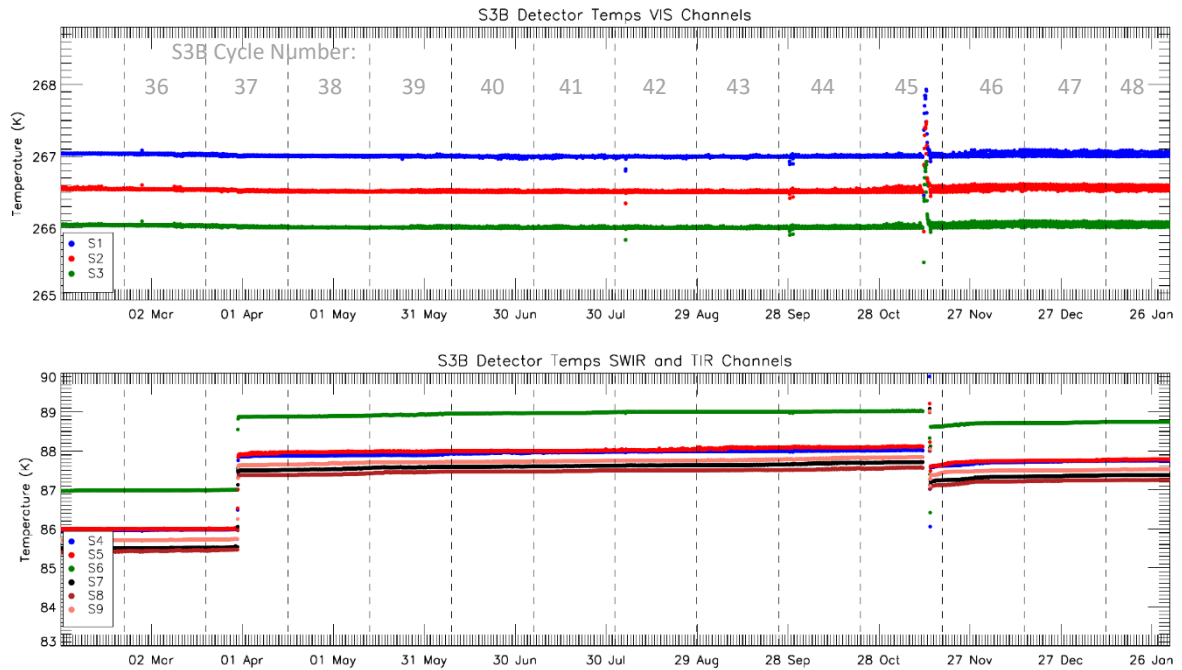


Figure 92: SLSTR-B detector temperatures for each channel from 1st Feb 2020 to end of January 2021. The discontinuity occurs for the infrared channels where the cold tip temperature was increased on 30th March and when the FPA was heated for decontamination in November. The vertical dashed lines indicate the start and end of each cycle.

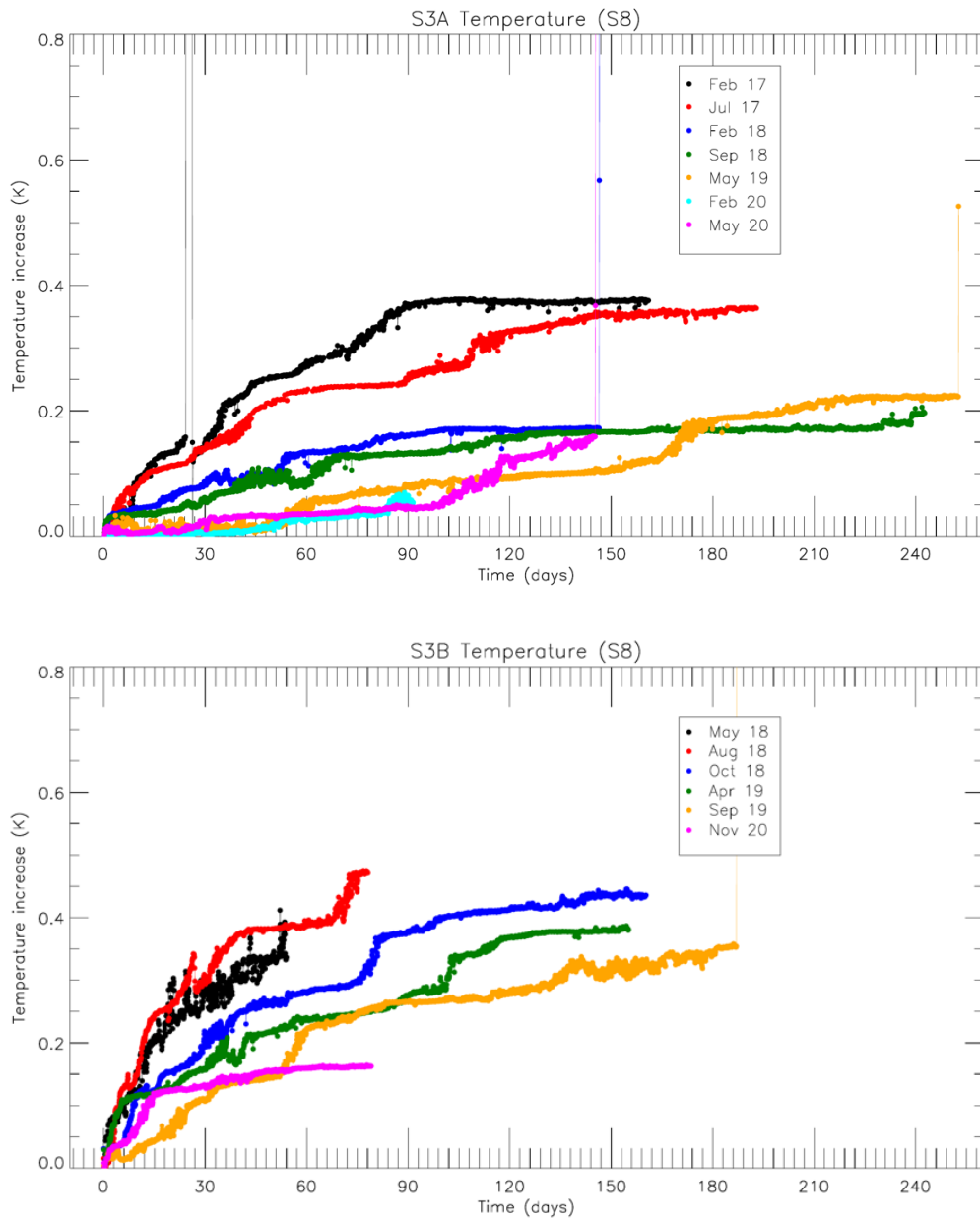


Figure 93: The increase in S8 temperature for SLSTR-A (top) and SLSTR-B (bottom) following recent decontaminations.

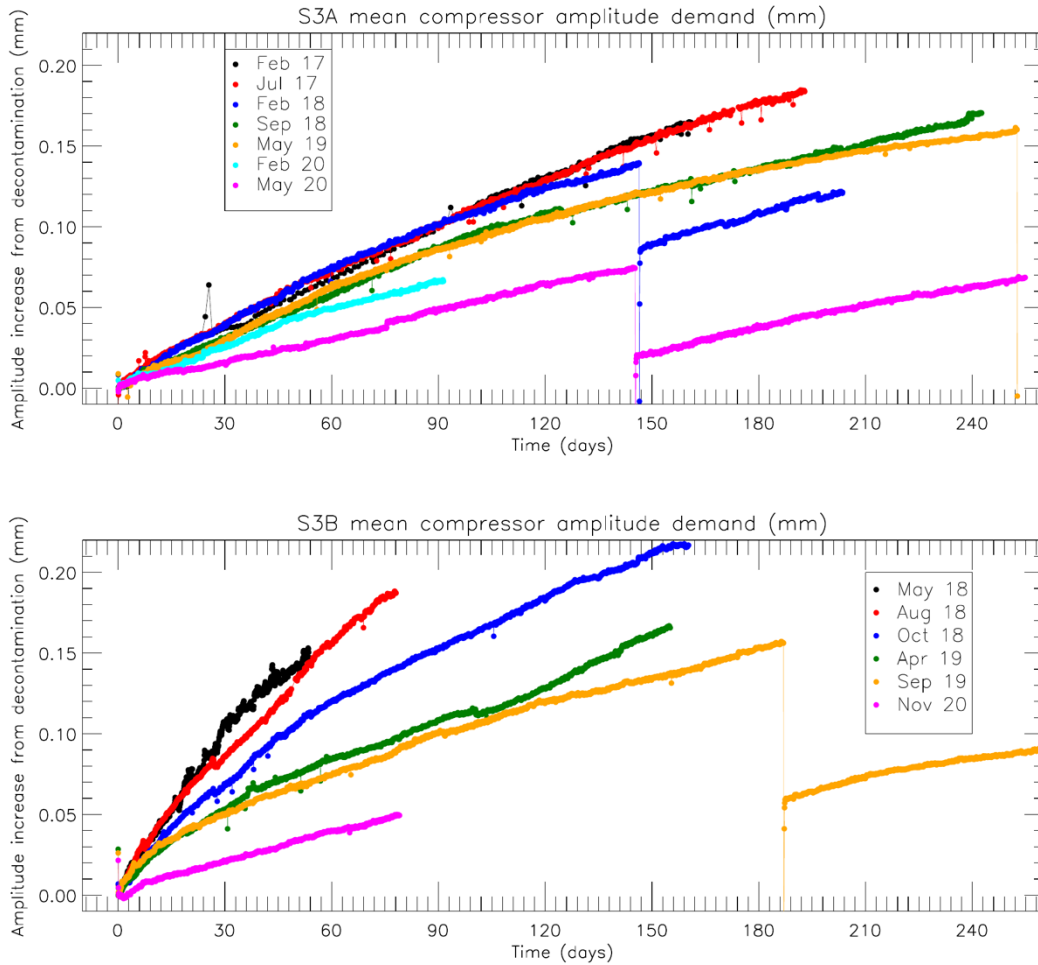


Figure 94: The increase in cooler drive amplitude following recent decontaminations on SLSTR-A (top) and SLSTR-B (bottom). Note that the step in the blue and magenta lines for SLSTR-A and the orange line for SLSTR-B correspond to the points at which the cooler cold tip temperature was increased (the increased temperature requires a lower drive amplitude).

6.1.3 Scanner performance

The scanners have performed consistently since launch, operating within required limits. The scanners are controlled and monitored by absolute encoders mounted on the drive shafts. Scan jitter statistics for SLSTR-A are shown in Figure 96 and for SLSTR-B in Figure 98 with respect to the linear control law within each orbit.

6.1.3.1 SLSTR-A scanner performance

The scanner statistics with respect to the linear control law for SLSTR-A over the past four years are shown in Table 21, with the past year highlighted in grey.

The histogram of the standard deviation in each orbit over the last year is shown in Figure 96. The standard deviation at the peak of the histogram has remained constant over the past 4 years for the scanners, and reduced slightly for the flip mirror. The statistic included in previous annual reports was the largest standard deviation encountered, and this is shown in parenthesis in Table 21.

The maximum and minimum deviation within each orbit gives a measure of the worst instantaneous jitter encountered. The histogram has several peaks for the nadir view for year 4, the highest of which is shown in Table 21.

Overall, the SLSTR-A scanner and flip statistics are as good or better than the previous years, showing that the mirror mechanisms are performing well.

Table 21: SLSTR-A scanner and flip mirror jitter statistics (each year runs from February to February).

View	Mirror	Largest mean deviation (")				Standard deviation at peak of histogram (and largest) (")				Maximum-minimum at peak of histogram (")			
		2017	2018	2019	2020	2017	2018	2019	2020	2017	2018	2019	2020
Nadir	scan	0.8	1	1.4	1.2	2.2 (3.6)	2.2 (3.0)	2.2 (4.8)	2.2 (7.4)	36	39	38	35
	flip	0.4	0.4	0.4	0.4	4.3 (7.4)	4.0 (8.6)	3.7 (7.4)	3.0 (8.0)	92	69	68	45
Obl.	scan	0.8	0.6	1	0.8	2.2 (3.6)	2.2 (3.6)	2.2 (3.2)	2.2 (7.0)	36	26	23	20
	flip	0.4	0.6	0.6	0.4	8.2 (11.8)	6.4 (13.4)	5.7 (13.6)	5.3 (13.8)	116	98	90	60

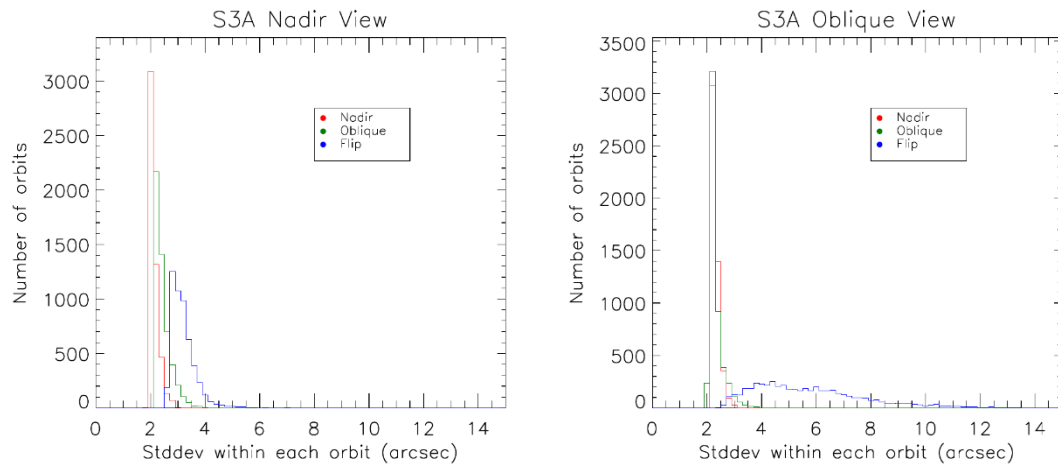


Figure 95: SLSTR-A histogram of standard deviation with respect to the linear control law of the scanners and flip mirror in each orbit from February 2020 to February 2021 for nadir view (left) and oblique view (right).

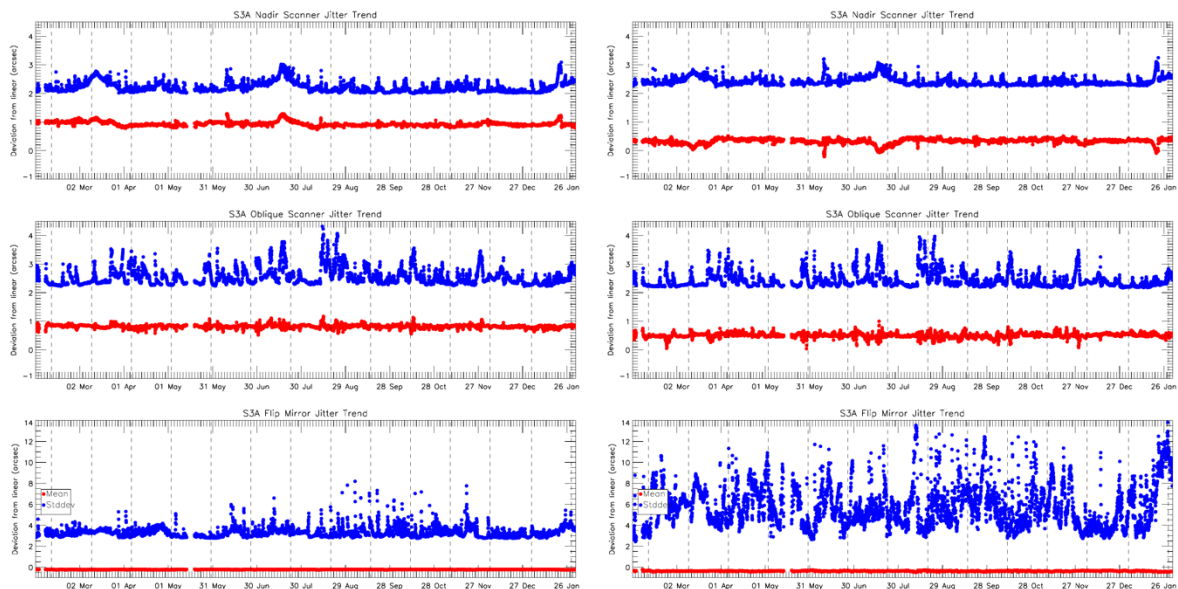


Figure 96: SLSTR-A scanner and flip jitter from February 2020 to February 2021, showing mean (red) and stddev (blue) compared to the expected one for the nadir view (left) and oblique view (right). The vertical dashed lines indicate the start and end of each cycle.

6.1.3.2 SLSTR-B scanner performance

The scanner statistics for SLSTR-B are shown in Table 22 and are generally consistent with the previous years. The SLSTR-B scanner and flip mean and standard deviations from their expected positions are broadly consistent with SLSTR-A, although the oblique scanner has a slightly larger mean deviation of $<3''$.

In previous years, it had been highlighted that the flip mirror maximum-minimum deviation was high, and its performance should be carefully monitored. However, the flip mirror statistics for the past year appear to be slightly better than the previous year, and no deterioration in performance has been observed. In

fact the standard deviation has improved for the oblique view during the year (see Figure 98), and the histogram in Figure 97 shows two peaks (only the higher value is shown in Table 22).

Table 22: SLSTR-B scanner and flip mirror jitter statistics (each year runs from February to February).

View	Mirror	Largest mean deviation (")			Standard deviation at peak of histogram (and largest) (")			Maximum-minimum at peak of histogram (")		
		2018*	2019	2020	2018*	2019	2020	2018*	2019	2020
Nadir	scanner	0.4	0.2	0.4	2.8 (3.4)	2.8 (3.6)	2.8 (5.4)	39	47	38
	flip	0.4	0.4	0.4	4.4 (6.8)	3.9 (8.2)	3.8 (7.8)	94	155	145
Oblique	scanner	3	3	3	4.2 (5.6)	4.0 (5.8)	4.9 (6.0)	56	56	75
	flip	0.6	0.6	0.6	5.6 (9.4)	5.7 (12.6)	5.6 (9.4)	87	120	112

* October 2018 to February 2019

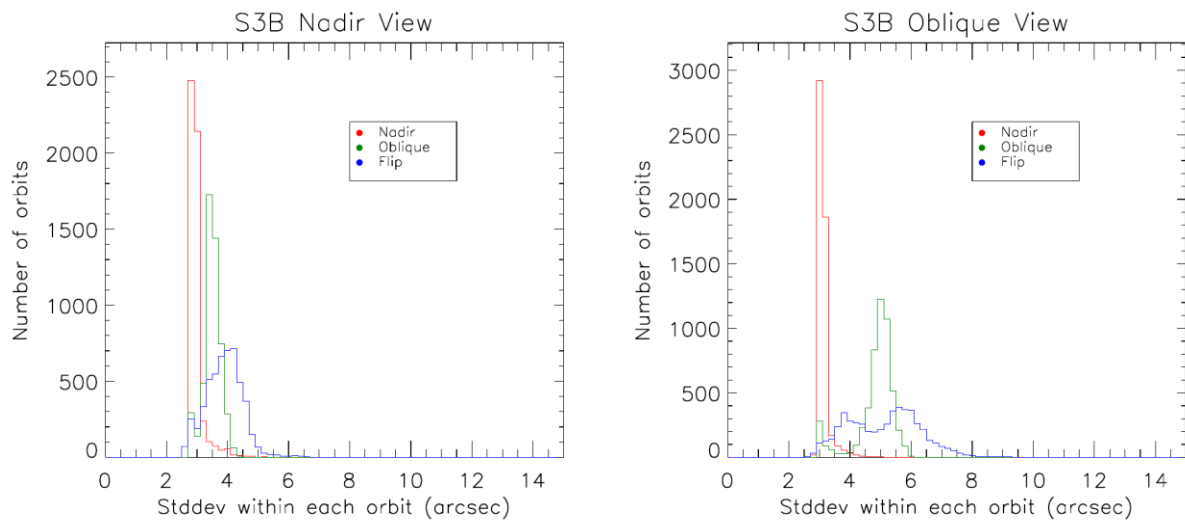


Figure 97: SLSTR-B histogram of standard deviation with respect to the linear control law of the scanners and flip mirror from February 2020 to February 2021.

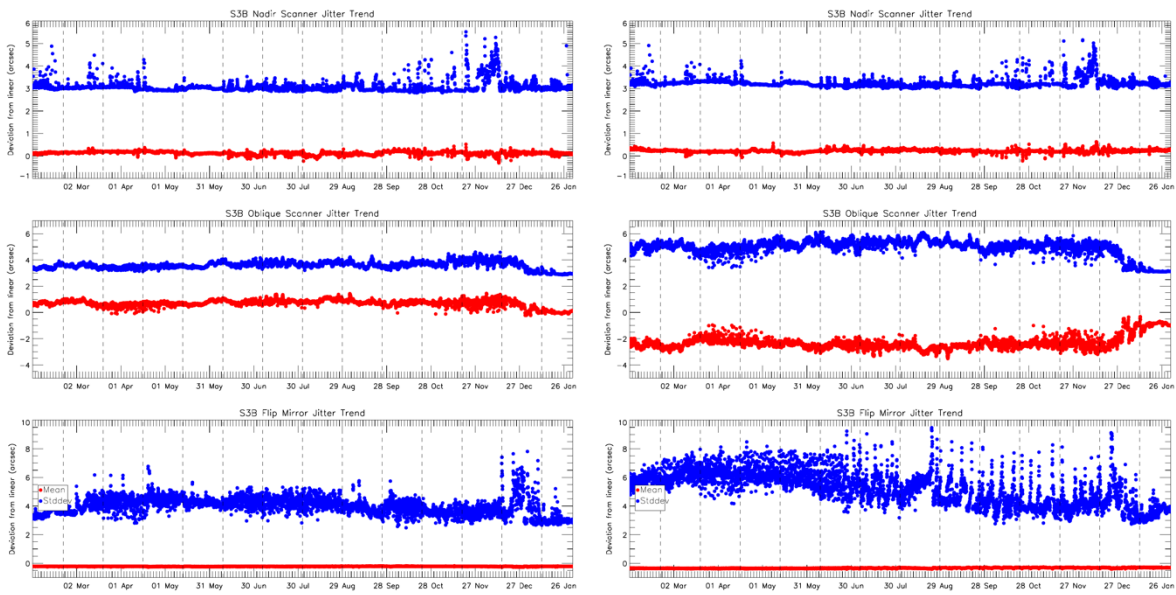


Figure 98: SLSTR-B scanner and flip jitter, showing mean (red) and stddev (blue) compared to the expected one for the oblique view for February 2020 to February 2021. The vertical dashed lines indicate the start and end of each cycle.

6.1.4 Black-Bodies

The blackbodies have functioned well over the reporting period. The heated blackbody (+YBB) is being maintained by the heaters approximately 37-38 K above the cool blackbody (-YBB). The long-term trends show no discernible degradation in the performance of the heaters.

6.1.4.1 SLSTR-A Black-Bodies

Figure 99 shows the blackbody temperatures and baseplate gradients for SLSTR-A. During December 2020, the heated BB increased to above 304 K as the satellite approached perihelion. This is only marginally higher than the temperature reached in previous years and still within acceptable limits. The maximum BB temperature should be monitored carefully to ensure that the BBs remain below 305 K to avoid saturation of S7.

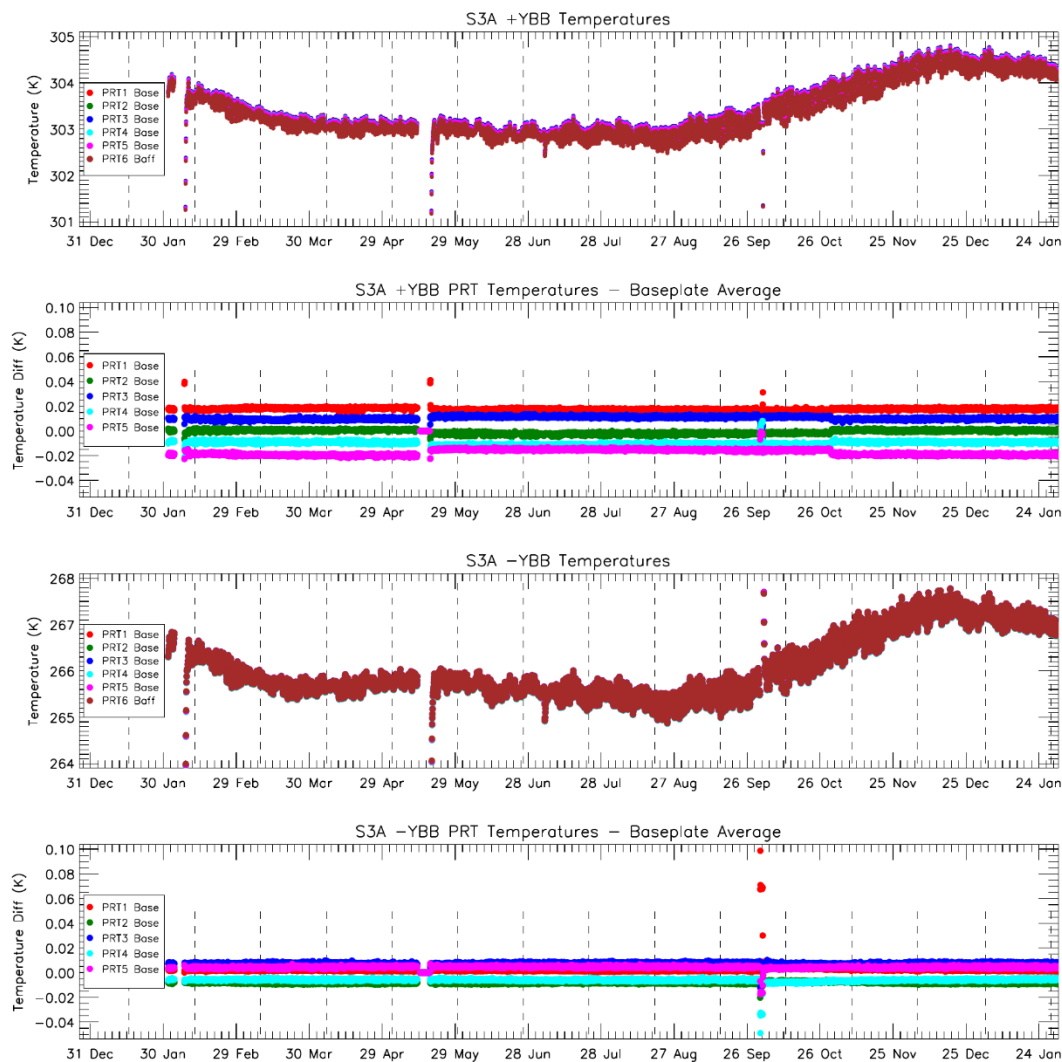


Figure 99: SLSTR-A blackbody temperature and baseplate gradient trends for Feb 2020 to Jan 2021. The vertical dashed lines indicate the start and end of each cycle. Discontinuities are caused by the decontaminations, and a black-body crossover test.

6.1.4.2 SLSTR-B Black-Bodies

Figure 100 shows the blackbody temperatures and baseplate gradients for SLSTR-B. The difference of the 5 PRTs located on the blackbody baseplate with the average base temperature are also plotted in Figure 100. The spread in temperature of the baseplate PRTs is largest when the blackbody is heated. In particular when the +YBB is hot, PRT1 is warmer than the average by approximately 70 mK whereas the other PRTs all cluster closely together. This difference was expected before launch, and is consistent with measurements made during the ground testing.

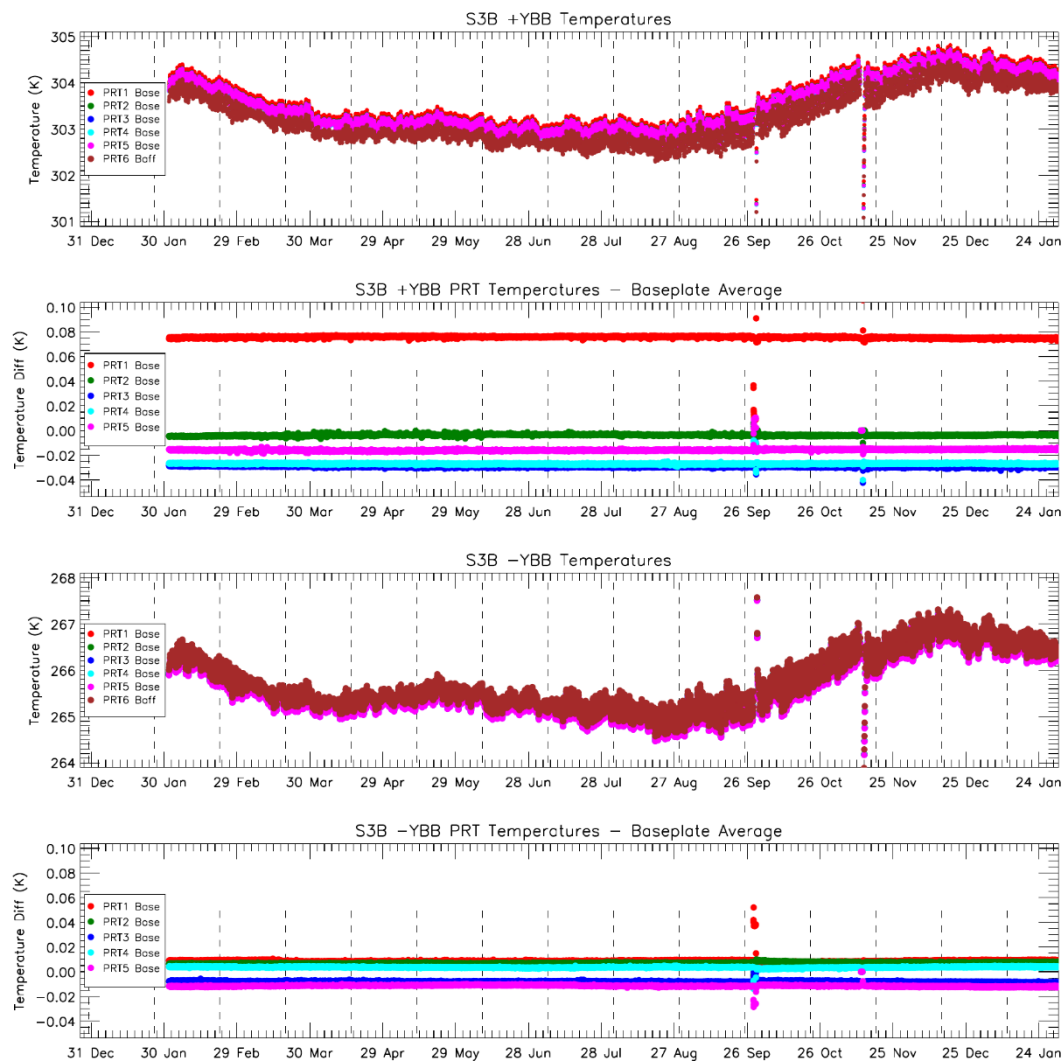


Figure 100: SLSTR-B blackbody temperature and baseplate gradient trends for Feb 2020 to Jan 2021. The vertical dashed lines indicate the start and end of each cycle. Discontinuities are caused by the decontaminations, and a black-body crossover test.

6.1.4.3 Blackbody Cross-Over Tests

Blackbody cross-over tests are carried out at yearly intervals to compare the radiometric signals in the thermal channels when the two blackbodies are at identical temperatures. The test is performed to determine the effects of any drifts in the blackbody thermometer calibration or change in target emissivity caused by a deterioration of the black surface finish.

The method is based on that for AATSR on ENVISAT and has been performed for SLSTR during pre-launch calibration, then in-flight during commissioning and at yearly intervals to determine any changes in the blackbody performance.

It is important to note that this is not an absolute test of the blackbody performance since we do not have an independent method to evaluate the absolute radiances from the blackbodies on-orbit to sufficient accuracy (SLSTR is intended to have a radiometric error <0.1K which is at the limit for most space-borne instruments). However, we are able to deduce any relative calibration errors between channels or trends in the blackbody thermometer calibration or change in target emissivity caused by a deterioration of the black surface finish. The method does not distinguish which effect is dominant because the two are highly correlated. However, the results do provide a means to verify the uncertainty in the BB radiances.

The test was performed by switching the heated blackbody from the +YBB to the -YBB (and vice versa) and allowing the temperatures to cross over and stabilise. The most recent tests for this reporting period were performed between 28th September and 2nd October 2020, with crossover temperatures of 290.284/291.774K for SLSTR-A and 289.785/291.070 K for SLSTR-B.

The analysis is performed by comparing the radiometric signals close to the cross-over times as a function of the baseplate temperatures as measured by the PRTs. Here, we can estimate the effective temperature difference between the two BBs from the slope dN/dT , which is obtained by a simple linear fit to the data. So,

$$\Delta T = \frac{dT}{dN} \Delta DN$$

The detector counts versus temperatures at the cross-over for the SLSTR-A test are shown in Figure 101 and for SLSTR-B in Figure 102. Figure 103 shows ΔT versus time for all of the BB cross-over tests performed to date, including the pre-launch measurements (6 tests for SLSTR-A and 4 tests for SLSTR-B).

For SLSTR-A, the results show that there has been some steady drift with time, and there is a possible correlation with the baseplate gradients for the second cross-over. For SLSTR-B, the results show a change from the pre-launch measurements to on-orbit, with the largest variations seen for S8 and S9 in the Nadir view. At the time of writing the cause of the differences is not fully understood. Further blackbody cross-over tests performed during the lifetime of the mission will show if this is an evolving trend or an artefact of the test conditions.

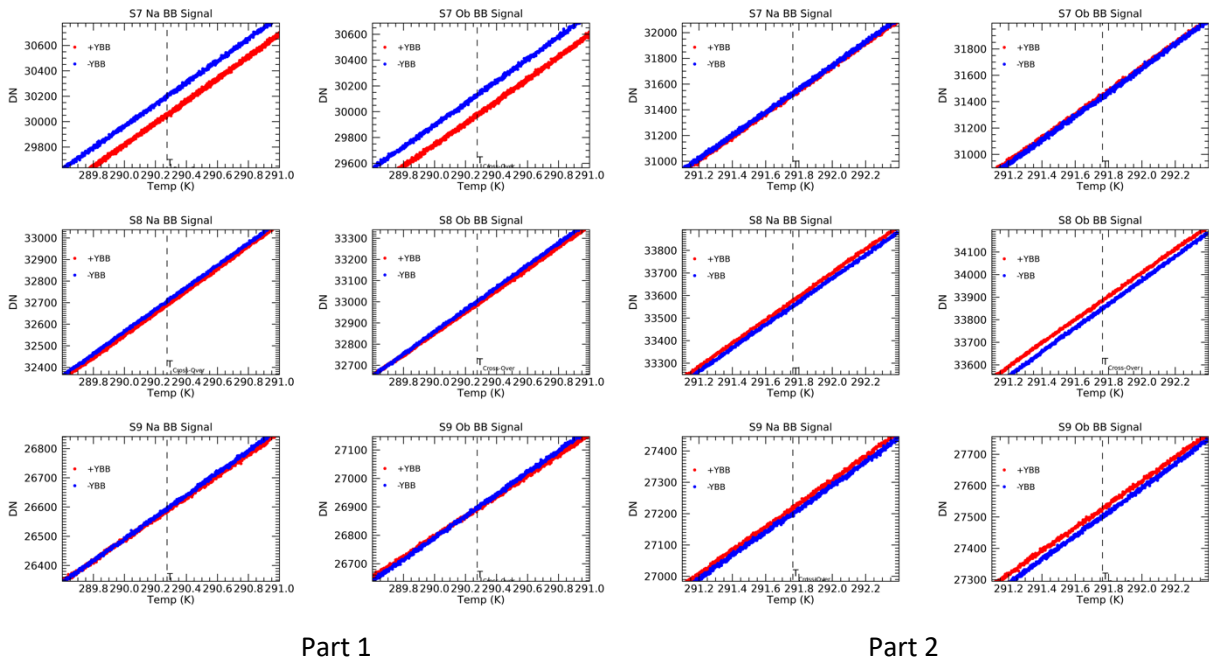


Figure 101: SLSTR-A detector counts vs. temperatures at the blackbody cross-over points for the BB cross-over test on 1st and 2nd October 2020. Part 1 of the test is shown on the left and part 2 on the right.

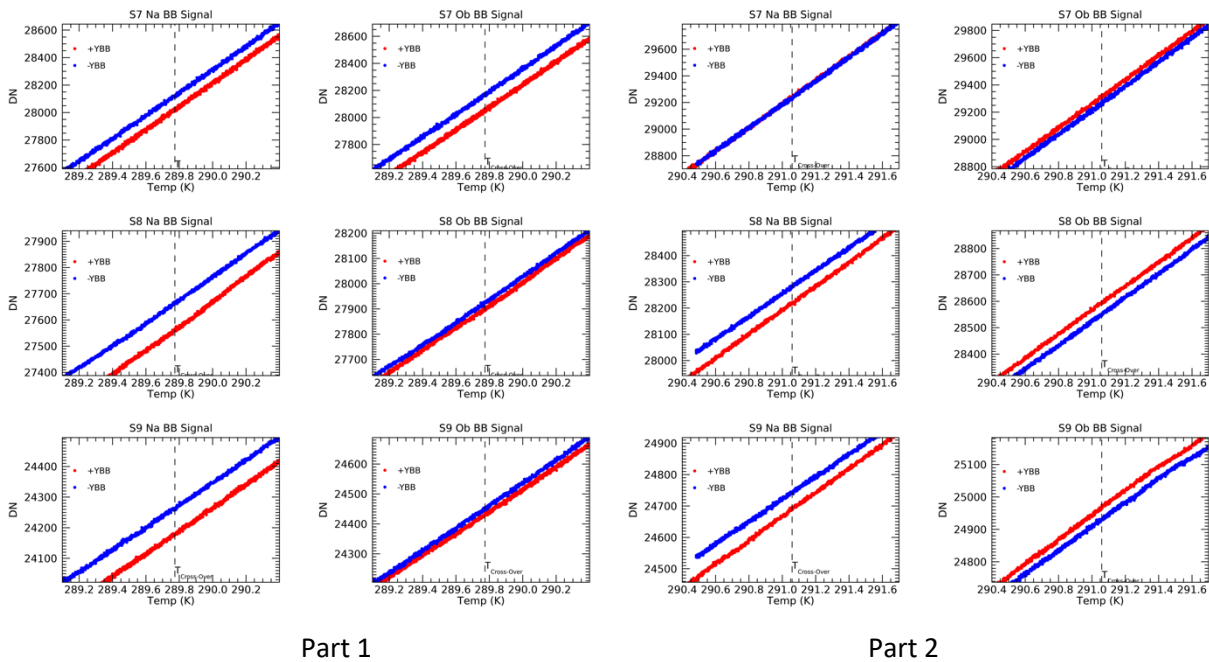


Figure 102: SLSTR-B detector counts vs. temperatures at the blackbody cross-over points for the BB cross-over test on 28th and 29th September 2020. Part 1 of the test is shown on the left and part 2 on the right.

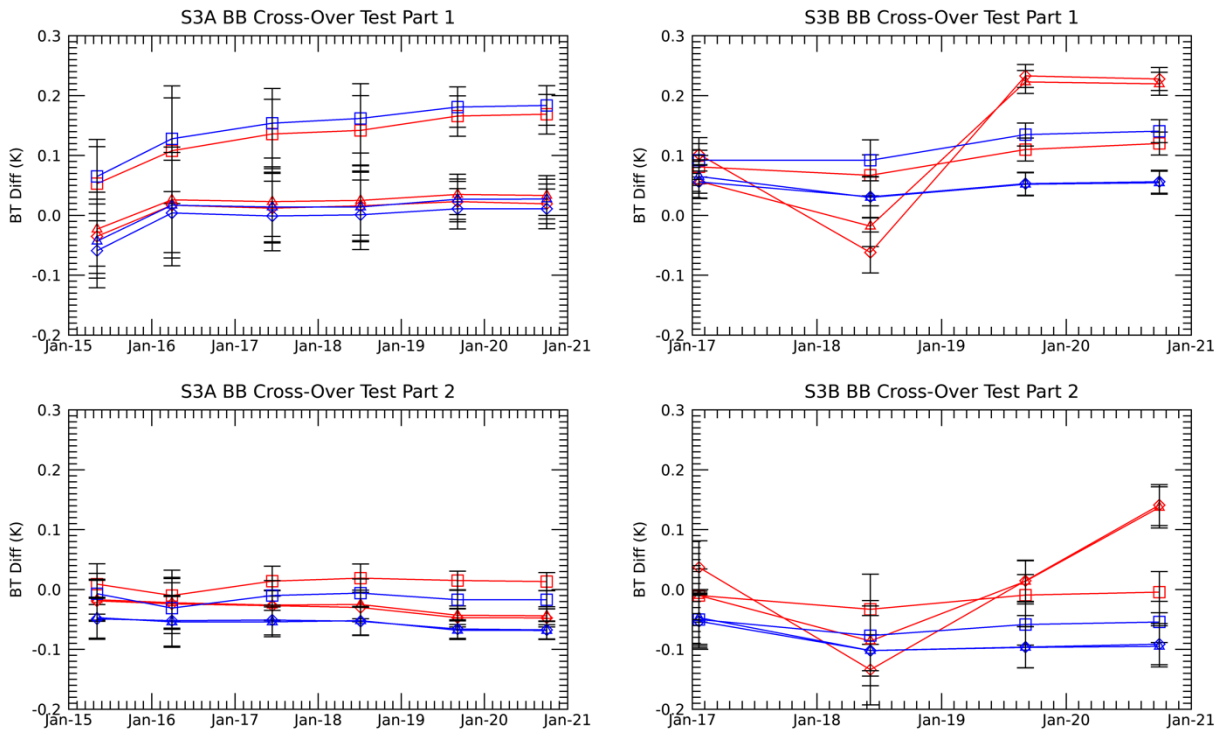


Figure 103: BT differences vs time for all of the blackbody cross-over tests performed to date (including pre-launch measurements) for SLSTR-A (left) and SLSTR-B (right). The part 1 crossover is shown in the top plots, and part 2 in the lower plots. Different symbols indicate different channels (S7: square, S8: triangle, S9: diamond) and different colours indicate nadir (red) and oblique (blue) views. Error bars are derived from the blackbody temperature gradients and standard deviations of the BB signals during the cross-over.

6.1.5 VISCAL System

6.1.5.1 VISCAL illumination

The VISCAL system is illuminated by the Sun once per orbit. For the calibration signal to be used in L1 processing, it is important that the diffuser has a clear view of the full solar disk for at least 100 scans. If the illumination period is too short, then the IPF will not generate a VISCAL file. The number of scans where the VISCAL is fully illuminated is seasonally dependent and affected by the satellite attitude. So, it is important to keep track of the variation in the illumination period to make sure that it does not drop below the threshold needed for processing.

Figure 104 shows the variation of the number of clear scans covered by the VISCAL peak during the last two years of operation for SLSTR-A and SLSTR-B in nadir and oblique views. The number of scans in the SLSTR-A VISCAL peak decreases from ~180 scans in January, to a minimum of ~125 scans in June. The number of scans in the SLSTR-B VISCAL peak decreases from ~160 scans in January, to a minimum of ~125 scans in June. This variation is well correlated with the satellite beta angle, which is defined as the angle between the satellite orbital plane and the sun vector, and determines how much time the satellite is in direct illumination by the sun.

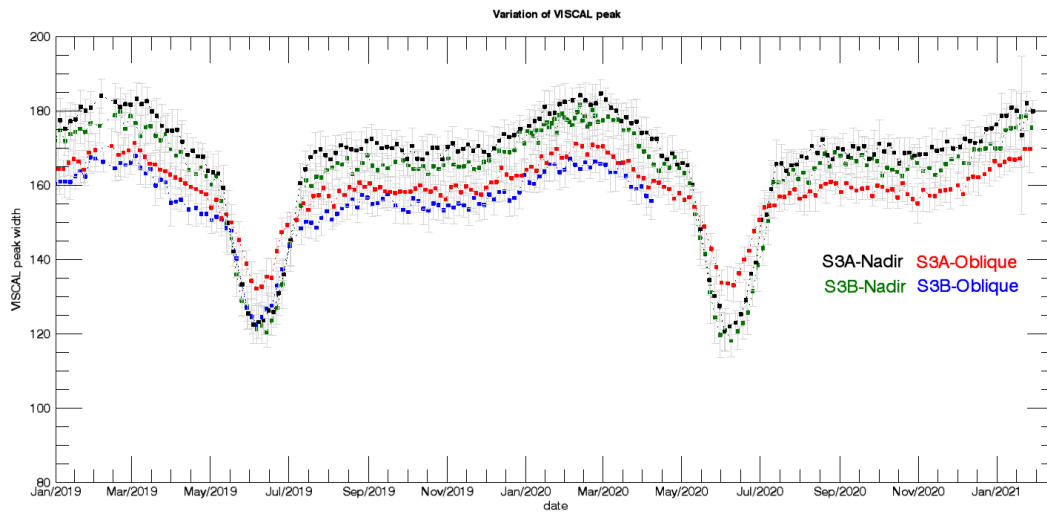


Figure 104: Variation of the SLSTR-A and SLSTR-B VISCAL peak width during the last two years of operations for the nadir (black/green) and oblique (red/blue) views.

6.1.6 IR Channels

6.1.6.1 Dynamic Range and Digitisation

The TIR channels (S7-S9, F1 and F2) are all functioning with no reported loss of data or digital resolution. The IR gains show an increase as detector temperatures warm-up between decontamination cycles (Figure 105 and Figure 106, left). Comparisons between nadir and oblique views show that the radiometric gains are consistent (Figure 107), within 1-2%.

The IR offsets show small variations due to detector and optics temperature variations (Figure 105 and Figure 106, right). These offset variations determine the minimum BTs detectable for channels S8 and S9, which also change with time. Note that each detector and odd/even pixels have different offset values. The offsets for channels S8 and S9 changed sharply on 14th October 2020 for SLSTR-A and on 30th March 2020 for SLSTR-B due to the increase in cooler cold tip temperature. This increased the lower limit of the dynamic range for these channels. The normal lower limit is approximately 180-184K (the exact value drifts upwards slowly following each decontamination), but after the change, some detectors increased to approximately 195K. In order to mitigate the effect of the cold tip temperature increase, the commanded S8 and S9 detector offset voltages were updated on the satellite for SLSTR-A on 26th January 2021 and for SLSTR-B on 5th August 2020. These updates returned the lower limit of the dynamic range to the expected level.

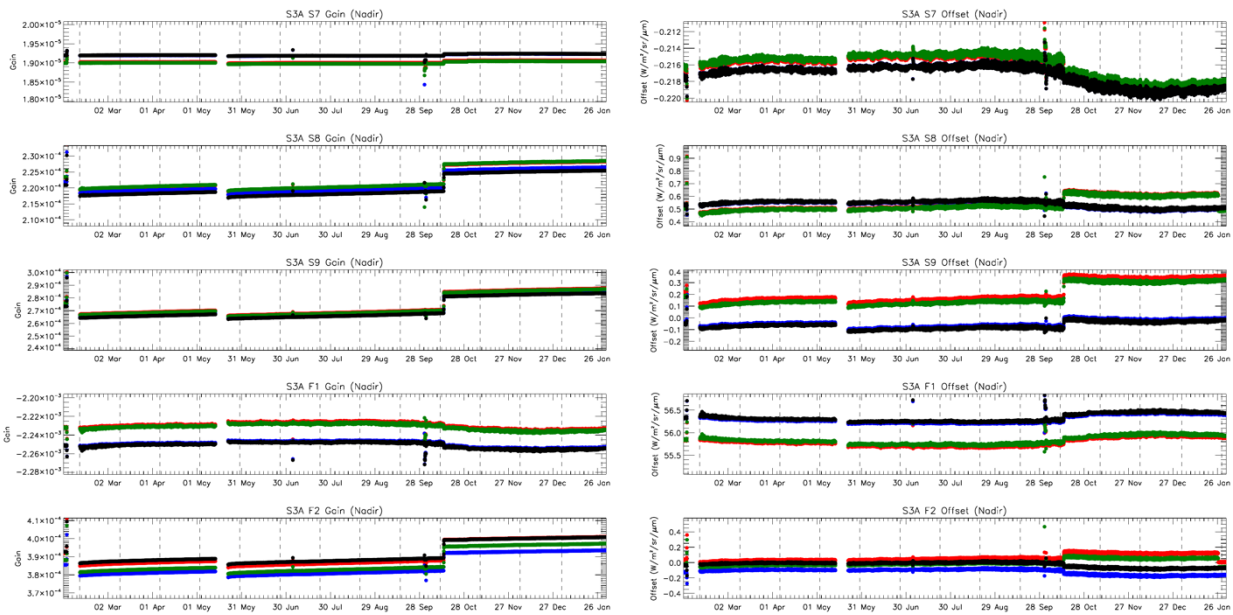


Figure 105: SLSTR-A gain (left) and offset (right) trends for the TIR channels in nadir view. The different colour symbols show the response for each of the detector elements and integrators in the channels. The discontinuities are due to the decontamination (February and May 2020) and the cold tip temperature increase (October 2020).

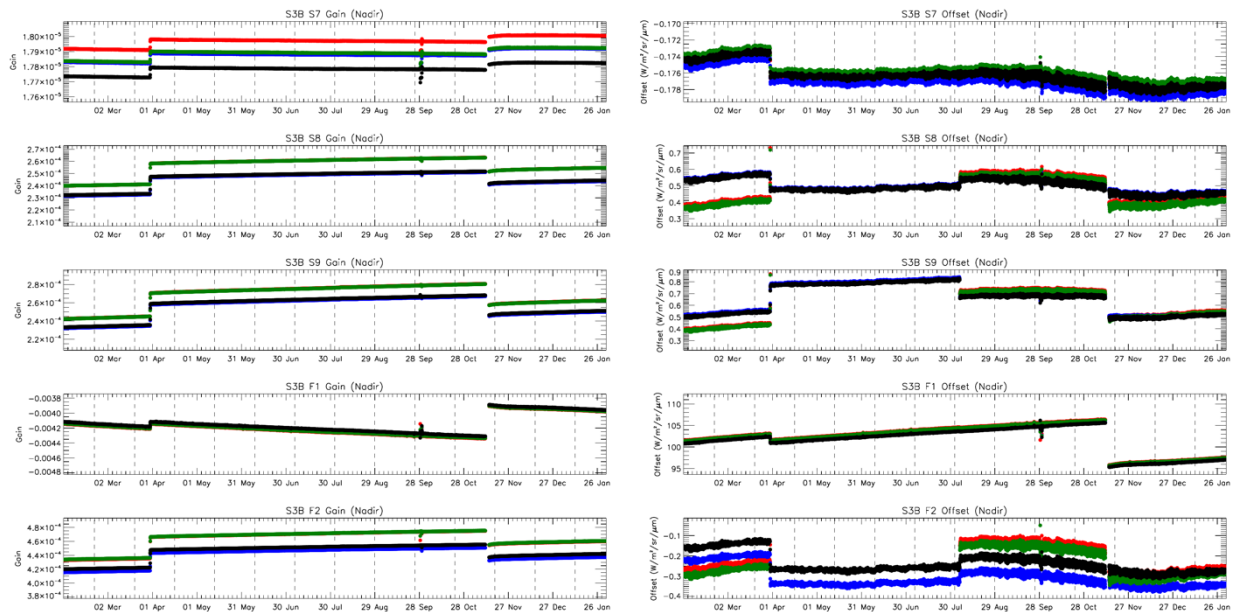


Figure 106: SLSTR-B gain (left) and offset (right) trends for the TIR channels in nadir view. The different colour symbols show the response for each of the detector elements and integrators in the channels. The discontinuities are due to the cold tip temperature increase (March 2020), the decontamination (November 2020), and in the offset plot only, for the update of dynamic range in August 2020.

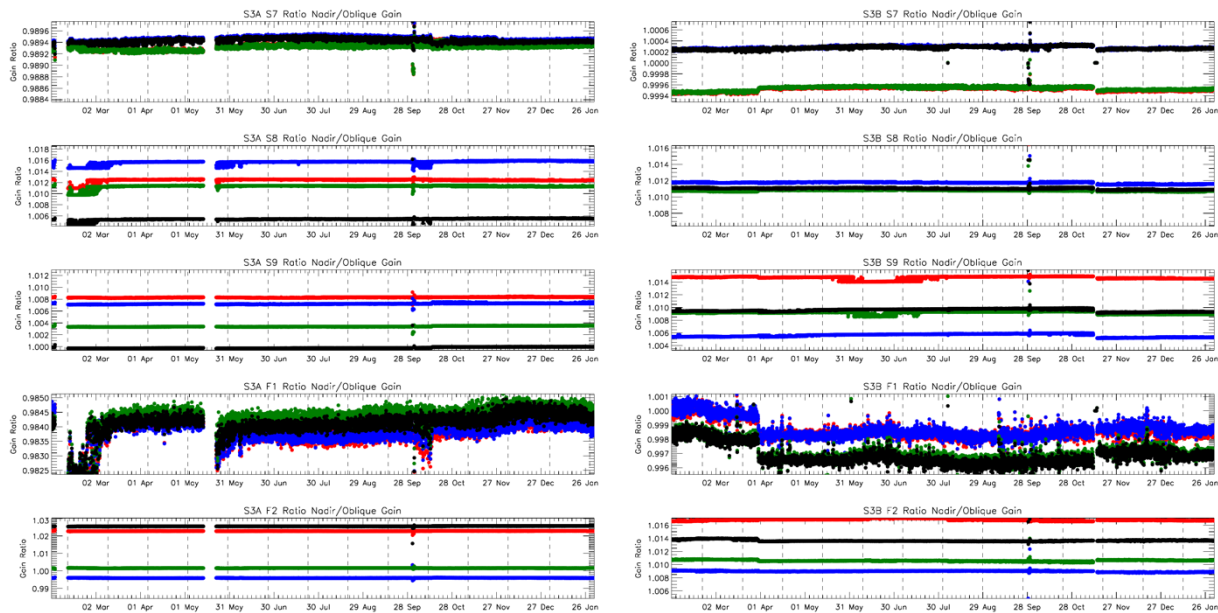


Figure 107: Ratio between nadir and oblique view gains for TIR channels for SLSTR-A (left) and SLSTR-B (right). The different colour symbols show each of the detector elements and integrators in the channels.

6.1.6.2 Radiometric Noise

The thermal channel NEDT values derived from the on-board blackbody sources are consistent with previous operations and within the requirements – see Figure 108 and Table 23 and Table 24. Noise levels haven't changed significantly following the decontaminations. The NEDT levels are roughly consistent between SLSTR-A and SLSTR-B, except for F1, which shows more orbit-to-orbit variation and higher noise values. This may be caused by motional chopping of the F1 detectors, which are known to be close to the edge of the aperture for SLSTR-B.

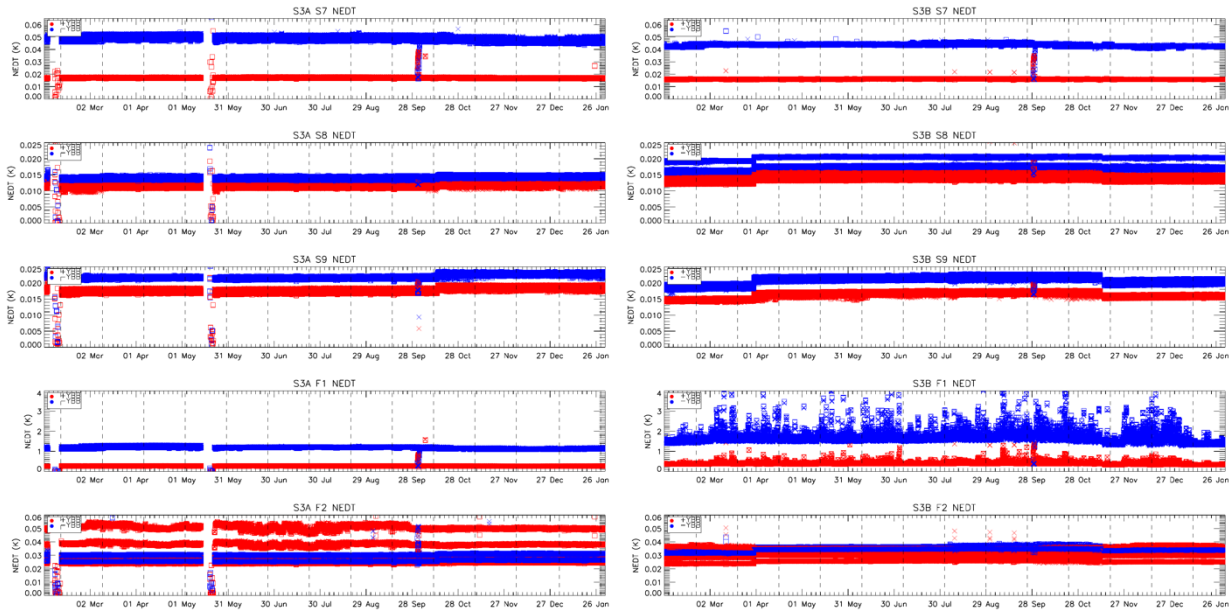


Figure 108: NEDT trend for the thermal channels for SLSTR-A (left) and SLSTR-B (right). Blue points were calculated from the cold blackbody signal and red points from the hot blackbody.

Table 23: NEDT for SLSTR-A in cycles 054-067 averaged over all detectors for both Earth views towards the hot +YBB (top) and the cold -YBB (bottom).

SLSTR-A	Cycle 054	Cycle 055	Cycle 056	Cycle 057	Cycle 058	Cycle 059	Cycle 060	Cycle 061	Cycle 062	Cycle 063	Cycle 064	Cycle 065	Cycle 066	Cycle 067
+YBB temp (K)	304.073	303.560	303.181	303.067	303.078	302.957	302.920	302.914	302.962	303.265	303.700	303.981	304.190	304.250
NEDT (mK)														
S7	16.8	17.2	17.1	17.2	17.2	17.3	17.4	17.4	17.3	17.9	17.2	16.9	16.9	16.9
S8	11.4	11.2	11.4	11.4	11.2	11.3	11.4	11.5	11.4	11.6	11.8	11.9	11.8	11.9
S9	17.8	17.4	17.5	17.6	17.3	17.5	17.5	17.6	17.6	17.8	18.5	18.6	18.6	18.6
F1	261	271	274	276	268	274	277	277	274	342	271	267	266	267
F2	34.9	35.8	36.0	35.3	35.3	35.3	35.0	35.1	36.0	35.1	35.2	35.4	35.5	35.4

SLSTR-A	Cycle 054	Cycle 055	Cycle 056	Cycle 057	Cycle 058	Cycle 059	Cycle 060	Cycle 061	Cycle 062	Cycle 063	Cycle 064	Cycle 065	Cycle 066	Cycle 067
-YBB temp (K)	266.707	266.088	265.669	265.675	265.797	265.645	265.545	265.438	265.401	265.731	266.335	266.751	266.930	266.930
NEDT (mK)														
S7	48.4	48.8	49.9	50.0	50.4	49.5	49.4	49.5	49.6	48.0	48.7	47.6	47.0	47.1
S8	14.1	14.0	14.1	14.1	14.1	14.1	14.1	14.1	14.1	14.2	14.6	14.7	14.5	14.6
S9	22.0	21.5	21.7	21.7	21.5	21.5	21.6	21.7	21.7	21.6	22.7	22.8	22.8	22.8
F1	1141	1176	1232	1231	1196	1197	1205	1204	1206	1173	1150	1128	1118	1128
F2	28.0	27.8	28.0	28.0	27.8	27.8	27.8	27.8	27.9	28.2	28.8	28.9	28.9	28.9

Table 24: NEDT for SLSTR-B in cycles 035-048 averaged over all detectors for both Earth views towards the hot +YBB (top) and the cold -YBB (bottom)

SLSTR-B	Cycle 035	Cycle 036	Cycle 037	Cycle 038	Cycle 039	Cycle 040	Cycle 041	Cycle 042	Cycle 043	Cycle 044	Cycle 045	Cycle 046	Cycle 047	Cycle 048	
+YBB temp (K)	303.991	303.566	303.220	303.115	303.145	302.971	302.930	302.882	303.045	303.435	303.951	304.224	304.339	304.187	
NEDT (mK)	S7	15.9	16.1	16.0	16.0	16.0	16.2	16.3	16.3	16.2	16.7	16.0	15.8	15.8	15.8
	S8	13.0	13.1	13.9	14.3	14.4	14.5	14.5	14.5	14.5	14.6	14.3	13.8	13.8	13.9
	S9	14.6	14.7	15.7	16.4	16.5	16.6	16.7	16.8	16.9	17.0	16.6	15.7	15.8	15.8
	F1	369	412	414	395	413	442	406	435	466	481	410	396	404	339
	F2	30.0	29.9	30.2	30.4	30.5	30.5	30.5	30.4	30.3	30.5	30.6	30.7	30.9	30.7

SLSTR-B	Cycle 035	Cycle 036	Cycle 037	Cycle 038	Cycle 039	Cycle 040	Cycle 041	Cycle 042	Cycle 043	Cycle 044	Cycle 045	Cycle 046	Cycle 047	Cycle 048	
-YBB temp (K)	266.112	265.579	265.263	265.293	265.443	265.224	265.105	264.952	265.097	265.506	266.184	266.547	266.643	266.385	
NEDT (mK)	S7	42.7	44.0	43.9	43.9	44.1	44.0	44.2	44.8	44.5	42.8	42.9	42.5	42.5	42.5
	S8	16.8	16.9	17.6	18.2	18.2	18.2	18.2	18.3	18.4	18.2	18.2	17.8	17.9	17.9
	S9	18.6	18.8	20.2	21.1	21.2	21.3	21.5	21.6	21.7	21.5	21.4	20.0	20.1	20.3
	F1	1520	1762	1774	1669	1756	1875	1687	1844	2002	1871	1696	1667	1717	1396
	F2	30.9	31.0	32.5	33.5	33.6	33.6	33.8	34.1	34.2	34.1	33.8	32.9	33.0	33.1

6.1.7 VIS/SWIR Channels

6.1.7.1 Radiometric gain variation SLSTR-A

Overall the S1-S6 channels are functioning well with no reported loss of data or digital resolution.

The main issue affecting the S1-S3 channels are oscillations in the radiometric response due to the build-up of ice on the optical path within the FPA. This is illustrated in Figure 109, which shows the variation of the radiometric gain derived from the VISCAL signals. These oscillations were observed for the corresponding channels on ATSR-2 and AATSR. Periodic decontamination of the IR FPA is necessary to remove the water ice contamination.

The trends of the radiometric gain variation clearly show where the decontamination took place, and that the signal was reset afterwards. During the decontamination, only the VIS channels are operating and the SWIR channels are switched off, causing a gap in the trends due to the loss of data.

The radiometric responses of S4-S6 appear to be more stable and not affected by the build-up of water ice contamination, Figure 110. There is a seasonal cycle of the response of $\pm 1\%$ that could be caused by variations in the solar zenith angle on the diffuser or partial vignetting of the Sun's disc by the VISCAL baffle.

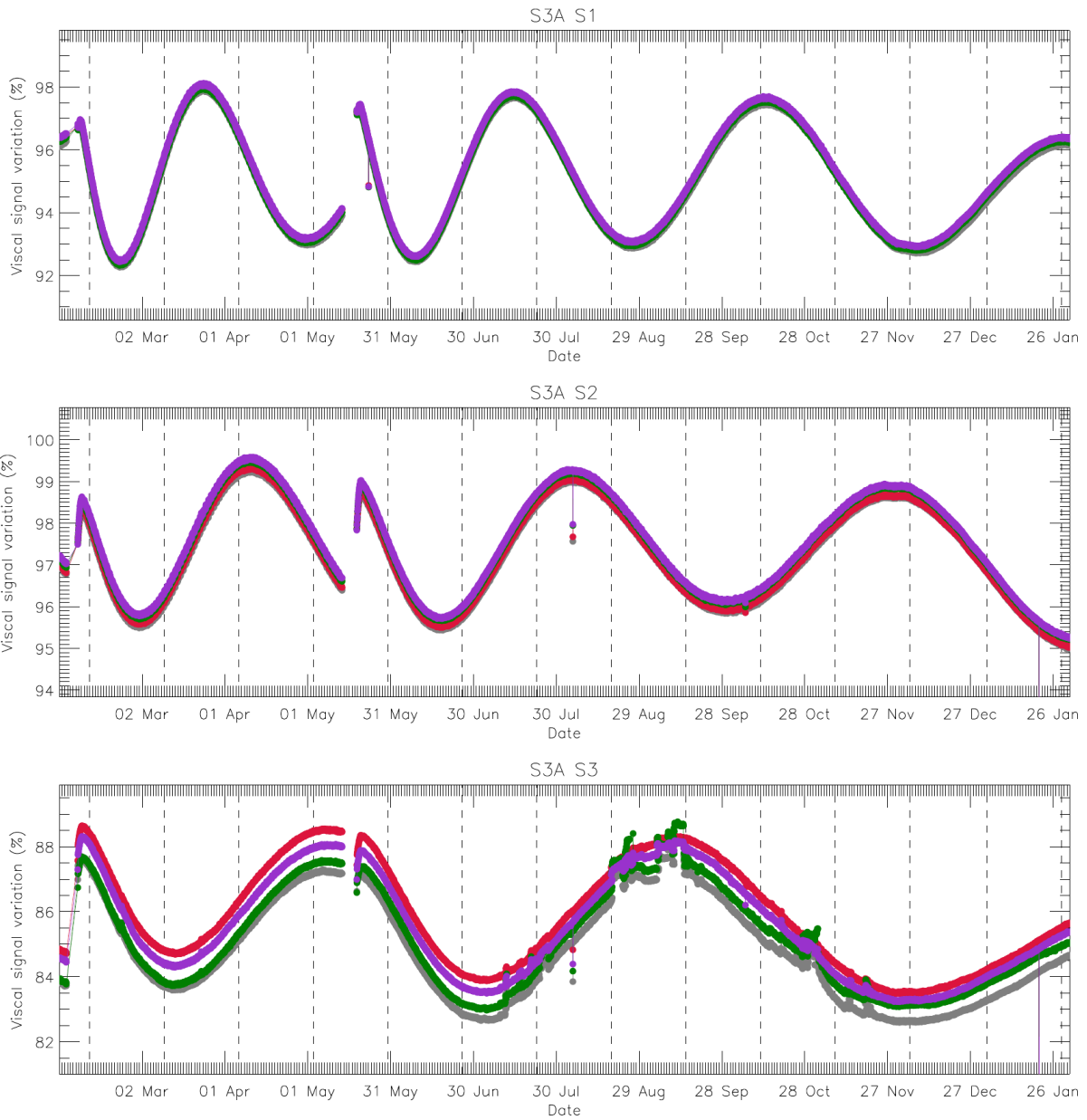


Figure 109: Gain trend for VIS channels (nadir view) for SLSTR-A. The data have been adjusted to allow for the variation of the solar intensity. The oscillations in the signal are due to the build-up of a thin condensation layer causing a thin film interference effect. The different colour symbols show the response for each of the 4 detector elements in the VIS channels.

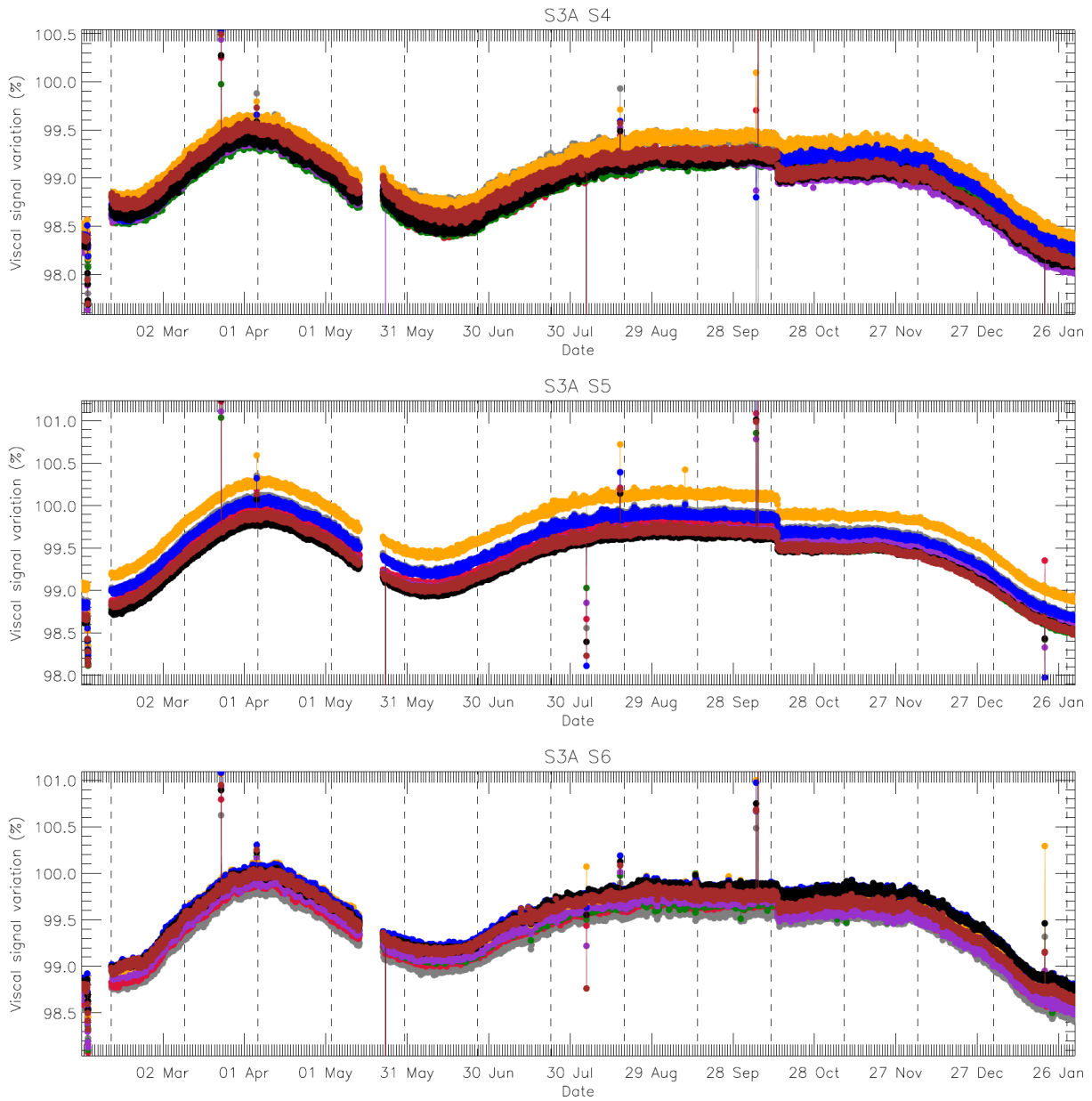


Figure 110: Gain trend for SWIR channels (nadir view) for SLSTR-A. Outliers in the plots are due to gaps in LO data or decontamination cycles. The different colour symbols show the response for each of the 8 detector elements of the A and B stripes of the SWIR channels.

6.1.7.2 Radiometric gain variation SLSTR-B

As in SLSTR-A, one of the main issues affecting the S1-S3 channels are oscillations in the radiometric response due to the build-up of ice on the optical path within the FPA. However, there is also a problem with S1 and S2 in particular, which show noisy behaviour and numerous drops in signal as shown in Figure 111. This gives 2-3% errors in the radiometric calibration of these channels. The effect has been the subject of a major NCR led by ESA-ESTEC. A number of candidate root causes have been identified, with the most likely due to motional chopping of the VIS detectors by an internal aperture in the VIS optical bench. Because the effect appears to be random it is most likely affecting all the data for S1 and S2.

The radiometric responses of S4-S6 appear to be more stable and not affected by the build-up of water ice contamination, Figure 112.

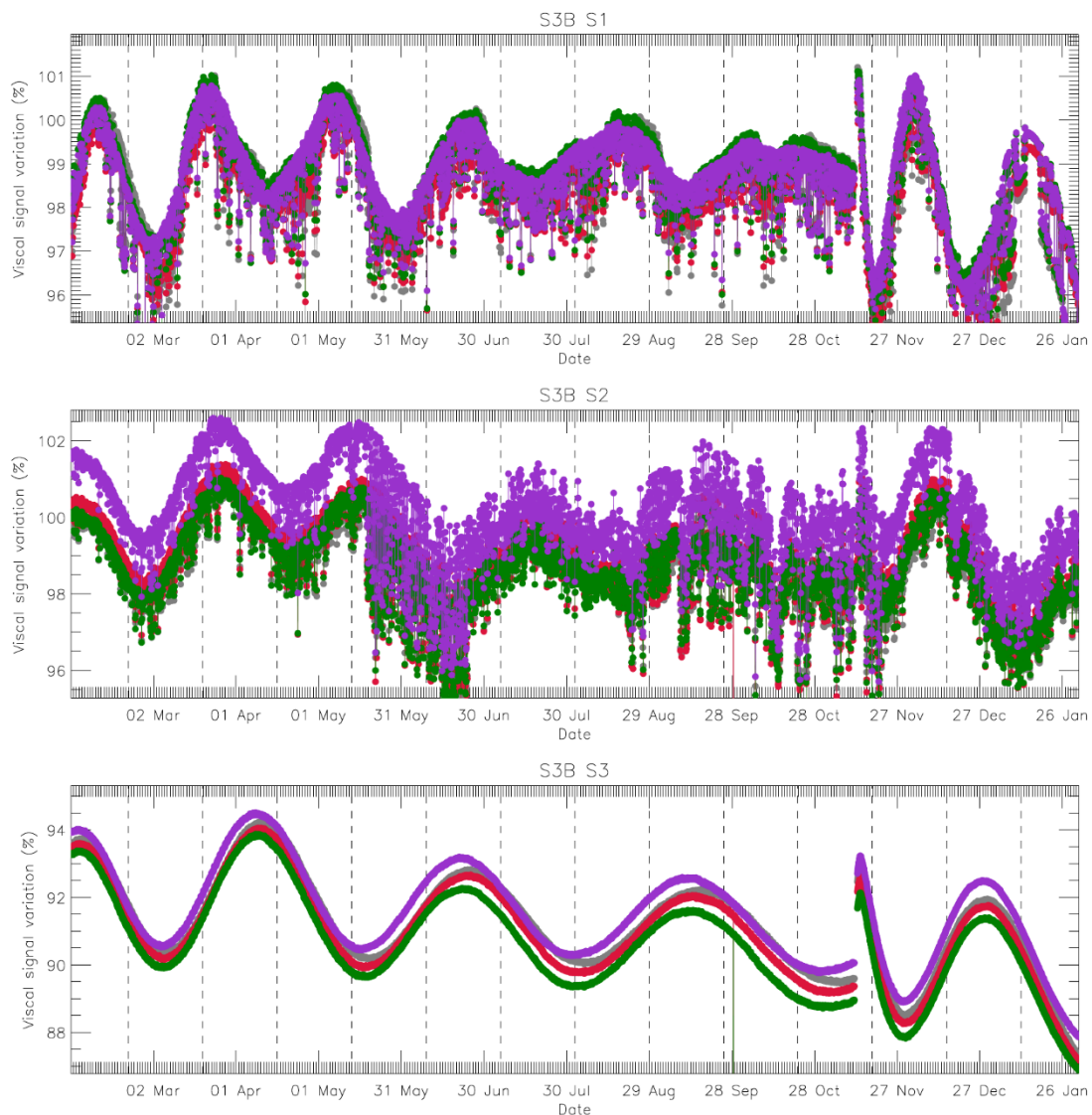


Figure 111: Gain trend for VIS channels (nadir view) for SLSTR-B. The data have been adjusted to allow for the variation of the solar intensity. The oscillations in the signal are due to the build-up of a thin condensation layer causing a thin film interference effect. The different colour symbols show the response for each of the 4 detector elements in the VIS channels.

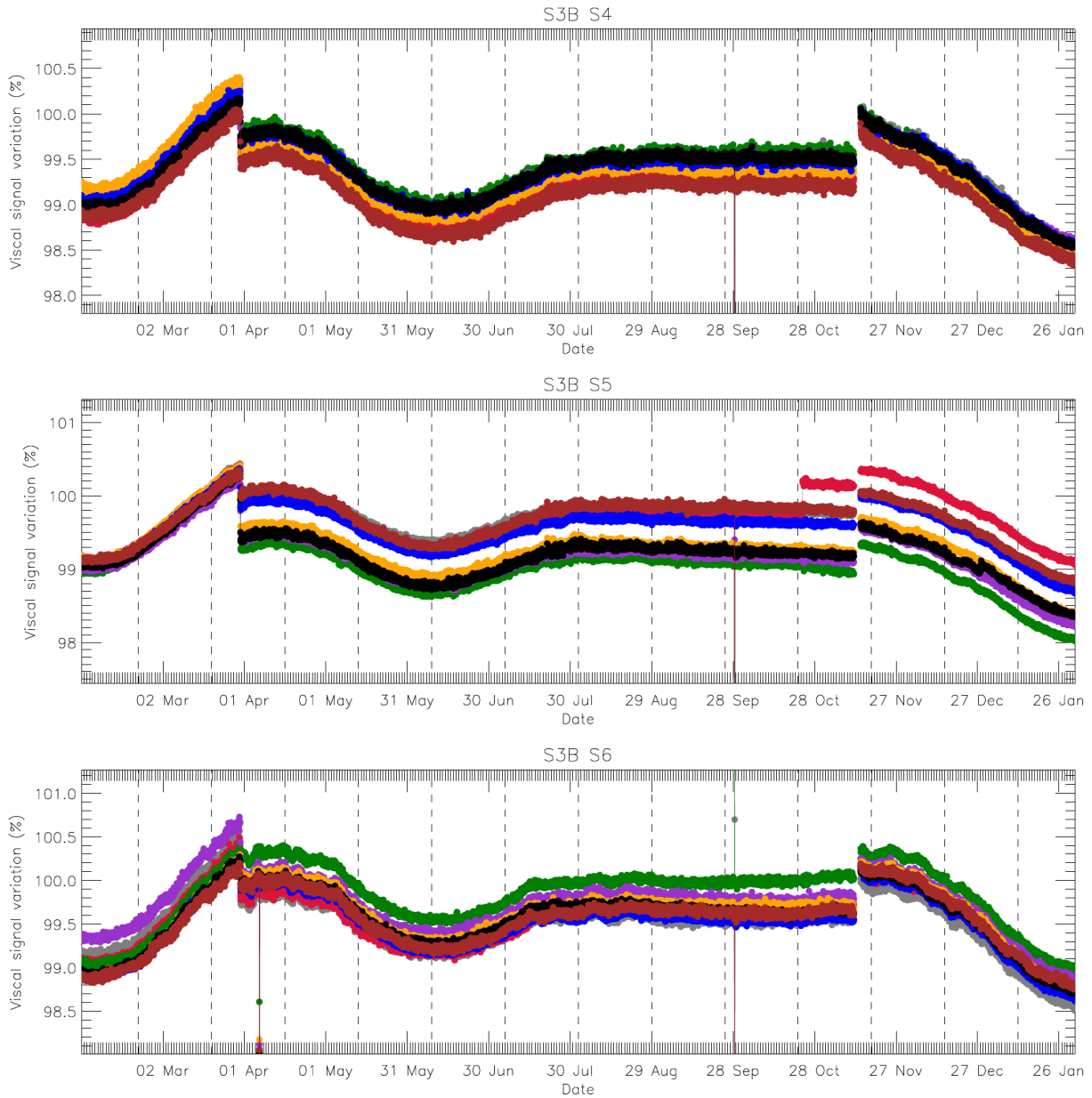


Figure 112: Gain trend for SWIR channels (nadir view) for SLSTR-B. Outliers in the plots are due to gaps in L0 data or decontamination cycles. The different colour symbols show the response for each of the 8 detector elements of the A and B stripes of the SWIR channels.

6.1.7.3 Dark signal variation SLSTR-A

The dark signal variation derived from the nadir blackbody signals for the VIS and SWIR channels is stable – see Figure 113 and Figure 114.

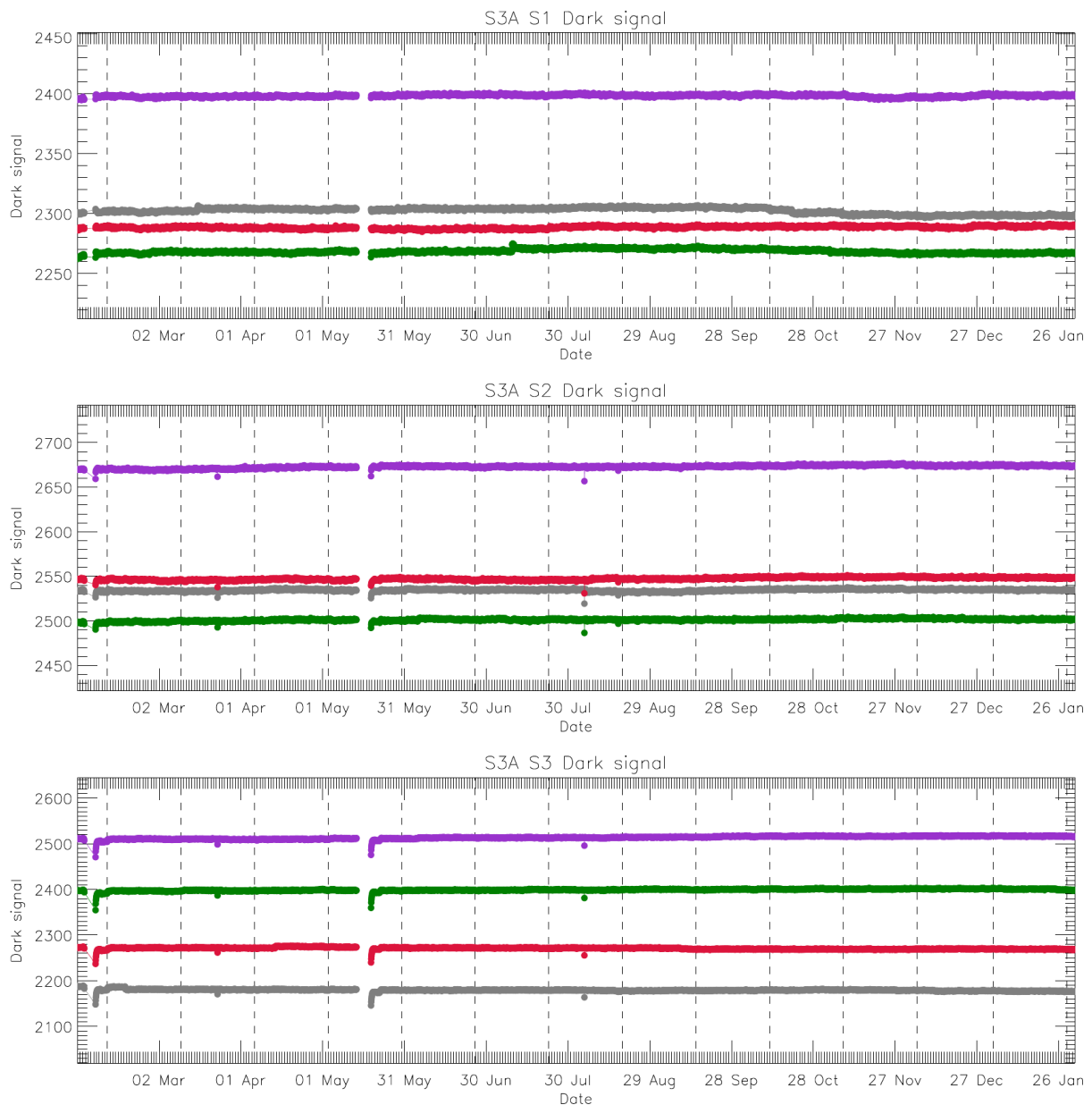


Figure 113: Dark signal trend for VIS channels (nadir view) for SLSTR-A. The different colour symbols show the signal for each of the 4 detector elements in the VIS channels. The gaps in February and May are due to the decontaminations.

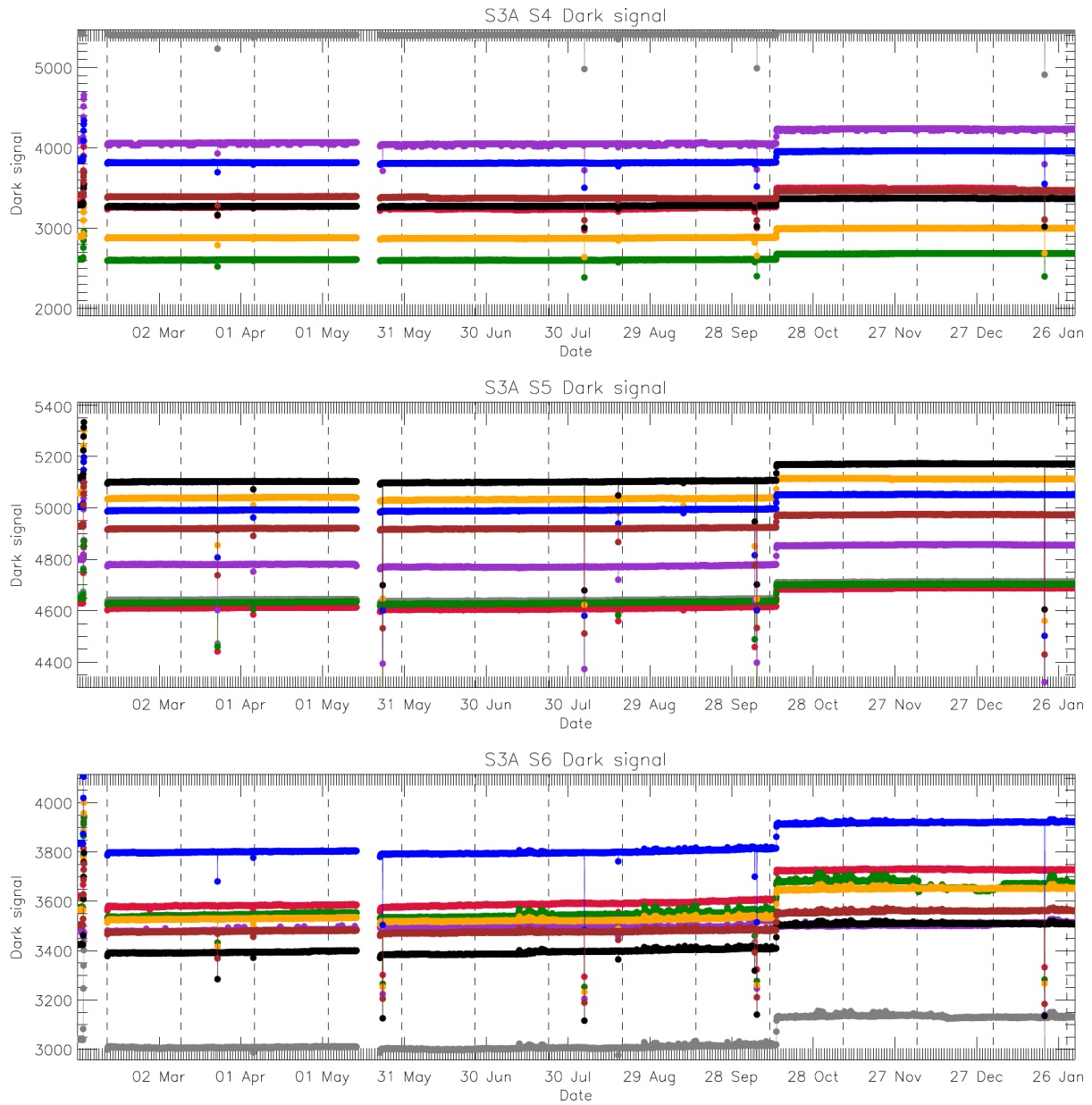


Figure 114: Dark signal trend for SWIR channels (nadir view) for SLSTR-A. The different colour symbols show the signal for each of the 8 detector elements of the A and B stripes of the SWIR channels. The gaps in February and May are due to decontaminations and the step in October is due to the cooler cold tip temperature increase.

6.1.7.4 Dark signal variation SLSTR-B

The dark signal variation derived from the nadir blackbody signals for the VIS and SWIR channels is stable for SLSTR-B (Figure 115).

The dark signal measured by the SWIR channels is stable and presents a gap at the end of September due to the loss of data during the decontamination (Figure 116).

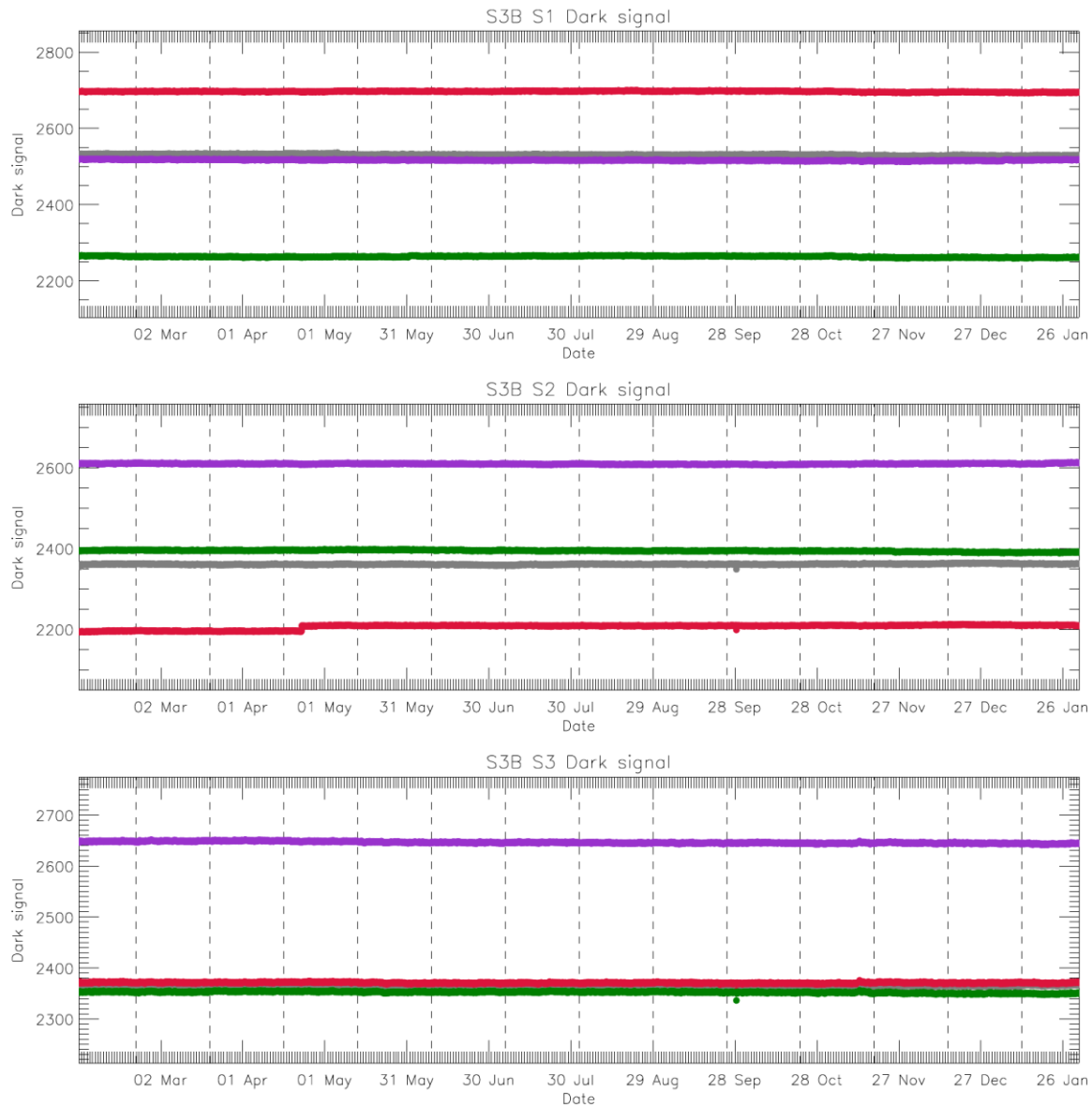


Figure 115: Dark signal trend for VIS channels (nadir view) for SLSTR-B. The different colour symbols show the signal for each of the 4 detector elements in the VIS channels.

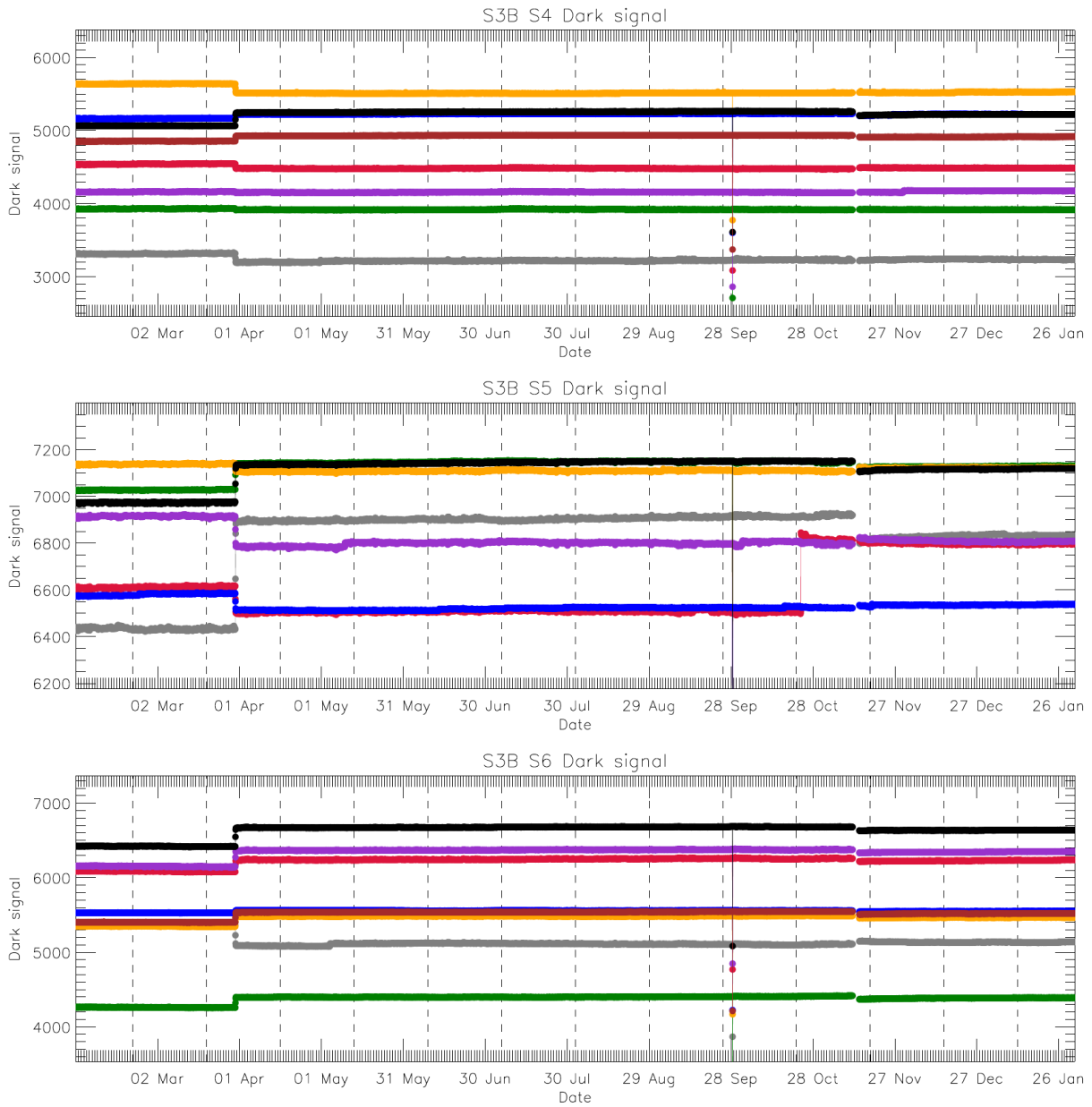


Figure 116: Dark signal trend for SWIR channels (nadir view) for SLSTR-B. The different colour symbols show the signal for each of the 8 detector elements in the SWIR channels. The step on 30th March is due to the cooler cold tip temperature increase and the discontinuity in November is due to the decontamination.

6.1.7.5 Radiometric noise for SLSTR-A

The VIS/SWIR channel signal-to-noise ratio is derived from the VISCAL signal at full solar illumination. The measurements show that the SNR is stable and consistent over the year and largely unaffected by anomalies and decontamination.

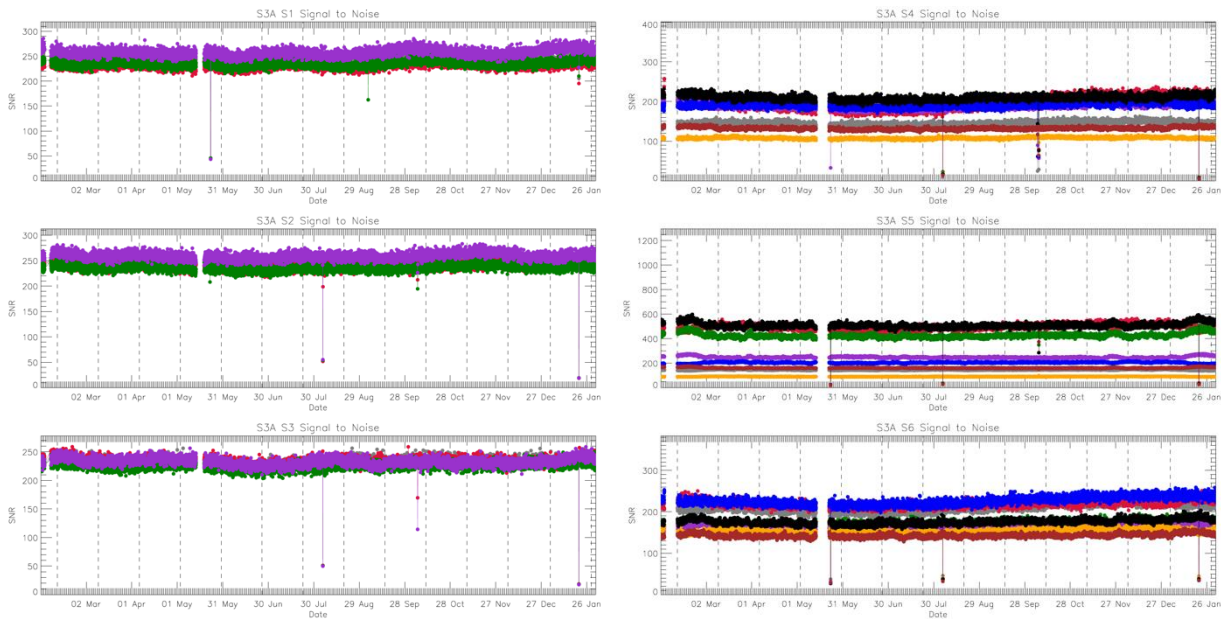


Figure 117: SLSTR-A VIS and SWIR channel signal-to-noise. Different colours indicate different detectors.

6.1.7.6 Radiometric noise for SLSTR-B

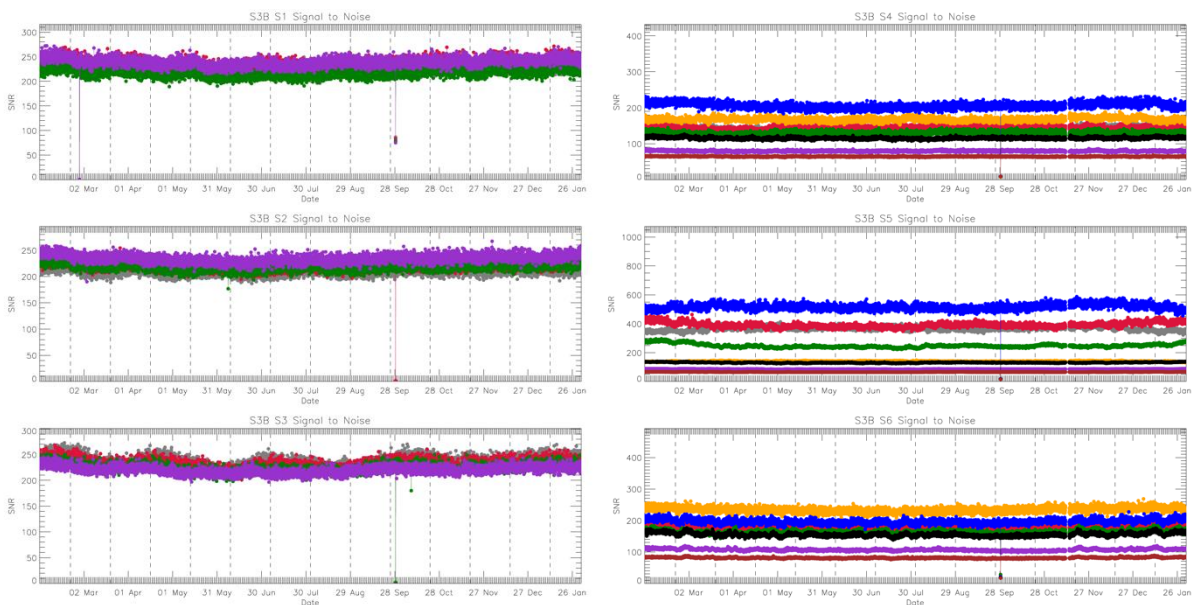


Figure 118: SLSTR-B VIS and SWIR channel signal-to-noise. Different colours indicate different detectors.

6.1.7.7 Contamination

The monitoring of the VISCAL signal shows that the performance of the VIS and the SWIR channels has been affected by the build-up of a condensation layer on the FPA. The build-up of condensation on the optics was expected since similar patterns were observed previously in AATSR and ATSR-2.

The periodic pattern observed in the VISCAL signals depends on the rate of build-up of the condensation layer and the wavelength of the channel. So, an estimation of the layer thickness can be obtained from the oscillations in the visible channels signal that occurred at $x = \lambda/2, \lambda, 3\lambda/2$, etc.

The growth of the ice layer is slow and decontamination activities are performed only once or twice per year. The rate of growth of the ice layer has reduced significantly with respect to that observed after the first cool down. It is expected that the rate of build-up will decrease with time resulting in longer periods between decontamination cycles.

Figure 119 shows the growth of the condensation layer on the SLSTR-A and SLSTR-B FPA.

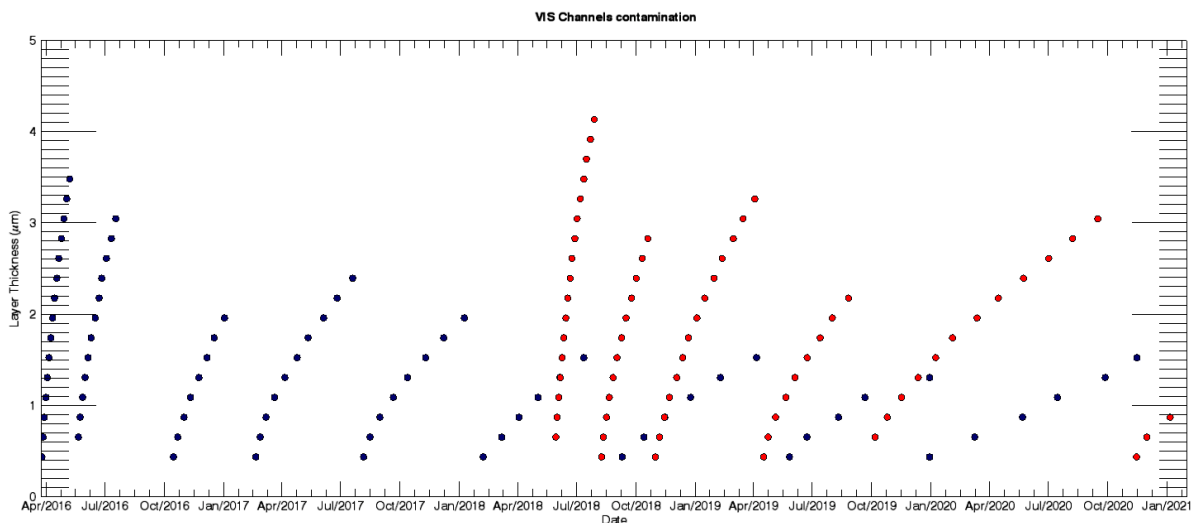


Figure 119 Condensation layer thickness throughout the mission for SLSTR-A (blue) and SLSTR-B (red)

6.2 L1 products performances

6.2.1 TIR Channel Calibration

6.2.1.1 SLSTR comparisons with IASI

The absolute radiometric calibration of the IR channels is being validated by EUMETSAT using comparisons against IASI-A and B (Tomazic et al 2018). Comparisons were performed during the commissioning phases for SLSTR-A and SLSTR-B. Currently there are no updates since 2018. The mission requirement is that the absolute radiometric calibration should be accurate to 0.2 K traceable to ITS-90, and that at a minimum this should be met in the temperature range between the two blackbodies.

The latest results have not changed since the previous annual report – i.e. from Tomazic et al (2018). These results confirmed very good performance with almost no bias (<0.1 K) for channels S8 and S9 in the nadir view over the temperature range 220 – 280 K.

6.2.2 VIS/SWIR Channel Calibration

Vicarious calibration methods are used to verify the radiometric calibration of the SLSTR visible (VIS) and shortwave infrared (SWIR) channels, and currently two methods are used.

1. Inter-comparisons of SLSTR with similar sensors such as OLCI, AATSR and MODIS using stable desert targets.
2. Compare SLSTR observed radiances over scenes containing sun-glint against the predicted top-of-atmosphere radiances computed radiative transfer models.

Both approaches provide consistent results. Table 25 and Table 26 show the relative differences obtained with the different calibration methods.

For analysis over desert sites we have used the extractions provided by the S3ETRAC tool, which contain the sensor reflectance values, cloud fraction, geometric and meteorological information needed for the analysis. For analysis over sun-glint regions we have used L1 products directly rather than the S3ETRAC analysis as the latter only contains a single value, and the analysis requires the full image context to model the sunglint.

6.2.2.1 Inter-comparisons of SLSTR over desert sites

The analysis performed follows the methodology used for the comparisons of AATSR with MERIS and MODIS-A (see Smith and Cox 2013). The analysis needs to take into consideration a number of effects:

- ❖ Temporal differences: in particular, direct comparisons of SLSTR with AATSR or MERIS are not possible because the latter are no longer operating. Also, sensors such as MODIS-A do not observe the site at the same time. So, to perform the comparisons we compare for the same view/solar geometry assuming that the site is stable over long timescales.

- ❖ Spectral differences: although SLSTR and OLCI have common spectral bands, the spectral responses are not exactly the same, which can give rise to differences in spectral reflectance of a few percent if not accounted for. Hence, we need to account for differences in atmospheric transmission and surface spectral reflectance.
- ❖ Geometric differences: although the method attempts to perform the comparisons with the same view/solar geometry, an exact match is not always possible. To account for this, we construct a basic geometric model from the reference sensor to interpolate to the correct geometry.

The data are extracted by S3ETRAC tool over a series of pre-defined sites. These sites have been selected for their appropriate optical properties to validate the radiometry of optical sensors. Table 25 shows the desert sites and their geographical limits used for the assessment and monitoring of the VIS and SWIR radiometric calibration.

Table 25: The list of these sites and their geographical limits

Site	North Latitude	South Latitude	East Longitude	West Longitude
CEOS_ALGERIA-3	30.82	29.82	8.16	7.16
CEOS_ALGERIA-5	31.52	30.52	2.73	1.73
CEOS_LIBYA-1	24.92	23.92	13.85	12.85
CEOS_LIBYA-4	29.05	28.05	23.89	22.89
CEOS_MAURITANIA-1	19.9	18.9	-8.8	-9.8
CEOS_MAURITANIA-2	21.35	20.35	-8.28	-9.28
RAL_Algeria-1	24.3	23.3	0.1	-0.9
RAL_Algeria-2	26.59	25.59	-0.88	-1.88
RAL_Algeria-4	30.54	29.54	6.09	5.09
RAL_Arabia-1	19.38	18.38	47.26	46.26
RAL_Arabia-2	20.63	19.63	51.46	50.46
RAL_Arabia-3	29.42	28.42	44.23	43.23
RAL_Sundan-1	22.24	21.24	28.72	27.72
RAL_Niger-1	20.17	19.17	10.31	9.31
RAL_Niger-2	21.87	20.87	11.09	10.09
RAL_Niger-3	22.07	21.07	8.46	7.46
RAL_Egypt-1	27.62	26.62	26.6	25.6
RAL_Libya-2	25.55	24.55	20.98	19.98
RAL_Libya-3	23.65	22.65	23.6	22.6

Site	North Latitude	South Latitude	East Longitude	West Longitude
RAL_Mali-1	19.62	18.62	-4.35	-5.35

6.2.2.1.1 Results of inter-comparisons of SLSTR-A over desert sites

Figure 120 shows the combined results for all the desert sites when SLSTR-A is compared with AATSR in nadir view, for the VIS and S5 channels.

Figure 121 shows comparisons between SLSTR-A and OLCI visible channels, and Figure 122 shows inter-comparisons between SLSTR-A and MODIS for the VIS and the SWIR channels.

Overall the calibration of SLSTR-A is very stable over the mission lifetime. However, there does appear to be a small drift of ~1% in channel S3.

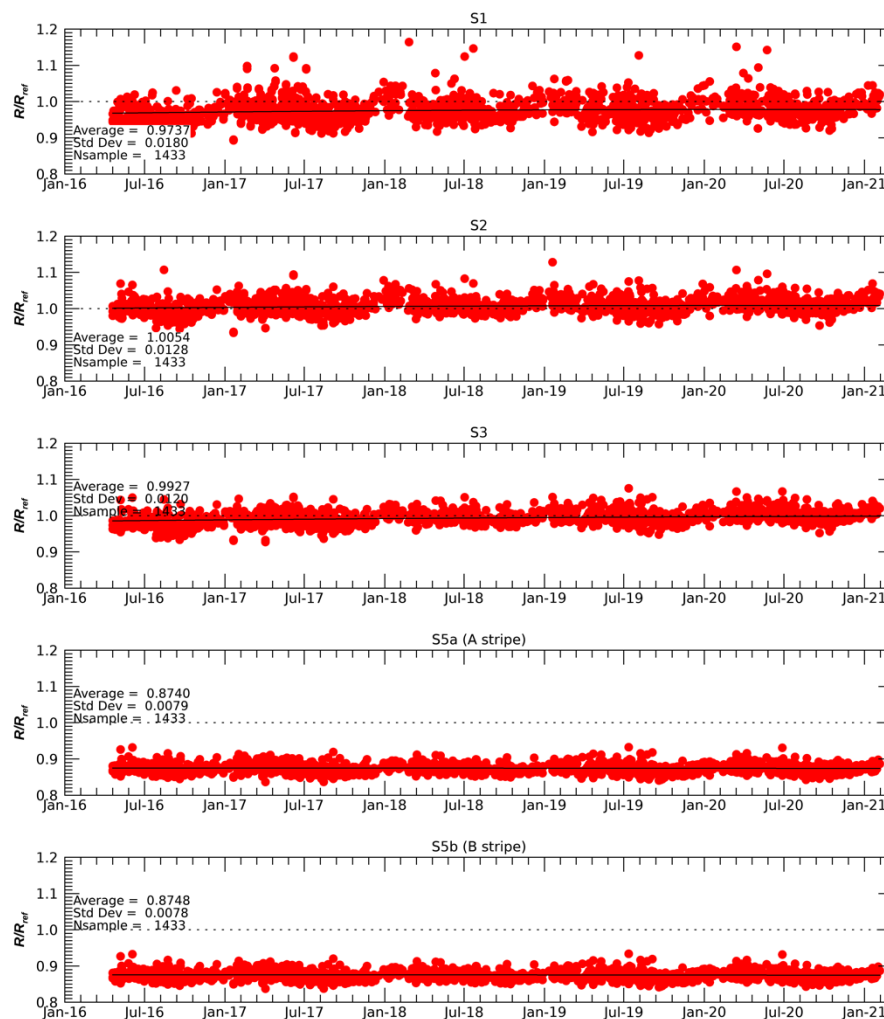


Figure 120: Comparisons of SLSTR-A S1-S3 and S5a and S5b channels vs. the corresponding channels for AATSR over desert sites.

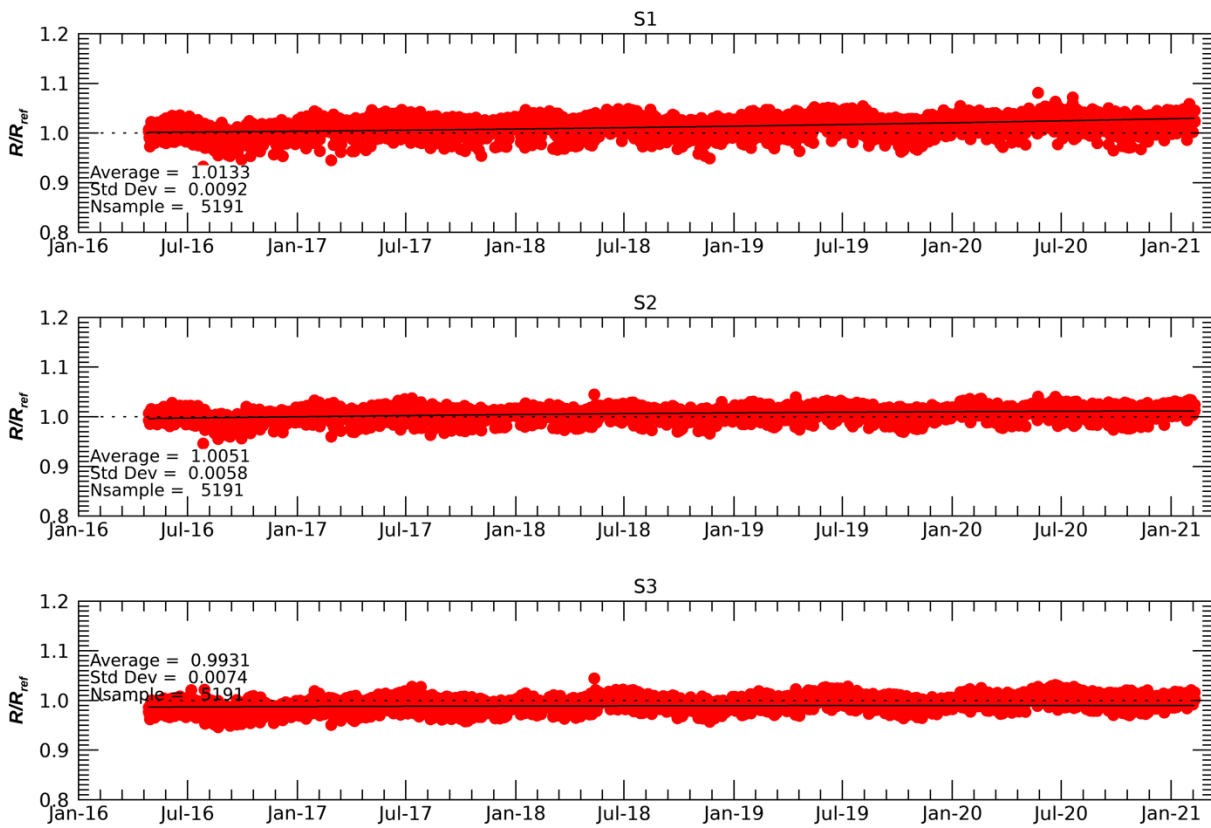


Figure 121: Inter-comparisons between SLSTR-A and OLCI VIS channels for all desert sites in nadir view.

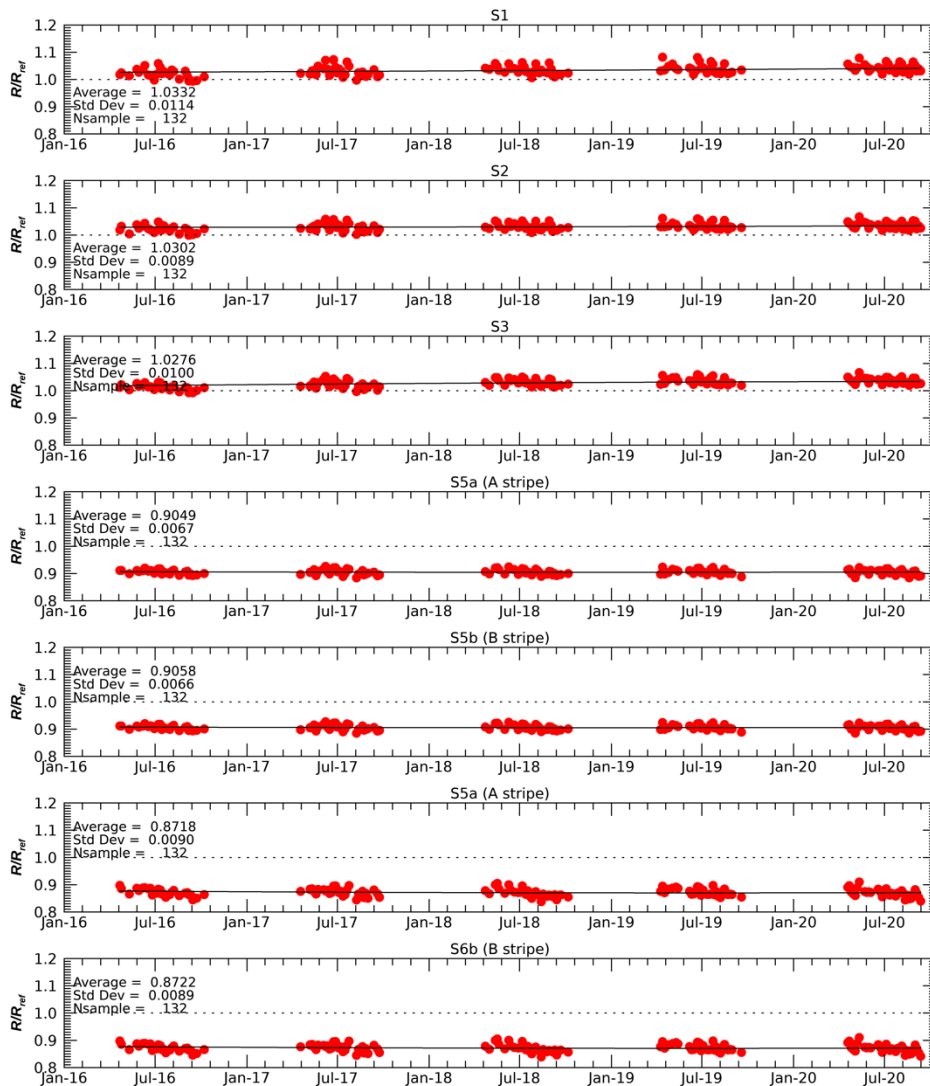


Figure 122: Inter-comparisons between SLSTR-A and MODIS NIR and SWIR channels in nadir view.

While comparisons between SLSTR-A and OLCI show a good agreement for the visible channels with differences of less than 1%, the measured radiances by the SWIR channels are ~12% lower than those observed by MODIS and AATSR over deserts, respectively. A summary of the results is presented in Table 26.

Currently, the inter-comparisons between SLSTR-A and other sensors can only be performed in nadir view, since the SLSTR-A and the other sensors' oblique viewing geometry is not equivalent. Radiative transfer models over sun-glints can be used in order to analyse the SLSTR radiometric calibration in oblique view.

6.2.2.1.2 Results of Inter-comparisons of SLSTR-B over desert sites

Figure 123 shows the combined results for all the desert sites when SLSTR-B is compared with AATSR in nadir view, for the VIS and S5 channels. Figure 124 shows comparisons between SLSTR-B and OLCI visible channels, and Figure 125 shows inter-comparisons between SLSTR-B and MODIS for the VIS and the SWIR channels.

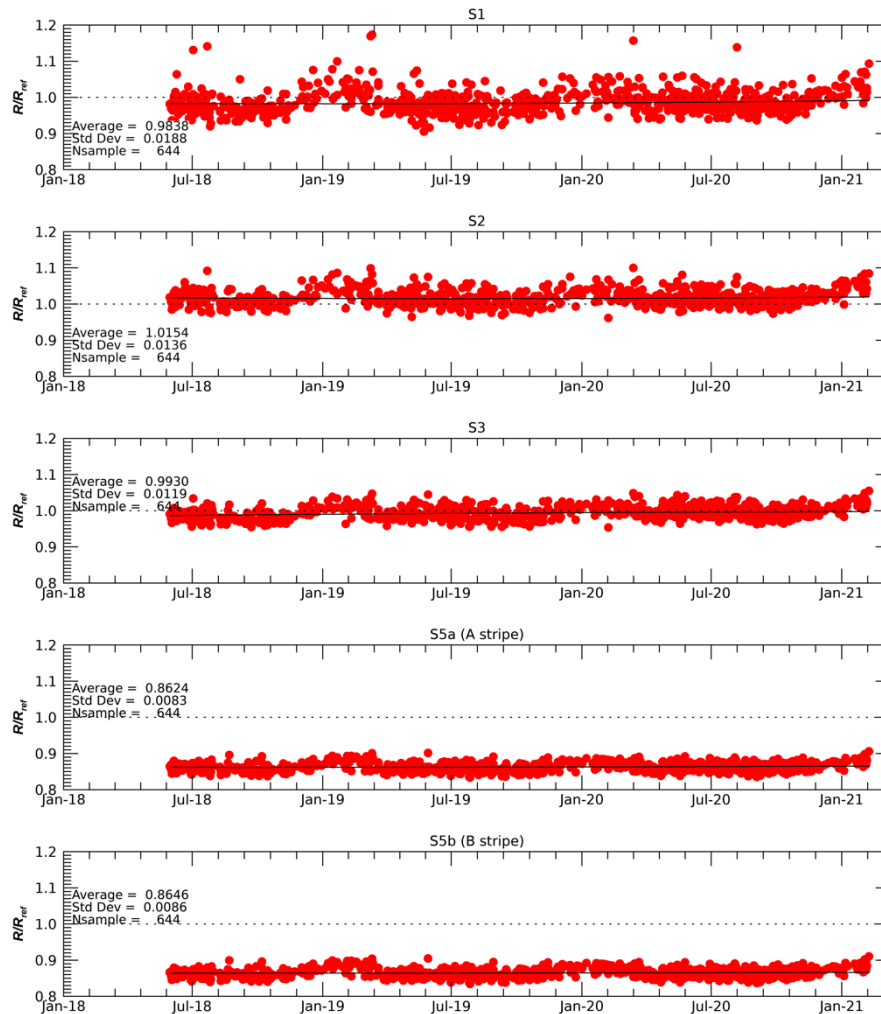


Figure 123: Comparisons of SLSTR-B S1-S3 and S5a and S5b channels vs. the corresponding channels for AATSR over desert sites.

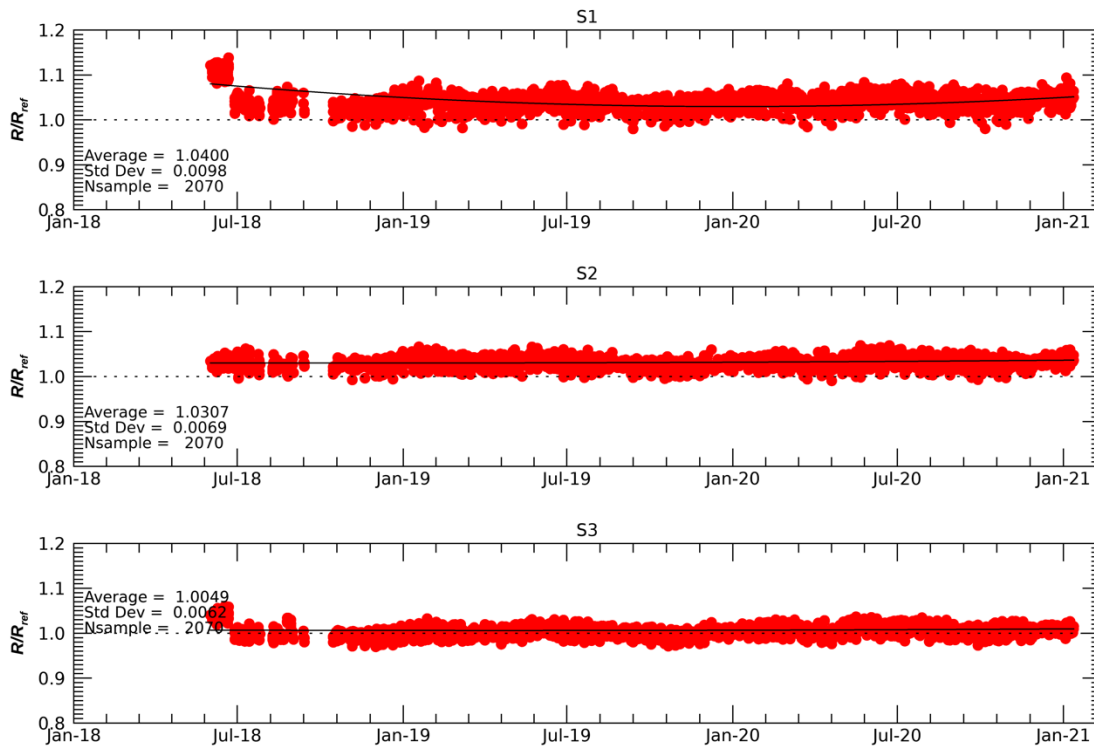


Figure 124: Inter-comparisons between SLSTR-B and OLCI VIS channels for all desert sites in nadir view.

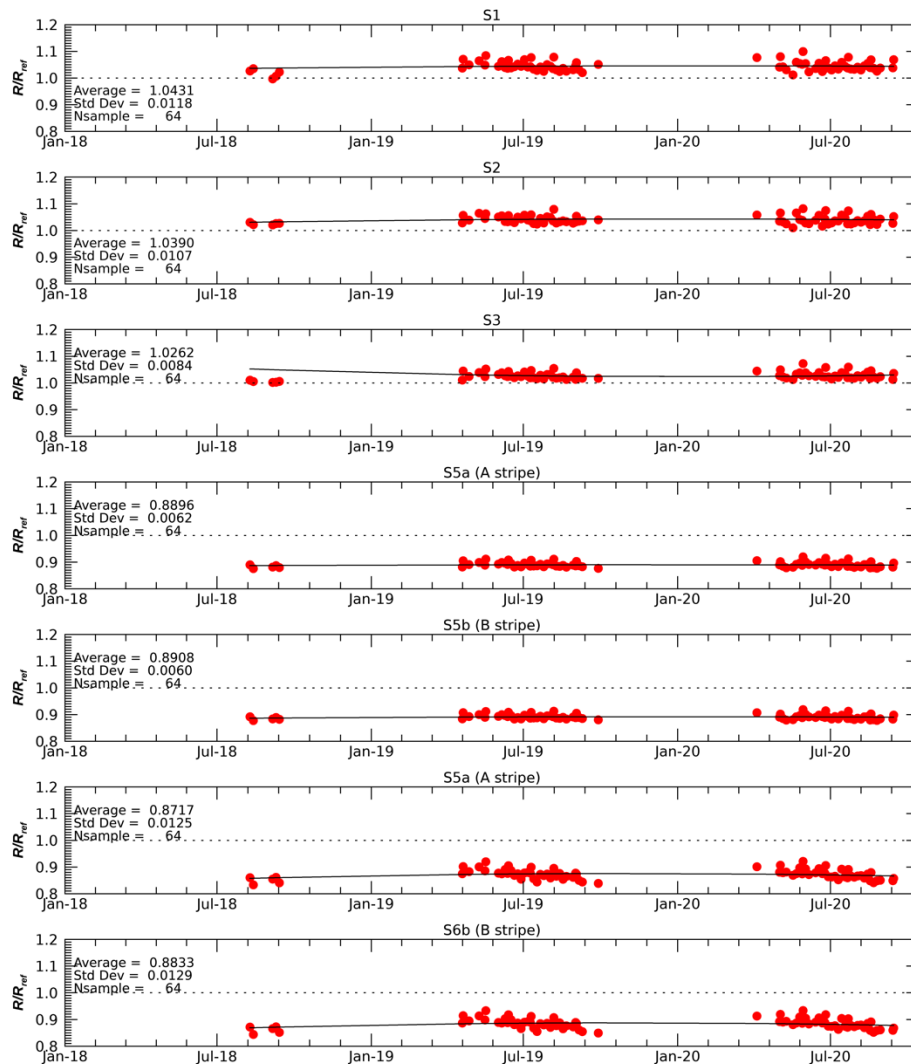


Figure 125: Inter-comparisons between SLSTR-B and MODIS VIS and SWIR channels in nadir view.

Comparisons between SLSTR-B and AATSR show a good agreement for the visible channels with differences of less than 1%. However, comparisons between SLSTR-B and OLCI-B show that the measured radiances by the channels S1 and S2 are ~3.5% larger than those measured by OLCI-B.

For the SWIR channels, the measured radiances are ~12% and ~12% lower than those observed by MODIS and AATSR over deserts, respectively, showing good agreement between SLSTR-A and SLSTR-B at the SWIR channels. A summary of the results is presented in Table 27.

6.2.2.2 Inter-band calibration with radiative transfer models

The sun glint calibration method is an inter-band calibration procedure that uses the specular reflection of the sun on the ocean surface to transfer the absolute calibration of one reference spectral band to other spectral bands, from visible to shortwave infrared wavelengths.

The radiative transfer code was developed based on the Oxford-RAL Aerosols and Clouds (ORAC) retrieval algorithm and on the approach of Cox and Munk (1954). The model accounts for contributions to the observed reflectance from whitecaps, sun-glint and under-light over the Pacific Ocean. Level-1 products contain all the inputs needed for the modelling, except the aerosol optical depth, which are taken from AERONET observations.

This calibration method is a relative calibration of the SWIR channels with respect to the VIS channels. Therefore, only the SWIR channels models are shown in Figure 126 and Figure 127.

The relative difference of the measured radiances from the model for SLSTR-A is -9% and -15% for S5 and S6 in nadir view. The results are similar to the relative differences measured by MODIS and AATSR over deserts. For SLSTR-B is -9% and -20% for S5 and S6 in nadir view

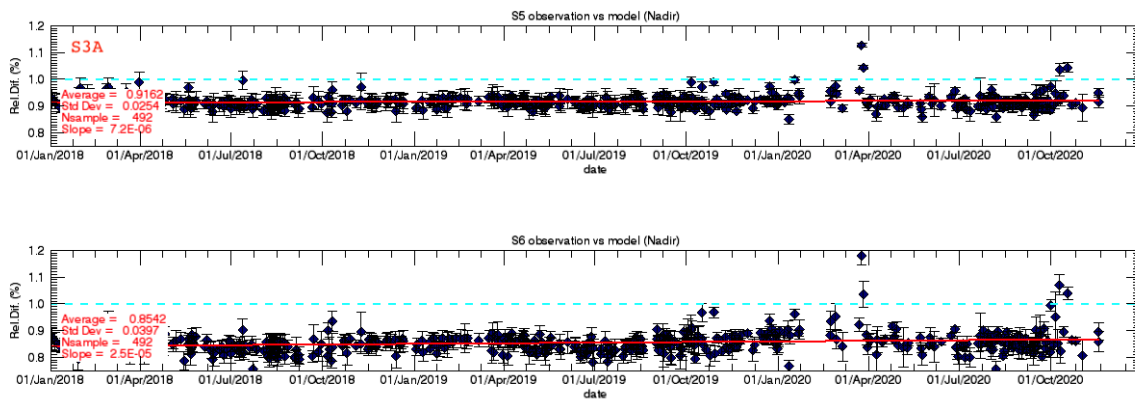


Figure 126: SLSTR-A measured radiance with respect to the computed radiance over sun-glints using radiative transfer models for the Nadir view.

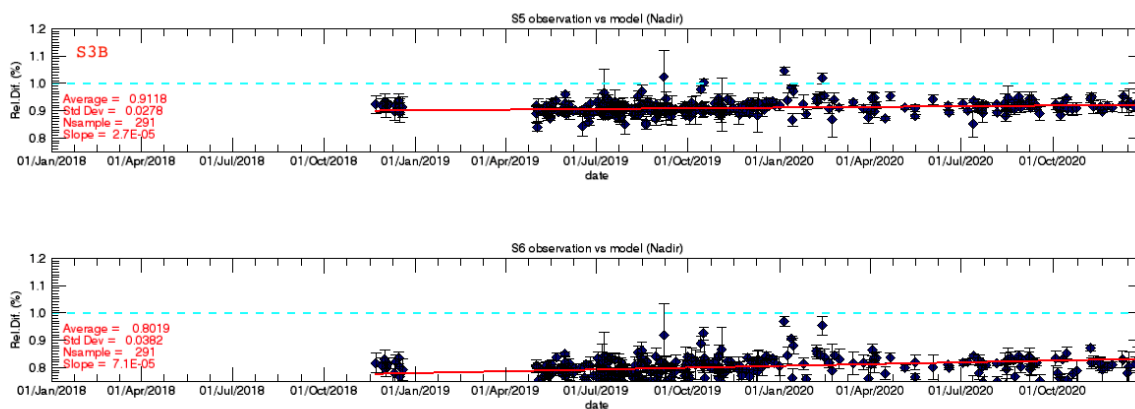


Figure 127: SLSTR-B measured radiance with respect to the computed radiance over sun-glints using radiative transfer models for the Nadir view.

6.2.2.3 Combined Results

The goal of the vicarious calibration analyses is to determine the offsets of SLSTR to a common reference that can be traced to a primary standard, and to implement these in the IPF.

In addition to the analysis performed by the MPC, independent studies by different groups have also been conducted to assess the post launch calibration of these channels. We have compared the results the analyses performed by RAL Space using comparisons with AATSR and MODIS-A over desert sites, CNES using the SADE/MUSCLE vicarious calibration system over desert sites, Rayference using a Radiative Transfer Model of the Libya-4 site, and the University of Arizona’s comparisons against in-situ field measurements of the Railroad Valley Playa RadCalNet site.

The comparisons performed by RAL and CNES have been made against other satellite sensors where there are known differences that need to be accounted for. For example, previous analyses of AATSR found systematic offsets compared to MERIS of approximately 1.03 for channels S1-S3. So, for instance, where AATSR is used as the reference for SLSTR channels S1-S3, the results are adjusted to MERIS by applying the corresponding difference reported in the literature. The analysis performed by Rayference and University of Arizona are independent of any satellite measurements and so no adjustment is needed.

For the reported uncertainties we attempt to combine the information provided using the Guide to expression of Uncertainties in Measurement (GUM). Uncertainties in the calibration factors are based on those reported by the different teams and are the best estimate at the time of writing.

Results presented in Table 26 and Figure 128 show good agreement within the reported uncertainties. We do not attempt to state which method is closest to the true value since all methods are relative to a different reference.

Table 26: Summary of Vicarious Radiometric Calibration Results performed by all groups. Comparisons are performed by comparing the measured reflectance vs. reference reflectance. Results presented here are the ratios R_{meas}/R_{ref} .

Nadir View

Method	S1		S2		S3		S5		S6	
	Rmeas/Rref	Uncert								
MPC (RAL)	-	-	1.02	0.04	1.02	0.04	0.89	0.04	0.88	0.03
CNES	1.02	0.05	1.02	0.05	1.01	0.04	0.89	0.03	0.89	0.04
RTM (Rayference)	1.05	0.03	1.03	0.03	1.02	0.03	0.90	0.03	0.90	0.03
RailRoad Valley	1.02	0.04	1.02	0.04	1.02	0.04	0.92	0.04	0.88	0.04
Median	1.02		1.02		1.02		0.90		0.89	
Average	1.03	0.03	1.02	0.02	1.02	0.02	0.90	0.02	0.89	0.02
Weighted Average	1.03	0.03	1.02	0.02	1.02	0.02	0.90	0.02	0.89	0.02

Oblique View

Method	S1		S2		S3		S5		S6	
	Rmeas/Rref	Uncert								
MPC (RAL)	-	-	1.04	0.04	1.06	0.04	0.95	0.04	-	-
CNES	1.03	0.06	1.04	0.07	1.04	0.05	0.95	0.06	0.89	0.08

RTM (Rayference)	1.09	0.03	1.07	0.03	1.07	0.03	0.99	0.03	0.96	0.03
RailRoad Valley	-	-	-	-	-	-	--	-	-	-
Median	1.09		1.04		1.06		0.95		0.96	
Average	1.06	0.06	1.05	0.04	1.06	0.03	0.96	0.03	0.92	0.07
Weighted Average	1.07	0.05	1.05	0.03	1.06	0.03	0.97	0.03	0.94	0.05

Note: Uncertainty estimates are based on the reported uncertainties at k=1 and do not necessarily account for all effects.

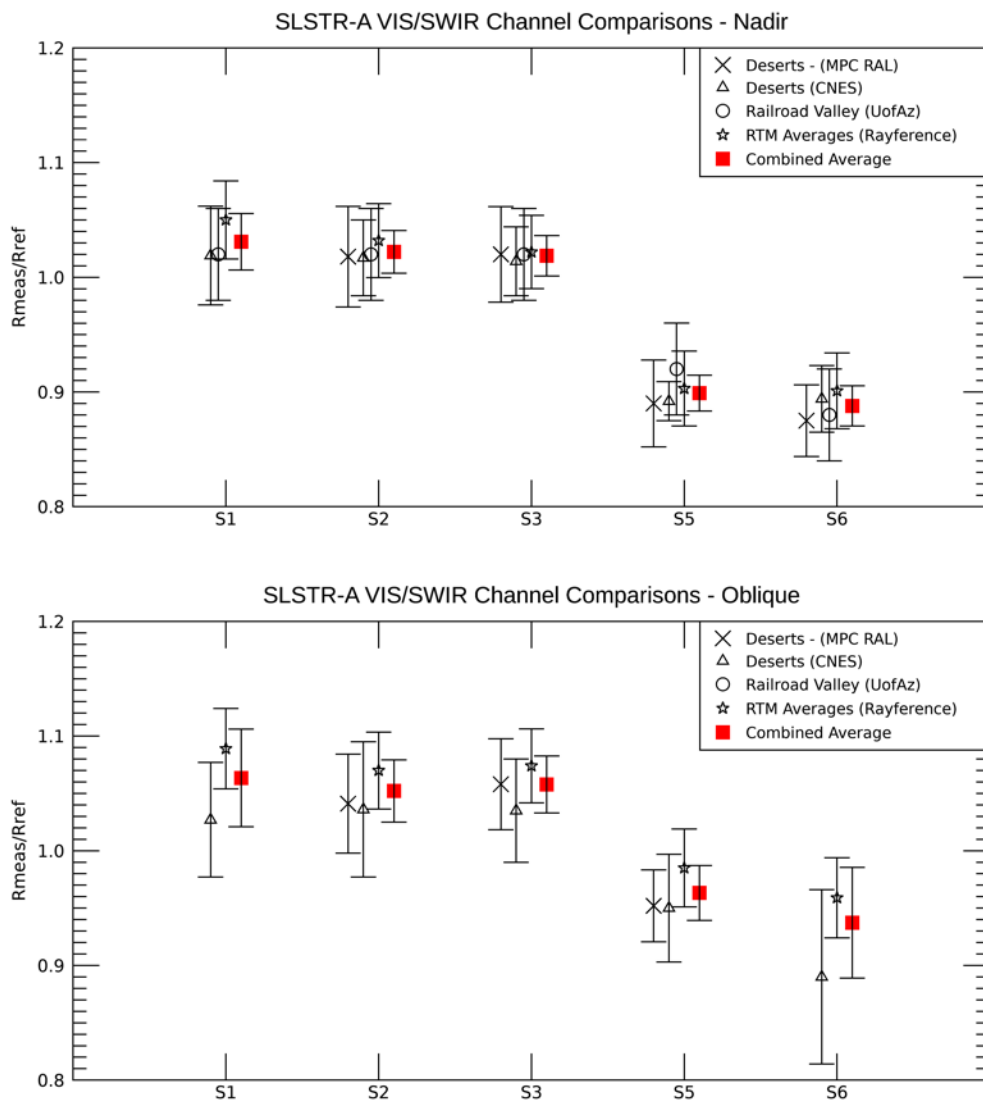


Figure 128: Summary of comparisons of SLSTR VIS/SWIR channel reflectances vs. Reference methods used to provide vicarious correction factors.

Using the combined weighted averages, we are able to provide vicarious adjustment factors to align SLSTR reflectances to MERIS and MODIS Aqua L1 calibrations, Table 27. This is on the basis that MERIS and MODIS calibrations have been assessed over many years and are considered as reference sensors in the VIS/SWIR and relative differences with other sensors are reported. Alignment to a different reference sensor, e.g. Sentinel-2 would be possible provided that relative differences and uncertainty estimates are provided. The correction factor is the inverse of the vicarious calibration results – i.e. $1/(R_{meas}/R_{ref})$.

Table 27: Proposed VIS-SWIR Calibration Adjustments Based on Vicarious Calibration analysis. Note S4 is not included because the vicarious calibration techniques do not extend to this band.

Nadir View

	S1	S2	S3	S5	S6
Correction	0.97	0.98	0.98	1.11	1.13
Uncertainty	0.03	0.02	0.02	0.02	0.02
Input Analysis	UoAz Rayference CNES	UoAz MPC (RAL) Rayference CNES	UoAz MPC (RAL) Rayference CNES	UoAz MPC (RAL) Rayference CNES	UoAz MPC (RAL) Rayference CNES

Oblique View

	S1	S2	S3	S5	S6
Correction	0.94	0.95	0.95	1.04	1.07
Uncertainty	0.05	0.03	0.03	0.03	0.05
Input Analysis	Rayference CNES	MPC (RAL) Rayference CNES	MPC (RAL) Rayference CNES	MPC (RAL) Rayference CNES	Rayference CNES

Note: Uncertainty estimates are at k=1.

6.2.3 Geometric Calibration

The verification of the geolocation accuracy of the SLSTR Level-1 products is performed using the GEOCAL tool developed by ACS under ESTEC contract and running within the MPC. GEOCAL monitors the geolocation performance in Level-1 images by correlation of images with ground control points (GCP). GEOCAL takes into account each GCP's pixel position, the predicted and the found direction cosines in the satellite control frame, and using the thermo-elastic quaternions, provides an estimation of the SLSTR orientation with respect to the satellite control frame in the form of boresight distortions angles, error estimates in the form of covariance matrices, and the optimal direction of each GCP.

Each Level-1 granule typically contains several hundred GCPs. Only GCPs with signal-to-noise ratio larger than 10 are taken into account to obtain a daily average of positional offsets in the across and along track directions.

Figure 129 and Figure 130 present the geolocation performance of SLSTR-A and SLSTR-B showing the average positional offsets in pixels (0.5 km) for Nadir and Oblique views since the beginning of the mission.

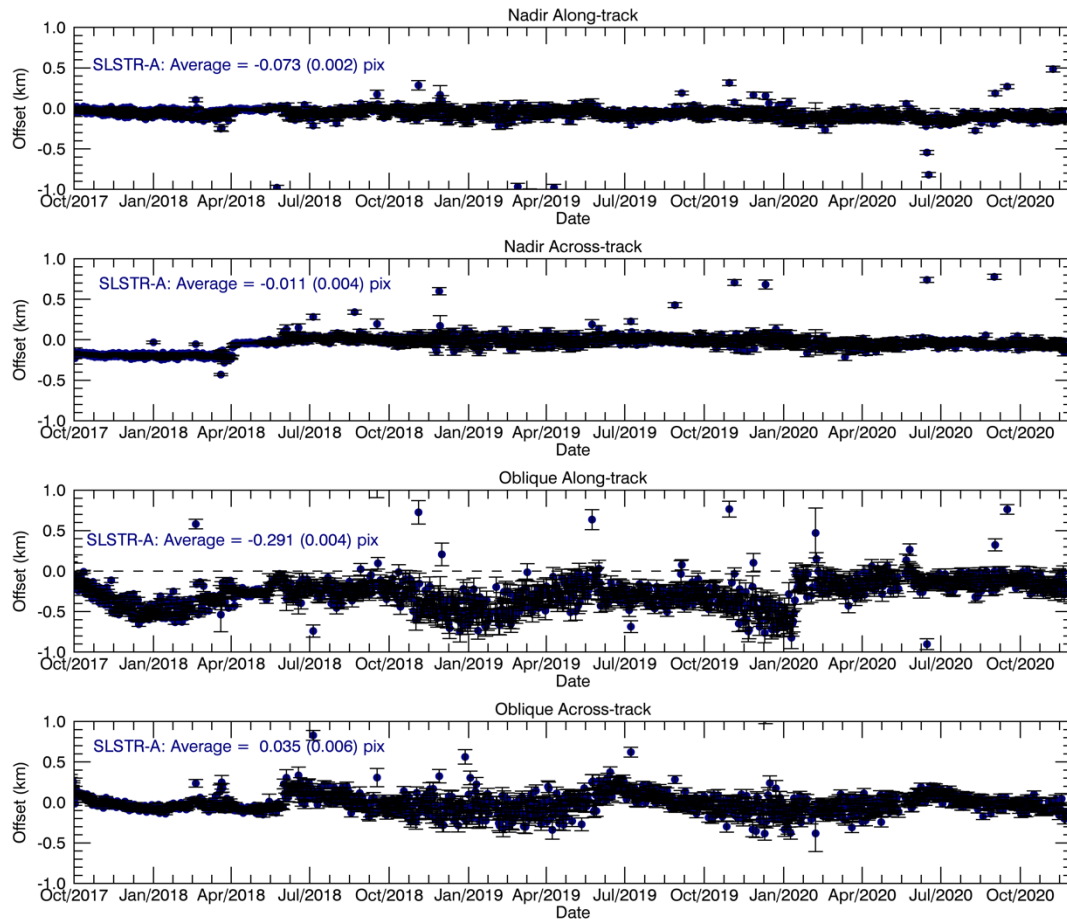


Figure 129: Daily offset results from the GEOCAL Tool analysis for Nadir view along and across track (top two plots) and Oblique view along and across track (bottom two plots) for SLSTR-A.

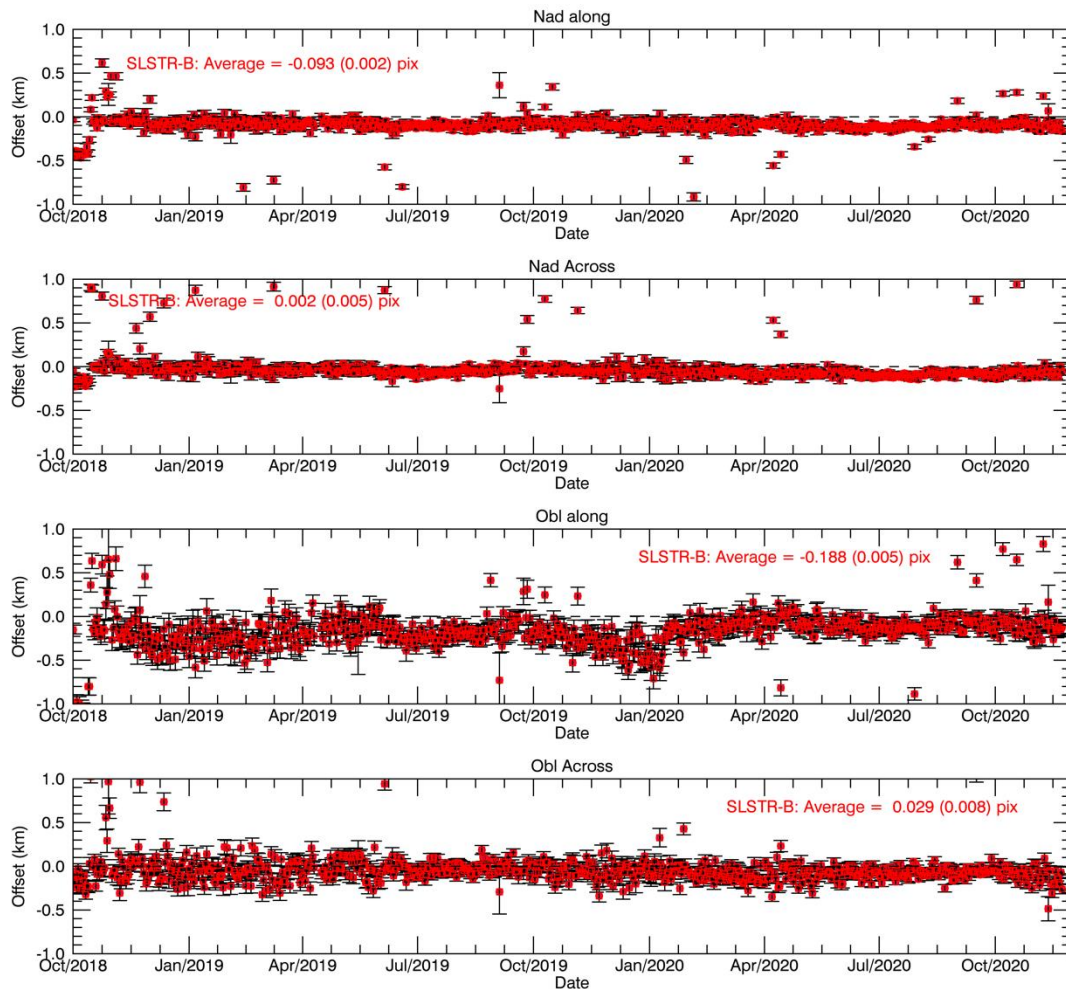


Figure 130: Daily offset results from the GEOCAL Tool analysis for Nadir view along and across track (top two plots) and Oblique view along and across track (bottom two plots) for SLSTR-B.

The positional offset in nadir view meets the mission requirements and remained constant throughout 2020 for both SLSTR-A and SLSTR-B. The average geometric offset for SLSTR-A and SLSTR-B is within 0.1 pixel in nadir view along- and across-track and in oblique view across-track. In oblique view, the offset varies seasonally. This offset variation is well correlated with a variation in the number of ground control points observed during the year, and is still within the requirements.

On the 15th January 2020, a new processing baseline was implemented which reduces the offset in the oblique view for both instruments.

Some satellite manoeuvres were performed throughout the year and although the manoeuvres only increase the positional offsets for two or three orbits, the offsets are big enough to affect the total daily average.

6.2.4 Cloud Screening

The Level 1 cloud screening monitoring continues in the fourth year of SLSTR-A operations, and third year of SLSTR-B. The cloud screening available within the Level 1 product consists of the basic cloud mask that uses a set of 14 different tests that combine to form the Basic 'summary_cloud' flag, the Bayesian, operating over ocean, and the Probabilistic, operating over land.

No specific algorithm development has taken place to the Basic Cloud Tests in the past year, although a technical note 'Recommended Updates to the L1 Cloud Mask' was issued in August 2020 and detailed the evolutions of a number of tests that are recommended to be explored.

6.2.4.1 Summary of basic cloud tests

Currently, all tests but one (infrared histogram test) are included in the summary cloud flag. A short test-by-test summary is provided below.

- ❖ Visible (NDVI) cloud test
 - The visible cloud test is a per-pixel test operating over land only. Two Normalised Differential Indices that are sensitive to vegetated and desert surfaces are calculated using the visible channels. An empirical-based look-up composed of a number of cloudy zones is used to determine if a pixel might contain cloud. There is, however, now an issue with this test missing patches of light cloud over vegetated areas. This could be fixed in the future by using land biome map in the algorithm.
- ❖ Fog/low stratus test
 - The fog/low stratus test is a per-pixel threshold test that only operates on both land and ocean at night. It uses brightness temperature differences between the 11 μm and 3.7 μm channels to determine if there is cloud present. However, cloud can still be missed at night time. This could be improved with further parametrisation of the look-up table.
- ❖ Gross cloud test
 - The gross cloud test identifies the coldest clouds, based on a threshold value on the 12 μm brightness temperatures. There is variation in the thresholds with latitude and season (month).
- ❖ Thin cirrus test
 - This test analyses the BT11-BT12 vs Threshold(BT11, across-track band). It operates on each view separately. This is a reliable test. There is some dependence on atmospheric path and therefore further tuning of the LUTs to reflect this may bring small improvements.
- ❖ Medium high cloud test
 - This test analyses BT3.7-BT12 vs Threshold(BT12). It operates on each view separately, only at night. The value of BT3.7 is always higher than BT12 due to partially cloud filled pixels and thin cirrus being present. There may be some discrepancies around twilight regions.
- ❖ 1.375 threshold test

- This test analyses R1.375 vs Threshold(across-track band). It is based on the high absorption from water vapour in this band, meaning any signal in this channel is likely to be from cloud.
- ❖ 1.6/2.25 large and small scale histogram tests
 - The large-scale part of this test works on the basis that the signal received from clear-sky pixels will have a low value that has little variation, whereas any cloudy pixels will have a higher-varying bright signal. The pixels from a small area are formed into a histogram and the 'shape' of the low dark clear pixels is automatically identified from the brighter, wider peak of the cloudy pixels. The small-scale part of this test looks at the variability of the signal. It is intended to be used in sun-glinted regions when the large-scale test cannot be operated. These tests are not optimized for sun-glinted regions and significant cloud is still missed when the sun-glint flag is raised. It is recommended that an update to the algorithms be developed to counter this.
- ❖ Spatial coherence test
 - This test assesses the standard deviation of the measured BTs over a small area of ocean. It is assumed that over clear sky, the signal variation will be small against the background of a homogeneous ocean. This test has a tendency to over-mask cloud and is one of the priorities for algorithm development.
- ❖ Infrared histogram test
 - This test uses the 11 μm brightness temperature to identify cloud that all other tests may have missed. This is not a reliable test and when used in AATSR, was often seen to falsely classify clear-sky as cloud. It is rarely set. This test is not yet included in the summary cloud.

6.2.4.2 Summary of Bayesian test

The Bayesian mask is carried through to Level-2 Marine Products, and is currently also provided in the Level 1 product. The Bayesian cloud screening method makes use of measurements in the S2, S3, S5, S8 and S9 channels during the day, and S7, S8 and S9 channels at night. These are compared to radiative transfer modelling and pre-calculated look-up tables to infer the probability of a pixel being cloudy given the observations and background meteorological state. The method has previously been applied successfully in the context of the ESA SST CCI to the AVHRR and other ATSR instruments.

6.2.4.3 Summary of Probabilistic tests

The Probabilistic Cloud Mask is implemented in the IPF at Level-1 and carried through to Level-2. Following the implementation of temporal interpolation of the ECMWF Skin Temperature in the meteorological input fields to the probabilistic clouds mask code, some excess cloud contamination and over masking did appear. These L1 releases were respectively PB 2.59 (S3A) and PB 1.31 (S3B) and were made on 15th January 2020. Any cloud contamination and over-masking were addressed in PB 2.73 (S3A) and PB 1.50 (S3B) with updated releases of the respective Probabilistic Cloud Mask ADFs.

6.2.4.4 Monitoring cloud masking performance

Comparisons between the Basic and Bayesian cloud masks can be made using the SST matchup database that is available to us through the Sentinel-3 Validation Team. This is a database of sea surface temperature made by various in-situ instrumentation, matched in time and space to Sentinel-3 Level-2 SST data. It provides a useful way to compare the Basic and Bayesian cloud masks, and to assess the Basic cloud test performance over ocean.

6.2.4.4.1 Confusion Matrices

Over the year, the total number of matchups which have been masked as cloudy or clear by each of the Basic and Bayesian cloud tests have been counted, and compared to see how many points agree.

The confusion matrices below for daytime and night-time in Figure 131 and Figure 132 show the number of points (and the percentage of total clear or cloudy matchups identified by the Basic mask, rounded to the nearest integer) where the Basic and Bayesian have agreed or disagreed for S3A and S3B respectively. The matrices shows that the Basic mask has a tendency to disagree most significantly on data that would be classed as cloudy by Bayesian, with up to 27% of the clear-sky cases found by the Basic mask actually being found cloudy by Bayesian. This points to the Basic missing cloud. This cloud ‘leakage’ appears to be worse for S3A compared to S3B. Both S3A and S3B agree to a similar level on the proportion of cloudy matchups found by the Basic mask.

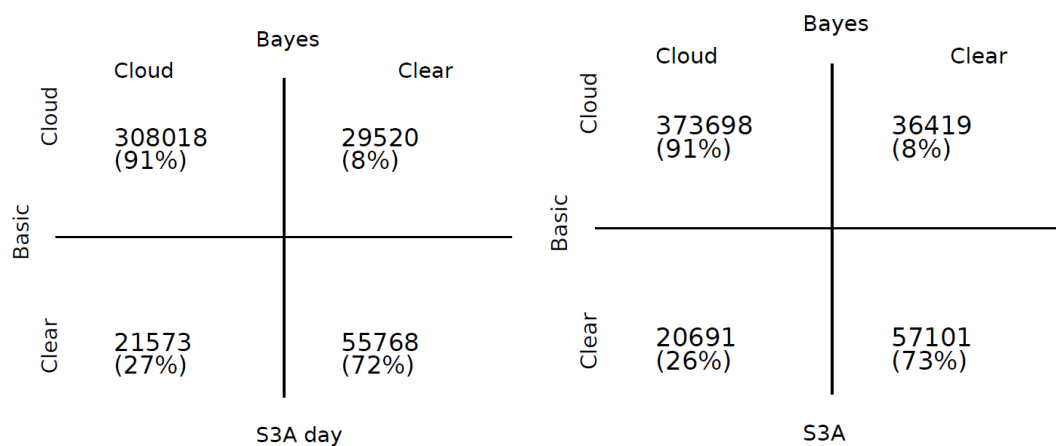


Figure 131: S3A cloud identification confusion matrices for matchups. Left shows daytime data and right shows night-time data.

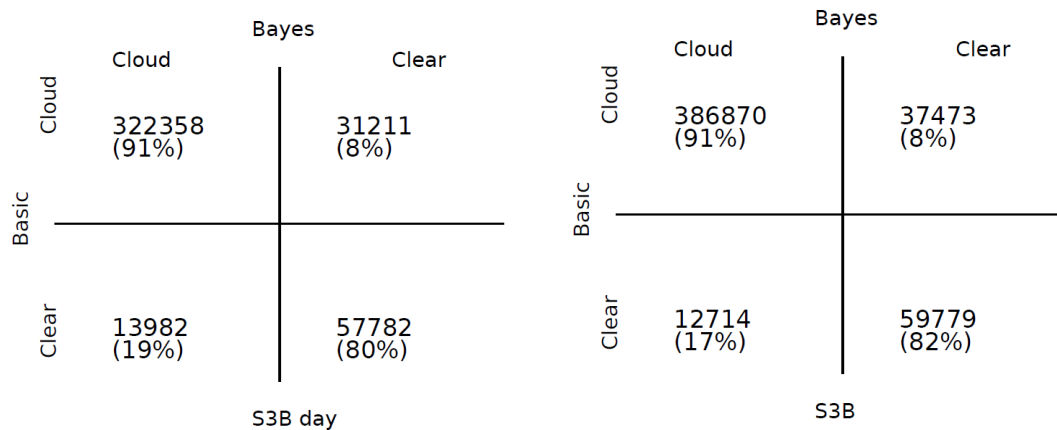


Figure 132: S3B cloud identification confusion matrices for matchups. Left shows daytime data and right shows night-time data.

6.2.4.4.2 Time series of cloud-free matchups

The performance of the cloud tests has been monitored using the SST matchup database. By looking for high SST biases, potential cloud missed can be identified and quantified. Figure 133 shows a time series for SLSTR-A and SLSTR-B of the total number of clear-sky matchups found using the Basic cloud mask. Also plotted are the percentage of those matchups which give a high SST bias (>3K), a possible indicator of cloud contamination. The SST result for the Nadir 2-channel (N2day), Dual view 2-channel (D2day), Nadir 3-channel (N3night) and Dual view 3-channel (D3night) algorithms are treated separately. We note that the N3-night SSTs consistently highest proportion of high SST biases, indicating that the cloud mask is missing more cloud at night and when the dual-view tests are not available over the entire swath. The number of N2-day points with a high SST bias peak in the summer months and this is likely a result of sun-glint being present in more of the images, where the basic cloud tests are known miss cloud.

In this figure, the matchups identified as 'cloudy' using the basic mask are also plotted, along with the proportion of those points with a low SST bias, an indicator of clear-sky incorrectly masked as cloud. The proportion of potential clear-sky misses is similar between S3A and S3B, at between 20-40%. The statistics imply that a proportion of clear-sky is being incorrectly identified as cloud, as similar statistic for the Bayesian cloud mask show the proportion of cloudy matchups giving a low SST bias at 2-30%.

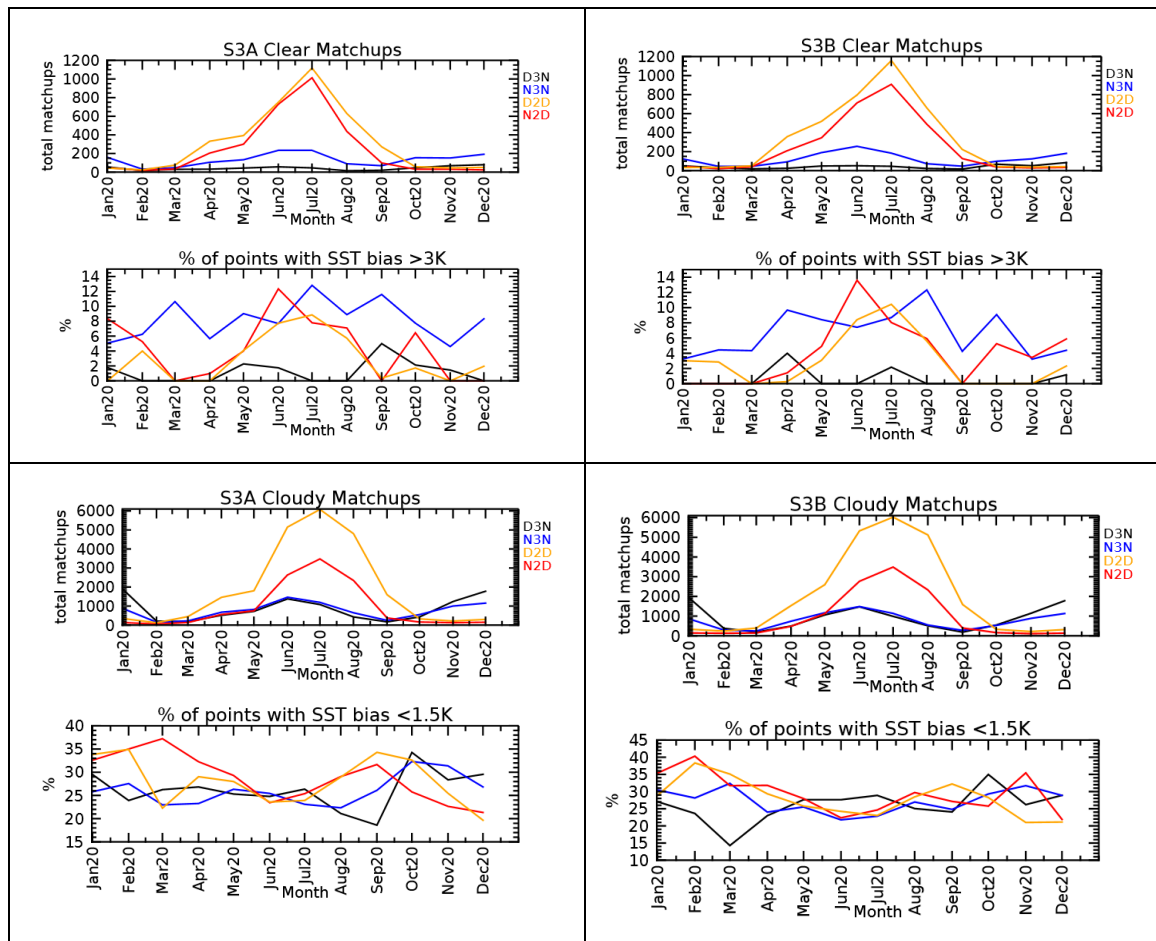


Figure 133: A time series of the total number of matchups indicated to be ‘clear-sky’ by the Basic and Bayesian masks for each of the 4 SST algorithms for SLSTR-A. The number of matchups with an SST bias > 3K is also plotted, as this can be indicative of unidentified cloud.

6.2.5 References

- ❖ Cox, C. and Munk, W., “Measurement of the Roughness of the Sea Surface from Photographs of the Sun’s Glitter”, Journal of the Optical Society of America, Vol. 44, Issue 11, p. 838 (1954)
- ❖ D. L. Smith and C. V. Cox, “(A)ATSR solar channel on-orbit radiometric calibration,” IEEE Trans. Geosci. Remote Sens. 51(3), 1370–1382 (2013)
- ❖ Tomazic, I., O’Carroll, A., Corlett, G., Piolle, JF., Hewison, T., Burini, A., Montagner, F., Santacesaria, V., Dash, P., Donlon, C., Dransfeld, S., Smith, D. “Sentinel-3 SLSTR CAL/VAL activities for sea surface temperature measurements”, Tallinn, Estonia, EUMETSAT Conference (2018)

6.3 L2 product performances

6.3.1 Land Surface Temperature (LST)

The formal missions' requirement for LST specifies that:

- ❖ S3-MR-420: Sentinel-3 shall be able to measure Land Surface Temperature (LST) to an accuracy of < 1K with a resolution of 1 km at nadir. This capability shall not reduce the quality of the SST retrievals

A four-phase approach is detailed in the S3 OPT Cal/Val plan, which follows both the ESA LST validation protocol (Schneider et al., 2012) and the CEOS LPV Best Practices guide for LST (Guillevic et al., 2017):

- ❖ Comparison of satellite-retrieved LST with in situ measurements collected from radiometers sited at a number of stations spread across the Earth, for which the highest-quality validation can be achieved;
- ❖ Radiometric-based validation, which offers an alternative to validation with in situ LST measurements as it does not require measurements of LST on the ground, and can provide a viable alternative for long-term, semi-operational LST product evaluation at the global scale;
- ❖ Inter-comparisons with similar LST products from other sources such as AATSR, AVHRR, MODIS, SEVIRI, and VIIRS, which give important quality information with respect to spatial patterns in LST deviations;
- ❖ Time series analysis to quantify trends and to identify potential instrument drift or persistent cloud contamination.

We have focussed on the first and third approaches, with the second approach developed offline. The first responds directly to the formal mission requirements on accuracy for LST. The third provides the context to which the product exhibits consistency on a larger regional basis. The fourth approach is dependent on multi-year data and will be addressed once we have a minimum of 3-4 years routine operational Level-2 data.

The SLSTR-A SL_2_LST product from SLSTR went operational in the Sentinel 3 PDGS on 5th July 2017 with PB 2.16. No additional updates to the retrieval algorithm have been implemented in the IPF since. However, Processing Baseline 2.29 released on 4th April 2018 included the new Probabilistic Cloud Mask implemented in the IPF at Level-1 and carried through to Level-2. Furthermore, from 26th February 2019 an updated ADF of retrieval coefficients has been implemented in PB 2.47, IPF 06.14. We show results on a monthly basis from 1st February 2020 to 31st January 2021. In all cases the Probabilistic Cloud Mask is applied. An improvement to the cloud coefficients ADF was made on 23rd October 2020 in PB 2.73.

The SLSTR-B SL_2_LST product from SLSTR went operational in the Sentinel 3 PDGS on 26th February 2019 with PB 1.19 IPF 06.14. We show results on a monthly basis from 1st February 2020 to 31st January 2021. In all cases the Probabilistic Cloud Mask is applied. An improvement to the cloud coefficients ADF was made on 23rd October 2020 in PB 1.50.

For both SLSTR-A and SLSTR-B all matchups have been performed for non-time critical (NTC) only since this is deemed to be the data of highest quality.



Sentinel-3 MPC

**S3MPC OPT Annual Performance
Report - Year 2020**

Ref.: S3MPC.ACR.APR.007

Issue: 1.1

Date: 28/04/2021

Page: 182

For the in situ validation twelve “Gold Standard” stations were used in the matchups process, seven from the SURFRAD network; two from the ARM network; and three from the USCRN network: i) Bondville, Illinois; ii) Desert Rock, Nevada; iii) Fort Peck, Montana; iv) Goodwin Creek, Mississippi; v) Penn State University, Pennsylvania; vi) Sioux Falls, South Dakota; vii) Table Mountain, Colorado; viii) Southern Great Plains, Oklahoma; ix) Barrow, North Slopes Alaska; x) Williams, Arizona; xi) Des Moines, Iowa; xii) Manhattan, Kansas. Overall the matchups show very good agreement between the satellite LST and the in situ LST across a broad range of LST values. This is the case for each of the “Gold Standard” stations (Figure 134 – SLSTR-A; Figure 135 – SLSTR-B).

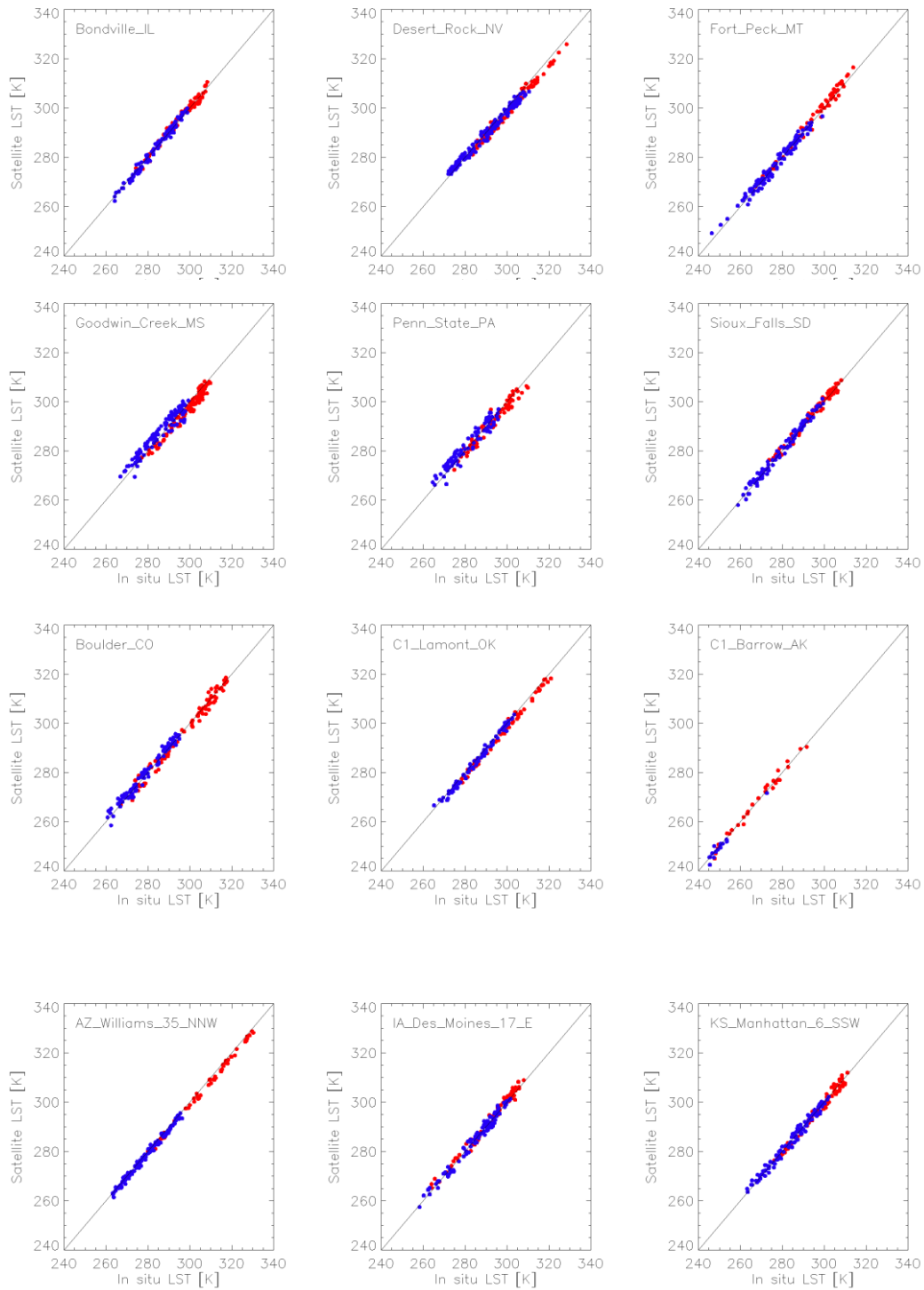


Figure 134: In situ validation of S3A SL_2_LST product at twelve “Gold Standard” stations for the period 1st February 2020 to 31st January 2021

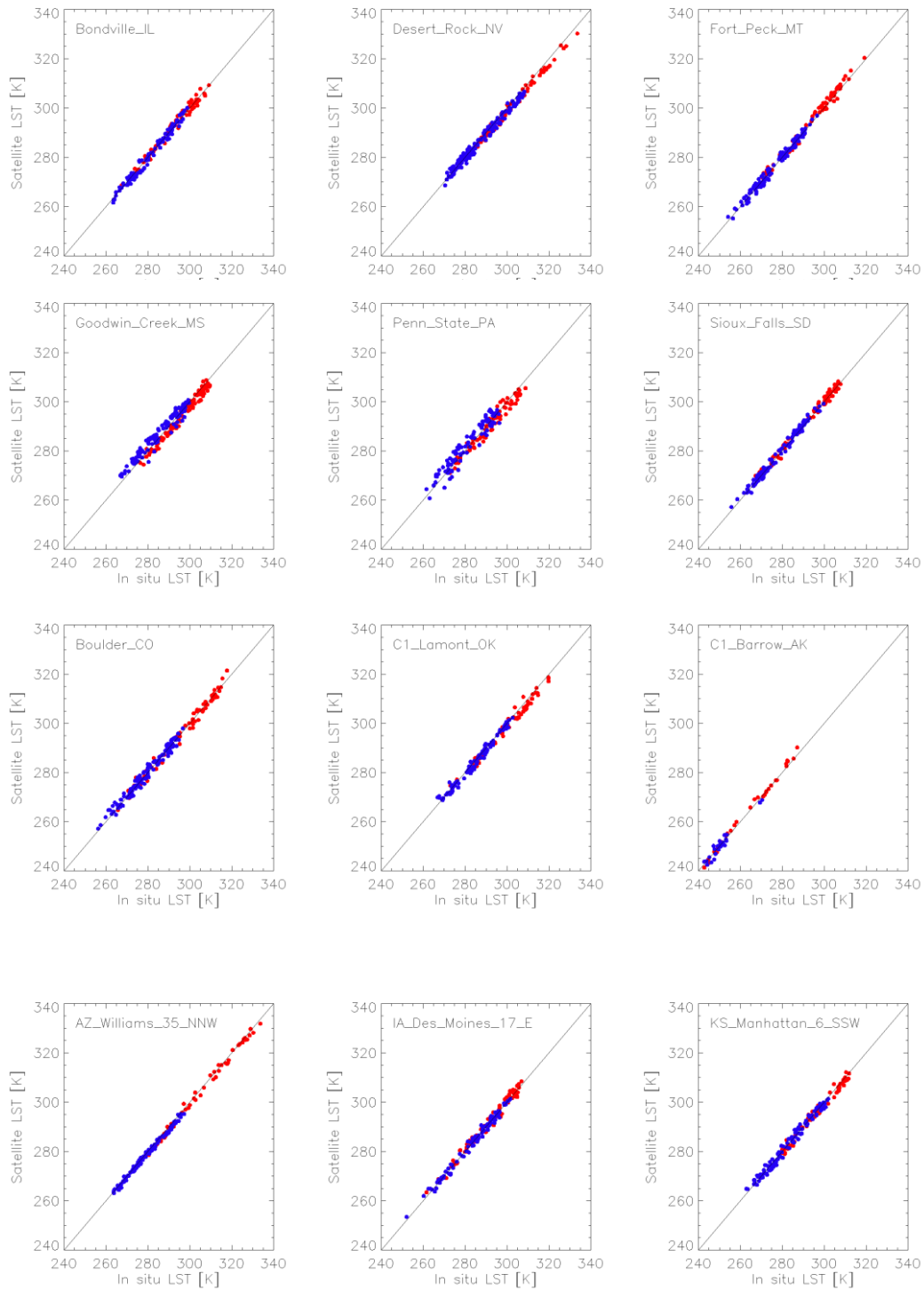


Figure 135: In situ validation of S3B SL_2_LST product at twelve “Gold Standard” stations for the period 1st February 2020 to 31st January 2021.

The statistics are shown in Table 28 (SLSTR-A) and Table 29 (SLSTR-B). The number of matchups are provided together with the accuracy and precision. The accuracy can be directly compared with mission requirement S3-MR-420. For SLSTR-A, overall the absolute daytime accuracy is 0.98 K and the absolute night-time accuracy is 0.56 K. Both of which are within the mission requirements for LST. For SLSTR-B, overall the absolute daytime accuracy is 0.90 K and the absolute night-time accuracy is 0.50 K. Both of which are within the mission requirements for LST.

Table 28: Statistics of In situ validation for S3A SL_2_LST product at twelve “Gold Standard” stations for the period 1st February 2020 to 31st January 2021

Network	Site	Day			Night		
		N	Acc.	Prec.	N	Acc.	Prec.
SURFRAD	Bondville	68	0.06	1.37	103	-0.12	1.13
SURFRAD	Table Mountain	78	-0.75	1.92	100	0.66	1.50
SURFRAD	Desert Rock	86	-1.62	1.38	137	-0.52	1.71
SURFRAD	Fort Peck	59	0.91	1.47	125	0.21	1.55
SURFRAD	Goodwin Creek	98	-1.90	1.55	115	1.61	2.25
SURFRAD	Penn State University	68	-1.43	1.78	84	0.87	2.25
SURFRAD	Sioux Falls	80	0.54	1.21	96	0.33	1.34
ARM	Southern Great Plains	52	-1.57	1.08	90	-0.82	1.00
ARM	North Slopes Alaska	32	-0.02	1.37	18	-0.62	1.18
USCRN	Williams, Arizona	52	-1.56	0.81	119	-0.84	0.90
USCRN	Des Moines, Iowa	69	0.66	1.40	96	-0.04	1.57
USCRN	Manhattan, Kansas	73	-0.80	1.39	110	-0.07	1.40

Table 29: Statistics of In situ validation for SL₂_LST product at twelve “Gold Standard” stations for the period 1st February 2020 to 31st January 2021

Network	Site	Day			Night		
		N	Acc.	Prec.	N	Acc.	Prec.
SURFRAD	Bondville	67	0.00	1.46	102	-0.23	1.37
SURFRAD	Table Mountain	63	-0.25	1.75	124	0.11	1.59
SURFRAD	Desert Rock	89	-1.43	1.25	148	-0.65	1.58
SURFRAD	Fort Peck	68	0.83	1.41	120	0.04	1.34
SURFRAD	Goodwin Creek	104	-1.99	1.40	121	1.63	1.96
SURFRAD	Penn State University	74	-1.51	1.85	94	0.99	2.74
SURFRAD	Sioux Falls	77	0.43	1.24	98	0.40	1.26
ARM	Southern Great Plains	59	-1.67	1.50	107	-0.59	1.23
ARM	North Slopes Alaska	42	0.25	1.28	27	-0.40	1.49
USCRN	Williams, Arizona	53	-1.01	1.11	117	-0.79	0.80
USCRN	Des Moines, Iowa	78	0.56	1.47	91	-0.04	1.27
USCRN	Manhattan, Kansas	71	-0.82	1.35	105	-0.12	1.47

For the satellite vs. satellite intercomparison both the SLSTR-A and SLSTR-B SL₂_LST products respectively were compared with the operational SEVIRI LST product available from the LSA SAF. Matchups were performed on a common 0.05° equal-angle grid following re-gridding of the Level-2 data. Individual matchups for a grid cell were only derived when the temporal difference between observation times was within 7.5 minutes, and both satellites were able to determine clear-sky LST for the grid-cell. These individual matchups were composited into monthly daytime and night-time differences. Monthly differences are shown in Figure 136 (SLSTR-A) and Figure 138 (SLSTR-B), with tabulated mean differences detailed in Table 30.

The differences are relatively consistent across different land cover types and regions of Europe and Africa. Higher differences occur at the edges of cloud masked features, suggesting some failures in one or other of the cloud algorithms for the respective products; or in areas of high topographical variance and towards the edge of the SEVIRI disk, a result of the differences in viewing geometry between the two instruments. For both SLSTR-A and SLSTR-B, overall all comparisons are generally within 1 K (Table 30) and all within the uncertainty range when considering the uncertainties from the reference products, and thus can be interpreted as consistent with each other.

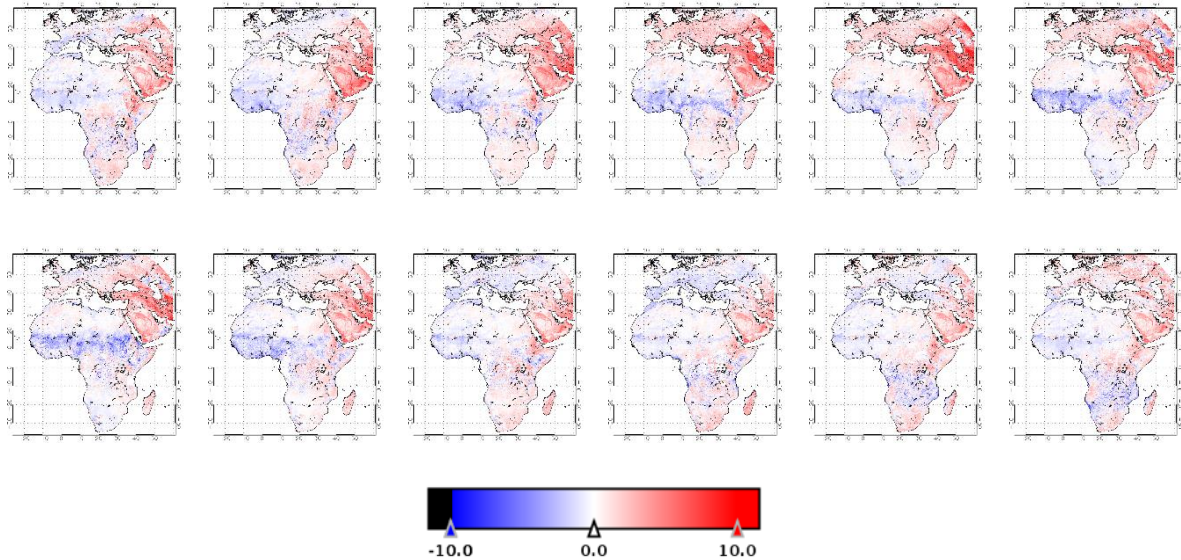


Figure 136: Monthly daytime LST difference between S3A SL_2_LST and operational SEVIRI from LSA SAF for each month from February 2020 to January 2021. Top row from left to right: Feb 2020, Mar 2020, Apr 2020, May 2020, Jun 2020, Jul 2020. Bottom row from left to right: Aug 2020, Sep 2020, Oct 2020, Nov 2020, Dec 2020, Jan 2021.

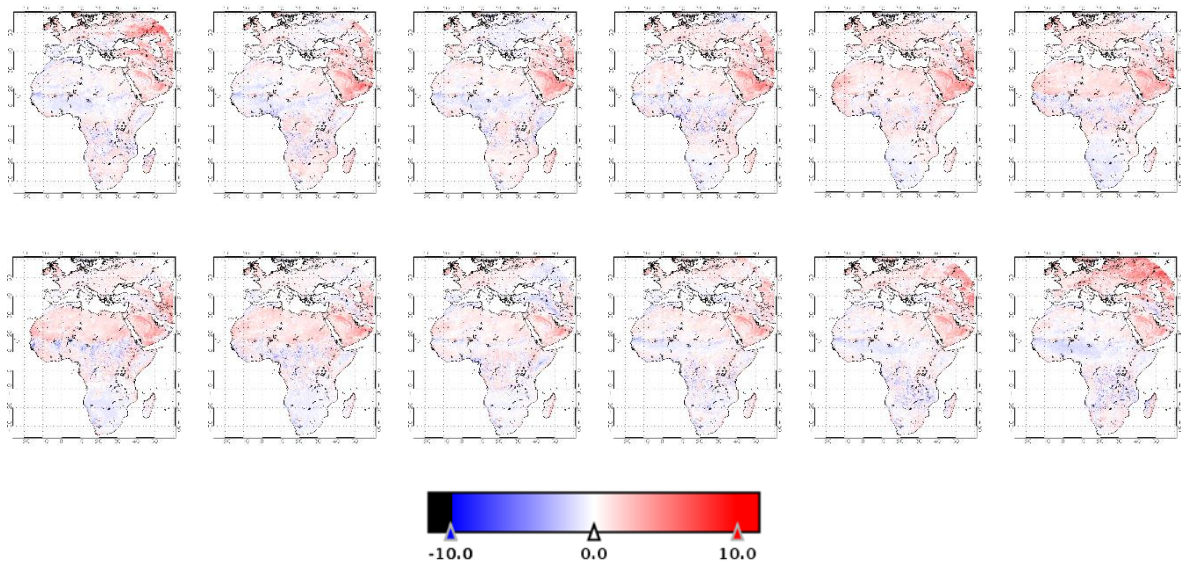


Figure 137: Monthly night-time LST difference between S3A SL_2_LST and operational SEVIRI from LSA SAF for each month from February 2020 to January 2021. Top row from left to right: Feb 2020, Mar 2020, Apr 2020, May 2020, Jun 2020, Jul 2020. Bottom row from left to right: Aug 2020, Sep 2020, Oct 2020, Nov 2020, Dec 2020, Jan 2021.

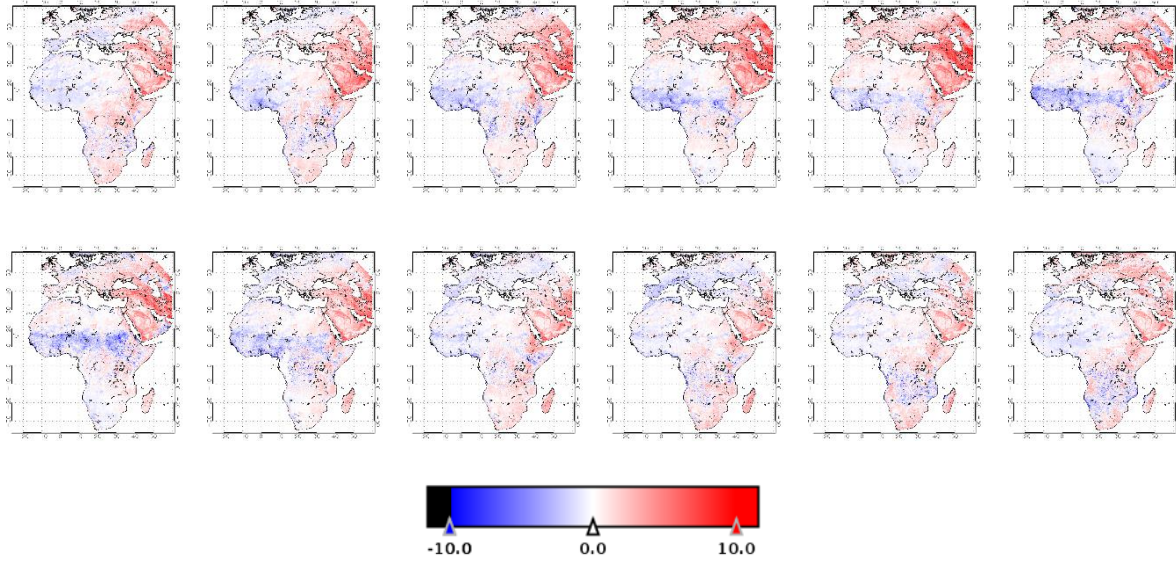


Figure 138: Monthly daytime LST difference between S3B SL_2_LST and operational SEVIRI from LSA SAF for each month from February 2020 to January 2021. Top row from left to right: Feb 2020, Mar 2020, Apr 2020, May 2020, Jun 2020, Jul 2020. Bottom row from left to right: Aug 2020, Sep 2020, Oct 2020, Nov 2020, Dec 2020, Jan 2021.

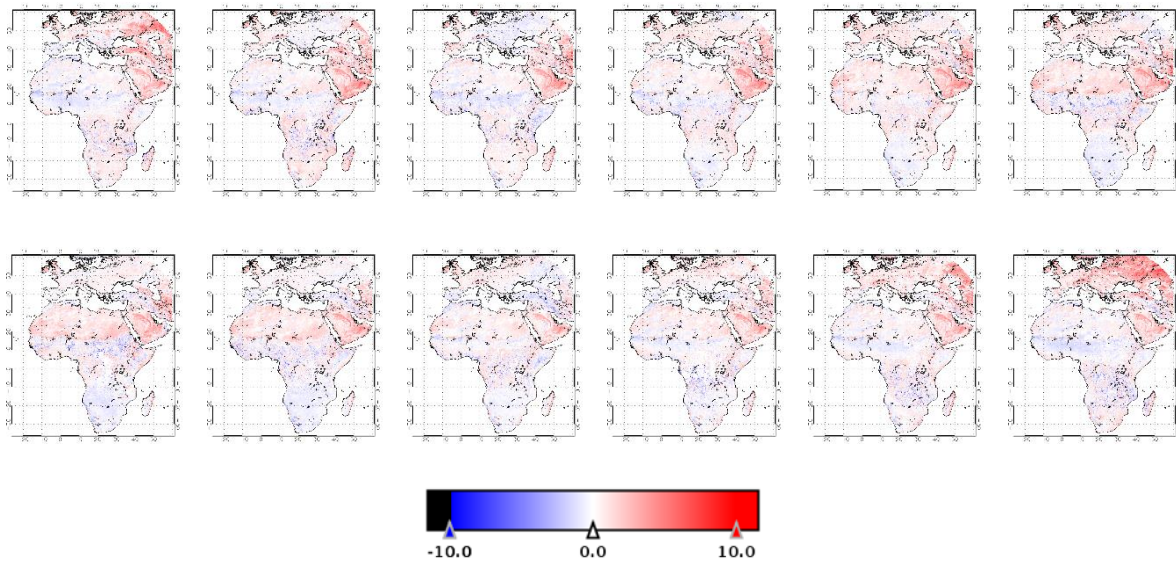


Figure 139: Monthly night-time LST difference between S3B SL_2_LST and operational SEVIRI from LSA SAF for each month from February 2020 to January 2021. Top row from left to right: Feb 2020, Mar 2020, Apr 2020, May 2020, Jun 2020, Jul 2020. Bottom row from left to right: Aug 2020, Sep 2020, Oct 2020, Nov 2020, Dec 2020, Jan 2021.

Table 30: Statistics of monthly LST difference between SLSTR-A and SLSTR-B SL_2_LST and operational SEVIRI from LSA SAF over Africa for each month from February 2020 to January 2021

		02/20	03/20	04/20	05/20	06/20	07/20	08/20	09/20	10/20	11/20	12/20	01/21
S3A	Day	0.1	0.1	0.0	-0.1	0.3	-0.2	-0.4	-0.1	0.2	0.2	0.1	-0.1
S3B	Day	0.3	0.2	0.0	-0.1	0.2	-0.3	-0.3	-0.1	0.3	0.3	0.2	0.0
S3A	Night	0.1	0.3	0.3	0.3	0.6	0.5	0.5	0.4	0.3	0.2	0.1	0.0
S3B	Night	0.2	0.3	0.1	0.2	0.5	0.4	0.4	0.3	0.2	0.2	0.2	0.1

Overall the validation and intercomparison indicate both the SLSTR-A and SLSTR-B SL_2_LST products are in line with expectations and meeting mission requirements. There are no distinct issues or non-physical values evident. Some cloud contamination is evident but this has been minimised following the update to the cloud coefficients ADF on 23rd October 2020.

6.3.1.1 Summary

The matchups with in situ observations show very good agreement across a broad range of LST values. This is the case for each of the “Gold Standard” stations. For SLSTR-A, overall the absolute daytime accuracy is 0.98 K and the absolute night-time accuracy is 0.56 K. Both of which are within the mission requirements for LST. For SLSTR-B, overall the absolute daytime accuracy is 0.90 K and the absolute night-time accuracy is 0.50 K, also both within the mission requirements for LST. This validation is complemented with satellite vs. satellite intercomparison between the SLSTR-A and SLSTR-B SL_2_LST products and operational SEVIRI LST available from the LSA SAF. For Africa the mean monthly differences are < 1 K. This is the case both for SLSTR-A and SLSTR-B, and for both daytime and night-time comparisons. These are both within the SL_2_LST mission requirements and the uncertainty range when considering the uncertainties from the reference products. Thus, the two products can be interpreted as consistent with each other. Some cloud contamination is evident, but this has been minimised following the update to the cloud coefficients ADF on 23rd October 2020.

6.3.2 Fire Radiative Power (FRP)

The SLSTR FRP product consists of both Active Fire Detection and Fire Radiative Power assessment. The algorithm was initially designed to detect and characterise vegetation fires burning on the land surface areas, whilst also identifying elevated temperature sites of active volcanism and sufficiently hot industrial heat sources, and has subsequently been adapted for the detection of offshore gas flares (i.e. detection of hotspots over the open ocean and in coastal regions and potentially large lakes). The algorithm is mainly reliant on data from the MIR 3.7 µm channel (bands S7 and F1) and thermal infrared (TIR) 10.8 µm channel (bands S8 and F2). However, non-linearity of the S7 band has been noted above a recorded Brightness Temperature (BT) of around 311 K (S7_{AT}) and full saturation of the channel at a reported brightness

temperature of around 312 K. This makes S7 quite commonly saturated over hotter ambient land surfaces, and very often saturated over active fires, and F1 is therefore required to be used in the AF detection and FRP retrieval process more commonly than expected pre-launch. AF detection is initially performed using S7, and FRP retrieval can then be performed in two ways: either using S7 when all active fire pixels in an identified active fire cluster remain unsaturated and F1 otherwise (the so called F1_OFF option), or always using F1 regardless of S7 saturation (the F1_ON option). Given these limitations, the current version of the FRP algorithm is designed to work at night, when the S7 channel almost always remains unsaturated over the ambient background pixels. Note that in any fire cluster where F1 is used to generate the FRP values, a version of the AF detection procedure initially made using S7 is repeated using F1. F1 has a smaller pixel footprint than S7, and this can lead to the (beneficial) detection of lower FRP active fire pixels in some cases. Some occasional daytime granules are processed as well where there is minimal S7 saturation over ambient temperature land, but these are only preliminary and fully trustable daytime data will be available only after a dedicated daytime algorithm is completed and tested.

To evaluate the performance of the night-time algorithm, an inter-comparison between the SLSTR NTC FRP and the FRP retrieved from the similar MODIS MOD14 product was designed and conducted, giving important information on both spatial patterns of fire detection and FRP quantification. Additionally, a comparison between SLSTR FRP products obtained using the F1_OFF and F1_ON options was performed. The validation procedure, initially based on previous work from M. Wooster and W. Xu on the FRP Prototype and on the evaluation of SEVIRI fire data, is divided into two main parts, the first one related to errors of omission and commission, and the second to fire clusters. A brief description of the base algorithm is given in the following.

Part 1, errors of omission and commission between SLSTR FRP and MODIS MOD14:

- ❖ Select and download MODIS MOD14 data with overpass time within ± 6 minutes of those of SLSTR;
- ❖ Restrict observations to a scan angle of $\pm 30^\circ$ or equivalent pixel area of 1.7 km^2 to avoid edge-of-swath data, and restrict to the common area of detection between the two products;
- ❖ Re-project the MODIS pixels to the SLSTR Level 1b data grid. If multiple MODIS active fire pixels (AFP) are present in the same equivalent SLSTR grid cell, their combined FRP is used;
- ❖ Evaluate SLSTR FRP errors of commission, i.e., when there is a fire pixel in the SLSTR grid without any MOD14 fire pixel in a 7×7 window around it;
- ❖ Evaluate SLSTR FRP errors of omission, i.e., when there is a MOD14 fire pixel without any SLSTR fire pixel in a 7×7 window around it.

Part 2, Fire Cluster FRP comparison between SLSTR FRP and MODIS MOD14:

- ❖ Apply an atmospheric correction to MODIS FRP data, calculated using transmittance and water vapour content of the column above the fire pixel;
- ❖ Find all the fire clusters detected by both SLSTR and MODIS, i.e., groups of one or more pixels spatially adjacent to each other and corresponding to a single fire; cases where a single SLSTR cluster corresponds to multiple MOD14 clusters and/or vice versa are merged together and the total FRP is used;

- ❖ Compute the total FRP for all active fire pixels in each fire cluster for MODIS and SLSTR data.
- ❖ Check for cloud/water/detection flags around each fire cluster that might affect the FRP value; if none is present, the cluster is flagged as well-detected;
- ❖ Check the SLSTR S7-S8 difference for possible issues and mismatches with the detected fire clusters;
- ❖ Generate statistics and analysis based on all the fire clusters detected by both MODIS and SLSTR.

Using the procedure delineated above, three sets of comparisons were made. The first evaluation was performed using 300 products covering heavily-fire-impacted areas of Africa, South America, and South-East Asia for the period between February and March 2020. These first results were later integrated with the more comprehensive set of reprocessed products covering the entire Fire Season 2019/2020 over Australia. Both sets of data made use of SLSTR FRP products with the F1_OFF option. A third set of results is obtained with the same data covering Australia but reprocessed using the F1_ON option. These products are then compared both to MODIS MOD14 and SLSTR F1_OFF FRP data. All evaluations are made using both SLSTR-A and SLSTR-B FRP data. A summary of the results is reported in Table 31.

Table 31: Comparison of FRP retrieval between MODIS and SLSTR using the F1_ON and F1_OFF option.

Variable	F1_OFF	F1_ON
Number of commission AFP	1282 (30%)	2511 (35%)
Number of omission AFP	307 (16%)	154 (7%)
Number of SLSTR AFP detected by both sensors	3019 (70%)	4632 (64%)
Total number of AFP detected by SLSTR	4301	7183
Number of MOD14 AFP detected by both sensors	1580 (84%)	2092 (93%)
Total number of MOD14 AFP	1887	2246
Mean number of SLSTR AFP per cluster	12.8	11.0
Total SLSTR FRP within clusters (MW)	55,653	72,193
Mean SLSTR FRP per cluster (MW)	229	172
Median SLSTR FRP per cluster (MW)	59	39
Mean number of MOD14 AFP per cluster	5.7	4.4
Total MOD14 FRP within clusters (MW)	72,406	79,831
Mean MOD14 FRP per cluster (MW)	298	191
Median MOD14 FRP per cluster (MW)	61	33

Variable	F1_OFF	F1_ON
Mean bias of FRP per cluster (MW)	-68.9	-18.2
Median of FRP scatter per cluster (MW)	6.7	4.2
Root-mean-square deviation of FRP per cluster	603.6	208.5
25-50-75 percentiles of SLSTR clusters FRP	28.6, 59.1, 146.2	19.2, 39.2, 100.8
25-50-75 percentiles of MOD14 clusters FRP	14.8, 60.6, 201.3	13.4, 32.8, 106.3

Overall, there is good agreement between SLSTR FRP and MODIS FRP, as can be seen in Figure 140. The comparison shows that SLSTR detects in general more fire pixels than MODIS (roughly double the number of pixels), albeit many of them with very low FRP. Furthermore, there is a large number of commission fire pixels, around 30% of the total, regardless of the F1_OFF or F1_ON option. Such commission fire pixels compared to MODIS are not necessarily incorrect detections, a significant fraction of these may represent real fires that are undetected by MODIS but are detected by the SLSTR product - for example because of the use of the smaller pixel footprint F1 channel. This is the subject of ongoing investigations. On the other hand, the errors of omission decrease from 17% with the F1_OFF option to 7% with the F1_ON option, hinting at the fact that the SLSTR FRP with the F1_ON option is more aligned with the MOD14 one. The same trend is visible when looking at the fire clusters detected by both sensors. A summary of results per dataset for omission, commission, and doubly detected fire pixels is visualised in Figure 142 and Figure 143, for F1_OFF and F1_ON respectively. The distribution of FRP, when looking at fire clusters detected

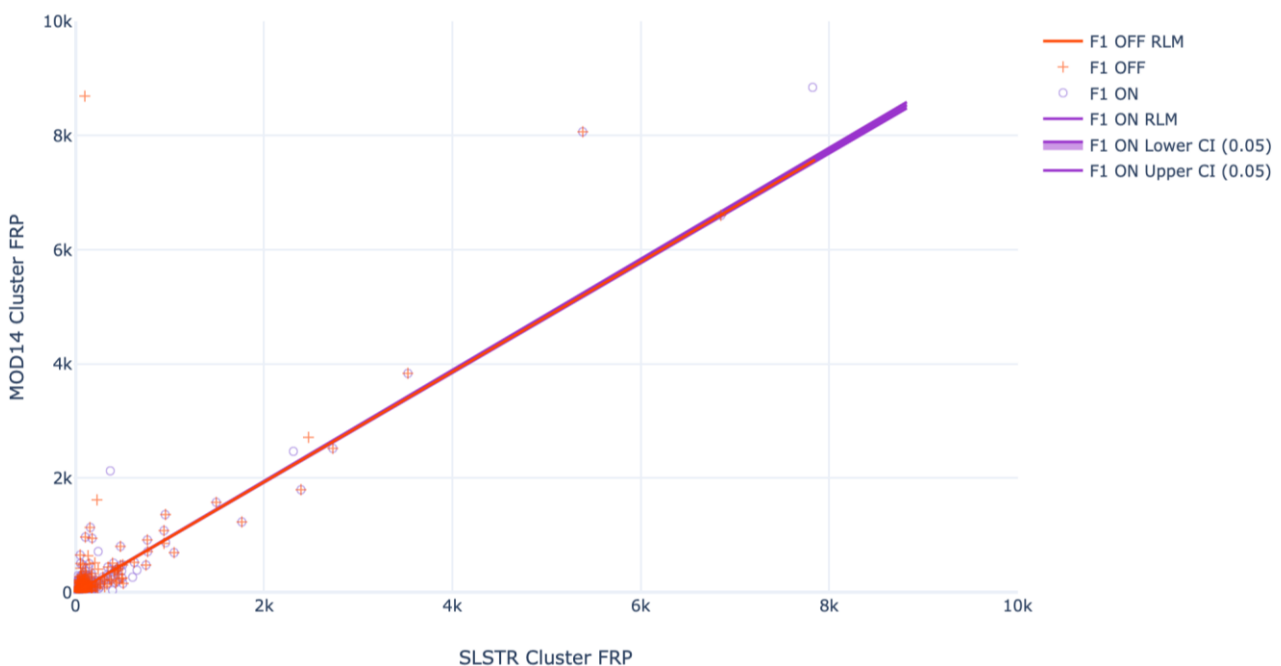


Figure 140: Comparison of fire clusters FRP [MW] between MODIS MOD14 and SLSTR with F1_ON (circles) and F1_OFF (crosses) options. The lines represent robust linear regressions (RLM) with 0.05 confidence intervals (CI).



by both sensors, is quite similar between SLSTR and MODIS, although SLSTR appears to detect a lower total FRP (see Figure 144 and Table 31). This, however, could also be affected by the fact that the different sensors do not observe the fires exactly at the same time and are not perfectly equivalent. Hence, some fluctuations are expected. Moreover, in line with the considerations on the decrease of errors of omission, the bias and scatter for the clusters are lower when using the F1_ON option, and the confidence intervals narrower (see Figure 140 and Figure 141). Note, finally, that some SLSTR fire pixels misreported the IFOV value, which was incorrectly set to zero, and had to be discarded, explaining some of the discrepancies between MODIS and SLSTR data, especially in the F1_OFF case. All results have been produced through python and have been collected in a dedicated web-application for internal communication.

Based on the results of this analysis and on the fact that it guarantees better geometric properties which are more consistent throughout the swath, it has been decided to keep the processing of SLSTR NTC FRP products using the F1_ON option. Further inter-comparisons with other satellite and overflight data are in progress, together with the development and refinement of the FRP day-time algorithm.

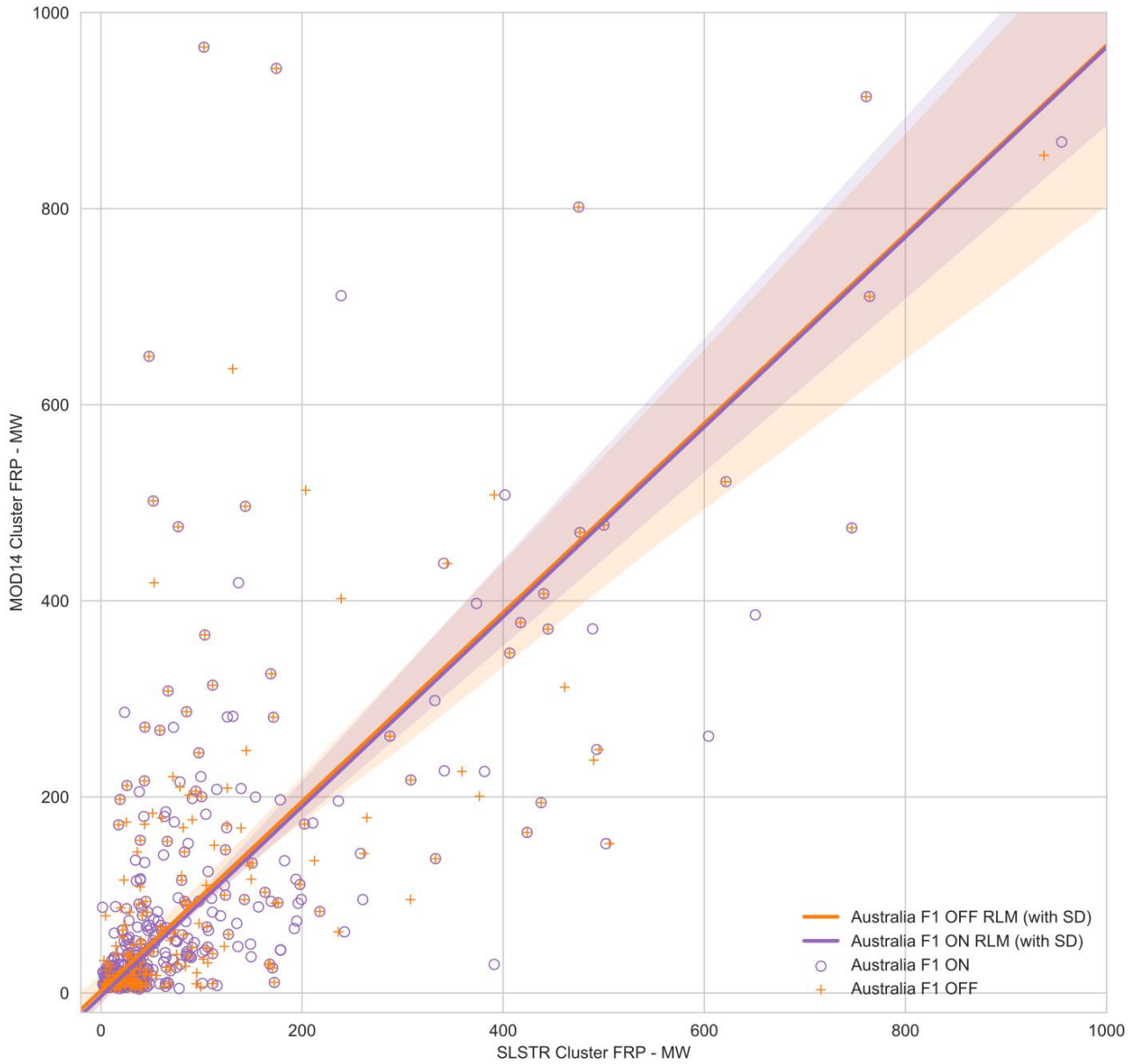


Figure 141: Comparison of fire clusters with FRP lower than 1000 MW between MODIS MOD14 and SLSTR with F1_ON (circles) and F1_OFF (crosses) options. The lines represent robust linear regressions (RLM) with the corresponding Standard Deviation (SD) intervals.



Figure 142: Summary of Omissions and Commissions errors (top), and fire pixels detected by both sensors (bottom) with the F1_OFF option.

Summary of FRP performance

The matchups with MODIS MOD14 data show good agreement when looking at products with overpass time within ± 6 minutes, minimising differences due to different acquisition times, and restricting the analysis to the central portion of the swath, where both sensors are less affected by geometric issues. In general, SLSTR detects roughly double the number of fire pixels with respect to MODIS, many of them with very low FRP. The comparison showed a large number of commission fire pixels, around 30% of the total, regardless of the F1_OFF or F1_ON option, however the number of omission fire pixels with the F1_ON option is significantly lower with the F1_ON option, 7% instead of 17%. Such commission fire pixels compared to MODIS are not necessarily incorrect detections, a significant fraction of these may represent real fires that are undetected by MODIS but are detected by the SLSTR product - for example because of the use of the smaller pixel footprint F1 channel. This is the subject of ongoing investigations. When focusing on fire clusters detected by both sensors, SLSTR FRP with the F1_ON option exhibits a negative

bias of 18.2 MW with respect to MODIS, significantly smaller than the bias with the F1_OFF option, and possibly driven by a few very big fires. Given the fact that the F1_ON options guarantees better geometric properties and more consistency throughout the swath, and in view of the results of this analysis, it has been decided to keep the processing of SLSTR NTC FRP products using the F1_ON option.

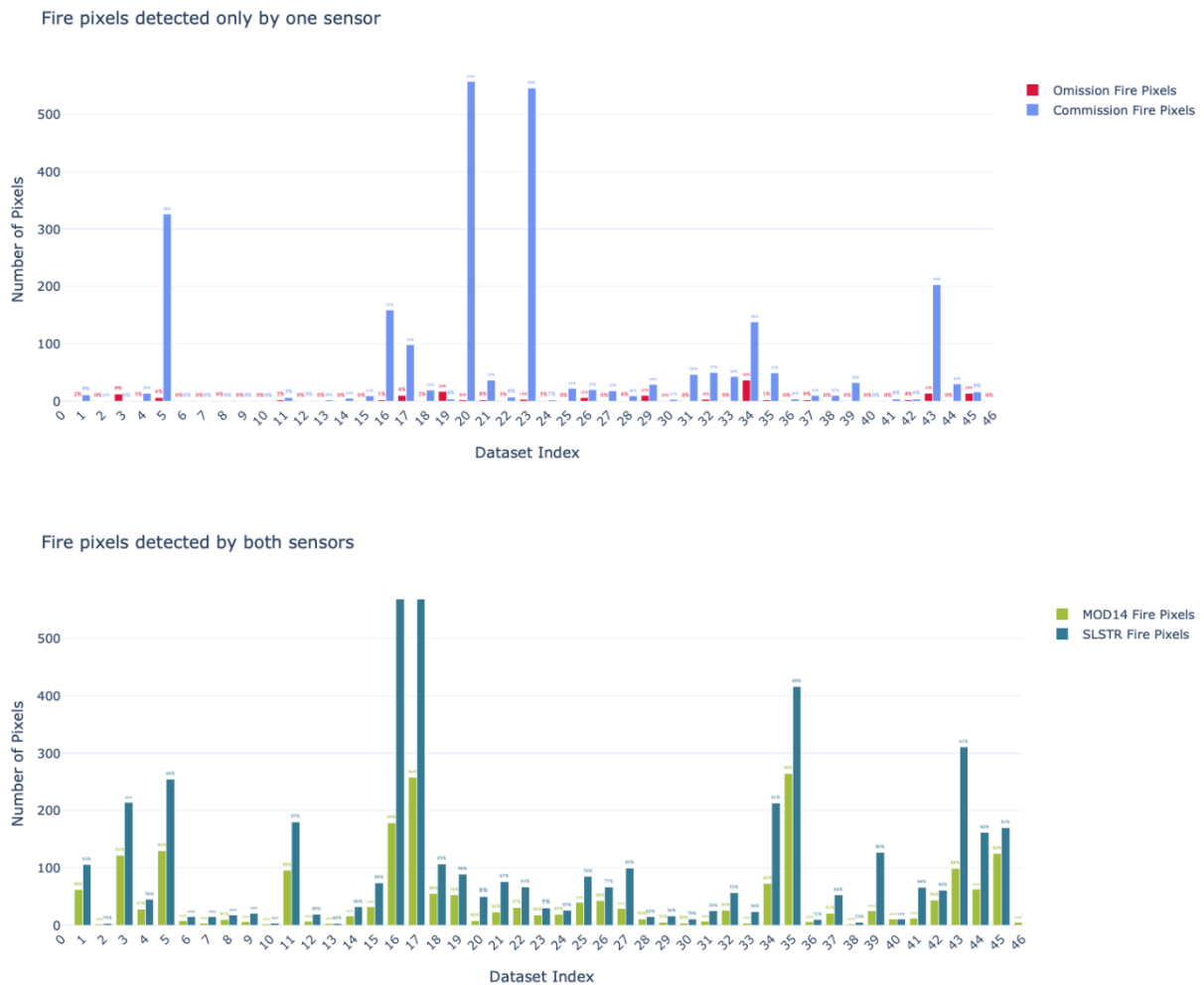


Figure 143: Summary of Omissions and Commissions errors (top), and fire pixels detected by both sensors (bottom) with the F1_ON option.

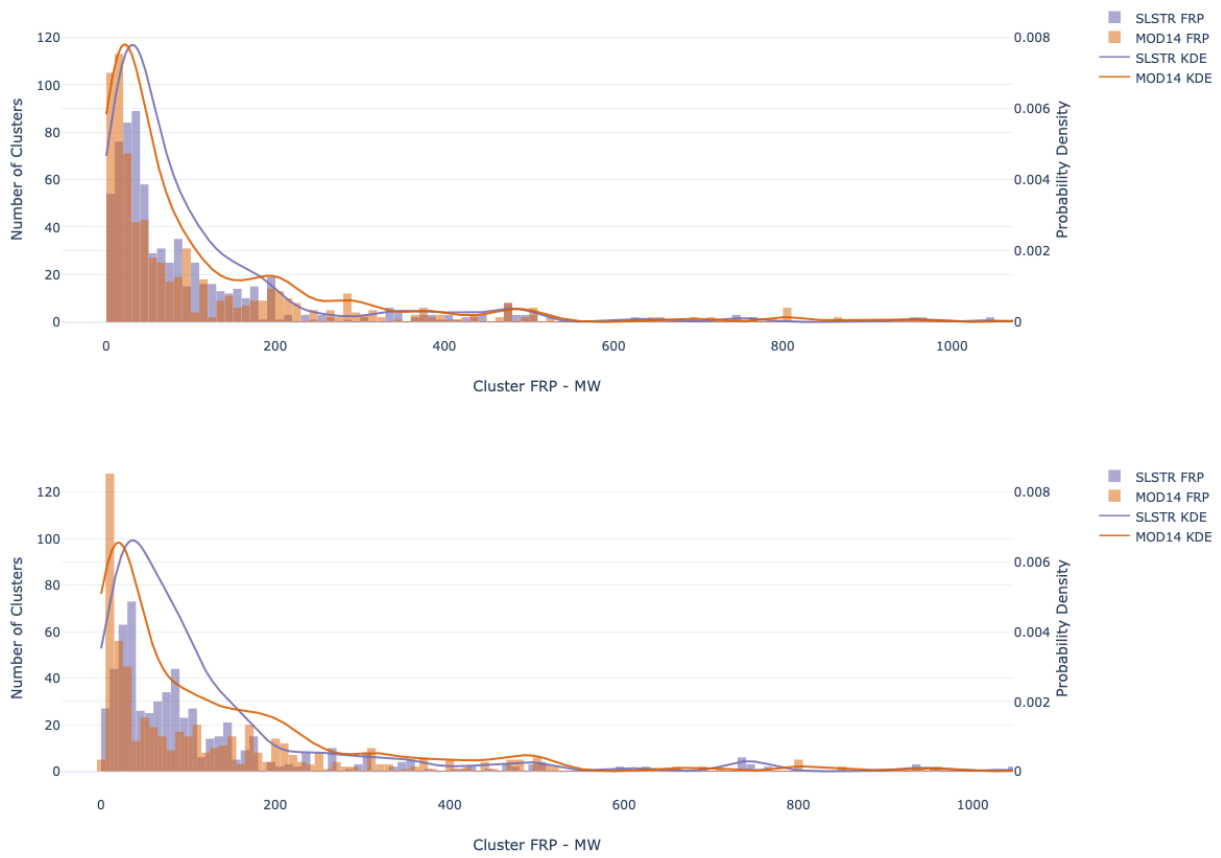


Figure 144: Comparison of the distribution of fire clusters FRP for MODIS and SLSTR F1_ON (top) and F1_OFF (bottom). The line represent estimations kernel densities underlying the observed distributions.

7 Summary of performances – SYN

7.1 L1 products performances

The quality assessment of the misregistration data between OLCI and SLSTR has been done before February 2017, in particular with the inclusion of updated intra-instrument misregistration Auxiliary Data files. As a consequence, we focused on operational issues to ensure the production of SYNERGY products all over the globe and at any time.

In particular, SYNERGY L1 processing was specified to be processed only on descending half-orbits. As consequences, the seasonal variation of OLCI orbit – implying a starting point of the Earth Observation acquisition in ascending mode – was not well handled by SYNERGY Level 1 module and was filtering out all SLSTR radiometric measurements from SYN L1 dataset. The resulting SYN L2 Aerosol optical thickness was then retrieved using only OLCI measurements and no SLSTR surface reflectance were included in affected products.

Following several discussions and investigations by the ground segment, the operational processing teams and the SYNERGY ESLs, this specificity is now considered and well-handled and SYN L2 product is not affected anymore by this seasonal variation.

The SYNERGY Level 1 processing is now performed without issue related to an incompatibility between SLSTR and OLCI products.

7.2 L2 product performances

7.2.1 SYN L2 quality assessment: inter-comparisons with ground-based measurements and MODIS

In order to improve the quality of SYNERGY Level 2 products, an extended analysis of products and algorithm have been performed in 2020. First outcomes of this work are a list of SYN L2 limitations and its behaviour with regards to reference data in terms of AOD (i.e., AERONET ground-based measurements) and surface reflectance (Modis normalised reflectance)

To enable the comparison with AERONET data, matchups have been created with the following rules:

- The temporal delay between AERONET and SYNERGY acquisition should be less than 1h;
- The AERONET AOT @550 nm is interpolated from the two surrounding measured AOTs;
- The SYNERGY retrieved AOT@550 is averaged over the 5 x 5 SYNERGY pixels around the AERONET station;
- Only SYNERGY L2 pixels associated with clear sky and successful retrieval are considered.

Figure 145 shows **the comparison between SYN L2 retrieved AOD@550 nm and AERONET derived AOD@550 nm** on all matchups obtained on a reference period from 23/01/2020 to 09/04/2020.

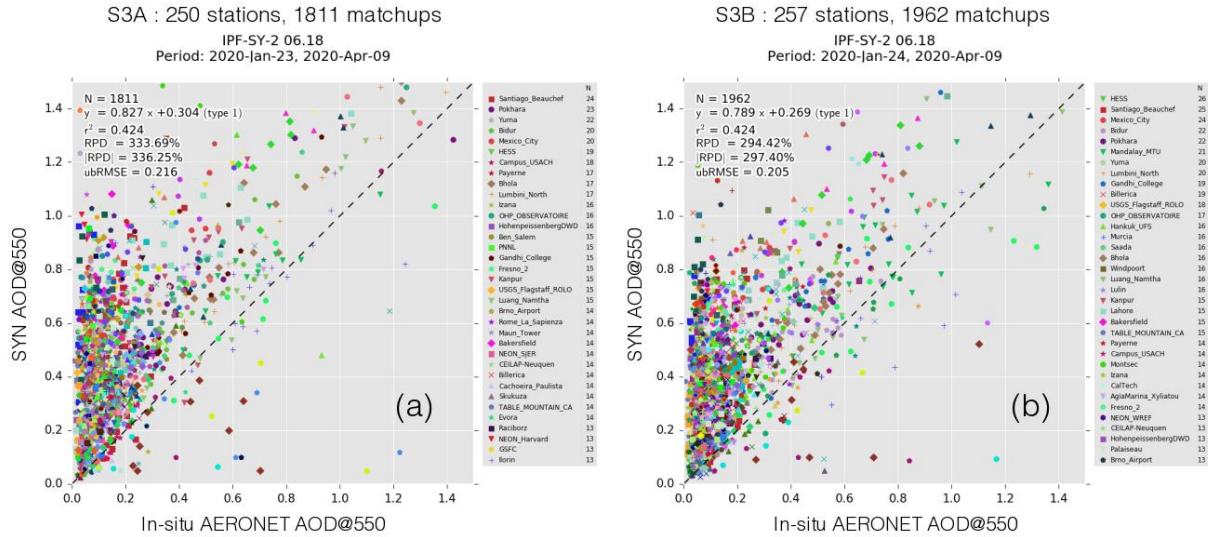


Figure 145 : AOD (550nm) matchups between SYNERGY L2 data and AERONET in-situ measurements for (a) S3A and (b) S3B.

A low correlation, high dispersion and global over-estimation of the SYN L2 AOD, clearly visible on Figure 145, is confirmed when computing statistical indicators such as:

- ❖ Square of the Bravais-Pearson linear correlation coefficient: $r^2 = \frac{[\sum_{i=1}^N (x_i - \bar{x})(y_i - \bar{y})]^2}{\sum_{i=1}^N (x_i - \bar{x})^2 \sum_{i=1}^N (y_i - \bar{y})^2}$
- ❖ Averaged (unsigned) Relative Percent Difference: $|RPD| = \frac{1}{N} \sum_{i=1}^N \frac{|y_i - x_i|}{x_i}$
- ❖ Unbiased Root Mean Square Error: $ubRMSE = \frac{1}{N} \sqrt{\sum_{i=1}^N [(x_i - \bar{x}) - (y_i - \bar{y})]^2}$

Table 32: Statistical indicators between AERONET and SYN L2 Aerosol Optical Thickness

S3A			S3B		
r^2	RPD	ubRMSE	r^2	RPD	ubRMSE
42.4%	336.25%	21.6%	42.4%	297.40%	20.5%

Concerning Surface reflectance dataset, which remains the main SYN L2 objective, an intercomparison with MODIS has been conducted on a reduced dataset (see Figure 146), including 8 scenes covering the whole range of NDVI, not affected by cloud coverage or only to a very limited extent and ensuring a good spatiotemporal overlap with MODIS data.

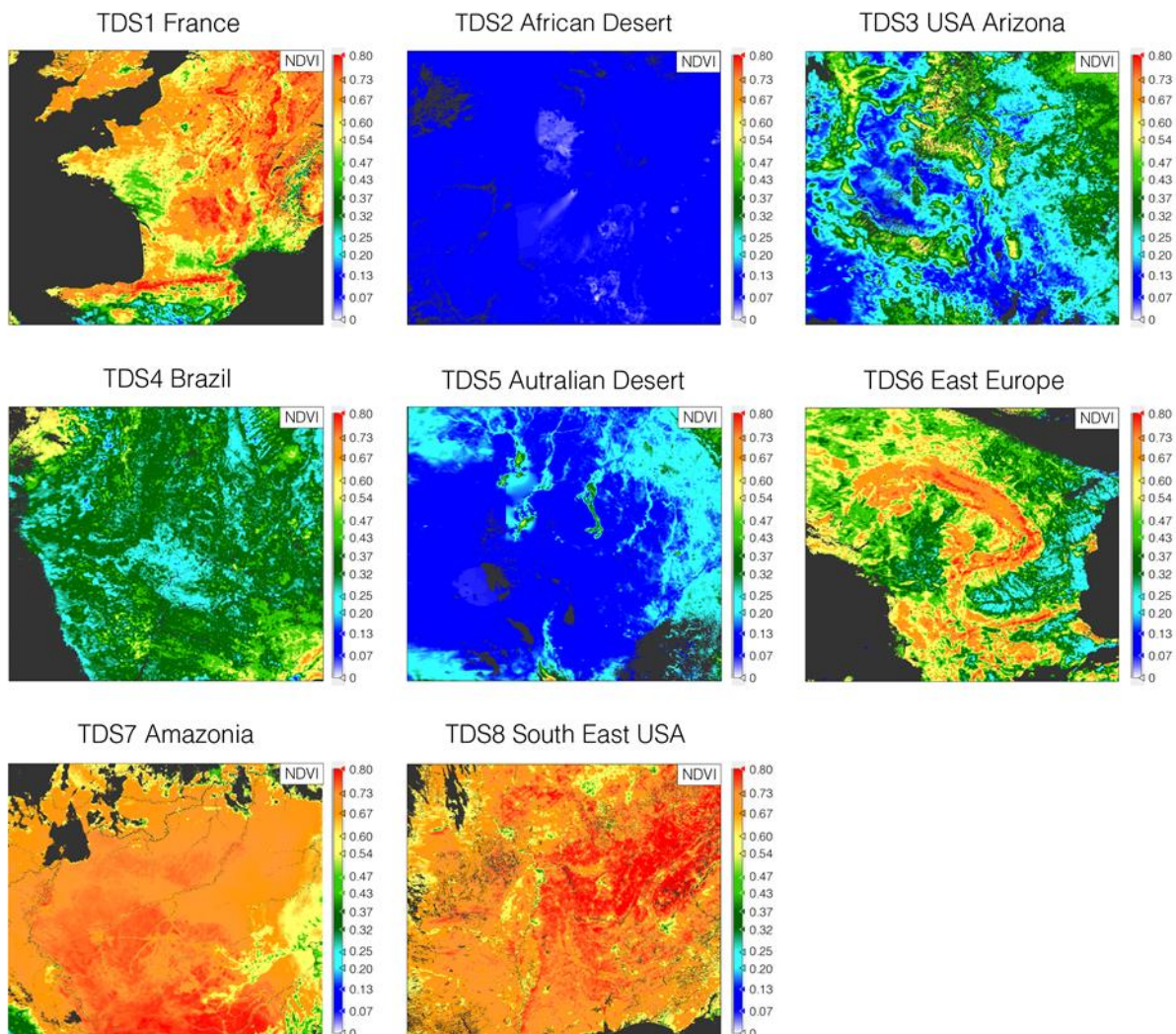


Figure 146: NDVI value obtained for the 8 scenes included in the dataset used for the SYN L2 quality assessment. This NDVI value is computed using OLCI NIR and RED top of atmosphere radiance normalized by the solar irradiance. Colorbars are the same for all scenes, from 0 to 0.8.

Focus has been put on SYN Oa17 band (OLCI, $865 \pm 20\text{nm}$) and b2 (MODIS, $860 \pm 20\text{nm}$), showing good radiometric overlap. In addition, to avoid misinterpretation due to the different acquisition geometry between MODIS and Sentinel 3, this intercomparison has been done using 500m nadir normalised SDR data in the MCD43A4 (NBAR) MODIS products. And the BDRF model used in MCD43A4 products for the normalisation of the surface reflectance (based on the Ross-Li polynomial albedo representation, see [Vermote et al, 2009]) has been also applied to SYNERGY L2 SDR.

A global satisfying correlation between SYNERGY and MODIS Surface reflectance can be observed in Figure 147, with low dispersion except over desert. This result is also confirmed by statistical indicators provided in Table 33.

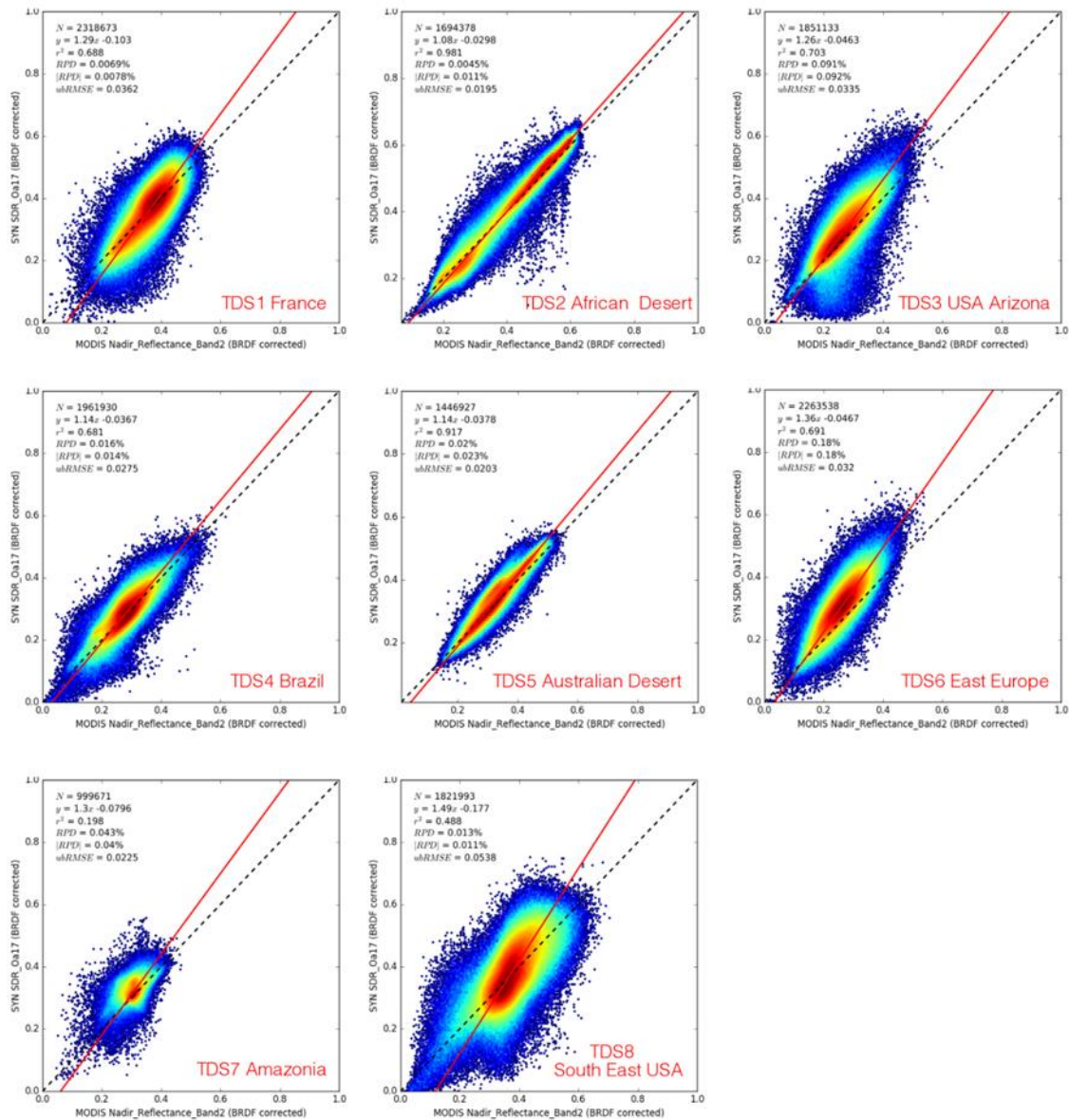


Figure 147: Inter-comparison between normalized SYN SDR (Oa17) products and normalized SDR MODIS (b2) products over the 8 reference scenes.

Table 33: Correlation and unbiased root mean square error for the reference normalised SDR.

REFERENCE SDR SYN (Oa17) vs. MODIS (b2)			
Scene	r^2	RPD	ubRMSE
TDS1	68.8%	0.8%	3.62%
TDS2	98.1%	1.1%	1.95%
TDS3	70.3%	9.2%	3.35%
TDS4	68.1%	1.4%	2.75%
TDS5	91.7%	2.3%	2.03%
TDS6	69.1%	18.0%	3.20%
TDS7	19.8%	4.0%	2.25%
TDS8	48.8%	1.1%	5.38%

Conclusion:

Despite a clear over-estimation of the SYN L2 retrieved AOD, the outputted surface directional reflectance shows correct correlation with reference data. One exception can be raised over site with low NDVI.

References:

- ❖ Vermote, E., Justice, C.O., and Bréon, F.-M. (2009), Towards a Generalized Approach for Correction of the BRDF Effect in MODIS Directional Reflectances, *IEEE Transactions on Geoscience and Remote Sensing*, **47**, no. 3. doi: 10.1109/TGRS.2008.2005977.

7.2.2 SY_2_VGP, SY_2_VG1, SY_2_V10: consistency checks with PROBA-V

In order to assess the possible extension of the SPOT/VGT – PROBA-V data with Sentinel-3 SYN VGT, the consistency between Sentinel-3 SYN VGT and PROBA-V products is evaluated. This analysis is based on the operational Sentinel-3 Level 2 synergy products, available on the Sentinel-3 Pre-operations Data Hub (S3A PB 2.56, S3B PB 1.28, with latest updates to the PB on 15/01/2020).

The temporal compositing scheme of the SY_V10 (10-daily composite) products was updated in the PDGS mid-May/2020 in alignment with the former VGT products, resulting in 3 composite products per month, i.e., 1-10, 11-20, 21-end of the month.

Since the time windows associated with the SYN_VG1 (daily composite) products was inconsistent with the former VGT products, and not consistent over different product timeliness (different for NTC and STC)

and satellites (different for S3A and S3B), the temporal compositing schemes of SY_VG1 were updated in the PDGS on 24/09/2020 to have VG1 for the same sensing window 00:00:00_23:59:59 for both S3A and S3B and both STC and NTC.

Only data with the latest compositing scheme updates were considered for intercomparison.

7.2.2.1 Data

The PROBA-V operational mission has ended on 30/06/2020, and PROBA-V has entered an experimental phase with limited data acquisitions over Europe and Africa only.

The following data was used for intercomparison:

- ❖ SY_VGP and PROBA-V L2A top-of-atmosphere (TOA) products with closest match in acquisition time over a 3 months period 01/07/2020 – 30/09/2020. The number of product match-ups is 608 for S3A, 610 for S3B. The number of pairwise valid observations is illustrated in Figure 148.
- ❖ SY_VG1 for the Europe and Africa tiles, and PROBA-V S1 products for 6 10°x10° tiles (Figure 149) over the period 01/10/2020 – 10/10/2020. The number of product match-ups is 10, per S3 sensor.
- ❖ SY_V10 for the Europe and Africa tiles, and PROBA-V S10 products for 6 10°x10° tiles (Figure 149) over the period 01/07/2020 – 30/09/2020. The number of product match-ups is 9, per S3 sensor.

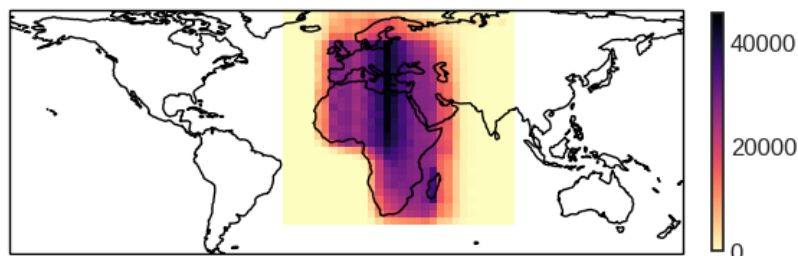


Figure 148: Number of pairwise TOA observations used in the intercomparison between SY_VGP and PROBA-V L2A from 01/07/2020 – 30/09/2020.

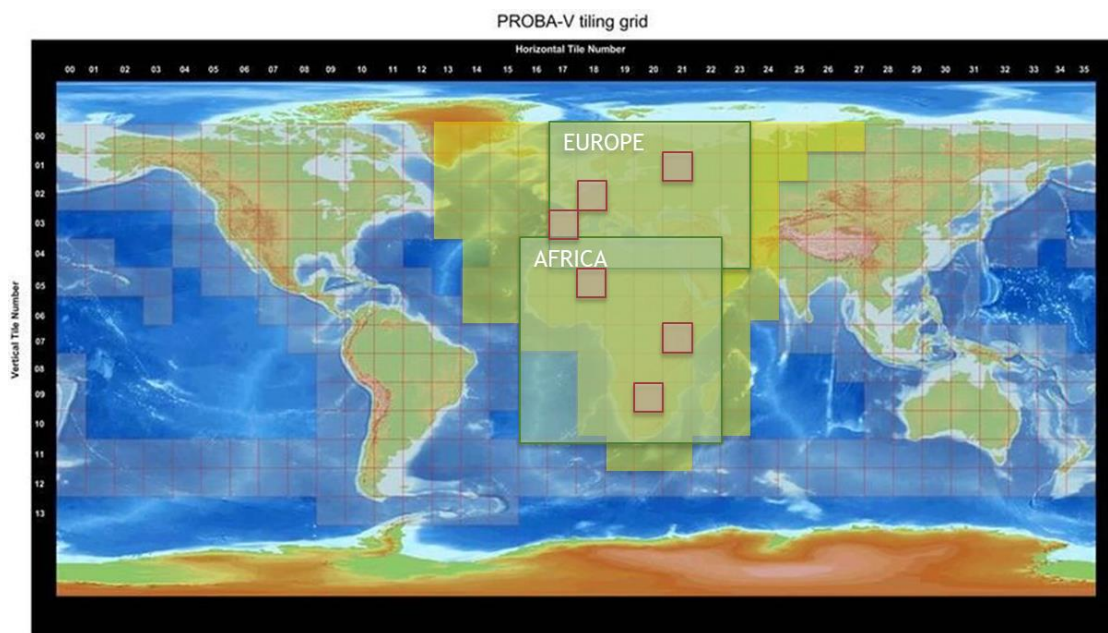


Figure 149: Sentinel-3 SYN VGT tiles over Europe and Africa (green), PROBA-V coverage since July 2020 (yellow), 10°x10° tiles considered in the intercomparison (red)

7.2.2.2 Methods

Product completeness and the occurrence of quality flags over land pixels are based on the bitwise interpretation of the status map (SM) layer.

Validation metrics for statistical consistency analysis are calculated over a large number of samples (pixels) [1]–[4]. For both the SYN VGT and PROBA-V products, the SM was interpreted in order to exclude pixels labelled as ‘cloud’, ‘shadow’ (in case of PROBA-V), ‘snow/ice’ or ‘water’, or with bad radiometric quality or bad coverage in one of the spectral bands. A systematic spatial subsample of 1.5% (every 8th pixel in both X and Y) is applied in order to reduce processing time. The analysis results are shown per Sentinel-3 source.

To identify the relationship between SYN VGT and PROBA-V, the geometric mean (GM) regression model is used. Such an orthogonal (model II) regression is appropriate, because – unlike when comparing to an absolute reference – both datasets are subject to noise. By applying an eigen decomposition to the X and Y covariance metrics, two eigenvectors are obtained that describe the principal axes of the point cloud [4], i.e., the regression line. The GM regression intercept and slope value are added as quantitative information related to the scatterplots.

The Root Mean Squared Difference (RMSD) expresses the difference magnitude between two datasets from 0 and is an expression of the overall difference. The GM regression model is also used to differentiate between systematic and random differences, providing additional information on the difference’s nature between two datasets. The coefficient of determination (R^2) indicates the agreement or covariation between two datasets with respect to the linear regression model, summarizing the total explained variance by this model.

The results focus on the Systematic Root Mean Product Difference (RMPDs), and the Mean Bias Error (MBE).

$$RMPD_s = \sqrt{MSD - MPD_u} = \sqrt{\frac{1}{n} \sum_{i=1}^n (X_i - Y_i)^2 - \frac{1}{n} \sum_{i=1}^n (|X_i - \hat{X}_i|)(|Y_i - \hat{Y}_i|)} \quad (1)$$

The MBE measures the average actual difference between two data sets and positive and negative differences between observations, and is defined as:

$$MBE = \frac{1}{n} \sum_{i=1}^n (X_i - Y_i) = \bar{X} - \bar{Y} \quad (2)$$

7.2.2.3 Results and discussion

1. Product completeness

Table 34 and Table 35 summarize the occurrence of quality flags over land pixels for both the daily and 10-daily composite products. An important drawback of the SY_VGT products is the lack of cloud shadow identification.

The differences in product completeness are especially considerable for the S1 products: since the SY_VG1 product is derived per S3 sensor, on average around 40% of the pixels remains ‘unfilled’ (Table 34). This means that product completeness would largely benefit from the combination of S3A and S3B in single composite products. The temporal evolution of the occurrence of quality flags over a 10°x10° tile in Western Europe illustrates the cyclic pattern in the percentage pixels covered by the SY_VG1 products.

Table 34: Occurrence frequency of quality flags over land pixels for SY_VG1 derived from S3A and S3B in comparison to PROBA-V S1, over 6 10°x10° tiles (01-10/10/2020)

% over land	Clear	Cloud	Snow/ice	Shadow	Uncertain	Unfilled
SY_VG1 S3A	29.3	27.4	0.0	-	3.2	40.1
SY_VG1 S3B	32.5	26.9	0.0	-	3.3	37.3
PROBA-V S1	32.2	59.8	0.2	1.7	6.3	-

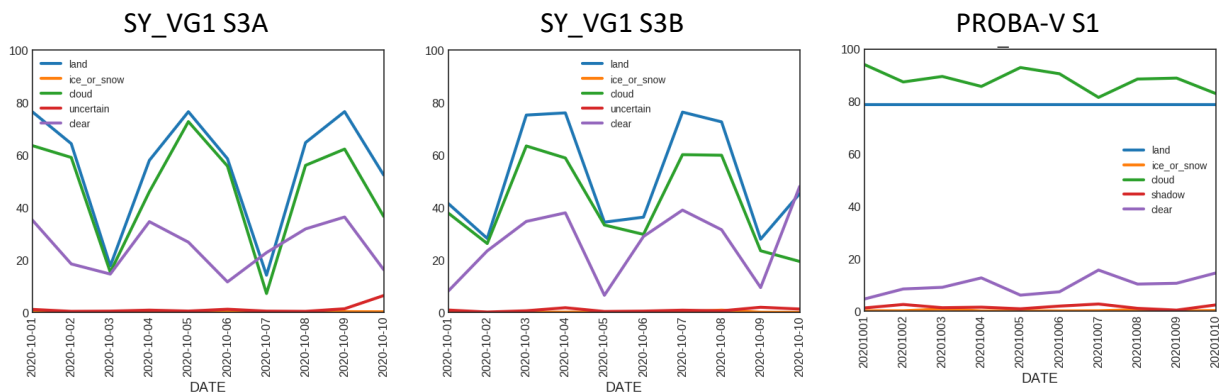


Figure 150: Temporal evolution of the occurrence frequency of quality flags for SY_VG1 S3A (left) and S3B (middle) in comparison to PROBA-V S1 (right) over a 10°x10° tile located in Western Europe (01-10/10/2020)

The differences in product completeness for SY_V10 in comparison to PROBA-V S10 are limited (Table 35). This indicates that the combination of both S3A and S3B in one single SY_V10 product would have limited impact on product completeness.

Table 35: Occurrence frequency of quality flags over land pixels for SY_V10 derived from S3A and S3B in comparison to PROBA-V S10, over 6 10°x10° tiles, 01/07/2020 – 30/09/2020

% over land	Clear	Cloud	Snow/ice	Shadow	Uncertain
SY_V10 S3A	95.8	3.0	0.0	-	1.1
SY_V10_S3B	96.1	3.0	0.1	-	0.9
PROBA-V S10	95.8	3.3	0.0	0.9	0.0

2. Statistical consistency of TOA reflectances (SY_VGP vs. PROBA-V L2A)

Figure 151 shows the distribution of the systematic differences and mean bias per match-up. The statistics show a large range, caused by angular effects (i.e., large ranges in illumination and observation angles for the different observations). For bands B0 (blue), B2 (red) and B3 (NIR), a mean bias of around 3% is observed, with SY_VGP being brighter than PROBA-V L2A (Figure 151). This is related to differences in absolute calibration, but also to the fact that SPOT4-VGT1 spectral response functions are used in the spectral band mapping procedure to generate SYN VGT products.

Both the systematic differences and the mean bias indicate large inconsistencies between SY_VGP and PROBA-V L2A for the MIR band, with biases of around 8%. This can be largely attributed to the calibration issues of SLSTR, as reported in [5].

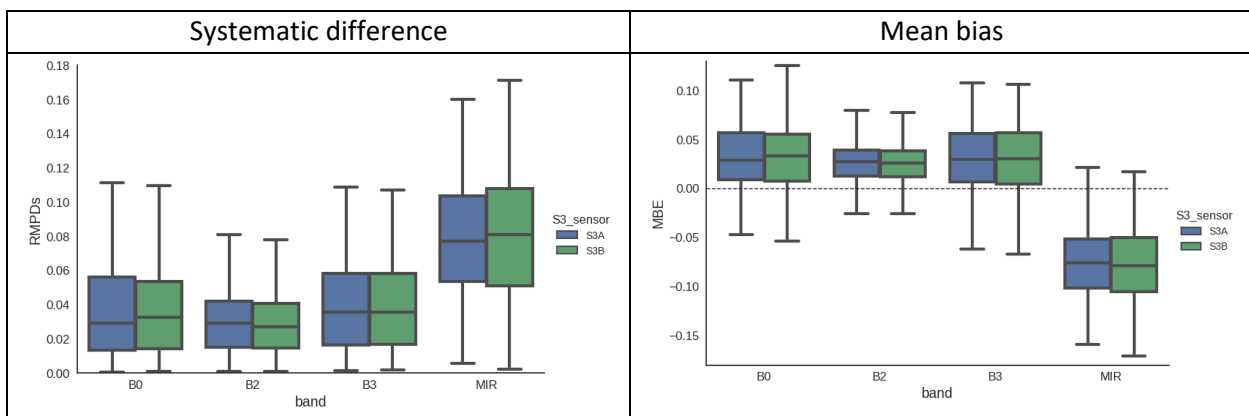


Figure 151: Systematic difference (left) and mean bias (right) between SY_VGP and PROBA-V L2A per band and per S3 sensor (01-10/10/2020)

3. Statistical consistency of TOC reflectances (SY_V10 vs. PROBA-V S10)

Figure 152 shows the distribution of the systematic differences and mean bias per match-up (N=9 for both S3A and for S3B). Similar to the intercomparison at TOA level, the bias for the MIR band is around 8%. The bias for B0 is relatively small (1%), while B2 and B3 remain 2% to 3% brighter compared to PROBA-V S10. The consistency is slightly better for S3B compared to S3A, possibly related to differences in radiometric calibration between S3A-OLCI and S3B-OLCI. The impact of the atmospheric correction (e.g., the impact of spectral response functions in LUT generation) needs further investigation.

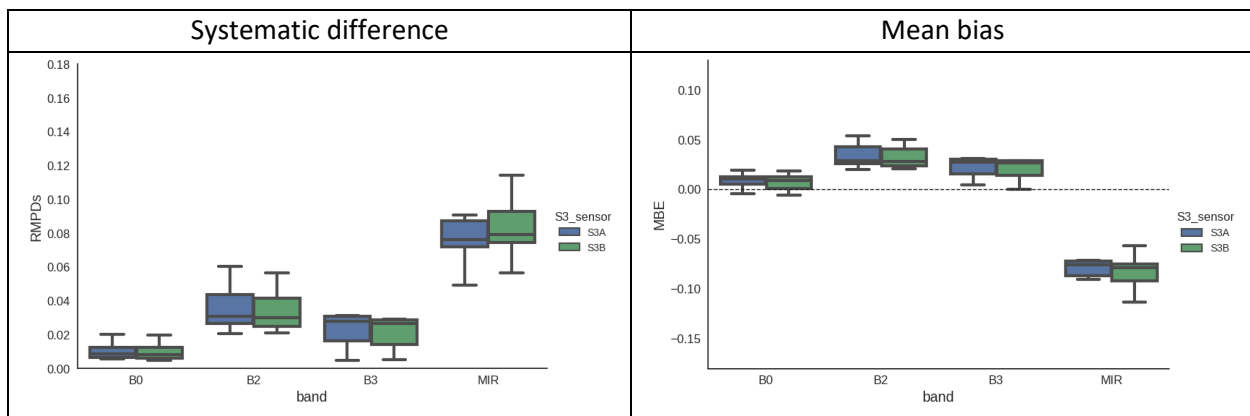
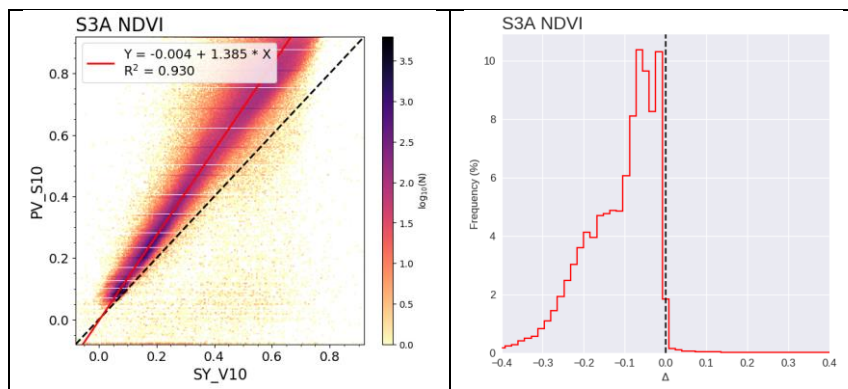


Figure 152: Systematic difference (left) and mean bias (right) between SY_V10 and PROBA-V S10 per band and per S3 sensor (01/07/2020 – 30/09/2020)

4. Statistical consistency of NDVI (SY_V10 vs. PROBA-V S10)

The statistical consistency analysis of SY_V10 NDVI in comparison to PROBA-V S10 NDVI indicates large inconsistencies between both datasets (Figure 153). The systematic bias is 0.13 and the MBE is -0.11 for both S3A and S3B. SY_V10 largely underestimates the NDVI. This is related to the fact that the NDVI in the SY_V10 product is based on TOA reflectances, instead of TOC reflectances.



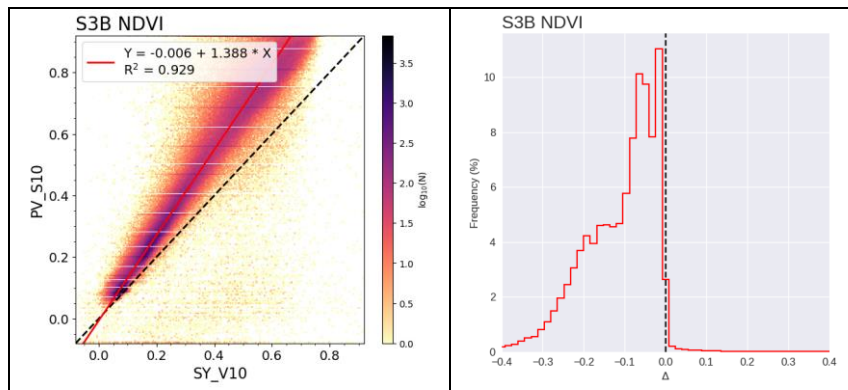


Figure 153: Statistical consistency of SY_V10 NDVI vs. PROBA-V S10 NDVI: scatter density plots and GM regression (left), bias frequency plots (right)

7.2.2.4 Conclusions

A number of issues in the SYN VGT processing line are impacting the quality of the S3 SYN VGT products, and hamper the consistency with the SPOT-VGT (1998-2014) and PROBA-V (2013-2020) data archives:

- ❖ SY_VG1 and SY_V10 NDVI products are based on TOA reflectances instead of TOC reflectances.
- ❖ In the spectral resampling procedure, SPOT4-VGT1 spectral response functions (SRFs) are used. Better consistency would be reached when using SPOT5-VGT2 (or PROBA-V) SRFs.
- ❖ Large systematic differences for SWIR are related to the absolute calibration of SLSTR. Whether this can be tackled by applying the proposed correction factors [5] still needs to be investigated.
- ❖ S3A and S3B are not combined in one composite product (VG1 and V10).
- ❖ No cloud shadow detection is done for the SYN VGT products.
- ❖ Interpolation errors, artefacts in the AOT and artefacts in the land/sea mask cause visual artefacts (see previous APR).

While a number of recently solved issues have improved the quality of the SYN VGT products (e.g., the temporal compositing schemes for SY_V10 and SY_VG1), a reprocessing action on the SYN VGT archive is required for users to have access to a continuous consistent data series, and to allow for consistency analysis with nominal PROBA-V data.

7.2.2.5 References

- [1] M. Claverie, E. F. Vermote, M. Weiss, F. Baret, O. Hagolle, and V. Demarez, "Validation of coarse spatial resolution LAI and FAPAR time series over cropland in southwest France," *Remote Sens. Environ.*, vol. 139, pp. 216–230, 2013, doi: 10.1016/j.rse.2013.07.027.
- [2] E. Vermote, C. O. Justice, and F. M. Bréon, "Towards a generalized approach for correction of the

BRDF effect in MODIS directional reflectances," *IEEE Trans. Geosci. Remote Sens.*, vol. 47, no. 3, pp. 898–908, 2009, doi: 10.1109/TGRS.2008.2005977.

- [3] L. Ji and K. Gallo, "An agreement coefficient for image comparison," *Photogramm. Eng. Remote Sens.*, vol. 72, no. 7, pp. 823–833, Jul. 2006, doi: 10.14358/PERS.72.7.823.
- [4] G. Duveiller, D. Fasbender, and M. Meroni, "Revisiting the concept of a symmetric index of agreement for continuous datasets," *Sci. Rep.*, vol. 6, no. January, pp. 1–14, 2016, doi: 10.1038/srep19401.
- [5] D. Smith, "Assessment of visible and short wavelength radiometric calibration using vicarious calibration methods," 2020.

8 Problems encountered in the reporting period

8.1 Product Notices Reports

Product notices are issued when a new processing baseline is deployed. Hereafter, for each instrument, the list of product notices issued are displayed.

8.1.1 OLCI

Table 36: List of OLCI Product Notices issued in 2020

Level	Thematic	Reference	Date of issue	Version	Last update	Comments
L2	Land	S3.PN.OLCI-L2L.03	23/06/2020	1.0		PB 2.66 (S3A) and PB 1.40 (S3B)

8.1.2 SLSTR

Table 37: List of SLSTR Product Notices issued in 2020

Level	Thematic	Reference	Date of issue	Version	Last update	Comments
L1	Global	S3.PN.SLSTR-L1.07	15/01/2020	1.0		PB 2.59 (S3A) and PB 1.31 (S3B)
L2	Land	S3.PN.SLSTR-L2L.03	15/01/2020	1.0		PB 2.61 (S3A) and PB 1.33 (S3B)
L2	FRP	S3.PN.SLSTR-FRP.01	18/03/2020	1.0		PB 2.64 (S3A) and PB 1.37 (S3B)
L1	Global	S3.PN.SLSTR-L1.07	09/06/2020	1.1		PB 1.40 (S3B)
L2	FRP	S3.PN.SLSTR-FRP.02	19/08/2020	1.0		PB 2.70 (S3A) and PB 1.46 (S3B)

8.1.3 SYN

Table 38: List of SYN Product Notices issued in 2020

Level	Thematic	Reference	Date of issue	Version	Last update	Comments
L2	Land	S3.PN.SYN-L2.05	15/01/2020	1.0		PB 2.56 (S3A) and PB 1.28 (S3B)
L2	Land	S3.PN.SYN-L2.06	23/06/2020	1.0		PB 2.66 (S3A) and PB 1.40 (S3B)

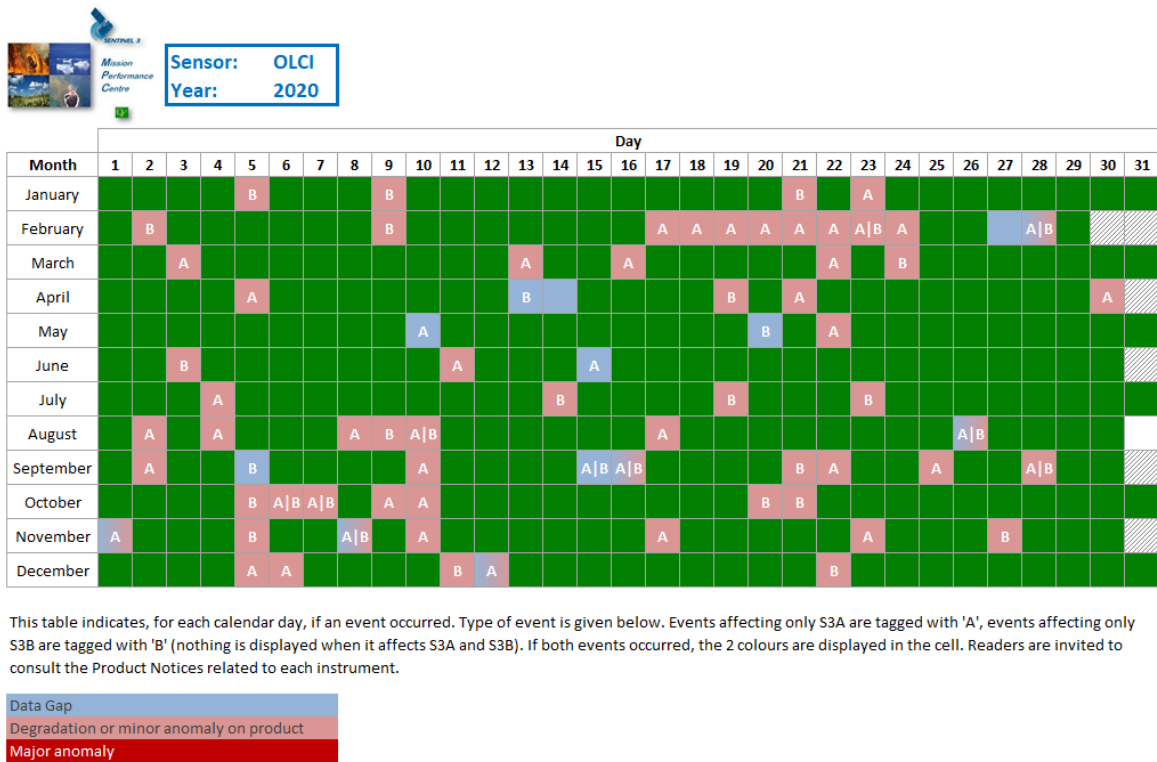
8.2 Instrument anomalies

8.2.1 OLCI

The OLCI anomalies or events recorded by the S3MPC operators in 2020 are displayed in 2 forms:

- ❖ A calendar view, in Figure 154
- ❖ A table providing more details is available at

<https://sentinel.esa.int/documents/247904/3810702/OLCI-Anomaly-Events.pdf>



© S3MPC

Figure 154: OLCI anomalies/events in 2020

8.2.2 SLSTR

The SLSTR anomalies or events recorded by the S3MPC operators in 2020 are displayed in 2 forms:

- ❖ A calendar view, in Figure 155
- ❖ A table providing more details is available at

<https://sentinel.esa.int/documents/247904/3810820/SLSTR-Anomaly-Events.pdf>



Sensor: SLSTR
 Year: 2020

Month	Day																																	
	1	2	3	4	5	6	7	8	9	10	11	12	13	14	15	16	17	18	19	20	21	22	23	24	25	26	27	28	29	30	31			
January					B				B													B												
February			A	A	A B	A	A	A	A	A	A													B						A				
March									B	A	B					A							A	B				A			B			
April				A	B		B						B	B A								A	B								A			
May													A	A	A	A	A	A	A	A	A	A	A								B			
June	B		B								A				A	A	A	A														B		
July				A									A		A									B				B	B	A B		B	B	
August	B	A			A B			B A	B A	B A				A		B		A												A B				
September		A	B	A B		B					A			A B		B A	B A														B	A		
October	A	A	A		A	A	A B							A						B			B	B	A B						A			
November								B A		A	B	B	B						A													B		
December		A			A	A										A B																		

This table indicates, for each calendar day, if an event occurred. Type of event is given below. Events affecting only S3A are tagged with 'A', events affecting only S3B are tagged with 'B' (nothing is displayed when it affects S3A and S3B). If both events occurred, the 2 colours are displayed in the cell. Readers are invited to consult the Product Notices related to each instrument. In case of **Decontamination**, data are usually not available; if they are, they shall not be used.

Data Gap
Degradation or minor anomaly on product
Major anomaly
Decontamination

© S3MPC

Figure 155: SLSTR anomalies/events in 2020

8.2.3 SYN

The SYN anomalies or events recorded by the S3MPC operators in 2020 are displayed in 2 forms:

- ❖ A calendar view, in Figure 156
- ❖ A table providing more details is available at

<https://sentinel.esa.int/documents/247904/3810953/SYNergy-Anomaly-Events.pdf>



Sensor: SYN
 Year: 2020

Month	Day																															
	1	2	3	4	5	6	7	8	9	10	11	12	13	14	15	16	17	18	19	20	21	22	23	24	25	26	27	28	29	30	31	
January									B									A			B		A						B			
February		B	A	A	A	B	A	A	A	A	A						A			A				B	A							
March												A				A							A	B								
April					A	B		B		A	A		B	A	B				B				B		B						A	
May										A			A	A	A	A	A	A	A	A	B	A	A									
June			B								A					A	A															
July				A										B										B	B	A	B		B			
August		A		A	B				B	A		B			B		A															
September	A	B	A			A				A						A	B	A	B				B	A								
October				B		A	A	B		A									B			B	B	B								
November	A				B			A	B		A	B	B	B				A							A							
December		A			A	A							A				A	B							B							

This table indicates, for each calendar day, if an event occurred. Type of event is given below. Events affecting only S3A are tagged with 'A', events affecting only S3B are tagged with 'B' (nothing is displayed when it affects S3A and S3B). If both events occurred, the 2 colours are displayed in the cell. Readers are invited to consult the Product Notices related to each instrument.

Data Gap
SYN specific anomaly
OLCI or SLSTR anomaly which impacts SYN products

© S3MPC

Figure 156: SYN anomalies/events in 2020



Sentinel-3 MPC
S3MPC OPT Annual Performance
Report - Year 2020

Ref.: S3MPC.ACR.APR.007
Issue: 1.1
Date: 28/04/2021
Page: 214

End of document